Copyright

by

David Wayne Neilsen

1999

Extremely Relativistic Fluids in Strong-Field Gravity

by

David Wayne Neilsen, B.S., M.S.

Dissertation

Presented to the Faculty of the Graduate School of

The University of Texas at Austin

in Partial Fulfillment

of the Requirements

for the Degree of

Doctor of Philosophy

The University of Texas at Austin

December 1999

Extremely Relativistic Fluids in Strong-Field Gravity

Approved by
Dissertation Committee:

To Grace from outer space.

Acknowledgments

It is a pleasure to sincerely thank Matthew Choptuik for all of his help, encouragement, and guidance during the course of my graduate studies in Texas. I could not have chosen a better advisor and teacher.

I also appreciate the members of the Center for Relativity—past and present—for their friendship and help while traveling neighboring geodesics.

I owe special gratitude to my parents, Wayne and Wanda Neilsen, for their love and support over many years.

Finally, my deepest love and appreciation go to Tracianne, who makes the sun shine even on cloudy days.

This work was supported in part by the National Science Foundation under Grants PHY93-18152 (ARPA supplemented), PHY94-07194, PHY97-22068, by a Texas Advanced Research Project grant, and by an NPACI award of computer time.

David Wayne Neilsen

The University of Texas at Austin
December 1999

Extremely Relativistic Fluids in Strong-Field Gravity

Publication No. ____________________

David Wayne Neilsen, Ph.D.
The University of Texas at Austin, 1999

Supervisor: Matthew William Choptuik

This dissertation is primarily concerned with the numerical solution of Einstein-fluid systems, focusing on extremely relativistic fluids at the threshold of black hole formation in critical gravitational collapse.

A new computer code is presented for studying critical phenomena in spherical symmetry. The perfect fluid obeys the ultrarelativistic state equation $P = (\Gamma - 1)\rho$, where Γ is a constant, $1 < \Gamma \leq 2$. The code, using Roe's linearized Riemann solver, is capable of simulating the extremely relativistic flows—Lorentz factors greater than one thousand—encountered in critical collapse. The high performance is achieved through a novel definition of the fluid variables, and care in calculating the fluid variables.

The study of perfect fluid critical collapse is restricted to the ultrarelativistic ("kinetic-energy-dominated", "scale-free") limit where black hole formation is anticipated to turn on at infinitesimal black hole mass (Type II behavior). The critical solutions are found by solving the system of ODEs which result from a self-similar *ansatz, and* by solving the full Einstein-fluid PDEs in spherical symmetry. These latter PDE solutions extend the pioneering work of Evans and Coleman ($\Gamma = 4/3$) and verify that the continuously self-similar solutions previously found by Maison and Hara *et al.* for $1.05 \leq \Gamma \lesssim 1.89$ *are* (locally) unique critical solutions. In addition, strong evidence is given that globally regular critical solutions *do* exist for $1.89 \lesssim \Gamma \leq 2$, that the sonic point for $\Gamma_{\rm dn} \simeq 1.8896244$ is a degenerate node, and that the sonic points for $\Gamma > \Gamma_{\rm dn}$ are nodal points, rather than focal points as previously reported. Mass-scaling exponents for all of the critical solutions are calculated by evolving near-critical initial data, with results which confirm and extend previous calculations based on linear perturbation theory.

The final chapters describe a new two-dimensional perfect fluid code which uses higher order Godunov methods. The fluid is coupled to a simplified—if unphysical—scalar gravitational model. The code is tested by evolving a spherically symmetric, static solution. The code's capabilities for solving dynamic axisymmetric systems is demonstrated by colliding two objects centered on the symmetry axis.

Contents

Acknowledgments **v**

Abstract **vi**

List of Tables **ix**

List of Figures **x**

Chapter 1 Introduction **1**

1.1 Conventions and notation 6

Chapter 2 Theoretical Foundation **8**

2.1 Geometry 9

2.2 The perfect fluid 14

2.3 The classical (Newtonian) perfect fluid equations 17

2.4 Equations of state 18

  2.4.1 Relativistic ideal gas 18

  2.4.2 Ultrarelativistic equation of state 20

  2.4.3 Cold nuclear matter equation of state 21

  2.4.4 A simple nuclear equation of state 21

2.5 Derivation of equations 22

2.6 Solving for the primitive variables 27

2.6.1 Ultrarelativistic equation of state 28
2.6.2 Ideal gas equation of state 29
2.7 Spectral decomposition 30
2.8 Simple exact solutions 33
2.8.1 The Riemann initial value problem 34
2.8.2 The Tolman-Oppenheimer-Volkoff solution 35
2.9 The $P = \rho$ perfect fluid and a massless scalar field 44

Chapter 3 Numerical methods **47**

3.1 Finite differences 48
3.1.1 Two example finite-difference schemes 50
3.1.2 Error and numerical solutions 52
3.2 Conservation laws 56
3.3 Godunov's method 58
3.4 The Reconstruct-Solve-Average algorithm 60
3.4.1 Slope Limiters 62
3.4.2 Other reconstructions 66
3.5 Approximate Riemann solvers 67
3.5.1 Nonlinear solvers 68
3.5.2 The Harten-Lax-van Leer-Einfeldt approximate Riemann solver 68
3.5.3 Roe's approximate Riemann solver 72
3.5.4 An "entropy fix" for the Roe solver 75
3.5.5 Marquina's method 76
3.6 The failure of approximate Riemann solvers 78
3.7 Method of Lines 79
3.8 Boundary conditions 80
3.9 Numerical tricks for ultrarelativistic flow 82
3.9.1 Floor 82

3.9.2 Calculation of primitive variables: ultrarelativistic equation of state 83
3.9.3 Calculation of primitive variables: ideal-gas equation of state 84

Chapter 4 Spherical symmetry **87**
4.1 The ADM equations for spherical symmetric fluids 88
4.2 The fluid equations 89
4.2.1 New conservative fluid variables 91
4.3 Characteristic structure 92
4.4 Numerical algorithm 94
4.4.1 The floor 95
4.4.2 Regularity and boundary conditions 96
4.4.3 Grid 97
4.4.4 Details of the integration procedure 99
4.5 Tests 104

Chapter 5 Critical phenomena (Type II) **122**
5.1 Introduction to critical phenomena 122
5.1.1 Basic properties of critical solutions 123
5.1.2 Critical solutions and one-mode instability 124
5.1.3 Critical solutions and self-similarity 125
5.1.4 Review of previous perfect-fluid studies 128
5.2 Fluid equations 131
5.2.1 The sonic point 134
5.2.2 Solving the ordinary differential equations 137
5.2.3 Degenerate node 138
5.2.4 $\Gamma = 2$ 146
5.3 The full PDE critical solutions 147

5.3.1 Initial data 147

5.3.2 The transformation from r to x 148

5.3.3 Results 152

5.3.4 Mass scaling 154

5.3.5 Ideal gas equation of state 155

Chapter 6 A two-dimensional fluid code **162**

6.1 The fluid equations for the two-dimensional code 164

6.2 Numerical methods 165

6.2.1 Calculating the primitive variables 166

6.2.2 Riemann initial value problem tests 167

6.3 Axial symmetry 167

6.4 Conclusion 173

Chapter 7 Scalar gravity **174**

7.1 The scalar gravity model 176

7.2 Potentially “negative” matter? 178

7.3 Conserved quantities: the tale of three masses 180

7.4 Gravitational radiation 180

7.5 The spherically symmetric static solution 181

7.6 Axisymmetric scalar gravity 186

Chapter 8 Conclusion **203**

Bibliography **206**

Vita **220**

List of Tables

3.1 Table of finite difference approximations. 49
3.2 Definition of various norms 55

5.1 Classifications of the sonic point using ϑ. 146
5.2 The mass-scaling exponent γ as a function of the adiabatic constant Γ. 158

List of Figures

2.1 A schematic diagram of two hypersurfaces in the ADM formulation of general relativity showing the lapse and shift. 11
2.2 A schematic diagram of a fluid shock tube's initial configuration. . . 33
2.3 A space-time diagram of a shock tube problem showing the waves and principal parts of the solution. 34
2.4 A single state labeled 'A' is shown in this $P - v$ diagram, and the lines indicate all other states that can be connected to A by either rarefaction or shock waves. 36
2.5 The graphical solution of the Riemann problem in the non-relativistic regime. 37
2.6 The graphical solution of the Riemann problem in the relativistic regime for a $\Gamma = 5/3$ fluid. 38
2.7 Plots of the total mass vs. the central density and radius, respectively, for a Tolman-Oppenheimer-Volkoff (TOV) star. 39
2.8 The relative error in the Central density of TOV star vs. time in the evolution of a stable star. 40
2.9 The relative error in the Central density of TOV star vs. time in the evolution of a stable star near an inflection point. 41
2.10 Central density of TOV star vs. time for an unstable configuration . 42

3.1 The three frames of this plot show different ways a discretized function can be reconstructed in a control-volume numerical method. . . 63
3.2 The four slope limiters discussed in the text are demonstrated here by solving the advection equation. 64
3.3 A shock tube test with the HLLE approximate Riemann solver, for a $\Gamma = 5/3$ fluid. 69
3.4 A shock tube test with the HLLE approximate Riemann solver, for a $\Gamma = 5/3$ fluid. 70
3.5 Pseudo-code for the primitive variable solver using Newton's method for the ideal-gas state equation, optimized for ultrarelativistic flow. . 85

4.1 These plots show various fluid quantities at four different instances (equally spaced in time) in a flat spacetime, slab-symmetric evolution with $\Gamma = 1.9$. The initial configuration is a time-symmetric Gaussian pulse. 93
4.2 The radial grid, r, is created with logarithmic spacing using a uniform grid, U, in log-space. This figure graphically displays the connection between r and U. 100
4.3 Illustration of the re-meshing algorithm used in investigations of critical collapse. 101
4.4 The number of grid points as a function of time for a $\Gamma = 2$ near critical evolution. 102
4.5 Illustration of some of the convergence properties of the solution algorithm discussed in the text. 105
4.6 The residual of the Hamiltonian constraint, written here as $\mathrm{Res}(a)$, for a $\Gamma = 1.9$ sub-critical evolution near the threshold of black hole formation. 107

4.7 The shock compression of a diffuse relativistic gas is demonstrated in this shock tube test of a $\Gamma = 4/3$ fluid. 109
4.8 The shock compression of a relativistic fluid is shown in this shock tube test for $\Gamma = 4/3$. 110
4.9 A shock tube test with a $\Gamma = 5/3$ fluid at $t = 0.4$ 111
4.10 A relativistic shock tube test of a $\Gamma = 1.6$ fluid using the minmod limiter. 112
4.11 A relativistic shock tube test of a $\Gamma = 1.6$ fluid using the MC-limiter. 113
4.12 This figure shows the independent residual test for a subcritical evolution of a $\Gamma = 2$ fluid at $t = 0.62$. 115
4.13 Detail near the origin of the independent residual test for a subcritical evolution of a $\Gamma = 2$ fluid at $t = 0.62$. 117
4.14 A plot of $\ln ||\mathrm{Res}(E)||_2 / \ln ||E||_2$ as a function of time for a subcritical evolution at three different resolutions. 118
4.15 A plot of $\ln ||\mathrm{Res}(a)||_2$ as a function of time for a subcritical evolution at three different resolutions. 119
4.16 This figure shows a small "glitch" in E that develops at the floor level after the fluid rebounds from the origin in the subcritical evolution of Figure **??**. 120
4.17 The residual of the Hamiltonian constraint for a $\Gamma = 2$ sub-critical solution calculated with three different floors at the same resolution. 121

5.1 A schematic diagram showing a continuously self-similar (CSS) pulse at five different times as it moves toward the origin $r = 0$. 126
5.2 The geometric variable a of the critical solution for several values of Γ. 139
5.3 The fluid variable ω of the critical solution for several values of Γ. The sonic point is at $x = 0$. 140

5.4 The fluid velocity v of the critical solution for several values of Γ. The sonic point is at $x = 0$. 141
5.5 The logarithm of the Lorentz factor for the fluid velocity, $W = 1/\sqrt{1 - v^2}$, of the critical solution for several values of Γ. 142
5.6 The degeneracy of the eigenvalues in the perfect fluid critical solution as $\Gamma \to \Gamma_{\rm dn}$. 143
5.7 The $\Gamma = 1.9$ critical solution. 149
5.8 The $\Gamma = 1.99$ critical solution. 150
5.9 The $\Gamma = 2$ critical solution. 151
5.10 Illustration of black-hole mass scaling for the case $\Gamma = 2$. 156
5.11 The black hole mass as a function of critical parameter for $\Gamma = 2$ super-critical evolutions with three different floors with the same resolution. 157
5.12 A comparison of the critical solutions for the ideal-gas and ultrarelativistic equations of state for $\Gamma = 1.4$. 160
5.13 P and ρ_o are shown at the moment of maximum compression in this log-log plot of a marginally subcritical evolution of a $\Gamma = 1.4$ ideal gas. 161

6.1 Pseudo-code for the primitive variable solver using Newton's method in the two-dimensional code for the ideal-gas equation of state. . . . 168
6.2 A Riemann shock tube test performed with the 2D code with a $\Gamma = 4/3$ fluid. The initial discontinuity is along the diagonal. 169
6.3 A Riemann shock tube test performed with the 2D code with a $\Gamma = 5/3$ fluid. The initial discontinuity is along the diagonal. 170
6.4 Shock heating of a $\Gamma = 5/3$ fluid calculated with the 2D code. The initial discontinuity is along the diagonal 171

7.1 Spherically symmetric, static "star" solutions in scalar gravity for $\Gamma = 1.35$ for $0.1 \leq k \leq 2$. 182
7.2 Spherically symmetric, static "star" solutions in scalar gravity for $\Gamma = 1.35$ for $3 \leq k \leq 6.5$. 183
7.3 Spherically symmetric, static "star" solutions in scalar gravity for $\Gamma = 1.35$ for $6.9921875 \leq k \leq 6.999998092651367$. 184
7.4 Spherically symmetric, static "star" solutions in scalar gravity for $\Gamma = 1.35$ for $7.01 \leq k \leq 10$. 185
7.5 The central density of a "star" in scalar gravity and the ℓ_2 norm of the error from a two-dimensional evolution. 190
7.6 The central Ψ of a "star" in scalar gravity and the ℓ_2 norm of the error from a two-dimensional evolution. 191
7.7 A time series showing v^R for a scalar gravity static star. 192
7.8 A time series showing ρ_o for a two-body collision. 193
7.9 A time series showing ρ_o for a two-body collision (continued). 194
7.10 A time series showing v^z for a two-body collision. 195
7.11 A time series showing v^z for a two-body collision (continued). 196
7.12 A time series showing v^R for a two-body collision. 197
7.13 A time series showing v^R for a two-body collision (continued). 198
7.14 A time series showing Ψ for a two-body collision. 199
7.15 A time series showing Ψ for a two-body collision (continued). 200
7.16 A time series showing Ξ for a two-body collision. 201
7.17 A time series showing Ξ for a two-body collision (continued). 202

Chapter 1

Introduction

One of the most surprising discoveries in general relativity, Albert Einstein's theory of gravitation, is the possibility of inexorable gravitational collapse. This type of collapse can begin when a massive star—much heavier than our sun—exhausts its fuel supply, and the nuclear reactions at the star's center, which have hitherto supported the star's weight, come to a halt. The collapsed star leaves behind a region of space called a black hole, where the gravitational force—or spacetime curvature, in the language of general relativity—is so strong, that not even light can escape. The collapse of a dying star is just one possible way to form a black hole; a variety of circumstances can lead to black hole formation. Black holes can also form in the collision of two stars, which individually are stable, but their combined mass triggers the onset of collapse. This scenario is currently of interest because this system will generate gravitational waves, which may soon be detectable here on Earth.

Black holes are fascinating objects in and of themselves, and considerable research has been devoted towards understanding their peculiar properties. Physics near a black-hole can be counter-intuitive, and historically, some early, insightful questions have proven crucial in guiding productive lines of inquiry. Recently, intriguing behavior was discovered in gravitational collapse near the threshold for black hole formation, and this discovery was prompted by such a question. Demetrios Christodoulou [38, 39, 40, 41] studied a massless, spherically symmetric, scalar field in general relativity. Beginning with an arbitrary configuration of a scalar field at an initial time, Christodoulou was able to prove that at late times, the scalar field either dispersed to infinity, or was trapped in a black hole. However, his work could not address specific questions about the black hole's formation, and particularly, it could not answer whether a black hole needed some minimum mass before it could form, or rather a black hole could be as small as desired. Christodoulou posed the question to Matthew Choptuik: Does a black hole have a minimum, finite mass, or can it have an infinitesimal mass? In answering this question, Choptuik discovered rich, generic behavior in gravitational collapse, and initiated an exciting subfield in numerical relativity. (This *critical phenomena* is not unique to general relativity, but appears in a variety of physical models, independent of gravitation.)

To answer Christodoulou's question, Choptuik studied the Einstein/scalar-field system using the full set of partial differential equations. Using careful numerical analysis, he created families of initial data characterized by a single parameter, p, and then solved the Einstein/scalar-field equations to determine the future state of the scalar field. By varying the p in a bisection search, Choptuik found a solution that exists precisely on the verge of black-hole formation. This solution, called the *critical solution,* is inherently unstable—the smallest deviation in p leads either to the formation of a black hole, or the dispersal of the field to infinity. While these solutions most likely play no role in our universe—the chances of encountering a critical solution in nature are akin to the odds of finding a pencil perfectly balanced on its point—these solutions display unique behavior, including scale-invariance, scaling, and universality, which make them especially interesting. Here we briefly discuss these properties of critical solutions; a more complete discussion is given in Chapter 5.

The critical solution is *universal,* meaning that it is independent of the initial scalar field configuration. The careful tuning of any initial data family always produces the same critical solution. This characteristic of critical solutions is now understood in light of the critical solution's stability properties, as shown by studies using perturbation theory. The critical solutions have a single unstable mode, which can be suppressed by carefully tuning the initial data, making them the most stable members of naturally unstable solutions.

During the collapse, as one examines smaller and smaller scales in both time and space, the spacetime and matter fields do not appear to change. Thus, critical solutions display an additional symmetry, *scale-invariance,* that is not observed in generical collapse. As the solution becomes smaller and smaller, relative to a fiducial scale, the curvature of spacetime increases until a singularity appears when the solution reaches the origin. As an event horizon, the signature of a black hole, has not formed, this uncovered singularity is "naked." At a naked singularity the predictive power of general relativity breaks down, a consequence counter to some of our most fundamental—and cherished—notions regarding predictability and causality in physics. The Cosmic Censorship Conjecture posits that a naked singularity can not generically be created, and thus far, this conjecture continues to hold.

When black holes form as the end result of near-critical initial data, their masses are well described by a simple scaling law. This law is also a direct consequence of the critical solutions single unstable mode, and the scaling behavior can be predicted by doing a perturbation analysis of the critical solutions.

The majority of this dissertation examines the critical behavior of a general relativistic perfect fluid. The perfect fluid is one of the most studied models for matter in general relativity, with wide application to astrophysical systems. The study of perfect fluid critical phenomena began with the pioneering work of Evans and Coleman [52], who found the critical solution for the radiation fluid with the equation of state $P = \frac{1}{3}\rho$. Additional insights came from subsequent work by Maison and Koike, Hara, and Adachi with the more general equation of state, $P = (\Gamma - 1)\rho$, where Γ is a constant. Maison and Koike *et al.* used the scale-invariance property to construct solutions for $\Gamma \lesssim 1.89$, and used perturbation theory to verify that they had a single unstable mode (in spherical symmetry), and thus predicted the scaling behavior of the black hole masses. The work here traces the approach of Evans and Coleman in a study of critical phenomena in spherical symmetry. I develop a new, robust computer code to solve the full Einstein-fluid equations and directly study the dynamically constructed critical solutions, verifying that the solutions for $\Gamma \lesssim 1.89$ discovered by Maison and Koike *et al.* are the critical solutions, i.e., they exist at the threshold of black hole formation, as well as finding the critical solutions for $1.89 \lesssim \Gamma \leq 2$. The scale-invariance property is then used to generate all of these solutions analytically.

The second part of the dissertation moves beyond spherical symmetry, and begins the first steps towards multi-dimensional problems. Although most studies of critical phenomena focus on the spherically symmetric problem, studies of axisymmetric critical solutions from a perturbation stand point have begun. Here a new computer code for relativistic fluids in two-dimensions is presented. This code is designed to solve the fluid equations for an arbitrary spacetime, although currently only static spacetimes are possible. The code is demonstrated using a simple gravitational model called *scalar gravity,* where the gravitational force is given by the four-gradient of a scalar field, which obeys a nonlinear wave equation. While this theory is not physical, failing the classical tests of general relativity, it provides a simple means to incorporate gravitation into our fluid code. While this work is really in its infancy, this dissertation concludes with a proof-of-principle, showing the evolution of a two-body collision in cylindrical coordinates.

The journey begins in Chapter 2, where the Einstein equations and perfect fluid equations of motion are written in a form compatible with numerical work. The presentation here is general, allowing for easy extension to the two-dimensional work that comprises the second part of this dissertation. This chapter also presents the equations of state used herein, and discusses the link between irrotational fluids and scalar fields.

Relativistic fluids are notoriously difficult to simulate numerically. While strong shocks and relativistic velocities often cause numerical methods to fail, methods based on Godunov's original work have proven especially reliable. Chapter 3 introduces these numerical methods, and further discusses techniques adapted for ultrarelativistic velocities. Some of the more mundane details, such as boundary conditions, are also discussed here.

After two chapters of generalities, we finally get down to cases, and discuss a robust code for spherically symmetric, fully relativistic fluids. This code was designed to study perfect fluid critical solutions, especially as $\Gamma \rightarrow 2$, and these physical results are presented in the following chapter. A change of computational variables is advantageous in spherical symmetry, and this chapter provides all relevant information for implementing this code. Extensive tests of this code are also presented, including a demonstration of convergence in the *strong-field* regime.

Chapter five presents our extensive study of perfect fluid critical solutions. The chapter begins with an introduction to perfect fluid critical phenomena, more complete and technical than given above. The scale-invariant symmetry is used to reduce the Einstein-fluid equations to a set of ordinary differential equations, which are then solved numerically for the critical solution. The solutions for $\Gamma \gtrsim 1.89$ are of primary interest, and can be found using very careful numerical analysis. Exploiting the arbitrary-precision capabilities of *Maple V*, a computer program for symbolic manipulation, we thoroughly investigate the solutions near $\Gamma \approx 1.89$, and find that the sonic point is a degenerate node for $\Gamma_{\rm dn} \simeq 1.8896244$, rather than a focal point as previously reported. Using the code described in the previous chapter, we examine the perfect fluid critical solutions for the full range of Γ, $1.05 \leq \Gamma \leq 2$. In addition to confirming the expected picture for $1.05 \leq \Gamma \leq 1.889$, we present further evidence that one-mode unstable CSS solutions exist in the regime $\Gamma \gtrsim 1.89$, up to and including, the limiting case $\Gamma = 2$, and use the code to compute mass scaling exponents in the regime $1.89 \lesssim \Gamma \leq 2$.

Chapter 6 briefly introduces the two-dimensional fluid code. While this code is still being developed, preliminary results indicate that this code can accurately solve the relativistic fluid equations for dynamic systems. Some shock tube tests are given, followed by some comments on axisymmetric systems in cylindrical coordinates.

The scalar gravity model is the topic of Chapter 7. Scalar gravity was originally a gravitational model for dust, and here the extension to perfect fluids is presented. The coupling of the scalar field to the perfect fluid presents immediate physical problems for $\Gamma > 4/3$, and therefore attention is restricted to $\Gamma = 4/3$. We then test our axisymmetric fluid code coupled to scalar gravity by evolving a static, spherically symmetric "star." The chapter closes with a demonstration of the axisymmetric code by colliding two spherically symmetric objects centered on the $R = 0$ axis.

Concluding remarks, and directions for future research are briefly discussed in Chapter 8.

1.1 Conventions and notation

Here we summarize the conventions and notation used in this dissertation:

- The metric has the signature $(-+++)$.
- The sign conventions of Misner, Thorne, and Wheeler [95] are used throughout.
- Geometric units are used throughout: $G = 1$ and $c = 1$. However, G is shown explicitly in some of the scalar gravity equations.

- Boldface *sans serif* letters are tensors (including four-vectors), e.g., $\mathsf{\mathbf{T}}$, $\mathsf{\mathbf{g}}$, $\mathsf{\mathbf{u}}$.

- Spatial three-vectors are written in bold italic with an arrow, e.g., $\vec{\boldsymbol{p}}$, $\vec{\boldsymbol{v}}$.

- Boldface Latin letters represent state vectors, e.g., $\mathbf{q}$, $\mathbf{f}$.

- The Einstein summation convention is implied by repeated upper and lower indices. Summations in non-tensor equations, e.g., numerical methods, are sometimes shown explicitly for clarity.

- Greek indices (α,β,γ, etc.) take the values 0, 1, 2, 3.

- Latin indices (a, b, c, etc.) take the values 1, 2, 3.

- The canonical spherical coordinate labels (t, r, θ, ϕ) do *not* sum as indices.

- The canonical cylindrical coordinate labels (t, R, z, θ) do *not* sum as indices.

- Partial differentiation is indicated by ∂, i.e. $\partial_x f \equiv \partial f/\partial x$.

- A colon (:) symbolizes a double contraction, e.g., $\mathsf{\mathbf{A}} : \mathsf{\mathbf{B}} \equiv A^{\mu\nu}B_{\mu\nu}$.

- ∇ is the covariant derivative operator compatible with the metric, $\nabla_\alpha g_{\beta\sigma} = 0$.

- Square brackets in indices denote the anti-symmetrization operation

$$T_{[\alpha\beta]} = \frac{1}{2!}\left(T_{\alpha\beta} - T_{\beta\alpha}\right).$$

Chapter 2

Theoretical Foundation

Einstein's theory of relativity is a geometric theory of gravitation, wherein the familiar gravitational forces of Newtonian mechanics are explained as the local curvature of spacetime. Since geometry is at the heart of relativity, it comes as no surprise that the theory is most elegantly expressed covariantly in terms of geometric objects, in this case tensors, which are generalizations of the familiar vectors. To study a particular system, however, the covariant formulation must be abandoned for a coordinate-dependent form. The Cauchy problem for general relativity is of particular concern to the numericist. Here initial data are given on a hypersurface, and one solves for the subsequent evolution of the system. The Einstein equations do not naturally lend themselves to solving the Cauchy problem, which inherently requires a separation of "space" and "time." Arnowitt, Deser, and Misner [4] (ADM) introduced a formulation of general relativity for solving the Cauchy problem, which is used in the numerical work presented here. This chapter introduces the perfect fluid, and writes the equations of motion for the general ADM metric. Four state equations are briefly presented, followed by a discussion of two exact solutions important for testing numerical codes. A discussion of a link between perfect fluids and massless scalar fields closes the chapter.

2.1 Geometry

Einstein's theory of general relativity unfolds on a manifold, $\mathcal{M}$, which is endowed with a metric, $\mathbf{g}$. The Einstein equations couple the spacetime geometry, encoded in the Einstein tensor, $\mathbf{G}$, to the stress-energy tensor, $\mathbf{T}$, associated with the energy (matter and fields) content of the spacetime:

$$\mathbf{G} = 8\pi\mathbf{T}. \tag{2.1}$$

In addition, the Einstein tensor also satisfies the contracted Bianchi identities

$$\nabla \cdot \mathbf{G} = 0, \tag{2.2}$$

which further require that

$$\nabla \cdot \mathbf{T} = 0. \tag{2.3}$$

This latter equation gives the equations of motion for the matter, and also represents the *local* conservation of energy and momentum.

The Einstein equations (2.1) are ten coupled, second order partial differential equations for the metric components $g_{\mu\nu}$. However, these equations are not all independent because their solution must also satisfy the contracted Bianchi identities (2.2), which in explicit index notation are

$$\partial_0 G^{0\nu} = -\partial_i G^{i\nu} - \Gamma^{\mu}{}_{\lambda\mu} G^{\lambda\nu} - \Gamma^{\nu}{}_{\lambda\mu} G^{\mu\lambda}. \tag{2.4}$$

The Einstein tensor, $\mathbf{G}$, contains second order derivatives of $\mathbf{g}$. The right-hand side of (2.4), therefore, contains only time derivatives of highest order ∂_0^2, and $G^{0\mu}$ therefore can contain only first order time derivatives. The equations

$$G_{0\mu} = 8\pi T_{0\mu} \tag{2.5}$$

therefore comprise four constraint equations. The remaining equations,

$$G_{ij} = 8\pi T_{ij}, \tag{2.6}$$

are six dynamical equations. This mixture of constraint and evolution equations arises from the covariant formulation of general relativity, which contains four coordinate degrees of freedom.

The Cauchy problem in general relativity consists of setting initial data on a hypersurface at an initial time, and then evolving the data forward in time with the Einstein equations. The initial value problem of interest here is where the initial data are specified on a *space-like* hypersurface. The ADM formulation of Einstein's equations is suited for solving this problem.

Arnowitt, Deser and Misner [4] introduced their 3+1 decomposition of spacetime in 1962. Several good introductions to this formulation of general relativity exist—see especially York [137], Choptuik [31], and Evans [50]—and here only a heuristic description is given. The ADM formalism slices the spacetime $\mathcal{M}$ into a sequence of space-like hypersurfaces, Σ_t, parameterized by a global time function t. $\mathbf{n}$ is the future-directed time-like vector field normal to Σ_t, providing a "connection" from one hypersurface to another. The metric $\mathbf{g}$ induces a spatial metric, $\boldsymbol{\gamma}$, on Σ_t with components γ_{ij} given by

$$\gamma_{ij} = g_{ij} + n_i n_j. \tag{2.7}$$

The mixed form of $\boldsymbol{\gamma}$ defines a projection tensor

$$\perp^{\mu}{}_{\nu} \equiv \delta^{\mu}{}_{\nu} + n^{\mu} n_{\nu}, \tag{2.8}$$

which projects tensors onto Σ_t. In particular, a covariant derivative on the hypersurface is

$$D_j \equiv \perp_j{}^{\nu} \nabla_{\nu}. \tag{2.9}$$

This covariant derivative operator, D_i, is compatible with the submetric $\boldsymbol{\gamma}$, in the sense that

$$D_i \gamma_{jk} = 0. \tag{2.10}$$

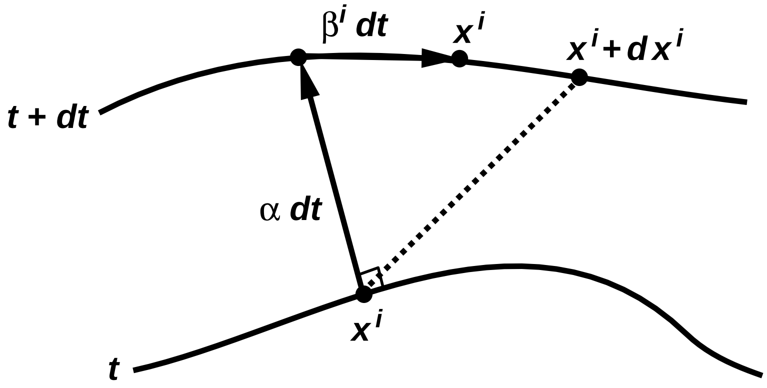

Figure 2.1: A schematic diagram of two hypersurfaces in the ADM formulation of general relativity showing the lapse and shift.

The spacetime description is completed by uniquely specifying how the slices are connected together. The connection is enabled by defining a lapse function, α, and a shift vector field, β^i (see Figure 2.1). The lapse gives the proper time between slices Σ_t and $\Sigma_{t+\mathrm{d}t}$ for observers moving normal to the slices. The shift describes how the coordinates x^i change from hypersurface to hypersurface. The general metric can then be written

$$\mathrm{d}s^2 = -\alpha^2\,\mathrm{d}t^2 + \gamma_{ij}\left(\mathrm{d}x^i + \beta^i\,\mathrm{d}t\right)\left(\mathrm{d}x^j + \beta^j\,\mathrm{d}t\right). \tag{2.11}$$

The first term is the proper time between Σ_t and $\Sigma_{t+\mathrm{d}t}$, and the second term gives the proper distance for a displacement within Σ. For future reference, the determinants of $g_{\mu\nu}$ and γ_{ij} are

$$g \equiv \det \mathbf{g} \tag{2.12}$$

$$\gamma \equiv \det \gamma_{ij}. \tag{2.13}$$

The determinants are related by

$$\sqrt{-g} = \alpha\sqrt{\gamma}. \tag{2.14}$$

The curvature of each individual hypersurface can be specified by calculating the Riemann or Ricci tensors of the intrinsic metric γ_{ij}. The spacetime curvature which describes the embedding of each Σ_t in the spacetime $\mathcal{M}$ is given by the *extrinsic curvature* tensor,

$$K_{ij} = K_{ji} = -\nabla_j n_i. \tag{2.15}$$

It can be shown that K_{ij} is the time derivative of the spatial metric components

$$K_{ij} = -\frac{1}{2}\pounds_{\mathbf{n}}\gamma_{ij}. \tag{2.16}$$

The geometric equations in the 3+1 formalism are found by projecting the Einstein equations along $\mathbf{n}$ and onto the hypersurface Σ_t. As a full description is not given here, we simply define the following projections of $\mathbf{T}$

$$\rho_{\mathrm{ADM}} \equiv n_\mu n_\nu T^{\mu\nu}, \tag{2.17}$$

$$j^\mu \equiv -\perp^\mu{}_\nu n_\lambda T^{\lambda\nu}, \tag{2.18}$$

$$S^{\mu\nu} \equiv \perp^\mu{}_\lambda \perp^\nu{}_\gamma T^{\lambda\gamma}. \tag{2.19}$$

The first geometric equation is the *Hamiltonian constraint*

$$^3R - K^i{}_j K^j{}_i + K^2 = 16\pi\rho_{\mathrm{ADM}}, \tag{2.20}$$

where ^3R is the trace of the three-dimensional Ricci tensor, $^3R_{ij}$, calculated from $\boldsymbol{\gamma}$

$$^3R \equiv \gamma_{ij}{}^3R^{ij}, \tag{2.21}$$

and K is the trace of the extrinsic curvature tensor

$$K \equiv g_{ij}K^{ij}. \tag{2.22}$$

The *momentum constraint* is

$$D_i K_i{}^j - D_i K = 8\pi j_i \tag{2.23}$$

The evolution equations are

$$\partial_t \gamma_{ij} = -2\alpha K_{ij} + \pounds_{\boldsymbol{\beta}} g_{ij}, \tag{2.24}$$

$$\begin{aligned} \partial_t K_{ij} = & -D_i D_j \alpha + \alpha \left[R_{ij} + K K_{ij} - 2K_{im} K^m{}_j \right] + \pounds_{\boldsymbol{\beta}} K_{ij} \\ & -\alpha \left[S_{ij} - \frac{1}{2} g_{ij} (S - \rho_{\mathrm{ADM}}) \right], \end{aligned} \tag{2.25}$$

where

$$\pounds_{\boldsymbol{\beta}} g_{ij} = D_i \beta_j + D_j \beta_i \tag{2.26}$$

$$= \beta^k \partial_k g_{ij} + g_{kj} \partial_i \beta^k + g_{ik} \partial_j \beta^k, \tag{2.27}$$

$$\pounds_{\boldsymbol{\beta}} K_{ij} = \beta^m \partial_m K_{ij} + K_{mj} \partial_i \beta^m + K_{im} \partial_j \beta^k. \tag{2.28}$$

The metric (2.11) is often written

$$\mathrm{d}s^2 = -\left(\alpha^2 - \beta_i \beta^i\right) \mathrm{d}t^2 + 2\beta_i \, \mathrm{d}t \, \mathrm{d}x^i + \gamma_{ij} \, \mathrm{d}x^i \, \mathrm{d}x^j. \tag{2.29}$$

The overdetermined nature of the the Einstein equations allows some freedom in solving the system. One may choose to update (or evolve) one or more of the geometric variables γ_{ij}, K_{ij} using some of the constraints (2.20)–(2.23), instead of the evolution equations, (2.24)–(2.25). This is called a *constrained evolution.* However, numerical methods for solving hyperbolic equations are generally simpler and faster than those for elliptic equations, and often only the evolution equations are used to solve the system. In this *free evolution,* the initial data is chosen to satisfy the constraints, then the contracted Bianchi identities guarantee that the constraints are satisfied throughout an evolution

$$\nabla_0 \left(G^{0\mu} - T^{0\mu}\right) = -\nabla_i \left(G^{ij} - T^{ij}\right). \tag{2.30}$$

Historically, some authors (e.g., [104], [125]) claimed that numerical solutions obtained from a free evolution were incompatible with the constraints. However, Choptuik [28] later demonstrated the consistency of the solutions using convergence property of numerical solutions. (See Section 3.1.2 for a brief discussion of convergence of numerical solutions.)

2.2 The perfect fluid

A fluid is a continuum model for a large number of particles that uses the macroscopic properties of a thermodynamic system, such as internal energy and pressure, as fundamental dynamical variables. For introductions to relativistic fluids, see the treatments by Landau [77], Landau and Lifshitz [78], Lichnerowicz [82], Taub [128], Chorin and Marsden [37], and Anile [3]. A perfect fluid has no shear stresses or dissipative forces, and has a stress-energy tensor

$$\mathbf{T} = (\rho + P)\mathbf{u} \otimes \mathbf{u} + P\mathbf{g}, \tag{2.31}$$

where ρ is the energy density, P is the pressure, $\mathbf{u}$ is the fluid's four-velocity, and $\mathbf{g}$ is the spacetime metric. (All scalar quantities are evaluated in the fluid's rest frame.) The four-velocity satisfies

$$\mathbf{u} \cdot \mathbf{u} = -1. \tag{2.32}$$

The energy density ρ contains *all* contributions to the total energy, which for a perfect fluid include the rest mass energy density, ρ_o, and the internal energy density, giving

$$\rho = \rho_o + \rho_o \epsilon, \tag{2.33}$$

where ϵ is the specific internal energy. The fluid's enthalpy is

$$w \equiv \rho + P, \tag{2.34}$$

and the specific enthalpy is

$$h = 1 + \epsilon + \frac{P}{\rho_o}. \tag{2.35}$$

We characterize the constituent particles of the fluid by the the number density, n, and consider only simple, one-component fluids with particles of equal rest mass, m. The rest energy density is then simply

$$\rho_o = mn, \tag{2.36}$$

and the fluid's four-current vector is defined by

$$\mathbf{J} \equiv \rho_o \mathbf{u}. \tag{2.37}$$

The fluid equations of motion are derived from the conservation of the stress-energy

$$\nabla \cdot \mathbf{T} = 0. \tag{2.38}$$

The standard derivation of the fluid equations projects $\nabla \cdot \mathbf{T} = 0$ along the fluid's four velocity, $\mathbf{u}$, and onto the plane perpendicular to $\mathbf{u}$. The former yields the "energy equation"

$$\mathbf{u} \cdot (\nabla \cdot \mathbf{T}) = 0, \tag{2.39}$$

or

$$u^\mu \nabla_\mu \rho + (\rho + P) \nabla_\mu u^\mu = 0. \tag{2.40}$$

Defining a tensor to project onto the hypersurface perpendicular to $\mathbf{u}$

$$\mathbf{h} \equiv \mathbf{g} + \mathbf{u} \otimes \mathbf{u}, \tag{2.41}$$

the *Euler equations* are

$$\mathbf{h} \cdot (\nabla \cdot \mathbf{T}) = 0. \tag{2.42}$$

After simplifications using (2.40), these become

$$(\rho + P) u^\mu \nabla_\mu u^\nu + h^{\mu\nu} \nabla_\mu P = 0. \tag{2.43}$$

If the fluid is subject to a particle-number conservation law, e.g., conservation of baryon number, then the fluid is also subject to the continuity equation

$$\nabla \cdot (n\mathbf{u}) = 0. \tag{2.44}$$

For our fluid systems then, the continuity equation is just

$$\nabla \cdot \mathbf{J} = 0. \tag{2.45}$$

The perfect fluid must also satisfy the first law of thermodynamics,

$$T\mathrm{d}s = \mathrm{d}\epsilon + P\mathrm{d}\left(\frac{1}{\rho_o}\right), \tag{2.46}$$

where s is the specific entropy, and here T is the temperature. Combining the first law of thermodynamics with the fluid equations of motion gives

$$\mathbf{u} \cdot \nabla s = 0, \tag{2.47}$$

and thus the perfect fluid is adiabatic. To these fluid equations (2.40), (2.43), and (2.45), one must adjoin an equation of state, $P = P(\rho_o, s)$, which, must also be consistent with the first law of thermodynamics.

Finally, as presented here, the fluid equations are derived as a set of partial differential equations. The more fundamental derivation, however, follows from conservation laws expressed with *integral* equations. A simple example of using integral equations to express a conservation law is given in Section 3.2. The transformation to the differential form carries the added assumption of differentiability. This additional assumption is not always satisfied, as shocks, which are discontinuities in the fluid variables, form generically in fluid systems. While shocks are legitimate solutions of the fundamental (integral) fluid equations, they are manifestly *not* solutions of the differential equations. Thus the concept of a *weak solution* has been developed, for the formal study of discontinuous solutions. A complete discussion of weak solutions will not be given here, and we note simply that the inclusion of weak solutions can add some ambiguity in determining which weak solutions of the differential equations are physical. The unique physical solution can be found, however, by identifying the solution with the largest entropy. This point will become important in the discussion of approximate methods for solving some fluid problems (see Section 3.5), which can produce unphysical results. When using approximate methods to calculate a numerical solution, unphysical solutions can be prevented by adding a small amount of numerical dissipation, effectively adding “entropy,” Such techniques for adding dissipation are therefore known as "entropy fixes." Further information on weak solutions in fluid dynamics can be found in [37, 79], among other places.

2.3 The classical (Newtonian) perfect fluid equations

After introducing the relativistic fluid in Section 2.2, it is instructive to review the corresponding equations for the *classical* perfect (inviscid) fluid. The classical fluid is completely described by standard Newtonian mechanics. The fluid equations are derived from the conservation of particle number, energy, and momentum, and just as the relativistic equations, they rightfully are *integral* equations. With the additional assumption of differentiability, the equations can be written in the customary differential form. The full derivation of the equations lies outside the focus of this dissertation, thus the equations are simply presented here.

Let ρ_o be the fluid rest-energy density as before, and let $\vec{\boldsymbol{v}}$ be the fluid's (classical) three velocity. The conservation of momentum gives the *Euler equation*, which is

$$\partial_t \vec{\boldsymbol{p}} + \vec{\nabla} \cdot (\vec{\boldsymbol{p}}\, \vec{\boldsymbol{v}}\,) = -\vec{\nabla} P + \rho_o \vec{\boldsymbol{f}}_N, \qquad \text{(classical)} \tag{2.48}$$

where $\vec{\boldsymbol{p}}$ is the classical momentum density

$$\vec{\boldsymbol{p}} \equiv \rho_o \vec{\boldsymbol{v}}, \tag{2.49}$$

and $\vec{\boldsymbol{f}}_N$ is the force per unit mass exerted on the fluid by an external object. When (Newtonian) gravity is the only external force, then $\vec{\boldsymbol{f}}_N = \vec{\boldsymbol{g}}$, where $\vec{\boldsymbol{g}}$ is the acceleration of gravity. The term $\vec{\nabla} \cdot (\vec{\boldsymbol{p}}\, \vec{\boldsymbol{v}}\,)$ is expanded as

$$\vec{\nabla} \cdot (\vec{\boldsymbol{p}}\, \vec{\boldsymbol{v}}\,) = \vec{\boldsymbol{p}} \cdot \vec{\nabla} \vec{\boldsymbol{v}} + \vec{\boldsymbol{v}}\, \vec{\nabla} \cdot \vec{\boldsymbol{p}}. \tag{2.50}$$

Energy conservation gives the *energy equation*

$$\partial_t E_N + \vec{\nabla} \cdot [(E_N + P)\, \vec{\boldsymbol{v}}\,] = \rho_o \left(\vec{\boldsymbol{f}}_N \cdot \vec{\boldsymbol{v}} \right), \qquad \text{(classical)} \tag{2.51}$$

where E_N is the classical energy density

$$E_N \equiv \rho_o \epsilon + \frac{1}{2}\rho_o \vec{\boldsymbol{v}} \cdot \vec{\boldsymbol{v}}. \tag{2.52}$$

The continuity is

$$\partial_t \, \rho_o + \vec{\nabla} \cdot (\rho_o \vec{\boldsymbol{v}}) = 0. \qquad \text{(classical)} \tag{2.53}$$

These Euler and energy equations are often simplified by combining them with the continuity equation. The Euler equation then becomes

$$\rho_o \partial_t \, \vec{\boldsymbol{v}} + \rho_o \vec{\boldsymbol{v}} \cdot \vec{\nabla} \, \vec{\boldsymbol{v}} = -\vec{\nabla} P + \rho_o \vec{\boldsymbol{f}}_N, \qquad \text{(classical)} \tag{2.54}$$

and the energy equation is now

$$\rho_o \partial_t \, \epsilon + \vec{\boldsymbol{v}} \cdot \vec{\nabla} \epsilon = -P \vec{\nabla} \cdot \vec{\boldsymbol{v}}. \qquad \text{(classical)} \tag{2.55}$$

2.4 Equations of state

The equation of state closes the fluid equations by providing a relationship between the pressure and (in our case) the rest energy density and internal energy. The nature of this relationship provides much of the physics for a given system. This section presents four equations of state, of which the first two—the relativistic ideal gas and ultrarelativistic equations of state—are the most important for the work presented in this dissertation.

2.4.1 Relativistic ideal gas

Perhaps the best known, and most widely used equation of state is the ideal gas law

$$P = \frac{k_{\mathrm{B}}}{m} \rho_o T \tag{2.56}$$

where k_{B} is the Boltzmann constant. Chandrasekhar [27] and Synge [126] studied the relativistic extension of this equation of state for a non-degenerate, monatomic gas. The relativistic equation of state can be written in the same form as its classical counterpart

$$P = (\Gamma - 1)\rho_o \epsilon, \tag{2.57}$$

however, here Γ is not the ratio of specific heats, but is a function of the fluid variables,

$$\Gamma = 1 + \frac{P}{\rho_o \epsilon}. \tag{2.58}$$

A detailed analysis shows that the physically acceptable range of Γ is $4/3 \leq \Gamma \leq 5/3$, with $\Gamma = 5/3$ corresponding to non-relativistic flow and $\Gamma = 4/3$ corresponding to ultrarelativistic flow (see also [117]). However, in the remainder of this work, we treat Γ simply as a constant satisfying $1 < \Gamma \leq 2$.

The speed of sound in the relativistic ideal gas is

$$c_{\mathrm{s}}^2 = \left.\frac{\mathrm{d}P}{\mathrm{d}\rho}\right|_s, \tag{2.59}$$

where s is the entropy per particle. In terms of ρ_o and ϵ, the sound speed is [3]

$$c_{\mathrm{s}}^2 = \frac{1}{h}\chi + \frac{P}{\rho_o^2 h}\kappa \tag{2.60}$$

where

$$\chi \equiv \left.\frac{\partial P}{\partial \rho_o}\right|_\epsilon \tag{2.61}$$

and

$$\kappa \equiv \left.\frac{\partial P}{\partial \epsilon}\right|_{\rho_o}. \tag{2.62}$$

An important subclass of fluid solutions are those with constant entropy, or *isentropic* flows. The first law of thermodynamics for isentropic flow,

$$T\mathrm{d}s = \mathrm{d}\epsilon + P\mathrm{d}\left(\frac{1}{\rho_o}\right) = 0, \tag{2.63}$$

combined with the state equation gives

$$\frac{1}{\rho_o}\mathrm{d}P = \Gamma\frac{P}{\rho_o^2}\mathrm{d}\rho_o. \tag{2.64}$$

This can be integrated to obtain the familiar relation

$$P = k(s)\rho_o^\Gamma. \tag{2.65}$$

Note that k appears here as an integration constant owing to the isentropic assumption. In general, however, k is a function of the entropy, as is explicitly indicated by the notation $k(s)$ in (2.65). It is well known that shocks compressively heat the fluid entering the shock front, causing an entropy jump across shocks. Thus the the isentropic formulation (2.65) should *never* be used in place of (2.57) in numerical work, unless one can self-consistently require the fluid to be isentropic.

2.4.2 Ultrarelativistic equation of state

A *barotropic* equation of state has the form

$$P = P(\rho), \tag{2.66}$$

i.e., P is a function only of ρ. The evolution of a barotropic fluid is completely determined by $\nabla \cdot \mathbf{T} = 0$, because knowledge of ρ_o, normally evolved using the continuity equation, is not required. A simple example of a barotropic equation of state is

$$P = (\Gamma - 1)\rho, \tag{2.67}$$

where Γ is a constant. Weinberg [135] lists some examples of physical systems in thermodynamic equilibrium where this state equation (with $\Gamma = 4/3$) is applicable. These include: a photon gas, massless neutrinos, and ultrarelativistic e^-–e^+ pairs. Heuristically, one can motivate this equation of state as the ultrarelativistic limit of the ideal gas equation of state as follows. In the ultrarelativistic limit, the kinetic energy of the constituent particles of the fluid (or internal energy of the fluid in a thermodynamic context) is much larger than the mass energy, $\rho_o\epsilon \gg \rho_o$, giving $\rho \approx \rho_o\epsilon$. Thus, we expect (2.67) to arise naturally in the ultrarelativistic limit.

The sound speed for this state equation is a constant

$$c_{\mathrm{s}}^2 = \frac{dP}{d\rho} = \Gamma - 1, \tag{2.68}$$

independent of density, a fact that makes this equation of state important for the consideration of perfect fluid critical solutions [51]. This point is discussed further in Chapter 5. Causality requires that $\Gamma \leq 2$, and $\Gamma = 1$ gives a pressureless fluid (dust). As in the relativistic ideal-gas case, we require $1 < \Gamma \leq 2$ in the work below.

2.4.3 Cold nuclear matter equation of state

In white dwarfs, the atomic nuclei and electrons can be modeled as separate gases in thermodynamic equilibrium [117, 116]. The nuclei provide essentially all of the star's gravitational mass, while the degeneracy pressure of the electrons provides the pressure against collapse. The relation between the pressure and density for the entire star can be written

$$P = k\rho^{\Gamma}. \tag{2.69}$$

Again, a complete analysis shows that the physically meaningful range of Γ is $4/3 \leq \Gamma \leq 5/3$, with $\Gamma = 5/3,\ 4/3$ corresponding to the non-relativistic limit, ultrarelativistic limit, respectively [117].

2.4.4 A simple nuclear equation of state

Gravitational collapse is a natural phenomenon to study in general relativity, and astrophysically relevant work requires a realistic nuclear equation of state. Such state equations are very complicated, and are frequently given in tabular form. (For a brief description of several realistic nuclear equations of state, see Nozawa *et al.* [99]

and references therein.) As a simple example of an approximate equation of state for nuclear matter, consider the state equation introduced by Van Ripper [133, 134]. This equation of state is written in Gamma-law form

$$P = (\Gamma - 1)\rho_o \epsilon, \tag{2.70}$$

where Γ, to a first approximation, varies only as a function of ρ_o

$$\Gamma = \Gamma_{\rm min} + \eta(\log \rho_o - \log \rho_b). \tag{2.71}$$

Here $\eta = 0$ if $\rho < \rho_b$, and $\eta > 0$ otherwise. ρ_b is the density at which the core of a collapsing star begins to rebound. $\Gamma_{\rm min} \le 4/3$, and Γ has an upper bound of $\Gamma_{\rm max} > 4/3$. This equation of state has not been used in the numerical work presented here, however our future plans include the incorporation of this equation of state, in order to generate more realistic models.

2.5 Derivation of equations

The fluid equations were written in their "standard" form in (2.40) and (2.43). As with the Einstein equations, the fluid equations must be cast into a form which allows a numerical solution. As discussed in chapter 3, we use numerical methods designed for conservation laws. The fluid equations are naturally in conservative form, $\nabla \cdot \mathbf{T} = 0$, and the quantities $T^{0\mu}$ are the natural computational variables, rather than the more familiar ρ and $\mathbf{u}$. This section derives the fluid equations of motion for the ADM line element,

$$\mathrm{d}s^2 = -\left(\alpha^2 - \beta_i\beta^i\right)\,\mathrm{d}t^2 + 2\beta_i\,\mathrm{d}t\,\mathrm{d}x^i + \gamma_{ij}\,\mathrm{d}x^i\,\mathrm{d}x^j, \tag{2.72}$$

following closely the derivation of Banyuls *et al.* [7]. From the definition of α and β^i,

$$\partial_t = \alpha\mathbf{n} + \beta^i\partial_i. \tag{2.73}$$

Eulerian observers [138] are the observers at rest in Σ_t, having a $\mathbf{n}$ as their four-velocity. These observers measure the fluid velocity to be

$$v_i = \frac{u^i}{-\mathbf{n} \cdot \mathbf{u}}, \tag{2.74}$$

with contravariant components, $v^j = \gamma^{ij} v_i$, given by

$$v^i = \frac{u^i}{\alpha u^0} + \frac{\beta^i}{\alpha}. \tag{2.75}$$

The Lorentz factor is the contraction $-\mathbf{u} \cdot \mathbf{n}$ appearing in (2.74),

$$W \equiv \alpha u^0, \tag{2.76}$$

which satisfies

$$W^2 = \frac{1}{1 - v_i v^i}. \tag{2.77}$$

The coordinate basis,

$$\mathbf{e}_{(\mu)} = \{\mathbf{n}, \partial_j\}, \tag{2.78}$$

is adapted to the Eulerian observers. Here (μ) is an index which labels the individual basis vectors, not the components of a single vector. The basis vector components are

$$e_{(0)\mu} = -\alpha \delta_{o\mu}, \tag{2.79}$$

$$e_{(j)\mu} = g_{j\mu} = (\beta_j, \gamma_{jk}). \tag{2.80}$$

We now define *conservation variables* as follows:

$$D \equiv -\mathbf{J}(\mathbf{n}) = -n_\mu J^\mu, \tag{2.81}$$

$$S_j \equiv -\mathbf{T}(\mathbf{n}, \mathbf{e}_{(j)}) = -n_\mu e_{(j)\nu} T^{\mu\nu}, \tag{2.82}$$

$$E \equiv \mathbf{T}(\mathbf{n}, \mathbf{n}) = n_\mu n_\nu T^{\mu\nu}. \tag{2.83}$$

In relativistic fluid dynamics the rest-mass density is often subtracted from the total energy, E, so that the relativistic energy equation reduces in the non-relativistic limit to the Newtonian expression (2.52). It is therefore convenient to define the conservation variable τ to be the difference

$$\tau \equiv E - D. \tag{2.84}$$

These variables—D, S_j, E, and τ—are the locally conserved quantities, and as such, allow the fluid equations of motion to be written in conservative form, a prerequisite for the high-resolution shock-capturing numerical methods we employ (see chapter 3). In contrast to the conservative variables, the more familiar quantities ρ_o, ρ, P, and the four-velocity, $\mathbf{u}$, are called the *primitive variables.*

The definitions of the conservation variables, given above in equations (2.81)–(2.84), are used to express them in terms of the primitive variables

$$D = \rho_o W, \tag{2.85}$$

$$S_j = (\rho + P)W^2 v_j, \tag{2.86}$$

$$E = (\rho + P)W^2 - P, \tag{2.87}$$

$$\tau = (\rho + P)W^2 - P - D, \tag{2.88}$$

and the components of $\mathbf{T}$ required in deriving the fluid equations are

$$T^{00} = \frac{1}{\alpha^2}\left[(\rho + P)\,W^2 - P\right] = \frac{1}{\alpha^2}E, \tag{2.89}$$

$$T^{0i} = \frac{1}{\alpha}(\rho + P)W^2\left(v^i - \frac{\beta^i}{\alpha}\right) + g^{0i}P, \tag{2.90}$$

$$T^0{}_i = \frac{1}{\alpha}(\rho + P)W^2 v_i = \frac{1}{\alpha}S_i, \tag{2.91}$$

$$T^i{}_j = (\rho + P)W^2\left(v^i - \frac{\beta^i}{\alpha}\right)v_j = S_j\left(v^i - \frac{\beta^i}{\alpha}\right). \tag{2.92}$$

Consider now the divergence of the vector $\mathbf{T}(\mathbf{e}_{(\gamma)},\cdot)$

$$\nabla\cdot\mathbf{T}(\mathbf{e}_{(\gamma)},\cdot) = (\nabla\cdot\mathbf{T})\cdot\mathbf{e}_{(\gamma)} + \mathbf{T}:\nabla\mathbf{e}_{(\gamma)}, \tag{2.93}$$

or in index notation

$$\nabla_\mu\left(T^{\mu\nu}e_{(\gamma)\nu}\right) = \left(\nabla_\mu T^{\mu\nu}\right)e_{(\gamma)\nu} + T^{\mu\nu}\nabla_\mu e_{(\gamma)\nu}. \tag{2.94}$$

The first term on the right-hand side is zero by virtue of conservation of $\mathbf{T}$, $\nabla\cdot\mathbf{T}=0$, and (2.93) becomes

$$\nabla\cdot\mathbf{T}(\mathbf{e}_{(\gamma)},\cdot) = \mathbf{T}:\nabla\mathbf{e}_{(\gamma)}. \tag{2.95}$$

From this equation we can express the fluid equations of motion in a form suitable for computational work. The source term on the right-hand side of (2.95) can be explicitly rewritten in terms of ordinary derivatives and Christoffel symbols as

$$\nabla_\mu e_{(\gamma)\nu} = \frac{\partial e_{(\gamma)\nu}}{\partial x^\mu} - \Gamma^\delta{}_{\nu\mu}e_{(\gamma)\delta}. \tag{2.96}$$

The energy equation is derived by choosing $\mathbf{e}_{(\gamma)}$ in (2.95) to be the time-like basis vector $\mathbf{e}_{(0)}$

$$\nabla_\mu(T^{\mu\nu}e_{(0)\nu}) = T^{\mu\nu}\left(\partial_\mu e_{(0)\nu} - \Gamma^\delta{}_{\nu\mu}e_{(0)\delta}\right). \tag{2.97}$$

Using

$$e_{(0)\nu} = -\alpha\delta_{0\nu}, \tag{2.98}$$

$$\sqrt{-g} = \alpha\sqrt{\gamma}, \tag{2.99}$$

and

$$\Gamma^\alpha{}_{\mu\alpha} = \frac{1}{\sqrt{-g}}\partial_\mu\sqrt{-g}, \tag{2.100}$$

the energy equation can then be written

$$\begin{aligned}\frac{1}{\sqrt{-g}}&\left\{\partial_0\sqrt{\gamma}\,E + \partial_i\left[\sqrt{-g}\,(E+P)\left(v^i - \frac{\beta^i}{\alpha}\right)\right]\right\}\\ &\qquad = \alpha\left(T^{\mu 0}\partial_\mu\ln\alpha - \Gamma^0{}_{\nu\mu}T^{\mu\nu}\right).\end{aligned} \tag{2.101}$$

Similarly, the Euler equations are derived by letting $\mathbf{e}_{(\gamma)}$ in (2.95) be one of the three space-like basis vectors, $\mathbf{e}_{(i)}$

$$\nabla_\mu (T^{\mu\nu} e_{(j)\nu}) = T^{\mu\nu} \left(\partial_\mu e_{(j)\nu} - \Gamma^\delta{}_{\nu\mu} e_{(j)\delta} \right). \tag{2.102}$$

From (2.80), this becomes

$$\frac{1}{\sqrt{-g}} \partial_\mu \left[\sqrt{-g}\, T^{\mu\nu} g_{j\nu} \right] = \left(\partial_\mu g_{j\nu} - \Gamma^\delta{}_{\nu\mu} g_{j\delta} \right) T^{\mu\nu}, \tag{2.103}$$

and after some simplification, we have

$$\frac{1}{\sqrt{-g}} \left[\partial_0 \sqrt{\gamma}\, S_j + \partial_i \sqrt{-g}\, T^i{}_j \right] = \left(\partial_\mu g_{j\nu} - \Gamma^\delta{}_{\nu\mu} g_{j\delta} \right) T^{\mu\nu}. \tag{2.104}$$

The fluid four-current, $\mathbf{J}$, has the components

$$J^0 = \frac{1}{\alpha} \rho_o W = \frac{1}{\alpha} D, \tag{2.105}$$

$$J^i = \rho_o W \left(v^i - \frac{\beta^i}{\alpha} \right) = D \left(v^i - \frac{\beta^i}{\alpha} \right), \tag{2.106}$$

so the continuity equation becomes

$$\frac{1}{\sqrt{-g}} \partial_\mu \left(\sqrt{-g}\, J^\mu \right) = 0. \tag{2.107}$$

Using (2.105) and (2.106) this becomes

$$\frac{1}{\sqrt{-g}} \left[\partial_0 \sqrt{\gamma}\, D + \partial_i \sqrt{-g}\, D \left(v^i - \frac{\beta^i}{\alpha} \right) \right] = 0. \tag{2.108}$$

In summary, the fluid equations of motion in the context of the ADM 3+1 formalism are: the energy equation (2.101), the Euler equations (2.104), and the continuity equation (2.108). To simplify the presentation we now introduce a "state-vector" notation. Let $\mathbf{q}$ be the state vector of conservative variables

$$\mathbf{q} = \begin{bmatrix} D \\ S_j \\ \tau \end{bmatrix}. \tag{2.109}$$

The fluid equations of motion can then be written in the compact notation

$$\frac{1}{\sqrt{-g}}\left[\partial_t\sqrt{\gamma}\,\mathbf{q}+\partial_i\sqrt{-g}\,\mathbf{f}^i\right]=\mathbf{\Sigma}(\mathbf{q}), \tag{2.110}$$

where the *flux vectors* are

$$\mathbf{f}^i=\begin{bmatrix} D\left(v^i-\dfrac{\beta^i}{\alpha}\right) \\ S_j\left(v^i-\dfrac{\beta^i}{\alpha}\right)+P\delta^i{}_j \\ \tau\left(v^i-\dfrac{\beta^i}{\alpha}\right)+Pv^i \end{bmatrix}, \tag{2.111}$$

and the *source vector* is

$$\mathbf{\Sigma}=\begin{bmatrix} 0 \\ T^{\mu\nu}\left(\partial_\mu g_{\nu j}-\Gamma^\delta{}_{\nu\mu}g_{\delta j}\right) \\ \alpha\left(T^{\mu 0}\partial_\mu\ln\alpha-T^{\mu\nu}\Gamma^0{}_{\nu\mu}\right) \end{bmatrix}. \tag{2.112}$$

Finally, we define a state vector of *primitive variables*

$$\mathbf{w}=\begin{bmatrix} \rho_o \\ v^j \\ P \end{bmatrix}. \tag{2.113}$$

2.6 Solving for the primitive variables

The conservative form of the fluid equations (2.110) are evolution equations for the conservative variables, e.g., D, S_j, and τ. However, the flux and source terms in the equations often must be formulated in terms of the primitive variables, ρ_o, v_j, and P. As the fluid equations contain both sets of variables, we must be able to find one set of variables from the other. The conservation variables are easily found from their definitions, such as equations (2.85)–(2.88). Computing the primitive variables from the conservative variables is more problematic; generally requiring the solution of a transcendental equation. This section presents straight-forward methods for finding the primitive variables for both the ultrarelativistic and ideal-gas equations of state.

In Section 3.9 we discuss improved algorithms optimized for extremely relativistic fluids.

2.6.1 Ultrarelativistic equation of state

The transformation to primitive variables for the ultrarelativistic equation of state is simpler than might be expected, and one can solve for P *algebraically.* The Lorentz factor squared is

$$W^2 = \frac{1}{1 - v_i v^i}, \tag{2.114}$$

and the velocity is given by

$$v_i = \frac{S_i}{E + P}. \tag{2.115}$$

Inserting this into the definition of E (2.87),

$$E = (\rho + P)W^2 - P, \tag{2.116}$$

one can derive

$$(E + P)^2 - (\rho + P)(E + P) - S_i S^i = 0. \tag{2.117}$$

ρ is a simple function of P for this barotropic equation of state

$$P = (\Gamma - 1)\rho. \tag{2.118}$$

This leaves a quadratic equation for P, with the solution

$$P = -2\beta E + \left[4\beta^2 E^2 + (\Gamma - 1)(E^2 - S_i S^i)\right]^{1/2}, \tag{2.119}$$

where β is a positive constant given by

$$\beta \equiv \frac{1}{4}(2 - \Gamma). \tag{2.120}$$

The specific root of the quadratic equation is chosen by requiring a physical pressure, $P > 0$. This demand ($P > 0$) further requires that $E > S_i S^i$. A second physical requirement is that the fluid velocity be bounded by the speed of light, $|v| < 1$, where $|v| \equiv \left(v^i v_i\right)^{1/2}$, and from (2.115) this will clearly be automatically satisfied when $E > S^i S_i$. These physical restrictions on the primitive variables can sometimes be violated in numerical solutions of the fluid equations. Some numerical techniques aimed at ameliorating such difficulties are discussed in Section 3.9.

2.6.2 Ideal gas equation of state

Finding the primitive variables for the ideal-gas equation of state is significantly more complicated than the ultrarelativistic case just discussed, as here we must solve a transcendental equation. The important relations are the equation of state,

$$P = (\Gamma - 1)\rho_o \epsilon, \tag{2.121}$$

the definitions of the conservation variables

$$D = \rho_o W, \tag{2.122}$$

$$S_i = (\rho + P) W^2 v_i, \tag{2.123}$$

$$\tau = (\rho + P) W^2 - P - D, \tag{2.124}$$

and the definition of the total energy

$$\begin{aligned} \rho &= \rho_o + \rho_o \epsilon & (2.125) \\ &= \rho_o + \frac{P}{\Gamma - 1}, & (2.126) \end{aligned}$$

where we have used the equation of state to arrive at the last expression. There is some freedom in obtaining the primitive variables from the conservation variables, $\mathbf{q}$. A common approach is to express ρ_o and v_j as functions of $\mathbf{q}$ and P, and then solve the remaining transcendental equation for the pressure [93, 89]. This approach is sketched below.

Assume a solution for P, then the velocity can be found from

$$v_i = \frac{S_i}{\tau + P + D}, \tag{2.127}$$

and the Lorentz factor is

$$W^2(P) = \frac{(\tau + D + P)^2}{(\tau + D + P)^2 - S_i S^i}. \tag{2.128}$$

ρ_o is then

$$\rho_o = \frac{D}{W}. \tag{2.129}$$

Finally, the pressure itself is to be computed from the definition of τ

$$\begin{aligned} P &= \left(\rho_o + \frac{P}{\Gamma - 1}\right) W^2 - \tau - D && (2.130) \\ &= \frac{PW^2}{\Gamma - 1} + D(W - 1) - \tau. && (2.131) \end{aligned}$$

The fluid must also the obey physical restrictions, $P > 0$, and $|v| < 1$. From (2.127), a lower bound on the pressure, P_{min}, necessary for a subluminal velocity can be found

$$P_{\text{min}} = \left(S_i S^i\right)^{1/2} - \tau - D. \tag{2.132}$$

Again, for highly relativistic flows this algorithm should be modified, as discussed in Section 3.9.3. These equations must be solved at every grid point for each step in the algorithm, and for our two-step integration scheme (see Section 3.7), they must be solved twice per time step. This transformation therefore requires a significant proportion of a code's total running time, an additional expense required in the solution of the relativistic fluid equations which the classical (Newtonian) fluid equations do not require.

2.7 Spectral decomposition

By introducing the variables $\mathbf{q} = (D, S_j, \tau)^T$, the relativistic fluid equations were written in conservation form (2.110)

$$\frac{1}{\sqrt{-g}}\left[\partial_t\sqrt{\gamma}\,\mathbf{q} + \partial_i\sqrt{-g}\,\mathbf{f}^i\right] = \mathbf{\Sigma}(\mathbf{q}). \tag{2.133}$$

The flux and source vectors, $\mathbf{f}^j$ and $\mathbf{\Sigma}$, respectively, were defined previously by equations (2.111) and (2.112). The numerical method used to integrate (2.133) employs Roe's approximate Riemann solver (see chapter 3). Roe's method solves a linearized set of equations, and requires the spectral decomposition of the Jacobian matrix flux vector,

$$\mathbf{B}^i \equiv \frac{\partial \mathbf{f}^i}{\partial \mathbf{q}}, \tag{2.134}$$

which we present here. We denote the eigenvalues of $\mathbf{B}$ by λ, and the eigenvectors by $\mathbf{r}$. These eigenvalues and eigenvectors for the relativistic ideal gas were first derived by Banyuls *et al.* [7], and later corrected by Miller [55, 72].

Let the three spatial directions be labeled by the indices x, y, and z. Previously we defined (2.62)

$$\kappa = \left.\frac{\partial P}{\partial \epsilon}\right|_{\rho_o} \tag{2.135}$$

and here we additionally define

$$\tilde{\kappa} \equiv \frac{\kappa}{\rho_o}, \tag{2.136}$$

and

$$\Lambda^i_{\pm} \equiv \frac{1}{\alpha}\left(\lambda + \beta^i\right). \tag{2.137}$$

Three of the eigenvalues of $\mathbf{B}^x$ are degenerate, and following the notation of [7], these are

$$\lambda_0 = \alpha v^x - \beta^x, \tag{2.138}$$

$$\lambda_1 = \alpha v^x - \beta^x, \tag{2.139}$$

$$\lambda_2 = \alpha v^x - \beta^x. \tag{2.140}$$

The remaining eigenvalues are

$$\begin{aligned}\lambda_\pm = {} & \frac{\alpha}{1 - v^2 c_\mathrm{s}^2}\Big\{ v^x \left(1 - c_\mathrm{s}^2\right) \\ & \pm \sqrt{c_\mathrm{s}^2 \left(1 - v^2\right) \left[\gamma^{xx} \left(1 - v^2 c_\mathrm{s}^2\right) - v^x v^x \left(1 - c_\mathrm{s}^2\right)\right]}\Big\} - \beta^x,\end{aligned} \tag{2.141}$$

where c_s is the sound speed. The corresponding eigenvectors are

$$\mathbf{r}_\pm = \begin{bmatrix} 1 \\ hW\left(v_x - \dfrac{v^x - \Lambda^x_\pm}{\gamma^{xx} - v^x \Lambda^x_\pm}\right) \\ hWv_y \\ hWv_z \\ \dfrac{hW\left(\gamma^{xx} - v^x v^x\right)}{\gamma^{xx} - v^x \Lambda^x_\pm} - 1 \end{bmatrix}, \tag{2.142}$$

$$\mathbf{r}_0 = \begin{bmatrix} \dfrac{\tilde{\kappa}}{hW(\tilde{\kappa} - c_\mathrm{s}^2)} \\ v_x \\ v_y \\ v_z \\ 1 - \dfrac{\tilde{\kappa}}{hW(\tilde{\kappa} - c_\mathrm{s}^2)} \end{bmatrix}, \tag{2.143}$$

$$\mathbf{r}_1 = \begin{bmatrix} Wv_y \\ h\left(\gamma_{xy} + 2W^2 v_x v_y\right) \\ h\left(\gamma_{yy} + 2W^2 v_y v_y\right) \\ h\left(\gamma_{yz} + 2W^2 v_y v_z\right) \\ Wv_y\left(2hW - 1\right) \end{bmatrix}, \tag{2.144}$$

$$\mathbf{r}_2 = \begin{bmatrix} W v_z \\ h\left(\gamma_{xz} + 2W^2 v_x v_z\right) \\ h\left(\gamma_{yz} + 2W^2 v_y v_z\right) \\ h\left(\gamma_{zz} + 2W^2 v_z v_z\right) \\ W v_z \left(2hW - 1\right) \end{bmatrix}. \tag{2.145}$$

The expressions for the other eigenvalues and eigenvectors can be found by symmetry. The eigenvalues for $\mathbf{B}^y$ are the same as above, with index y replacing the index x. The eigenvectors of $\mathbf{B}^y$ are found by interchanging the components of $\mathbf{r}$ corresponding to the S_x and S_y components in $\mathbf{q}$, and then interchanging the x and y index labels. That is, we exchange the second and third components of the eigenvectors, then interchange the x and y indices. The eigenvalues and eigenvectors of $\mathbf{B}^z$ follow the same prescription.

2.8 Simple exact solutions

Two exact solutions are discussed in this section, which are very useful in the initial testing phases of fluid codes. The first solution, the Riemann initial value problem for two discontinuous fluid states, is very useful in testing the code's shock-handling capabilities. This solution is also fundamental in designing numerical methods for conservation laws (see Chapter 3 for a discussion of Godunov's method and extensions). While the Riemann problem assumes a flat space-time and slab symmetry, the Tolman-Oppenheimer-Volkoff (TOV) solution is a general relativistic solution for a static, spherically symmetric "star." The TOV solution then can be used to test the combined fluid and geometric equations.

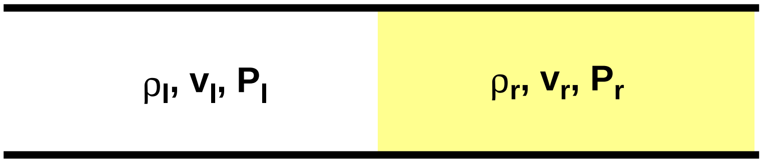

Figure 2.2: A schematic diagram of a fluid shock tube's initial configuration. A divider separates two independently prepared fluid states. The divider is removed at $t = 0$, and the Riemann initial value problem allows one to determine the subsequent evolution.

2.8.1 The Riemann initial value problem

The general Riemann initial value problem consists of a conservation law,

$$\partial_t \mathbf{q} + \partial_x \mathbf{f}(\mathbf{q}) = 0, \tag{2.146}$$

with the initial data

$$\mathbf{q}(x, 0) = \begin{cases} \mathbf{q}_\ell & \text{if } x < 0, \\ \mathbf{q}_r & \text{if } x > 0. \end{cases} \tag{2.147}$$

$\mathbf{q}_\ell$ and $\mathbf{q}_r$ are arbitrary *constant* state vectors, i.e., the individual vectors are not functions of the coordinates, and thus are generically separated by a discontinuity at $x = 0$. The divider is removed at $t = 0$, and Riemann's solution describes the subsequent interaction of the two states. The Riemann problem has a self-similar solution, in the similarity variable x/t.

The solution of the Riemann problem for Newtonian fluids is well-known (see, for example, Courant and Friedrichs [43], Chorin and Marsden [37], or Landau and Lifshitz [78] for further information), and the problem can be experimentally realized for gases in a shock tube, schematically shown in Figure 2.2. (Technically, a shock tube problem is one in which both states have initial velocities of zero.) This solution consists of (i) two waves, each of which may be either shock or rarefaction waves; (ii) four fluid states, the two initial states and two states behind the waves; and (iii) a contact discontinuity separating the states behind the waves. The solution is shown schematically in Figure 2.3. The solution of the Riemann problem (for

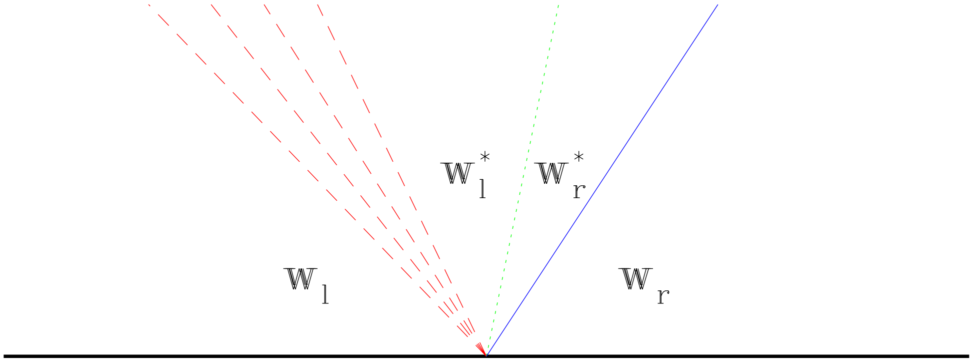

Figure 2.3: A space-time diagram of a shock tube problem showing the waves and principal parts of the solution. The initial states are $\mathbf{w}_\ell$ and $\mathbf{w}_r$. A rarefaction wave, indicated by the dashed lines, moves to the left, and a shock wave (solid line) moves to the right. A contact discontinuity (dotted line), across which P and v are constant and only the density varies, separates the states behind the waves, $\mathbf{w}_\ell^*$ and $\mathbf{w}_r^*$.

fluids) involves finding the locus of states that can be connected to an initial state via shock and rarefaction waves, as shown in Figure 2.4. A graphical solution of the Riemann problem for a relativistic fluid is shown in Figure 2.5 and Figure 2.6. The Riemann problem for relativistic fluids was solved by Martí and Müller [89] for the ideal-gas equation of state. The corresponding problem for the ultrarelativistic equation of state was solved by Smoller and Temple [123].

2.8.2 The Tolman-Oppenheimer-Volkoff solution

A second test problem is the spherically symmetric, static Tolman-Oppenheimer-Volkoff (TOV) solution. The line element is

$$\mathrm{d}s^2 = -\mathrm{e}^{2\varphi}\,\mathrm{d}t^2 + \left(1 - \frac{2m(r)}{r}\right)^{-1}\mathrm{d}r^2 + r^2\,\mathrm{d}\Omega^2, \tag{2.148}$$

where $m(r)$ is the mass-aspect function,

$$m(r) = 4\pi\int_0^r \rho(r')r'^2\,\mathrm{d}r'. \tag{2.149}$$

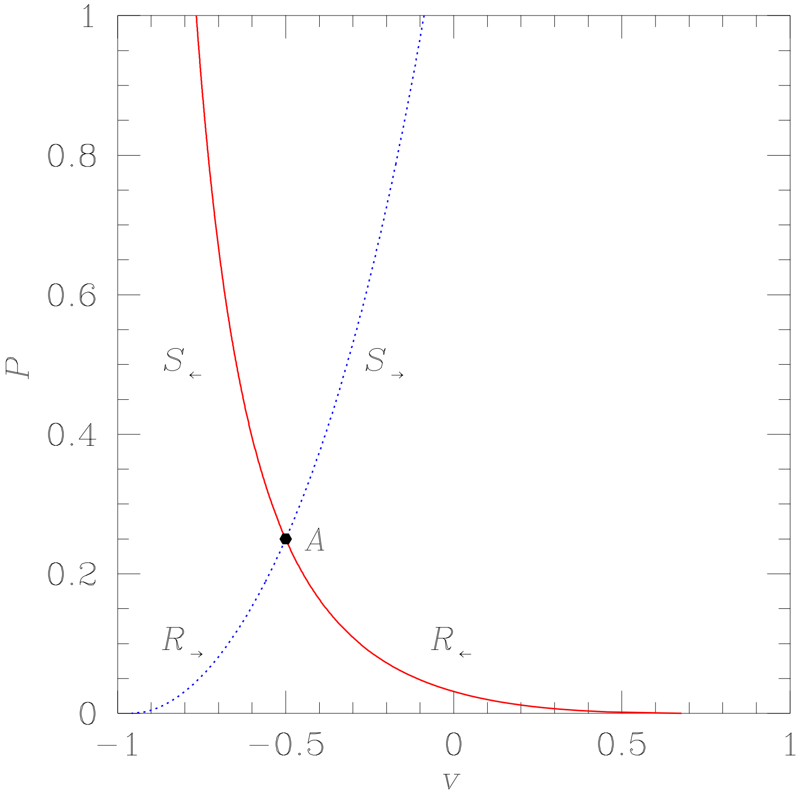

Figure 2.4: A single state labeled 'A' is shown in this $P - v$ diagram, and the lines indicate all other states that can be connected to A by either rarefaction (R) or shock (S) waves. Left-moving waves connect the states shown by the solid line, and right-moving waves connect the states shown by the dotted line.

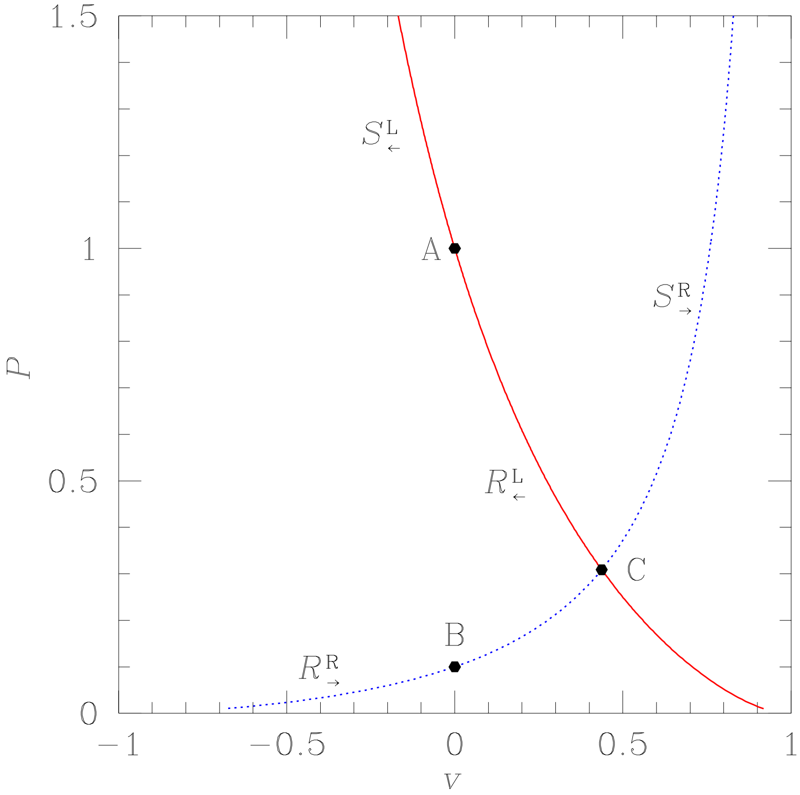

Figure 2.5: The graphical solution of the Riemann problem in the non-relativistic regime for a fluid with $\Gamma = 5/3$. The left state is indicated by point A ($(\rho_o)_\ell = 1$, $v_\ell = 0$, $P_\ell = 1$), the right state is at point B ($(\rho_o)_r = 0.125$, $v_r = 0$, $P_r = 0.1$). The solution of the Riemann problem is given by the intersection, C, of the two loci of states. Thus, a left-moving rarefaction ($R_{\leftarrow}$) connects states A and C, and a right-moving ($S_{\rightarrow}$) shock connects state C with B. These initial states and solution are not in the the regime where relativistic effects are important. A relativistic example is shown in Figure 2.6.

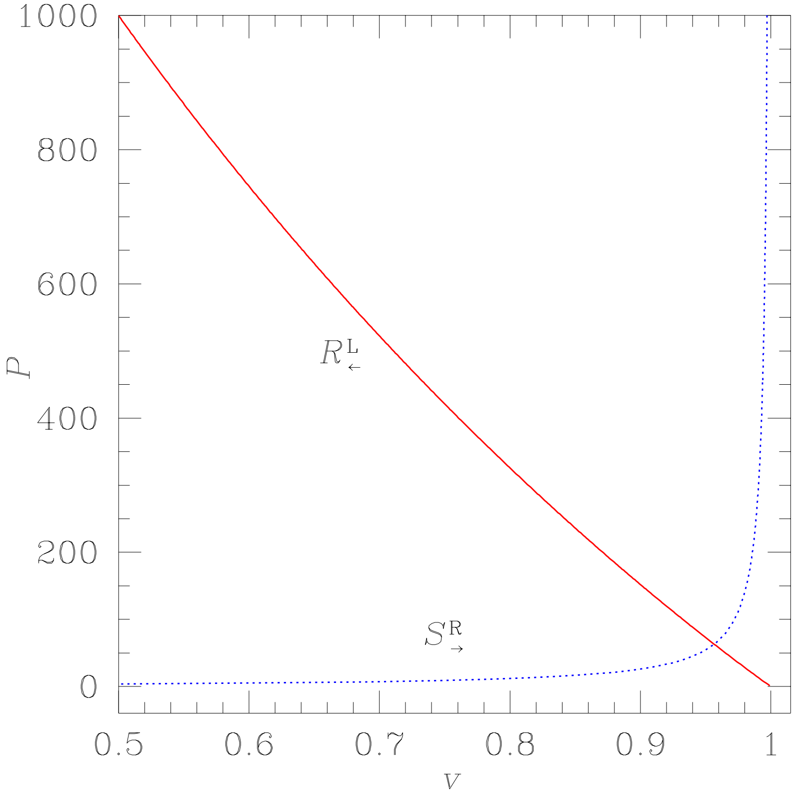

Figure 2.6: The graphical solution of the Riemann problem in the relativistic regime for a fluid with $\Gamma = 5/3$. The left state is $(\rho_o)_\ell = 1$, $v_\ell = 0.5$, $P_\ell = 10^3$, the right state is $(\rho_o)_r = 1$, $v_r = 0$, $P_r = 1$. Note the shape of the curves for this relativistic configuration, and compare this solution with the non-relativistic solution shown in Figure 2.5. As the fluid becomes more relativistic, the gradients of the curves become larger, and finding a numerical solution becomes more difficult.

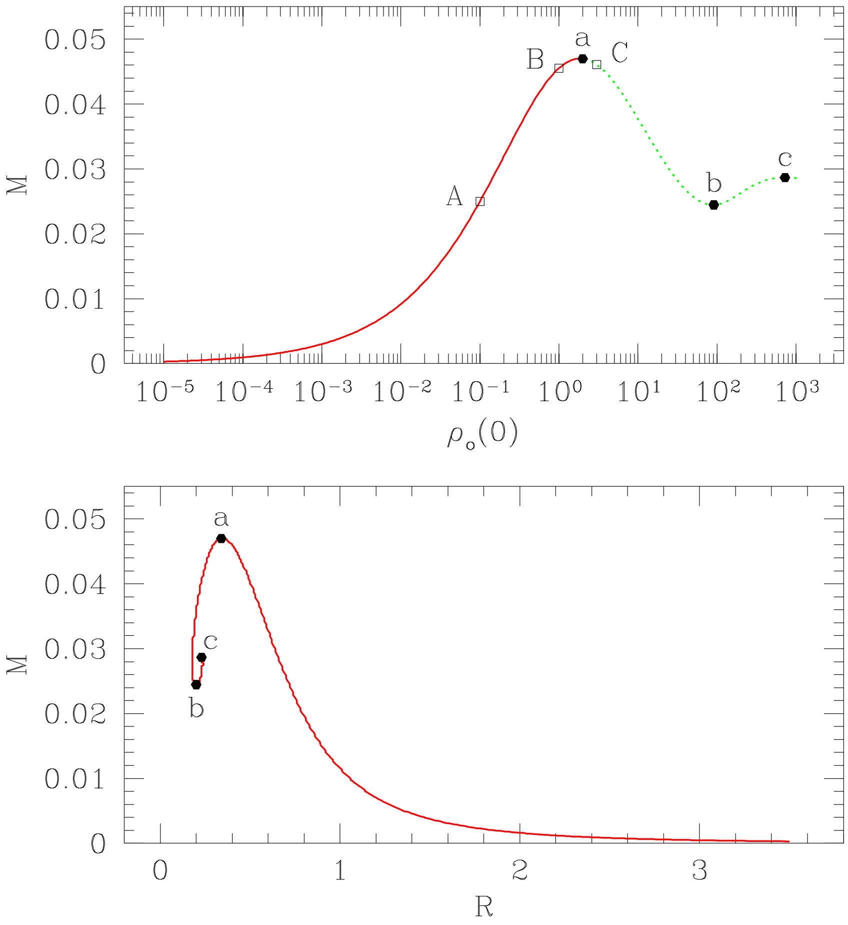

Figure 2.7: Plots of the total mass vs. the central density and radius, respectively, for a Tolman-Oppenheimer-Volkoff (TOV) star. These plots can be used to determine the stability properties of the star solutions. The isentropic equation of state, $P = k\rho_o^\Gamma$, is used with $k = 0.1$ and $\Gamma = 5/3$. The top frame shows the mass vs. the rest-energy density at the origin, $\rho_o(0)$. The squares show three different configurations which were used as initial data in an evolution code, as shown in Figures 2.8–2.10. The inflection points, $\mathrm{d}M/\mathrm{d}\rho_o(0) = 0$—here labeled a, b, and c—are points where the solution's stability properties may change. If only one inflection point exists, then it marks the transition between stable and unstable solutions. When multiple inflection points exist, as shown here, the plot of mass vs. radius shown in the bottom frame is also required to find the stability properties. An unstable mode appears at an inflection point if the mass vs. radius curve turns counter-clockwise with increasing $\rho_o(0)$. A clockwise turn indicates that the unstable mode changes to a stable mode. A complete discussion is given in Shapiro and Teukolsky [117].

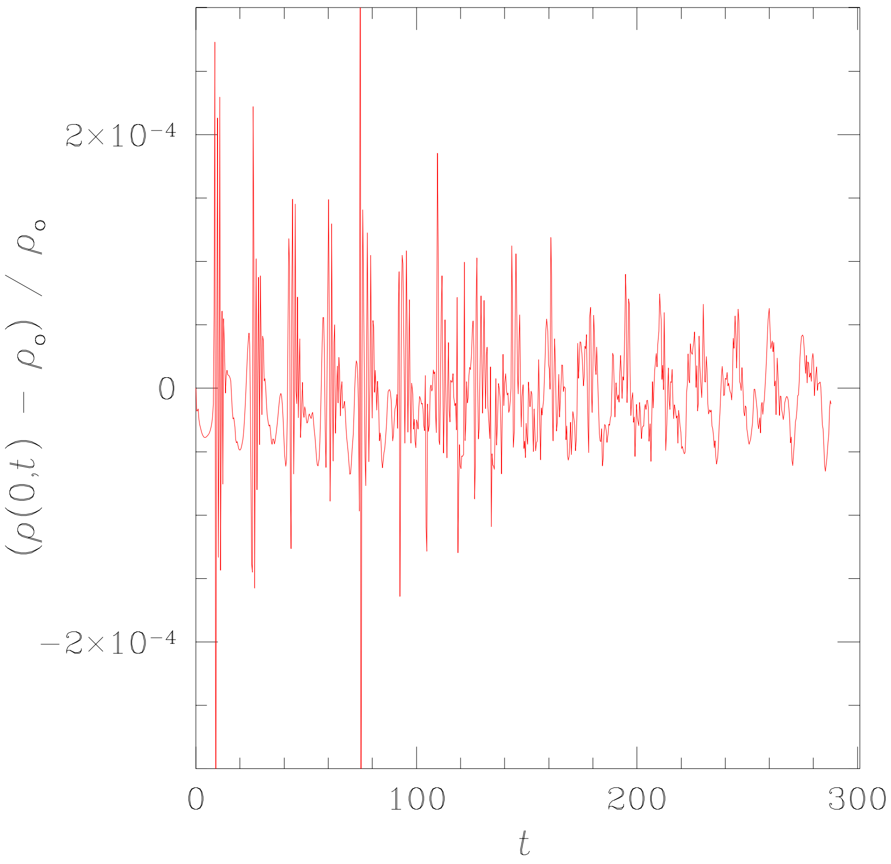

Figure 2.8: This plot shows the relative error in the central rest-energy density for a TOV star vs. time in the evolution of a stable star. The TOV star with central density $\rho_o(0)$ is specified as initial data for a relativistic fluid code, and the central density for the evolved solution is $\rho_o(0,t)$. This plot shows the relative error, $(\rho_o(0,t) - \rho_o(0))/\rho_o(0)$, as a function of time during the evolution. A non-zero floor is added to the edge of the star, and the fluid and geometric variables are fixed to their initial values at the outer boundary. The interaction of the floor with the star and boundary conditions causes noise which reflects between the origin and outer boundary, and is visible here as "spikes" in $\rho_o(0,t)$. Interestingly, these spikes allow us to calculate the dynamical time, the time for a signal to propagate through the star, and the evolution shown here continues for more than 30 dynamical times. The initial data for the TOV star are $\rho_o = 0.1$, $\kappa = 0.1$, and $\Gamma = 5/3$. This configuration is point A in the plot of M vs. ρ_o shown in Figure 2.7, and is well within the stable branch of the M vs. ρ_o curve.

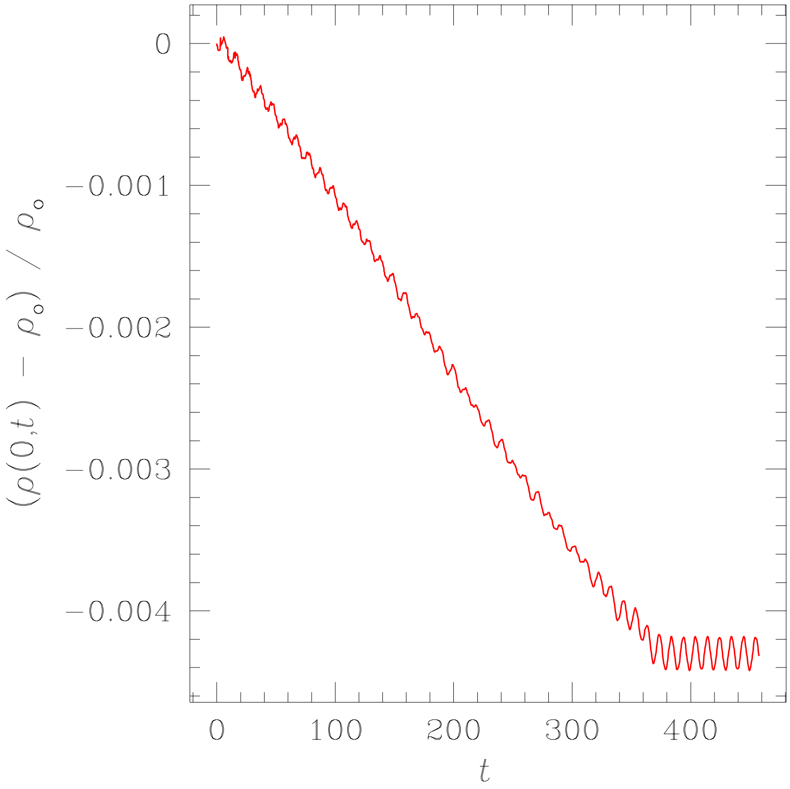

Figure 2.9: The relative error in the Central density of TOV star vs. time in the evolution of a stable star near an inflection point. This solution was evolved for over 50 dynamical times. The initial solution slowly relaxes to a configuration with a slightly smaller $\rho_o(0,t)$, and then appears to oscillate about this solution. The initial data for the TOV star are $\rho_o = 1$, $\kappa = 0.1$, and $\Gamma = 5/3$. This configuration is point B in the plot of M vs. ρ_o shown in Figure 2.7. This star is stable, but is near the inflection point a where the solutions become unstable.

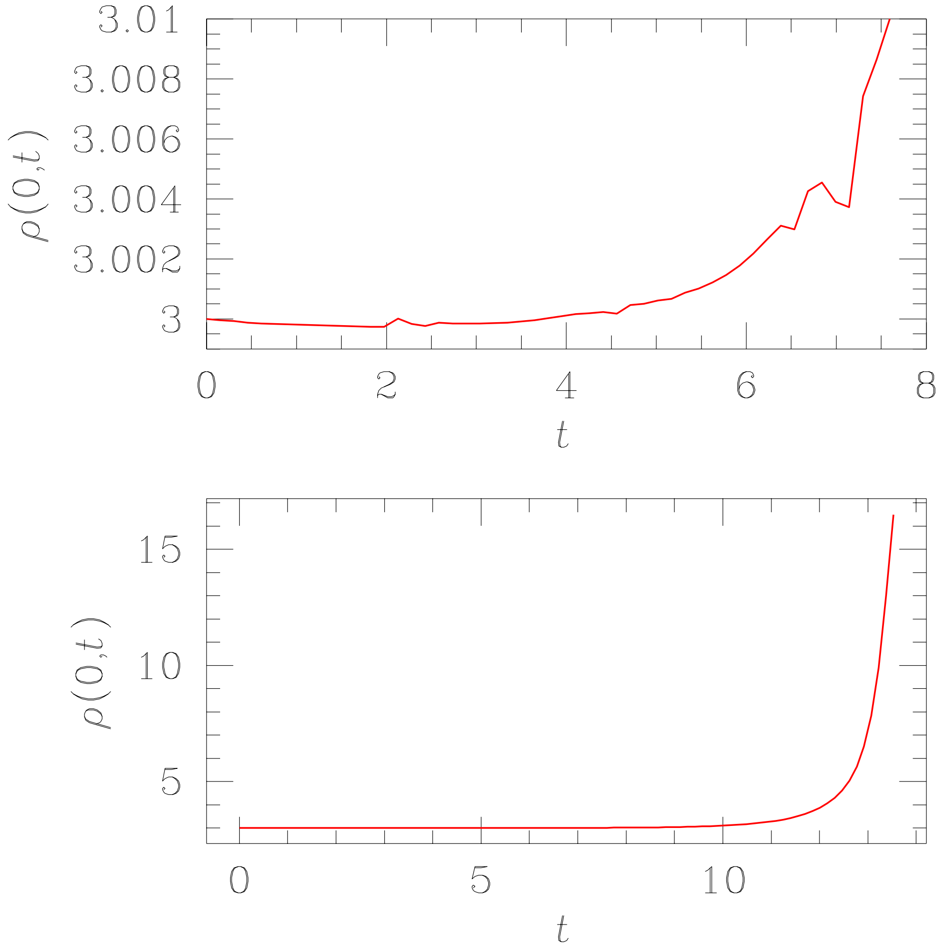

Figure 2.10: Central density of TOV star vs. time for an unstable configuration. Here the instability becomes apparent approximately after two dynamical times. The initial data for the TOV star are $\rho_o = 3$, $\kappa = 0.1$, and $\Gamma = 5/3$. This configuration is point C in the plot of M vs. ρ_o shown in Figure 2.7, and lies on the unstable branch of the mass curve, near the inflection point a.

This well-known solution is found by choosing the central pressure, P_o, and then integrating the coupled ordinary differential equations

$$\frac{\mathrm{d}\varphi}{\mathrm{d}r} = \frac{m(r) + 4\pi r^3 P}{r\left[r - 2m(r)\right]}, \tag{2.150}$$

$$\frac{\mathrm{d}P}{\mathrm{d}r} = -(\rho + P)\frac{m(r) + 4\pi r^3 P}{r\left[r - 2m(r)\right]}, \tag{2.151}$$

and

$$\frac{\mathrm{d}m}{\mathrm{d}r} = 4\pi r^2 \rho \tag{2.152}$$

outwards from $r = 0$. At some radius, $r_\star$, we typically find $P(r_\star) = 0$, at which point the outward integration ceases, and we deem $r_\star$ to be the radius of the star. We calculate this solution with the isentropic equation of state,

$$P = k\rho_o^\Gamma, \tag{2.153}$$

when testing perfect fluid codes.

The TOV solution is widely used in testing relativistic fluid codes, and as all of the solutions are not stable, some care must be taken to avoid inadvertently using an unstable solution. However, the stability properties can be easily determined by generating plots of the star's mass, as shown in Figure 2.7. A nice discussion of the TOV solution's stability properties is given by Shapiro and Teukolsky [117]. Sample evolutions of two stable TOV solutions are shown in Figure 2.8 and Figure 2.9. The evolution of an unstable TOV solution is shown in Figure 2.10. (These solutions were obtained with a code similar to the one described in Chapter 4, with the ideal-gas equation of state.)

One difficulty with using the TOV solution in an evolution code is that most fluid codes require $\rho_o > 0$ on the computational grid. This is usually accomplished by adding a small fluid "atmosphere" to the star, extending from the edge of the star to the outer boundary. This "atmosphere," or background fluid, is not part of the

TOV solution, and will interact with both the star and the outer boundary condition, thereby producing noise in the solution (see e.g., the "noise" in Figure 2.8). The evolution of a scalar gravity "star" is presented in Section 7.6.

Finally, *all* TOV solutions for the ultrarelativistic equation of state have density profiles

$$\rho \propto \frac{1}{r^2}. \tag{2.154}$$

This can be understood by dimensional arguments [116], as this equation of state contains no parameters with freely specifiable dimensions. The singularity at the origin, $r = 0$, usually prevents these TOV solutions from serving as test solutions in fluid codes using the ultrarelativistic state equation.

2.9 The $P = \rho$ perfect fluid and a massless scalar field

There is a well-known relation between an irrotational, stiff ($P = \rho$) perfect fluid and a massless Klein-Gordon scalar field, see e.g., Taub [127] and Lichnerowicz [82]. In this section we discuss the relationship between scalar fields and perfect fluids for $0 < \Gamma \leq 2$. The perfect fluid equations of motion can be written in terms of ρ, P, and u^a as

$$u^\mu \nabla_\mu \rho + (\rho + P) \nabla_\mu u^\mu = 0, \tag{2.155}$$

$$(\rho + P) u^\mu \nabla_\mu u^\nu + h^{\mu\nu} \nabla_\mu P = 0. \tag{2.156}$$

If we assume the ultrarelativistic equation of state, $P = (\Gamma - 1)\rho$, then these equations become

$$\nabla \cdot \left(\rho^{1/\Gamma} \mathbf{u} \right) = 0, \tag{2.157}$$

$$(\mathbf{u} \cdot \nabla) \mathbf{u} + \frac{(\Gamma - 1)}{\Gamma} \mathbf{h} \cdot \nabla \ln \rho = 0, \tag{2.158}$$

provided that $\rho \neq 0$.

We seek a specific combination of ρ and $\mathbf{u}$ that allows the fluid equations to be written in terms of a single variable, and therefore introduce the *ansatz*

$$\mathbf{w} \equiv \rho^B \mathbf{u}, \tag{2.159}$$

where B is a constant that will be determined below. From elementary contractions we can express both ρ and $\mathbf{u}$ in terms of $\mathbf{w}$

$$\rho = \left(-(\mathbf{w} \cdot \mathbf{w})\right)^{\frac{1}{2B}}, \tag{2.160}$$

$$\mathbf{u} = (-\mathbf{w} \cdot \mathbf{w})^{-\frac{1}{2}} \mathbf{w}. \tag{2.161}$$

However, it remains to see if B can be chosen such that $\mathbf{w}$ will satisfy the fluid equations of motion. We substitute expressions (2.160) and (2.161) into the momentum equation (2.156) to obtain

$$\begin{aligned} w^\mu \nabla_\mu w_\nu - \frac{\Gamma - 1}{B\Gamma} w^\mu \nabla_\nu w_\mu \\ + \left(1 - \frac{\Gamma - 1}{B\Gamma}\right) \left(-w_\lambda w^\lambda\right)^{-1} w^\mu w_\lambda w_\nu \nabla_\mu w_\lambda = 0. \end{aligned} \tag{2.162}$$

We choose

$$B = \frac{\Gamma - 1}{\Gamma}, \tag{2.163}$$

then momentum equation becomes

$$\nabla_{[\mu} w_{\nu]} = 0. \tag{2.164}$$

Equation (2.164) allows one to write $\mathbf{w}$ as the gradient of a scalar field

$$\mathbf{w} = \nabla \varphi. \tag{2.165}$$

The equation of motion for φ is obtained from (2.155)

$$\nabla \cdot \left[(-\nabla\varphi \cdot \nabla\varphi)^C \nabla\varphi \right] = 0, \tag{2.166}$$

where

$$C = \frac{2-\Gamma}{2(\Gamma-1)}. \tag{2.167}$$

The condition (2.164), $\nabla_{[\mu}w_{\nu]} = 0$, reduces to the requirement that the fluid be irrotational,

$$\nabla_{[\mu}u_{\nu]} = 0. \tag{2.168}$$

Thus, the fluid equations for an ultrarelativistic, irrotational fluid can be written in terms of a nonlinear equation for a scalar field, φ. For the stiff fluid ($\Gamma = 2$), we find that the equation of motion for φ becomes the massless Klein-Gordon equation

$$\Box\varphi = 0. \qquad (P = \rho) \tag{2.169}$$

This identification allows for a great simplification of the fluid equations. Petrich, Shapiro, and Teukolsky [102] were able to exploit this simplification to derive an axisymmetric accretion solution for relativistic fluids.

One typically places physically motivated conditions on the fluid variables, such as $\rho > 0$ and $\mathbf{u} \cdot \mathbf{u} = -1$. General solutions of the Klein-Gordon equation, however, have time-like, null, *and* space-like gradients ($\nabla\varphi$). With the usual physical constraints on the fluid, then, only a subset of possible Klein-Gordon solutions can be interpreted as $\Gamma = 2$ perfect fluids, namely those with $\nabla\varphi \cdot \nabla\varphi < 0$ everywhere in the space-time.

Chapter 3

Numerical methods

Differential equations have been at the heart of physics since Newton formulated his second law of motion, and, along with Leibnitz, initiated the study of differentials. While differential equations may appear deceptively simple—although not the case for the Einstein equations—their solution is notoriously difficult. The application of Newton's law to physical systems, especially in astronomy, drove the need for approximate solution techniques, wherein "brute force" could partially substitute for ingenuity. These approximate methods replace differential operators by algebraic operations, which are more easily manipulated. No doubt that the computer revolution of the past 50 years has greatly increased the importance of numerical solutions in contemporary physics, however, the basic ideas are centuries old. As an example of early numerical work—and certainly the fortitude required of its practitioners—consider the work by Clairaut, Lalande, and Lapaute in 1748 to accurately predict the return of Halley's comet by including the effects of Jupiter and Saturn on the comet's orbit. Lalande wrote:

> During six months we calculated from morning to night, sometimes even at meals; the consequence of which was, that I contracted an illness which changed my constitution for the rest of my life. The assistance rendered by Madame Lapaute was such that without her we should never

> have dared to undertake this enormous labor; in which it was necessary to calculate the distance of each of the two planets, Jupiter and Saturn, from the comet, separately for every successive degree, for 150 years. (Quoted by Grossman [62].)

Their prediction of the comet's perihelion on 13 April 1749 was off by only 31 days.

This chapter begins with a brief summary of fundamental concepts for numerical solutions of differential equations, and then focuses on the control volume methods for conservation laws. The literature on these methods is vast, and the reviews by LeVeque [79, 81] are excellent introductions to conservative methods. Our presentation here is in the spirit of his work. Furthermore, the application of these methods specifically to problems in relativistic astrophysics has been recently reviewed by Ibáñez and Martí [72]. There follows a brief summary of some important approximate methods for solving the Riemann problem, and an introduction to the Reconstruct-Solve-Average algorithm. This algorithm is a generalization of Godunov's method, and is used to create higher-order numerical methods for conservation laws. Optimizations for extremely relativistic fluids, an original contribution of this dissertation, are considered in the final section.

3.1 Finite differences

Perhaps the simplest way to approximate derivatives with algebraic expressions is finite differencing. Recall the formal definition of the derivative of a real function, $f(x)$,

$$\frac{\mathrm{d}f}{\mathrm{d}x} \equiv \lim_{h\to 0} \frac{f(x+h)-f(x)}{h}. \tag{3.1}$$

The finite difference approximation comes simply by removing the limit, and choosing h to be a small, but finite value, which we write now as $\triangle x$. A finite difference

Derivative		Finite-difference approximation
$\partial_x f_i$	$=$	$\dfrac{f_{i+1} - f_i}{h} + \mathrm{O}(h)$
$\partial_x f_i$	$=$	$\dfrac{f_i - f_{i-1}}{h} + \mathrm{O}(h)$
$\partial_x f_i$	$=$	$\dfrac{f_{i+1} - f_{i-1}}{h} + \mathrm{O}(h^2)$
$\partial_x f_i$	$=$	$\dfrac{3f_i - 4f_{i-1} + f_{i-2}}{2h} + \mathrm{O}(h^2)$
$\partial_x f_i$	$=$	$\dfrac{-3f_i + 4f_{i+1} - f_{i+2}}{2h} + \mathrm{O}(h^2)$
$\partial_x^2 f_i$	$=$	$\dfrac{f_i - 2f_{i+1} + f_{i+2}}{h^2} + \mathrm{O}(h)$
$\partial_x^2 f_i$	$=$	$\dfrac{f_i - 2f_{i-1} + f_{i-2}}{h^2} + \mathrm{O}(h)$
$\partial_x^2 f_i$	$=$	$\dfrac{f_{i+1} - 2f_i + f_{i-1}}{h^2} + \mathrm{O}(h^2)$
$\partial_x^3 f_i$	$=$	$\dfrac{f_{i+2} - 2f_{i+1} + 2f_{i-1} - f_{i-2}}{2h^3} + \mathrm{O}(h^2)$
$\partial_x^4 f_i$	$=$	$\dfrac{f_{i+2} - 4f_{i+1} + 6f_i - 4f_{i-1} + f_{i-2}}{h^4} + \mathrm{O}(h^2)$
$\partial_x^2 f_i$	$=$	$\dfrac{-f_{i+3} + 4f_{i+2} - 5f_{i+1} + 2f_i}{h^2} + \mathrm{O}(h^2)$
$\partial_x^2 f_i$	$=$	$\dfrac{2f_i - 5f_{i-1} + 4f_{i-2} - f_{i-3}}{h^2} + \mathrm{O}(h^2)$
$\partial_x^3 f_i$	$=$	$\dfrac{-3f_{i+4} + 14f_{i+3} - 24f_{i+2} + 18f_{i+1} - 5f_i}{2h^3} + \mathrm{O}(h^2)$
$\partial_x^3 f_i$	$=$	$\dfrac{5f_i - 18f_{i-1} + 24f_{i-2} - 14f_{i-3} + 3f_{i-4}}{2h^3} + \mathrm{O}(h^2)$
$\partial_x f_i$	$=$	$\dfrac{-f_{i+2} + 8f_{i+1} - 8f_{i-1} + f_{i-2}}{12h} + \mathrm{O}(h^4)$
$\partial_x^2 f_i$	$=$	$\dfrac{-f_{i+2} + 16f_{i+1} - 30f_i + 16f_{i-1} - f_{i-2}}{12h^2} + \mathrm{O}(h^4)$

Table 3.1: Table of finite difference approximations from Anderson *et al.* [2].

approximation to the derivative is then is

$$\frac{\mathrm{d}f}{\mathrm{d}x} \approx \frac{f(x+\triangle x) - f(x)}{\triangle x}. \tag{3.2}$$

Finite difference approximations can be derived in numerous ways, such as the Taylor expansion, which also allows us to determine the approximation's accuracy. For example, by expanding

$$f(x+\triangle x) = f(x) + \frac{\mathrm{d}f(x)}{\mathrm{d}x}(\triangle x) + \frac{1}{2}\frac{\mathrm{d}^2 f(x)}{\mathrm{d}x^2}(\triangle x)^2 + \mathrm{O}\left((\triangle x)^3\right). \tag{3.3}$$

and then solving for $\mathrm{d}f(x)/\mathrm{d}x$,

$$\frac{\mathrm{d}f}{\mathrm{d}x} = \frac{f(x+\triangle x) - f(x)}{\triangle x} + \mathrm{O}(\triangle x) \tag{3.4}$$

we find that the finite difference approximation (3.2) has the leading-order (truncation) error term $\mathrm{O}(\triangle x)$. The finite difference approximation can be improved by judiciously choosing the algebraic formulation, as guided by the Taylor expansion. For example, by expanding $f(x+\triangle x)$ and $f(x-\triangle x)$, we find that

$$\frac{\mathrm{d}f}{\mathrm{d}x} = \frac{f(x+\triangle x) - f(x-\triangle x)}{2\triangle x} + \mathrm{O}\left((\triangle x)^2\right) \tag{3.5}$$

is a more accurate approximation to the derivative. One can derive other approximations for a derivative, to any desired accuracy, and several finite difference approximations are shown in table 3.1.

A finite difference approximation used for solving differential equations must also satisfy other properties, such as stability. However, a complete discussion is beyond the scope of this dissertation.

3.1.1 Two example finite-difference schemes

This section presents two sample finite-difference schemes for hyperbolic equations, the Lax-Friedrichs method and the Crank-Nicholson method. The Lax-Friedrichs method is and *explicit* method, meaning that the dependent variable at the advanced time, $\mathbf{q}_i^{n+1}$, is a function only of $\mathbf{q}^n$ at the previous time. Crank-Nicholson, on the other hand, is an *implicit* method, and $\mathbf{q}_i^{n+1}$ is generally a function of neighboring points also at the advanced time, e.g., $\mathbf{q}_i^{n+1}$ is a function of $\mathbf{q}_{i\pm1}^{n+1}$. Although any of a number of methods could be chosen as examples, these common methods were chosen simply because they are referenced in latter sections of this dissertation.

Consider the hyperbolic, partial differential equation

$$\partial_t \mathbf{q} + \partial_x \mathbf{f}(\mathbf{q}) = \mathbf{\Sigma}(\mathbf{q}), \tag{3.6}$$

where $\mathbf{q}$ may be either a scalar or a 'vector' with multiple components. The source term $\mathbf{\Sigma}(\mathbf{q})$ is a function only of $\mathbf{q}$, and contains no derivatives of $\mathbf{q}$. We discretize the spatial domain, establishing grid points at

$$x_i = (i-1)\triangle x, \qquad i = 1, \ldots, N_x \tag{3.7}$$

and calculate the solution at discrete times given by

$$t^n = n\triangle t, \qquad n = 0, \ldots, N_t - 1 \tag{3.8}$$

The function $\mathbf{q}_i^n$ is the discretized solution at x_i and $t = t^n$,

$$\mathbf{q}_i^n \equiv \mathbf{q}(x_i, t^n). \tag{3.9}$$

The Lax-Friedrichs discretization is a very simple explicit scheme using a centered spatial difference, and calculates the time derivative with the average of $\mathbf{q}_{i+1}^n$ and $\mathbf{q}_{i-1}^n$ at the retarded time, instead of $\mathbf{q}_i^n$ for stability.

$$\frac{\mathbf{q}_i^{n+1} - (\mathbf{q}_{i+1}^n + \mathbf{q}_{i-1}^n)/2}{\triangle t} + \frac{\mathbf{f}_{i+1}^n - \mathbf{f}_{i-1}^n}{2\triangle x} = \mathbf{\Sigma}_i^n \tag{3.10}$$

Using the Taylor expansion, we can show that the truncation error for this scheme is $\mathrm{O}\left((\triangle x)^2/\triangle t, \triangle t\right)$.

The Crank-Nicholson method is an implicit method with good stability properties, and is used to integrate the scalar gravity equations of motion, of chapter 7. The Crank-Nicholson discretization of (3.6) is

$$\frac{\mathbf{q}_i^{n+1} - \mathbf{q}_i^n}{2\triangle t} + \frac{1}{2}\left[\frac{\mathbf{f}_{i+1}^n - \mathbf{f}_{i-1}^n}{2\triangle x} + \frac{\mathbf{f}_{i+1}^{n+1} - \mathbf{f}_{i-1}^{n+1}}{2\triangle x}\right] = \frac{1}{2}\left(\mathbf{\Sigma}_i^{n+1} + \mathbf{\Sigma}_i^n\right). \tag{3.11}$$

The derivatives are centered in space and time, and a more complete analysis shows the accuracy of this method to be $\mathrm{O}\left((\triangle x)^2, (\triangle t)^2\right)$. The Crank-Nicholson method is an implicit scheme because $\mathbf{q}^{n+1}$ appears in the flux terms as well as the time derivative in (3.11). We can solve for $\mathbf{q}^{n+1}$ in a variety of ways, and an iterative method with successive over-relaxation (SOR) is used for the scalar gravity equations of motion.

The Lax-Friedrichs and Crank-Nicholson methods discretize space and time simultaneously. An alternative technique is the *method of lines,* wherein the discretization of space and time is performed independently. This method is used to discretize the fluid equations, and is the subject of Section 3.7.

3.1.2 Error and numerical solutions

This section briefly summarizes some basic ideas and definitions used when working with finite difference techniques. This section follows lecture notes by Choptuik [36].

A differential equation can be written

$$L(q) = f, \tag{3.12}$$

where L represents a differential operator and f is a source term. Let L^h be a corresponding discretized differential operator, and write the difference equation as

$$L^h(q^h) = f^h, \tag{3.13}$$

where h represents the grid spacing and q^h is the discretized solution obtained with resolution h. (In the following we assume that there is a *single* discretization scale in the discrete problem.) In general, the continuum solution, q, is *not* a solution of L^h, which leads to the definition of the *truncation error*

$$\text{T.E.}^h \equiv L^h(q) - f^h. \tag{3.14}$$

The truncation error can be found from Taylor expansions of the finite difference operators and the differential equations.

By solving the finite difference equations, we obtain the discretized solution, q^h, while in actuality we are interested in the continuum solution, q. Thus, we require the difference equations to have the *convergence* property, which is

$$q^h \to q \qquad \text{as} \qquad h \to 0. \tag{3.15}$$

A finite difference approximation is *consistent* if

$$\text{T.E.}^h \to 0 \qquad \text{as} \qquad h \to 0. \tag{3.16}$$

The leading-order behavior of the truncation error as a function of the discretization scale gives the *order* of a difference approximation. A finite difference scheme is *p-th order* when

$$\lim_{h \to 0} \text{T.E.}^h = \text{O}\,(h^p), \tag{3.17}$$

where p is an integer.

The *solution error,* e^h, contains all error that arises from the replacement of the continuum problem with a discrete problem

$$e^h \equiv q - q^h. \tag{3.18}$$

The finite difference approximation (3.13) can be written

$$L^h(q^h) - f^h = 0. \tag{3.19}$$

Let $\hat{q}^h$ be an approximation of the true discretized solution, then the *residual,* r^h, is defined as

$$r^h \equiv L^h(\hat{q}^h) - f^h. \tag{3.20}$$

Round-off error is the error resulting from using finite precision arithmetic, and this error can be particularly important for relativistic fluid codes. The fluid equations contain quantities, such as the W, v, and ρ_o, which can vary over many orders of magnitude. Many of our optimizations for extremely relativistic flow come from a consideration of round-off error, and are further discussed in Section 3.9.

A common assumption is that

$$\mathrm{T.E}^h = \mathrm{O}\,(h^p) \qquad \rightarrow \qquad e^h = \mathrm{O}\,(h^p). \tag{3.21}$$

While this assumption is often valid, it is *not* automatically true. The connection comes from Richardson's *ansatz* [107], that the discrete solution can be expanded about the continuum solution in powers of h

$$q^h = q + he_1 + h^2 e_2 + h^3 e_3 + \cdots \tag{3.22}$$

where e_1, e_2, $\cdots$ are continuum *error functions* independent of h. When the difference scheme is completely centered, the *ansatz* is

$$q^h = q + h^2 e_2 + h^4 e_4 + \cdots \tag{3.23}$$

A solution q^h of a finite difference approximation can only used with confidence if it has been studied at different resolutions (different values of h), and we can verify that the solution converges. The Richardson *ansatz* enables one of the most crucial tests of a discrete solution's convergence properties. For example, consider a finite difference scheme with centered derivatives, and calculate the discrete solution at 3 different resolutions, h, $2h$, and $4h$. Using the Richardson *ansatz*, the discrete solutions can be expanded

$$q^h = qh^2 e_2 + h^4 e_4 + \cdots \tag{3.24}$$

$$q^{2h} = q(2h)^2 e_2 + (2h)^4 e_4 + \cdots \tag{3.25}$$

$$q^{4h} = q(4h)^2 e_2 + (4h)^4 e_4 + \cdots \tag{3.26}$$

Define the *convergence factor* to be

$$Q(t) \equiv \frac{||q^{4h} - q^{2h}||}{||q^{2h} - q^h||}, \tag{3.27}$$

	Vector	Matrix
one-norm	$\|\|\boldsymbol{x}\|\|_1 = \frac{1}{N}\sum_i^N \|x_i\|$	$\|\|\boldsymbol{A}\|\|_1 = \frac{1}{M}\max_j \sum_i^M \|a_{ij}\|$
two-norm	$\|\|\boldsymbol{x}\|\|_2 = \left(\frac{1}{N}\sum_i^N \|x_i\|^2\right)^{1/2}$	$\|\|\boldsymbol{A}\|\|_2 = \max_{x\neq 0} \frac{\|\|\boldsymbol{Ax}\|\|_2}{\|\|\boldsymbol{x}\|\|_2}$
Frobenius norm	$\|\|\boldsymbol{x}\|\|_F = \|\|\boldsymbol{x}\|\|_2$	$\|\|\boldsymbol{A}\|\|_F = \left(\frac{1}{MN}\sum_{ij} \|a_{ij}\|^2\right)^{1/2}$
infinity-norm	$\|\|\boldsymbol{x}\|\|_\infty = \max_i \|x_i\|$	$\|\|\boldsymbol{A}\|\|_\infty = \frac{1}{N}\max_i \sum_j^N \|a_{ij}\|$

Table 3.2: Definition of various norms for vectors and matrices normalized for ease of working with discrete approximations of numerical solutions. The vector $\boldsymbol{x}$ has N components, and $\boldsymbol{A}$ is an $M \times N$ matrix.

where $|| \cdot ||$ is a discrete norm. Table 3.2 contains the most common norms used in numerical work. If the difference scheme has been correctly implemented, if the scheme is consistent, and if the scheme converges, then from the Richardson *ansatz* it is elementary to show that

$$\lim_{h \to 0} Q(t) = 4. \tag{3.28}$$

In practice this test should be done at different resolutions to ensure that the scheme does in fact converge.

A second test of the discrete solution, q^h, is the *independent residual evaluation.* This tests that the discrete operator L^h has been correctly implemented, and hence that q^h converges to the correct continuum solution, q. For this test we construct an independently discretized differential operator, $\tilde{L}^h$, and evaluate the residual,

$$r^h = \tilde{L}^h(q^h) - f^h, \tag{3.29}$$

with q^h, the discrete solution of the original operator, L^h. If L^h and $\tilde{L}^h$ both correspond to the same continuum operator, L, then r^h will converge as expected from the Richardson *ansatz.* We note that often $\tilde{L}^h$ can be a very simple difference operator, as it is not used to produce the discretized solution, q^h. For example, the fluid updates that we use for the relativistic fluid equations are quite complicated. However, our independent residual evaluator uses the Leap-Frog scheme, which for (3.6) is simply

$$\frac{\mathbf{q}_i^{n+1} - \mathbf{q}_i^{n-1}}{2\triangle t} + \frac{\mathbf{q}_{i+1}^n - \mathbf{q}_{i-1}^n}{2\triangle x} = \Sigma_i^n. \tag{3.30}$$

3.2 Conservation laws

An important consideration for numerical solutions of compressible fluid flow is how the numerical method will respond to the presence or formation of shocks, i.e., discontinuities in the fluid variables. A shock is, strictly speaking, not a solution of the differential fluid equations, but rather a member of a larger class called *weak solutions.* (A particular weak solution is chosen to maximize the entropy.) As finite difference approximations are derived from the differential form of the equations, it is not surprising that they typically fail dramatically when shocks appear. As shocks form *generically* from smooth initial data, many special techniques have been developed for the numerical solution of fluid equations. One approach is to introduce an *artificial viscosity* that adds extra dissipation in the vicinity of a shock, spreading the would-be-discontinuity over a few grid points. Artificial viscosity is implemented by replacing

$$P \to P + Q \tag{3.31}$$

in the fluid equations, where the viscosity term, Q, is activated where the flow is compressive. (The artificial viscosity should only be applied to shocks, and not to rarefaction waves. In one dimension, this can be done by adding artificial viscosity only when $v(\mathrm{d}v/\mathrm{d}x) < 0$.) This technique has been widely used—including the very first relativistic fluid code by May and White [92]—and has the advantages of simplicity of implementation and computational efficiency. However, Norman and Winkler [98] investigated the use of artificial viscosity in relativistic fluid dynamics, and showed that an *explicit* numerical scheme treats the artificial viscosity term inconsistently in relativistic fluid dynamics. This leads to large numerical errors in the ultrarelativistic limit, $W \gg 1$. The inconsistency arises because the relativistic fluid conservation variables, e.g., S^i and E, contain P in their definitions. (The classical momentum and energy, on the other hand, are not functions of P.) A second approach to solving the fluid equations with shocks comes from methods developed specifically for conservation laws. These methods, usually variations or extensions of Godunov's original idea [58] to use piece-wise solution of the Riemann problem, have proven to be very reliable and robust.

Conservation laws greatly simplify the mathematical description of physical systems by focusing on quantities $\mathcal{Q}$—where $\mathcal{Q}$ may be a state vector with multiple components—that do not change with time

$$\partial_t \int_V \mathrm{d}\mathcal{Q} = 0. \tag{3.32}$$

In this section we discuss the derivation of numerical schemes for this specific and important case where $\int \mathrm{d}\mathcal{Q}$ is conserved on the computational domain. Our discussion will be general, and not specifically tailored for the fluid PDEs derived in Section 2.5, but for simplicity we restrict the discussion to one dimensional (in space) systems.

While conservation laws are often written in *differential* form (e.g., $\nabla \cdot \mathbf{T} = 0$) it is useful to first consider an *integral* formulation, which is often the more fundamental expression. Consider an arbitrary volume or cell, $\mathcal{C}_i$, with a domain $[x_i, x_{i+1}]$. The quantity of $\mathcal{Q}$ within $\mathcal{C}_i$ is denoted $\mathcal{Q}_i$, and we define a density function $\mathbf{q}$ such that

$$\mathcal{Q}_i = \int_{x_i}^{x_{i+1}} \mathrm{d}x\, \mathbf{q}. \tag{3.33}$$

The change of $\mathcal{Q}_i$ with time can be calculated from the flux, $\mathbf{f}(\mathbf{q})$, of $\mathbf{q}$ through the cell boundaries. This consideration thus expresses the conservation law:

$$\frac{\mathrm{d}}{\mathrm{d}t}\int_{x_i}^{x_{i+1}} \mathrm{d}x\,\mathbf{q}(x,t) = \mathbf{f}(\mathbf{q}(x_i,t)) - \mathbf{f}(\mathbf{q}(x_{i+1},t)). \tag{3.34}$$

The conservation law can be written in *integral* form by integrating (3.34) from an initial time, t^n, to a final time, t^{n+1},

$$\int_{x_i}^{x_{i+1}} \mathrm{d}x\,\mathbf{q}(x,t^{n+1}) = \\ \int_{x_i}^{x_{i+1}} \mathrm{d}x\,\mathbf{q}(x,t^n) + \int_{t^n}^{t^{n+1}} \mathrm{d}t\,\mathbf{f}(\mathbf{q}(x_i,t)) - \int_{t^n}^{t^{n+1}} \mathrm{d}t\,\mathbf{f}(\mathbf{q}(x_{i+1},t)) \tag{3.35}$$

and the differential form follows from further manipulation *if* we assume that $\mathbf{q}$ is differentiable:

$$\partial_t\mathbf{q} + \partial_x\mathbf{f}(\mathbf{q}) = 0. \tag{3.36}$$

It should be emphasized that the integral formulation should be viewed as *the* primary mathematical form for a conservation principle, because it is *not* dependent on an assumption of differentiability. For example, at a shock front in a fluid system, $\mathbf{q}$ is not differentiable, and the differential form of the conservation law fails, while the integral formulation is still satisfied. Discretizations of conservation equations via finite differences rely on the differential form, and artificial viscosity must be added near shock fronts, forcing $\mathbf{q}$ to be differentiable. An alternate strategy is to develop numerical algorithms based directly on the integral formulation of the conservation laws. The Godunov method and its extensions are examples of this latter approach, and are the topic of the next section.

3.3 Godunov's method

Numerical algorithms for conservation laws are typically developed by discretizing the equations in their fundamental integral form. These methods are often derived using a *control volume* discretization, whereby the domain is divided into *computational* cells, C_i, now defined to span the interval $[x - \triangle x/2, x + \triangle x/2] \equiv [x_{i-1/2}, x_{i+1/2}]$, where $\triangle x$ is the (local) spatial discretization scale. Following the derivation of the integral conservation law (3.35) for the computation cell C_i, we introduce the *averaged* quantities, $\bar{\mathbf{q}}_i^n$:

$$\bar{\mathbf{q}}_i^n = \frac{1}{\triangle x} \int_{x_{i-1/2}}^{x_{i+1/2}} \mathrm{d}x \, \mathbf{q}(x, t_n). \tag{3.37}$$

The discrete form of the conservation law (3.35) is then

$$\bar{\mathbf{q}}_i^{n+1} = \bar{\mathbf{q}}_i^n - \frac{\triangle t}{\triangle x} \left(\mathbf{F}_{i+1/2} - \mathbf{F}_{i-1/2} \right), \tag{3.38}$$

where the "numerical flux" is defined by

$$\mathbf{F}_{i+1/2} = \frac{1}{\triangle t} \int_{t_n}^{t_{n+1}} \mathrm{d}t \, \mathbf{f}(\mathbf{q}(x_{i+1/2}, t). \tag{3.39}$$

At first blush, a numerical method based on a discretization of the integral conservation law does not appear promising: the flux integral (3.39) does not appear readily solvable, and it generally is not. However, in his seminal work, Godunov [58] devised a technique to approximately evaluate the flux integral by replacing the function $\mathbf{q}(x, t_n)$ with $\tilde{\mathbf{q}}(x, t_n)$, where $\tilde{\mathbf{q}}(x, t_n)$ is a piece-wise constant function. In this approach, the individual cells ("control volumes") are treated as a sequence of "shock tubes", and a separate Riemann initial value problem is solved at each cell interface. Provided that the waves from neighboring cells do not interact—a proviso which gives a Courant-type condition on the time-step—each Riemann problem can be solved exactly to yield the local solution $\tilde{\mathbf{q}}(x, t)$ (for $t > t_n$) for each "shock tube." Furthermore, since the solution of each of the local Riemann problems is self-similar, $\tilde{\mathbf{q}}(x_{i+1/2}, t)$ is a constant in time, and the evaluation of the integral (3.39) becomes trivial. This then allows one to find explicit expressions for the cell averages at the advanced time, $\bar{\mathbf{q}}^{n+1}$, via (3.38). In summary, the Godunov method proceeds as follows: (i) From the average $\bar{\mathbf{q}}_i^n$, one "reconstructs" a piece-wise constant function

$\tilde{\mathbf{q}}(x,t_n)$ to approximate the solution in C_i; (ii) the Riemann problem is solved at the interfaces between cells, giving the solution $\tilde{\mathbf{q}}(x,t)$ for $t_n < t \leq t_{n+1}$; (iii) the solution $\tilde{\mathbf{q}}(x,t_{n+1})$ is averaged over the cell C_i to obtain the average at the advanced time, $\bar{\mathbf{q}}_i^{n+1}$. This is the *Reconstruct-Solve-Average* algorithm used to extend Godunov's method to higher-order methods. We note that methods for solving the Riemann problem exactly for relativistic fluids have been given by Smoller and Temple [123] for the ultrarelativistic equation of state, and by Martí and Müller [89] for the ideal-gas state equation.

Godunov's method has many nice properties: in particular, it is conservative and allows for the stable evolution of strong shocks. However, the original scheme *does* have some shortcomings: convergence is only first order, and the exact solution of the Riemann problem may be computationally expensive, especially for relativistic fluids. The convergence of the scheme can be improved by providing a more sophisticated reconstruction $\tilde{\mathbf{q}}(x,t_n)$, giving what are known as *high-resolution shock-capturing* methods. One such procedure is described in Section 3.4, and an example of the scheme's convergence given in Section 4.5. In order to address the issue of computational efficiency, approximate Riemann solvers have been developed that relate the problem-at-hand to a simpler system, for which the Riemann problem is easier to solve. Several approximate Riemann solvers have been developed for classical fluid dynamics, and many of these approximate methods have been extended to relativistic fluid systems. These include relativistic two-shock solvers (Section 3.5.1), a relativistic HLLE solver (Section 3.5.2), and the linearized solvers of Roe (Section 3.5.3), and Marquina (Section 3.5.5).

3.4 The Reconstruct-Solve-Average algorithm

Godunov-type numerical methods are based on solutions of the Riemann initial value problem at the interfaces between cells. As discussed above, during an update step we introduce functions $\tilde{\mathbf{q}}(x,t)$—defined piece-wise on the intervals $[x_{i-1/2}, x_{i+1/2}]$—to approximate the solution in the control volumes C_i. These functions are created from the cell averages $\bar{\mathbf{q}}_i^n$, and hence are called *reconstructions.* Consider the cell interface at $x_{_{i+1/2}}$: the state of the fluid immediately to the right (left) is $\tilde{\mathbf{q}}^r_{_{i+1/2}}$ ($\tilde{\mathbf{q}}^\ell_{_{i+1/2}}$). The simplest reconstruction is to assume that $\tilde{\mathbf{q}}$ is piece-wise constant

$$\tilde{\mathbf{q}}^\ell_{_{i+1/2}} = \bar{\mathbf{q}}_i, \qquad \tilde{\mathbf{q}}^r_{_{i+1/2}} = \bar{\mathbf{q}}_{i+1}, \tag{3.40}$$

as used in the original Godunov method and, as already discussed, this reconstruction results in a numerical scheme in which the spatial derivatives (and hence the overall scheme) have first order accuracy. The convergence can be improved by using a higher-order reconstruction for $\tilde{\mathbf{q}}$, but, as discussed below, care must be exercised so that the reconstruction does not induce spurious oscillations near discontinuities.

The work in this dissertation uses piece-wise *linear* reconstructions for $\tilde{\mathbf{q}}$, which formally results in a scheme with second order convergence. (The convergence properties are discussed in greater detail in Section 4.5, where convergence tests for a spherically symmetric code are presented.) A first choice for the reconstruction algorithm might be to compute the slope (derivative of the dynamical variable) centered at the cell boundaries

$$\mathbf{s}_{i+1/2} = \frac{\bar{\mathbf{q}}_{i+1} - \bar{\mathbf{q}}_i}{r_{i+1} - r_i}, \tag{3.41}$$

creating the reconstructed variables

$$\tilde{\mathbf{q}}^\ell_{i+1/2} = \bar{\mathbf{q}}_i + \mathbf{s}_i(r_{i+1/2} - r_i), \qquad \text{(naïve)} \tag{3.42}$$

and

$$\tilde{\mathbf{q}}^r_{_{i+1/2}} = \bar{\mathbf{q}}_{i+1} + \mathbf{s}_{i+1}(r_{i+1/2} - r_{i+1}). \qquad \text{(naïve)} \tag{3.43}$$

However, as shown in Figure 3.1, this reconstruction produces spurious oscillations at shocks, making the scheme unstable. One therefore introduces a *slope limiter,* designed to damp any oscillations near discontinuities [132, 61]. Using the mathematical property known as *total variation diminishing* (TVD), a variety of slope limiters have been published in the literature. (For an introduction to TVD limiters see LeVeque [79].) Four of the most common limiters are presented in Section 3.4.1. We let $\boldsymbol{\sigma}_i = \boldsymbol{\sigma}_i(\mathbf{s}_{i-1/2}, \mathbf{s}_{i+1/2})$ represent the "limited" slopes, and define the reconstruction to be

$$\tilde{\mathbf{q}}^{\ell}_{i+1/2} = \bar{\mathbf{q}}_i + \boldsymbol{\sigma}_i(r_{i+1/2} - r_i), \tag{3.44}$$

$$\tilde{\mathbf{q}}^{r}_{i+1/2} = \bar{\mathbf{q}}_{i+1} + \boldsymbol{\sigma}_{i+1}(r_{i+1/2} - r_{i+1}), \tag{3.45}$$

where algorithms for calculating the "limited slopes," $\boldsymbol{\sigma}$, are described in Section 3.4.1. The limiter forces $\tilde{\mathbf{q}}$ to be monotonic near discontinuities, and this reduces the (local) accuracy of the scheme to first order.

Finally, if we are unable to calculate physical values for $\tilde{\mathbf{w}}^{\ell}$ and $\tilde{\mathbf{w}}^{r}$ (a situation which *can* and *does* occur owing to the finite-precision nature of our computations) we revert to a piece-wise constant reconstruction for $\tilde{\mathbf{q}}^{\ell}$ and $\tilde{\mathbf{q}}^{r}$.

3.4.1 Slope Limiters

This section presents four total-variation-diminishing (TVD) limiters commonly used in the literature. A comparison of the different limiters discussed here is shown in Figure 3.2, for the advection equation,

$$\partial_t q + \partial_x q = 0. \tag{3.46}$$

The minmod and MC-limiters are compared for relativistic fluids in a shock tube problem, with results shown in Figures 4.10 and 4.11.

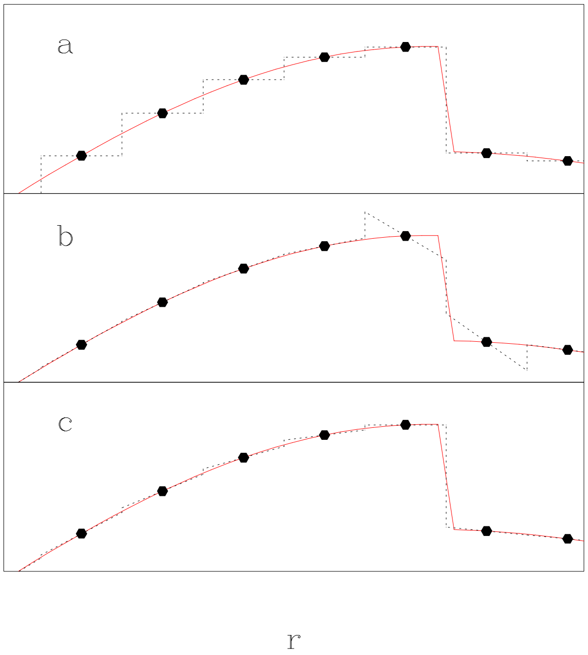

Figure 3.1: The three frames of this plot show different ways a discretized function can be reconstructed in a control-volume numerical method. The solid line represents a continuum (or “analytic”) function and the solid hexagons represent discrete, approximate values of the function defined at grid points. Frame (a) represents the piece-wise constant reconstruction. Frame (b) shows a naïve piece-wise linear reconstruction of each cell using $\mathbf{s}_{i+1/2}$. This reconstruction oscillates near discontinuities in the function—such oscillations can easily lead to instabilities. Frame (c) shows a piece-wise linear reconstruction performed with the minmod limiter as described in the text. This reconstruction produces a discrete representation of the dynamical variable which remains well-behaved near discontinuities.

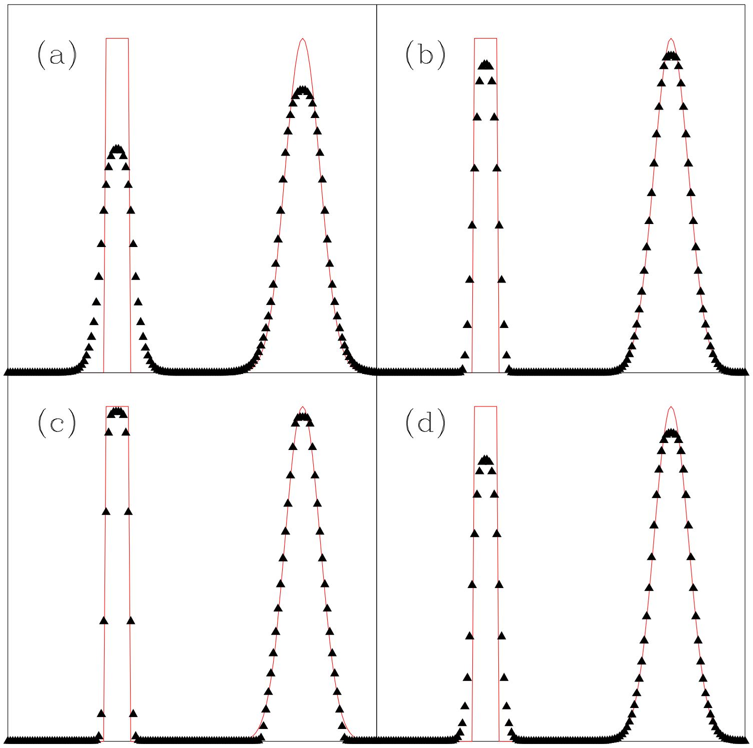

Figure 3.2: The four slope limiters discussed in the text are demonstrated here by solving the advection equation, $\partial_t q + \partial_x q = 0$, using a high-resolution Godunov-type scheme. Frame (a) shows the solution calculated using the minmod limiter after 800 iterations, frame (b) the solution resulting from the monotonized central-difference limiter (MC), frame (c) the solution obtained using the superbee limiter, and frame (d) the solution with the van Leer limiter. In each frame the evolution solution is shown with triangles, and the solid line shows the exact solution. These solutions calculated with a Courant factor of 1/2. This figure is modeled after a similar figure by LeVeque [81].

The minmod limiter

The most common slope limiter used in relativistic fluid dynamics is van Leer's [132] minmod limiter

$$\boldsymbol{\sigma}_i = \operatorname{minmod}(\mathbf{s}_{i-1/2}, \mathbf{s}_{i+1/2}), \tag{3.47}$$

where the minmod function gives the minimum modulus of the two arguments

$$\operatorname{minmod}(a,b) = \begin{cases} \operatorname{sgn}(a)\min(\,|a|, |b|\,) & \text{if } \operatorname{sgn}(a) = \operatorname{sgn}(b), \\ 0 & \text{otherwise.} \end{cases} \tag{3.48}$$

The sign function, $\operatorname{sgn}(a)$, is

$$\operatorname{sgn}(a) \equiv \begin{cases} +1 & a > 0 \\ -1 & a < 0. \end{cases} \tag{3.49}$$

The slopes $\mathbf{s}_{i-1/2}$ and $\mathbf{s}_{i+1/2}$ are calculated with (3.41). The minmod limiter is more diffusive than the MC-limiter or the superbee limiter (see Figure 3.2). However, we found this limiter to work best near the origin in spherical symmetry, and thus use this limiter exclusively for all critical solution studies.

The monotonized central-difference limiter

The monotonized central-difference limiter (MC-limiter) was also introduced by van Leer [131]. Here the limited slope is

$$\boldsymbol{\sigma}_i = \operatorname{minmod}\left(\mathbf{s}_i,\, 2\mathbf{s}_{i-1/2},\, 2\mathbf{s}_{i+1/2}\right), \tag{3.50}$$

where $\mathbf{s}_{i+1/2}$ and $\mathbf{s}_{i-1/2}$ are calculated as shown in (3.41), and

$$\mathbf{s}_i = \frac{\bar{\mathbf{q}}_{i+1} - \bar{\mathbf{q}}_{i-1}}{x_{i+1} - x_{i-1}}. \tag{3.51}$$

The minmod function with three arguments is

$$\operatorname{minmod}(a,b,c) = \begin{cases} \operatorname{sgn}(a)\min(\,|a|, |b|, |c|\,) & \text{if } \operatorname{sgn}(a) = \operatorname{sgn}(b) \\ & \textit{and } \operatorname{sgn}(b) = \operatorname{sgn}(c) \\ 0, & \text{otherwise.} \end{cases} \tag{3.52}$$

The van Leer limiter

The last of van Leer's limiters considered here is known simply as the van-Leer limiter [130]

$$\boldsymbol{\sigma}_i = \frac{|\mathbf{s}_{i+1/2}| - |\mathbf{s}_{i-1/2}|}{|\mathbf{s}_{i+1/2}| + |\mathbf{s}_{i-1/2}|}. \tag{3.53}$$

If the denominator is zero, then $\boldsymbol{\sigma}_i = 0$.

The superbee limiter

Roe's [111] superbee limiter is

$$\boldsymbol{\sigma}_i = \operatorname{maxmod}(\boldsymbol{\sigma}_i^{(1)}, \boldsymbol{\sigma}_i^{(2)}), \tag{3.54}$$

where

$$\boldsymbol{\sigma}_i^{(1)} = \operatorname{minmod}(\mathbf{s}_{i+1/2},\, 2\mathbf{s}_{i-1/2}), \tag{3.55}$$

$$\boldsymbol{\sigma}_i^{(2)} = \operatorname{minmod}(2\mathbf{s}_{i+1/2},\, \mathbf{s}_{i-1/2}), \tag{3.56}$$

and

$$\operatorname{maxmod}(a, b) = \begin{cases} \operatorname{sgn}(a) \max(|a|, |b|) & \text{if } \operatorname{sgn}(a) = \operatorname{sgn}(b), \\ 0 & \text{otherwise.} \end{cases} \tag{3.57}$$

3.4.2 Other reconstructions

For completeness, we note that other reconstructions have been used, which are more complicated. The natural extension of the piece-wise linear reconstruction is Colella and Woodward's [42, 136] piece-wise parabolic method (PPM). Martí and Müller [89] first used the PPM method with an exact Riemann solver in a relativistic ideal-gas code. Marquina [87] developed the piece-wise hyperbolic reconstruction (PHM). This reconstruction method has also been used in a relativistic fluid code [46]. Finally, there are the well-known Essentially Non-Oscillatory (ENO) schemes, see for example the implementation by Shu and Osher [121, 122]. Shu and Osher's ENO scheme, and Marquina's PHM both require an uniform grid. ENO schemes have also been used in relativistic fluid dynamics [46, 56].

3.5 Approximate Riemann solvers

Finding the exact solution for the Riemann problem for fluids is generally computationally expensive, requiring the solution of nonlinear, transcendental equations. The equations must be solved iteratively, and in Godunov's method, a different solution must be found for each point on the grid per update cycle. The computational effort in relativistic fluid dynamics is complicated by adiabats with steep gradients (see Section 2.8.1, especially Figure 2.6), and difficulties with round-off error. Godunov's method, however, does not require the full structure of the Riemann solution, but only uses the *average* quantities $\bar{\mathbf{q}}$. Given the computational expense of the exact problem, several methods have been developed for approximately solving the Riemann problem. The deficiencies of the approximate solutions are often compensated by the averaging process, such that the final result, $\bar{\mathbf{q}}$, differs only slightly from the average solution obtained with an exact solver.

The approximate Riemann solvers presented here do not solve the relativistic fluid initial value problem *per se,* but rather they solve a simplified, but related, system. (The theory of approximate Riemann solvers is given by LeVeque [79].) The first type of approximate solvers are (i) the nonlinear solvers, which replace rarefactions with discontinuities, producing a more efficient solver that still retains the nonlinear features of arbitrarily strong shocks. The second solver (ii) is the Harten-Lax-vanLeer-Einfeldt (HLLE) solver, which simplifies the structure of the Riemann problem by using only one intermediate state between two shock waves which connect the initial left and right states. The third type of solvers (iii) are the linearized solvers, such as the Roe and Marquina solvers, which solve a (related) linearized system whose solution is more easily found.

The most important approximate Riemann solvers for classical fluids have been extended to special relativity. Furthermore, Pons *et al.* [105] give a general method for extending any special relativistic Riemann solver to general relativity. Their method is based on the local flatness of curved spacetimes.

3.5.1 Nonlinear solvers

The initial states of the Riemann problem are connected by two intermediate states and two waves, which may be either shock or rarefaction waves, although only two waves will connect the state in a physical way. One simplification of the Riemann problem is to eliminate rarefaction waves and consider only shock waves. This simplifies both the equations that must be solved, and the resulting numerical implementation. Balsara [6] developed a multi-dimensional relativistic shock-shock solver. Dai and Woodward [44] have an alternative solver, which achieves slightly better performance by solving some of the equations in Lagrangian coordinates.

3.5.2 The Harten-Lax-van Leer-Einfeldt approximate Riemann solver

The Harten-Lax-vanLeer-Einfeldt (HLLE) algorithm is a very simple approximate Riemann solver [47]. The algorithm assumes that the maximum signal velocities, b_ℓ and b_r, for left and right moving waves, respectively, are known. The three states for this solver are the initial left (right) state, $\mathbf{q}_\ell$ ($\mathbf{q}_r$), for the region beyond the distance traveled by the fastest left (right)-moving signal, and a single intermediate state, $\mathbf{q}_{\ell r}$:

$$\mathbf{q}(x,t;\mathbf{q}_\ell,\mathbf{q}_r) = \begin{cases} \mathbf{q}_\ell & x < b_\ell t \\ \mathbf{q}_{\ell r} & b_\ell t \leq x \leq b_r t \\ \mathbf{q}_r & x > b_r t. \end{cases} \tag{3.58}$$

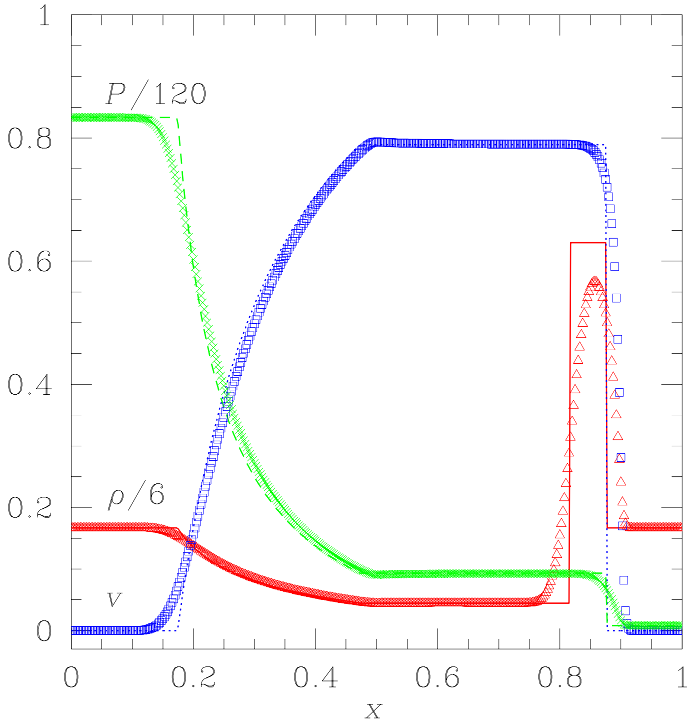

Figure 3.3: A shock tube test with the HLLE approximate Riemann solver, for a $\Gamma = 5/3$ fluid. The initial left state is $(\rho_o)_\ell = 1$, $v_\ell = 0$, and $P_\ell = 100$; the initial right state is $(\rho_o)_r = 1$, $v_r = 0$, and $P_r = 1$. The lines show the exact solution at $t = 0.4$. The PDE solution is indicated by triangles (ρ_o), squares (v), and crosses (P). The solution is calculated with 400 cells.

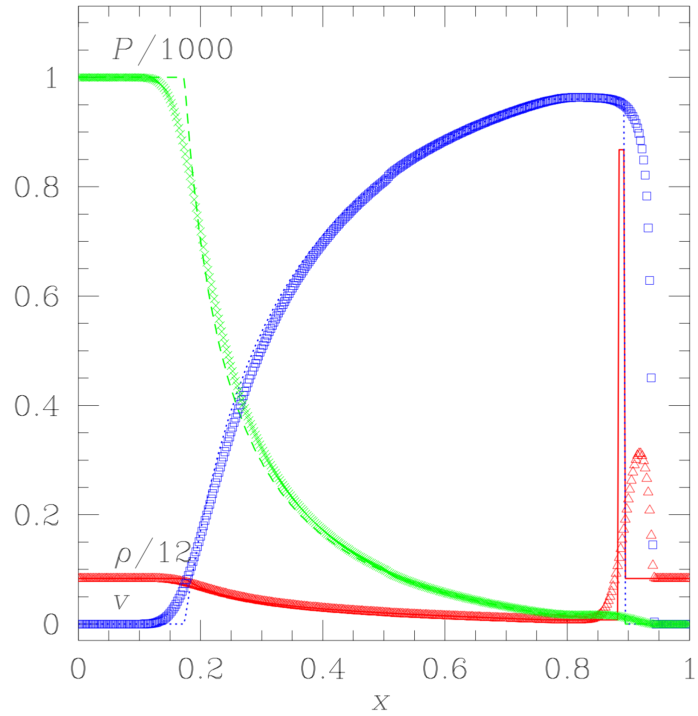

Figure 3.4: A shock tube test with the HLLE approximate Riemann solver, for a $\Gamma = 5/3$ fluid. The initial left state is $(\rho_o)_\ell = 1$, $v_\ell = 0$, and $P_\ell = 1000$; the initial right state is $(\rho_o)_r = 1$, $v_r = 0$, and $P_r = 0.01$. The lines show the exact solution at $t = 0.4$. The PDE solution is indicated by triangles (ρ_o), squares (v), and crosses (P). The solution is calculated with 400 cells. The dissipation of the HLLE scheme is evident, especially when compared to solution obtained using the Roe solver in the two-dimensional code, as shown in Figure 6.3.

The middle state $\mathbf{q}_{\ell r}$ is determined by requiring energy conservation in the computational cell

$$\mathbf{q}_{\ell r} = \frac{b_r \mathbf{q}_r - b_\ell \mathbf{q}_\ell - f(\mathbf{q}_r) + f(\mathbf{q}_\ell)}{b_r - b_\ell}. \tag{3.59}$$

The HLLE numerical flux is

$$\mathbf{F} = \frac{b_r^+ f(\mathbf{q}_\ell) - b_\ell^- f(\mathbf{q}_r) + b_r^+ b_\ell^- (\mathbf{q}_r - \mathbf{q}_\ell)}{b_r^+ - b_\ell^-}, \tag{3.60}$$

where

$$b_\ell^- = \min(0, b_\ell), \tag{3.61}$$

$$b_r^+ = \max(0, b_r). \tag{3.62}$$

Schneider *et al.* [114] first used the HLLE solver for relativistic fluids, and chose the signal speeds to be the Roe eigenvalues—the eigenvalues of the Jacobian matrix $\partial\mathbf{f}(q)/\partial\mathbf{q}$ from Section 2.7—as the signal speeds. In one dimension these are simply the sum and difference of the fluid bulk velocity, v, and the sound speed, c_s, using the relativistic addition of velocities:

$$b_r = \frac{v + c_s}{1 + v c_s}, \tag{3.63}$$

and

$$b_\ell = \frac{v - c_s}{1 - v c_s}. \tag{3.64}$$

We follow this choice in my implementation, but have found in critical solution searches for $\Gamma \gtrsim 1.95$ that the signal speeds must be set to their maximum values,

$$b_\ell = -1, \qquad b_r = 1. \tag{3.65}$$

The HLLE method is unfortunately very diffusive, with results similar to the Lax-Friedrichs scheme (3.10), but it remains an important approximate Riemann solver for at least three reasons. First, its simplicity makes it very easy to implement and computationally very efficient. This makes the HLLE solver ideal for an initial approach to a problem, and as a sanity check for more complicated schemes. (See Quirk [106] for a discussion of “subtle flaws” in the more popular linearized solvers.) Secondly, Einfeldt *et al.* [48] demonstrated that the HLLE solver, when beginning with physical initial data, always produces a physical intermediate state, a property they call *positively conservative.* In addition, they show that linear solvers, such as the Roe solver, do not have this property, and often produce solutions with negative pressures (internal energies) in regions where the fluid density is low. (The proofs are done in flat space ($\mathbf{\Sigma} = 0$), and are not strictly applicable for spherical symmetric and/or general relativistic systems.) Finally, as discussed in Section 3.6, approximate Riemann solvers sometimes produce unphysical results, especially in multiple dimensions. Quirk [106] found the HLLE solver to be free of many of the problems that plague the Roe solver.

3.5.3 Roe's approximate Riemann solver

Perhaps the most popular approximate Riemann solver is the linearized solver introduced by Roe [110]. This solver (and subsequent variants) has been used in a variety of applications involving general relativistic fluids [71, 49, 112, 7, 21, 55], and has proven to be robust and efficient. (The efficiency comparison is relative to solving either the exact Riemann problem for relativistic fluids, or a nonlinear approximation, such as the two-shock solvers of Section 3.5.1.) As the name suggests, the linearized solver approximates the full nonlinear problem by replacing the nonlinear equations by *linear* systems defined at each cell interface. The associated linear Riemann problems can then be solved exactly and cheaply, and the resulting solutions can be pieced together to produce an approximation to the solution of the original, nonlinear equations. Thus, in order to understand the Roe scheme, it is instructive to first consider linear conservation laws.

The linear, scalar advection equation

$$\partial_t q + \lambda \partial_x q = 0, \tag{3.66}$$

has the well-known solution $q(x,t) = q(x - \lambda t, 0)$, where λ is a constant and $q(x,0)$ specifies the initial state. This scalar solution can be extended to linear systems of conservation equations

$$\partial_t \mathbf{q} + \mathbf{A} \partial_x \mathbf{q} = 0, \tag{3.67}$$

where $\mathbf{A}$, an $M \times M$ *constant* matrix, is, by assumption, diagonalizable, with real eigenvalues, λ_B. Let $\mathbf{R}$ be the matrix of right eigenvectors, $\mathbf{r}_B$, of $\mathbf{A}$:

$$\mathbf{R} \equiv [\mathbf{r}_1 | \dots | \mathbf{r}_M], \tag{3.68}$$

and let $\mathbf{\Lambda}$ be the diagonal matrix:

$$\mathbf{\Lambda} \equiv \mathrm{diag}[\lambda_1, \dots, \lambda_M]. \tag{3.69}$$

We then have

$$\mathbf{A} = \mathbf{R} \mathbf{\Lambda} \mathbf{R}^{-1}, \tag{3.70}$$

and the solution of the system may be obtained by introducing “characteristic variables”, $\mathbf{v}$:

$$\mathbf{v} = \mathbf{R}^{-1} \mathbf{q}. \tag{3.71}$$

Using characteristic variables, the equations (3.67) decouple into a set of scalar advection equations

$$\partial_t \mathbf{v} + \mathbf{\Lambda} \partial_x \mathbf{v} = 0, \tag{3.72}$$

which can be immediately solved via:

$$\mathbf{v}_B(x,t) = \mathbf{v}_B(x - \lambda_B t, 0). \tag{3.73}$$

Given $\mathbf{v}(x,t)$, the transformation $\mathbf{q} = \mathbf{R}\mathbf{v}$ then produces the solution of (3.67) in terms of the original variables, $\mathbf{q}$.

Turning now to the nonlinear case, the key idea is to first write the nonlinear system in *quasilinear* form

$$\partial_t \mathbf{q} + \mathcal{A}(\mathbf{q})\, \partial_x \mathbf{q} = 0. \tag{3.74}$$

Here, $\mathcal{A}$ is an $M \times M$ matrix which is now a function of $\mathbf{q}$. Roe [110] gives three specific criteria for the construction of $\mathcal{A}$:

1. $\mathcal{A}(\tilde{\mathbf{q}}^\ell, \tilde{\mathbf{q}}^r)\left(\tilde{\mathbf{q}}^r - \tilde{\mathbf{q}}^\ell\right) = \mathbf{f}(\tilde{\mathbf{q}}^r) - \mathbf{f}(\tilde{\mathbf{q}}^\ell)$;
2. $\mathcal{A}(\tilde{\mathbf{q}}^\ell, \tilde{\mathbf{q}}^r)$ is diagonalizable with real eigenvalues;
3. $\mathcal{A}(\tilde{\mathbf{q}}^\ell, \tilde{\mathbf{q}}^r) \to \mathbf{f}'(\mathbf{q})$ smoothly as $\tilde{\mathbf{q}}^\ell, \tilde{\mathbf{q}}^r \to \mathbf{q}$.

The latter two criteria can generally be satisfied by letting $\mathcal{A}$ be the Jacobian matrix evaluated using the arithmetic average of the conservation variables at the interface:

$$\mathcal{A} = \left.\frac{\partial \mathbf{f}(\mathbf{q})}{\partial \mathbf{q}}\right|_{\mathbf{q}=\bar{\mathbf{q}}_{i+1/2}}, \tag{3.75}$$

where

$$\bar{\mathbf{q}}_{i+1/2} \equiv \frac{1}{2}\left(\tilde{\mathbf{q}}^\ell_{i+1/2} + \tilde{\mathbf{q}}^r_{i+1/2}\right). \tag{3.76}$$

While this construction does not generally satisfy the first criterion, (3.75) is often used in relativistic fluid dynamics (see for example [71, 112, 55]) on the basis of its relative simplicity, and we also adopt this approach. On the other hand, other authors [49] have constructed a linearized Riemann solver for relativistic fluids with true Roe averaging, and we therefore refer to our scheme as a "quasi-Roe" method.

Having defined a specific linearization, the scheme proceeds by evaluation of $\mathcal{A}(\bar{\mathbf{q}}_{i+1/2})$—which is now viewed as a matrix with (piecewise) constant coefficients—followed by the solution of the Riemann problem for the resulting linear system.

Carrying through an analysis not given here (see e.g., [79]), the Roe flux can be defined as

$$\mathbf{F}_{i+1/2} = \frac{1}{2}\left[\mathbf{f}(\tilde{\mathbf{q}}^{r}_{i+1/2}) + \mathbf{f}(\tilde{\mathbf{q}}^{\ell}_{i+1/2}) - \sum_{A} |\lambda_A| \triangle \boldsymbol{\omega}_A \mathbf{r}_A\right]. \tag{3.77}$$

where, again, λ_A and $\mathbf{r}_A$ are the eigenvalues and (right) eigenvectors, respectively, of $\mathcal{A}(\bar{\mathbf{q}}_{i+1/2})$. The quantities $\triangle \boldsymbol{\omega}_A$ are defined in terms of the the jumps in the fluid variables across the interface

$$\tilde{\mathbf{q}}^{r}_{i+1/2} - \tilde{\mathbf{q}}^{\ell}_{i+1/2} = \sum_{A} \triangle \boldsymbol{\omega}_A \mathbf{r}_A. \tag{3.78}$$

3.5.4 An "entropy fix" for the Roe solver

The Roe solver uses only discontinuities to construct its approximate Riemann solution, and thus can produce weak solutions of the fluid equations which are unphysical (see Section 2.2). This approximation as part of a numerical algorithm works very well, however, as the dissipation inherent in the numerical scheme naturally increases the solution's "entropy," smoothing out rarefaction fans. The Roe approximation can lead to unphysical results in the case of sonic rarefaction waves, where $\lambda_A < 0$ to the left of the cell interface at $x_{i+1/2}$, and $\lambda_A > 0$ to the right of the same interface.

Harten and Hyman [69] introduced a popular "entropy fix" for sonic rarefaction waves that modifies the wave speeds (the Roe eigenvalues λ_A) to ensure conservation. The fix is similar to the HLLE approach, whereby the wave speeds (λ) are increased near sonic rarefaction points, creating additional numerical diffusion at the point [5]. This extra diffusion is enough to ensure a physical solution. The Roe flux (3.77) becomes

$$\mathbf{F} = \frac{1}{2}\left[\mathbf{f}(\tilde{\mathbf{q}}^{r}) + \mathbf{f}(\tilde{\mathbf{q}}^{\ell}) - \sum_{A} \nu_A \triangle \boldsymbol{\omega}_A \mathbf{r}_A\right]. \tag{3.79}$$

where for simplicity we have neglected the $i + 1/2$ spatial indices and reconstruct the midpoint state with the arithmetic average,

$$\bar{\mathbf{q}} = \frac{1}{2}\left(\tilde{\mathbf{q}}^{\ell} + \tilde{\mathbf{q}}^{r}\right), \tag{3.80}$$

as before (3.76). The wave speeds are modified such that the maximum eigenvalue is used at a sonic rarefaction point

$$\nu_A = \Lambda^{+}|\lambda_A(\bar{\mathbf{q}})| - \Lambda^{-}\mathrm{max}\left(|\lambda_A(\tilde{\mathbf{q}}^{\ell})|, |\lambda_A(\tilde{\mathbf{q}}^{r})|\right), \tag{3.81}$$

where

$$\Lambda_A = \mathrm{sgn}\left(\lambda_A(\tilde{\mathbf{q}}^{\ell}) \cdot \lambda_A(\tilde{\mathbf{q}}^{r})\right), \tag{3.82}$$

$$\Lambda_A^{+} = \max(0, \Lambda_A), \tag{3.83}$$

$$\Lambda_A^{-} = \min(0, \Lambda_A). \tag{3.84}$$

We implement this form of the Roe flux in our codes; however we have found the extra diffusion to be unnecessary in critical solution studies, and thus use the original Roe flux (3.77) for greater computational efficiency.

3.5.5 Marquina's method

A second linear Riemann solver is the Marquina solver [45, 46], which expands earlier work by Shu and Osher [122] for scalar equations. This solver removes the need for the reconstructed states, $\bar{\mathbf{q}}_{i+1/2}$ of (3.76), used by the Roe solver, and additionally expands the fluxes, $\mathbf{f}$, in terms of the eigenvectors. The method uses the *left* eigenvectors, $\mathbf{l}$, as well as the right eigenvectors, $\mathbf{r}$, which are related by

$$\mathbf{l}_A \cdot \mathbf{r}_B = \delta_{AB}. \tag{3.85}$$

One first defines the coefficients

$$\omega_{\ell}^{A} = \mathbf{l}^{A}(\mathbf{q}_{\ell}) \cdot \mathbf{q}_{\ell}, \tag{3.86}$$

$$\omega_r^A = \mathbf{l}^A(\mathbf{q}_r) \cdot \mathbf{q}_r, \tag{3.87}$$

$$\phi_\ell^A = \mathbf{l}^q(\mathbf{q}_\ell) \cdot \mathbf{f}(\mathbf{q}_\ell), \tag{3.88}$$

$$\phi_r^A = \mathbf{l}^q(\mathbf{q}_r) \cdot \mathbf{f}(\mathbf{q}_r). \tag{3.89}$$

The algorithm then is:

```
For $A = 1, \ldots, M$ do
    If $\lambda_A(\mathbf{q})$ does not change sign in $[\mathbf{q}_\ell, \mathbf{q}_r]$ then
        If $\lambda_A(\mathbf{q}_\ell) > 0$ then
            $\phi_+^A = \phi_\ell^A$                                        (3.90)
            $\phi_-^A = 0$                                                  (3.91)
        else
            $\phi_+^A = 0$                                                  (3.92)
            $\phi_-^A = \phi_r^A$                                           (3.93)
        end if
    else
        $\alpha_A = \max|\lambda_A(\mathbf{q})|, \qquad \mathbf{q} \in \Gamma(\mathbf{q}_\ell, \mathbf{q}_r)$   (3.94)
        $\phi_+^A \frac{1}{2}\left(\phi_\ell^A + \alpha_A \omega_\ell^A\right)$   (3.95)
        $\phi_+^A \frac{1}{2}\left(\phi_r^A - \alpha_A \omega_r^A\right)$         (3.96)
    end if
end do
```

$\Gamma(\mathbf{q}_\ell, \mathbf{q}_r)$ is a curve connecting $\mathbf{q}_\ell$ and $\mathbf{q}_r$ in the state space $\mathbf{q}$. For any hyperbolic system, sign changes in $\lambda_A(\mathbf{q})$ can be identified by testing $\lambda_A(\mathbf{q}_\ell) \cdot \lambda_A(\mathbf{q}_r)$, and

$$\alpha_A = \max\left(|\lambda_A(\mathbf{q}_\ell)|, \lambda_A|(\mathbf{q}_r)|\right) \tag{3.97}$$

The numerical flux function is

$$\mathbf{F}(\mathbf{q}_\ell, \mathbf{q}_r) = \sum_{p=1}^{m} \left[\, \phi^p_+ \, \mathbf{r}^p(\mathbf{q}_\ell) + \phi^p_- \, \mathbf{r}^p(\mathbf{q}_\ell) \,\right] . \tag{3.98}$$

Marquina's method uses more numerical dissipation than Roe's method, using a Lax-Friedrichs update (3.10) at sonic rarefaction points. This additional dissipation eliminates some of the known problems with Roe's solver [45, 106].

3.6 The failure of approximate Riemann solvers

Finally, it is important to remember that *approximate* Riemann solvers produce *approximate* solutions, which, under certain conditions, may diverge from the physical solutions. For example, concentrating on the Roe solver, Quirk [106] has recently reviewed several "subtle flaws" in approximate solvers. Fortunately, the approximate solvers often fail in different ways, and where one solver produces an unphysical solution, another solver may give the physical solution. Thus, it may be necessary to investigate a particular problem with multiple approximate Riemann solvers. Quirk advocates the creation of a hybrid solver by combining the HLLE solver with the Roe solver.

In our work with perfect fluid critical solutions, we use the quasi-Roe approximate Riemann solver (with the entropy fix described in Section 3.5.4), and the HLLE solver. We find that the quasi-Roe solver (without the entropy fix) gives accurate solutions, and provides the best combination of resolution and efficiency for the critical collapse problem. Consequently, the results presented in Chapter 5 are obtained with this solver. Such tests will be even more important as we pursue two-dimensional calculations, as many of the errors catalogued by Quirk do not arise in one-dimensional problems.

3.7 Method of Lines

In Section 2.5 the fluid equations of motion were written in conservation form with an additional source term, $\mathbf{\Sigma}$. While this source term clearly breaks the strict conservation form of the equations, it can be self-consistently incorporated into numerical schemes for conservation laws by using the method of lines to discretize space and time separately. (For more information on the method of lines see Thornburg [129] and references therein.) Consider a PDE of the form

$$\partial_t \mathbf{q} + \partial_x \mathbf{f}(\mathbf{q}) = \mathbf{\Sigma}(\mathbf{q}). \tag{3.99}$$

We first perform the spatial discretization, producing an ordinary differential equation in time

$$\frac{\mathrm{d}\bar{\mathbf{q}}_i}{\mathrm{d}t} = \mathbf{F}_{i+1/2} - \mathbf{F}_{i-1/2} + \mathbf{\Sigma}(\bar{\mathbf{q}}_i), \tag{3.100}$$

where $\bar{\mathbf{q}}_i$ is the cellular average of $\mathbf{q}$, $\mathbf{F}_{i\pm1/2}$ are the numerical fluxes, and the source term is evaluated with $\bar{\mathbf{q}}_i$. These equations can be integrated in time using standard techniques for ODEs. In particular, Shu and Osher [121] have investigated different ODE integration methods, and have found that the modified Euler method (or Huen's method) is the optimal second-order scheme consistent with the Courant condition required for a stable evolution. Consider a general set of differential equations of the form

$$\frac{\mathrm{d}\mathbf{q}}{\mathrm{d}t} = L(\mathbf{q}), \tag{3.101}$$

where L is a spatial differential operator. Let $\mathbf{q}^n$ be the *discretized* solution at time $t = n\triangle t$, and $\hat{L}$ be the discretized differential operator. The modified Euler method is a predictor-corrector method, with predictor

$$\mathbf{q}^{(1)} = \mathbf{q}^n + \triangle t\, \hat{L}(\mathbf{q}^n), \tag{3.102}$$

and corrector

$$\mathbf{q}^{n+1} = \frac{1}{2}(\mathbf{q}^n + \mathbf{q}^{(1)}) + \frac{1}{2}\triangle t\, \hat{L}(\mathbf{q}^{(1)}). \tag{3.103}$$

$\triangle t$ is limited by a Courant (CFL) condition, which can be deduced empirically or possibly from a linearized stability analysis.

A third order integration scheme has also been used in conjunction with the method of lines for relativistic fluid codes [7, 21]. This algorithm is

$$\mathbf{q}^{(1)} = \mathbf{q}^n + \triangle t \, \hat{L}(\mathbf{q}^n), \tag{3.104}$$

$$\mathbf{q}^{(2)} = \frac{3}{4}\mathbf{q}^n + \frac{1}{4}\mathbf{q}^{(1)} + \frac{1}{4}\triangle t \, \hat{L}(\mathbf{q}^{(1)}), \tag{3.105}$$

$$\mathbf{q}^{n+1} = \frac{1}{3}\mathbf{q}^n + \frac{2}{3}\mathbf{q}^{(2)} + \frac{2}{3}\triangle t \, \hat{L}(\mathbf{q}^{(2)}). \tag{3.106}$$

While the method of lines is widely used in relativistic fluid dynamics, alternate update schemes have been developed for general relativistic fluids. These schemes are problem specific, depending on the method used to integrate the Einstein equations [55].

Looking ahead for a moment, in Chapters 6 and 7 we discuss a two-dimensional, relativistic fluid code currently development. Many of the physical problems we wish to examine with this code will require the ability to track features of the solutions over many different scales. For multidimensional system, these calculations can only be practical using adaptive mesh refinement, such as the Berger-Oliger [9] algorithm. However, it is not yet clear if (or how) the method of lines can be consistently combined with Berger-Oliger adaptive mesh refinement.

3.8 Boundary conditions

Two types of boundary conditions for the fluid equations of motion are of primary interest: an out-flow boundary condition, and a reflecting "wall" boundary condition. The outflow boundary condition is generally given as

$$\mathbf{q}_N = \mathbf{q}_{N-1}, \tag{3.107}$$

where the computational cells (grid points) are numbered from $1, \ldots, N$. The cellular reconstruction algorithm can complicate matters, as a linear piece-wise reconstruction typically requires a five-point computational stencil, i.e., $\mathbf{q}_i^{n+1}$ depends on $\mathbf{q}_k^n$, where $k = i-2, \ldots, i+2$. Other reconstructions (Section 3.4.2) may require even larger stencils. A convenient way to incorporate boundary information for the calculation of the numerical flux is to use *ghost cells* at the boundaries [81]. These cells are not part of the "physical" grid, and are simply an artifice to simplify coding. Let the cell at x_N be the edge of the physical grid, to which a boundary condition is applied. The cell at x_{N+1} is added as a ghost cell, and the out-flow boundary condition is

$$\mathbf{q}_N^n = \mathbf{q}_{N-1}^n \tag{3.108}$$

$$\mathbf{q}_{N+1}^n = \mathbf{q}_{N-1}^n. \tag{3.109}$$

The "wall" boundary condition requires the velocity component perpendicular the wall, $v_\perp$, to be zero at the wall. For concreteness, consider a wall at $x = x_{\text{wall}}$. (We include only the x dependence explicitly in the equations below, e.g., a function $\rho(x, y, z, t)$ is written simply as $\rho(x)$.) Then the boundary conditions are

$$v_\perp(x_{\text{wall}}) = 0 \tag{3.110}$$

$$v_\perp(x_{\text{wall}} + \triangle x) = -v_\perp(x_{\text{wall}} - \triangle x) \tag{3.111}$$

The wall reflects all other scalars and the velocity components parallel to the wall, $v_{||}$,

$$v_{||}(x_{\text{wall}} + \triangle x) = v_{||}(x_{\text{wall}} - \triangle x) \tag{3.112}$$

$$\rho(x_{\text{wall}} + \triangle x) = \rho(x_{\text{wall}} - \triangle x). \tag{3.113}$$

In addition to boundary conditions, numerical work in curvilinear coordinates may require regularity conditions, because these coordinate systems frequently contain *coordinate singularities.* These singularities are not "physical," but are simply points where the coordinate system fails. For example, the spherical coordinates θ and ϕ are undefined at the origin. A regularity condition is usually a requirement that the "physics" remains perfectly ordinary at coordinate singularities. In simple cases, such as spherical symmetry, regularity conditions can be determined from symmetry arguments alone. A general method for determining regularity conditions is given by Bardeen and Piran [8]. At coordinate singularities they write all tensors in Cartesian coordinates, and require all components to have a power series expansion in non-negative powers of the Cartesian coordinates x, y, and z. For an example of regularity conditions at the origin ($r = 0$) in spherical symmetry, see Section 4.4.2. The regularity conditions for the axis ($R = 0$) in cylindrical symmetry are discussed in Section 6.3.

3.9 Numerical tricks for ultrarelativistic flow

The numerical solution of ultrarelativistic fluids requires great care to minimize the ill effects of round-off errors, as well as some *ad hoc* tricks to retain physical values for P and v^i. This section discusses the floor, a condition applied to the conservation variables to ensure that they retain physical values, and methods for obtaining the primitive variables from the evolved, conservation variables.

3.9.1 Floor

The fluid model is a continuum approximation, and, at least naïvely, the fluid equations become singular as $\rho \to 0$. In these regions, which we term evacuation regions, both the momentum and mass density are very small, and therefore the velocity—which loosely speaking is the quotient of the two—is prone to fractionally large numerical errors. These errors then often result in the computation of unphysical values for the fluid variables, such as supraluminal velocities, negative pressures or negative energies. At least from the point of view of Eulerian fluid dynamics, it seems fair to say that a completely satisfactory resolution of the evacuation problem does not exist. In the absence of a mathematically rigorous and physically acceptable procedure, we adopt the *ad hoc* approach of demanding that $\rho > 0$ everywhere on the computational domain, i.e., we exclude the possibility that vacuum regions can form on the grid. In terms of our conservation variables $\mathbf{q}$, this requirement becomes $E > 0$ and $D > 0$. In a wide variety of situations, our numerical solutions of the fluid equations naturally satisfy these constraints. However, problems do occur with extremely relativistic velocities ($W > 10^6$) in regions where ρ is small. Specifically, at each step in the integration we require

$$E \geq \delta, \quad D \geq \delta, \tag{3.114}$$

where the floor δ is chosen to be several orders of magnitude smaller than the density associated with the physically relevant features of the solution. A typical value used for this dissertation work is $\delta = 10^{-10}$.

Given the *ad hoc* nature of this regularization procedure, the crucial question is whether the floor affects the computed solutions in a substantial way. This question has been investigated for the spherically symmetric, perfect fluid critical solutions (see Section 4.4.1, Figure 4.17, and Section 5.3.4).

3.9.2 Calculation of primitive variables: ultrarelativistic equation of state

When searching for critical solutions we routinely calculate fluid flows with $W \gtrsim 10^3$. Thus, when calculating v from the quotient (2.115), small numerical errors can easily conspire to give $|v| > 1$, rather than the correct $|v| \gtrsim 0.999999$. On the other hand, the combination

$$\varpi \equiv W^2 v \tag{3.115}$$

is insensitive to small numerical errors, and provides a better avenue for calculating v from the conservation variables. Using the equation of state, (3.115) can be written

$$\varpi = \frac{(\Gamma - 1)}{\Gamma} \frac{S}{P}. \tag{3.116}$$

The velocity can then be calculated from ϖ using

$$v = \frac{1}{2\varpi}\left(\sqrt{1 + 4\varpi^2} - 1\right). \tag{3.117}$$

To the limit of machine precision, v is then in the physical range $-1 < v < 1$. When $\varpi \ll 1$, we calculate v from a Taylor expansion of (3.117), although (2.115) could also be safely used.

$$v \approx \varpi\left(1 + \varpi^2\left(2\varpi^2 - 1\right)\right). \qquad (\varpi \ll 1) \tag{3.118}$$

3.9.3 Calculation of primitive variables: ideal-gas equation of state

In Section 2.6.2 we discussed solving for the primitive variables from the conservation variables, and presented one method that involved solving a transcendental equation for P. For ultrarelativistic flows this solution method can be improved by a more careful calculation of the velocity, motivated by the method presented in the previous section for the ultrarelativistic equation of state. In this approach we solve for the fluid's enthalpy,

$$w = \rho + P, \tag{3.119}$$

rather than the pressure. This allows the calculation of v from the quantity $W^2 v$, as in the ultrarelativistic equation of state case (Section 3.9.2). The algorithm we use is given by the pseudo-code in Figure 3.5.

Additional care must also be taken in the calculation of the sound speed, required to evaluate the eigenvectors and eigenvalues (see Section 2.7). The sound speed for the ideal-gas equation of state is

$$c_{\mathrm{s}}^2 = \frac{\Gamma(\Gamma - 1)P}{(\Gamma - 1)\rho_o + \Gamma P}. \tag{3.120}$$

```
$w_{\text{new}} = \rho_{\text{old}} + P_{\text{old}}$        ! an initial guess
do
    $w = w_{\text{new}}$
    $\varpi = \frac{S}{w}$
    $v = \frac{1}{2\varpi}\left(\sqrt{1+4\varpi^2} - 1\right)$
    $W(w) = \left(1 - v^2\right)^{-1/2}$
    $\left\{\rho_o = \frac{D}{W}\right\}$
    $P(w) = (\Gamma - 1)(w - \rho_o)$
    $f(w) = wW^2 - (\tau + P + D)$
    $f(w) = \frac{S}{v} - (\tau + P + D)$
    $w_{\text{new}} = w - \frac{f(w)}{f'(w)}$
while ( $|w_{\text{new}} - w| < \epsilon$ )
```

Figure 3.5: Pseudo-code for the primitive variable solver using Newton's method for the ideal-gas state equation, optimized for ultrarelativistic flow. A prime indicates differentiation with respect to w. The update for ρ_o is indicated in braces, $\{\cdot\}$, and is not actually calculated in the Newton solver loop.

When $P \gg \rho_o$, as is often the case for ultrarelativistic flow, a naïve calculation of the sound speed may give $c_{\mathrm{s}}^2 \simeq \Gamma - 1$, while a better approximation is found by expanding (3.120) in powers of ρ_o/P

$$c_{\mathrm{s}}^2 = (\Gamma - 1)\left(1 - \frac{\Gamma - 1}{\Gamma}\frac{\rho_o}{P} + \cdots\right). \qquad (\rho_o \ll P) \tag{3.121}$$

This expansion is especially important when calculating the eigenvectors, as the quantity $\tilde{\kappa} - c_s^2$ is very sensitive to this error.

Chapter 4

Spherical symmetry

This chapter describes a new computer code for simulating a self-gravitating, relativistic perfect fluid in spherical symmetry, with the ultrarelativistic equation of state $P = (\Gamma - 1)\rho$ (see Section 2.4.2). Here, as before, P and ρ are the fluid pressure, and total energy density, respectively, and Γ is a constant satisfying $1 < \Gamma \leq 2$. The code has been optimized for *ultrarelativistic* fluid flows with Lorentz factors much larger than unity. This optimization involves a novel definition of the fluid variables, the use of a modern high-resolution shock-capturing scheme, and care in reconstruction of the primitive fluid variables—the pressure and velocity—from the conserved quantities actually evolved by the code. A detailed specification of this code and the tests presented here have been reported earlier by Neilsen and Choptuik [97].

This code was specifically developed to study the critical gravitational collapse of perfect fluids, especially in the limit $\Gamma \to 2$. Critical collapse has become an interesting subfield in general relativity since its initial discovery in the massless Klein-Gordon system [29], and the perfect fluid model has played an important role in advancing our understanding of the critical phenomena which arise at the threshold of black hole formation. (Critical phenomena are discussed further in Chapter 5.) While the critical solutions for perfect fluids in spherical symmetry have been the subject of recent study [52, 73, 86, 68, 74, 16, 60, 24, 26], the precise nature of the critical solutions for $\Gamma \gtrsim 1.89$ was not previously known, and thus one of the chief goals of the current investigation was a thorough analysis of this regime. The main results from the study are given in Chapter 5.

4.1 The ADM equations for spherical symmetric fluids

The ADM equations were introduced in Section 2.1 for an arbitrary spacetime. This section specializes the ADM equations to spherically symmetric space-times with perfect fluids. We choose polar-areal coordinates for simplicity of the equations of motion and for singularity avoidance. Specifically, adopting a polar-spherical coordinate system (t, r, θ, ϕ), we write the spacetime metric as

$$\mathrm{d}s^2 = -\alpha(r,t)^2\,\mathrm{d}t^2 + a(r,t)^2\,\mathrm{d}r^2 + r^2\,\left(\mathrm{d}\theta^2 + \sin^2\theta\,\mathrm{d}\phi^2\right), \tag{4.1}$$

wherein the radial coordinate, r, directly measures proper surface area. In analogy with the usual Schwarzschild form of the static spherically symmetric metric, it is also useful to define the mass aspect function

$$m(r,t) \equiv \frac{r}{2}\left(1 - \frac{1}{a^2}\right). \tag{4.2}$$

The fluid's coordinate velocity, v, and the associated Lorentz gamma function, W, are defined for this spherical code by

$$v(r,t) \equiv \frac{a u^r}{\alpha u^t}, \qquad W(r,t) \equiv \alpha u^t. \tag{4.3}$$

Note that this definition differs slightly from (2.74). (The difference comes simply from a choice of convention made at the beginning of the project.) The identity $\mathbf{u}\cdot\mathbf{u} = -1$ gives the usual relation between W and v

$$W^2 = \frac{1}{1 - v^2}. \tag{4.4}$$

The fluid's *conservation* variables are

$$E(r,t) = (\rho + P)W^2 - P, \tag{4.5}$$

$$S(r,t) = (\rho + P)W^2 v, \tag{4.6}$$

and the non-zero components of the stress-energy tensor are given by

$$\begin{aligned} T^t{}_t &= -E & T^r{}_r &= Sv + P \\ T^t{}_r &= \frac{a}{\alpha} S & T^\theta{}_\theta &= T^\phi{}_\phi = P. \end{aligned} \tag{4.7}$$

A sufficient set of Einstein equations for the geometric variables a and α are given by (i) the non-trivial component of the momentum constraint

$$\partial_t a = -4\pi r \alpha a^2 S, \tag{4.8}$$

and by (ii) the polar slicing condition, which follows from the demand that metric have the form (5.3) for all t:

$$\partial_r (\ln \alpha) = a^2 \left[4\pi r \left(Sv + P \right) + \frac{m}{r^2} \right]. \tag{4.9}$$

An additional equation for $a(r,t)$,

$$\partial_r a = a^3 \left(4\pi r E - \frac{m}{r^2} \right), \tag{4.10}$$

follows from the Hamiltonian constraint (2.20).

4.2 The fluid equations

As mentioned previously in Section 2.4.2, the time evolution of a barotropic perfect fluid is completely determined by $\nabla \cdot \mathbf{T} = 0$. In addition, the derivation of the spherically symmetric equations of motion—which can can naturally be written in conservation form—is a straightforward piece of analysis, and will not be given in detail here. The fluid state vectors are

$$\mathbf{q}_* \equiv \begin{bmatrix} E \\ S \end{bmatrix}, \qquad \mathbf{w} \equiv \begin{bmatrix} P \\ v \end{bmatrix}, \tag{4.11}$$

and the flux and source vectors are

$$\mathbf{f}_* \equiv \begin{bmatrix} S \\ Sv + P \end{bmatrix} \qquad \mathbf{\Sigma}_* \equiv \begin{bmatrix} 0 \\ \psi \end{bmatrix}. \tag{4.12}$$

These variables have been introduced with an asterisk ($*$) to distinguish them from the new variables defined in Section 4.2.1, which are subsequently used in the actual numerical solution algorithm. Further, to expedite the discretization of the equations of motion, we decompose the source term, ψ, into two pieces, as follows:

$$\psi \equiv \Theta + \frac{2\alpha P}{ar}, \tag{4.13}$$

where

$$\Theta \equiv (Sv - E)\left(8\pi\alpha a r P + \alpha a \frac{m}{r^2}\right) + \alpha a P \frac{m}{r^2}. \tag{4.14}$$

We note that in spherically symmetric Minkowski spacetime we have $\Theta = 0$ and $\psi = 2P/r$. With the above definitions, we can now write the fluid equations of motion in the conservation form

$$\partial_t \mathbf{q}_* + \frac{1}{r^2}\partial_r\left(r^2 X \mathbf{f}_*\right) = \mathbf{\Sigma}_* \tag{4.15}$$

where

$$X \equiv \frac{\alpha}{a} \tag{4.16}$$

is a purely geometric quantity.

The primitive variables $\mathbf{w}$ can be expressed in terms of the conservation variables $\mathbf{q}_*$ by inverting the definitions (4.5) of the conservation variables, as shown in Section 2.6.1

$$P = -2\beta E + \left[4\beta^2 E^2 + (\Gamma - 1)(E^2 - S^2)\right]^{\frac{1}{2}} \tag{4.17}$$

$$v = \frac{S}{E + P}. \tag{4.18}$$

The positive constant β (2.120) is

$$\beta \equiv \frac{1}{4}\left(2-\Gamma\right). \tag{4.19}$$

The pressure equation (4.17) follows from the solution of a quadratic with a specific root chosen to yield a physical (non-negative) pressure. As mentioned in Section 2.6.1, a physical pressure and velocity are obtained when $E > |S|$.

4.2.1 New conservative fluid variables

Using the conservation variables, $\mathbf{q}_*$, defined above, and the numerical method described below in Section 4.4, we developed a preliminary code to solve the relativistic fluid equations. We then tested this code in Minkowski spacetime using slab and spherical symmetry. The tests in slab symmetry were completely satisfactory, modulo the convergence limitations of the numerical scheme (see Section 4.5). However, in spherical symmetry, the method frequently failed for "stiffer" fluids ($\Gamma \gtrsim 1.9$), most notably in "evacuation regions" where $\rho \to 0$ and $|v| \to 1$, a combination difficult for numerical work. These problems in spherical symmetry led us to seek a new set of conservation variables, and to motivate this change of variables, first consider the evolutions shown in Figure 4.1. Here we begin with a time-symmetric, spherical shell of fluid, which has a Gaussian energy density profile. Owing to the time-symmetry, as the evolution unfolds, the shell naturally splits into two sub-shells—one in-going and one out-going—and as the sub-shells separate, a new evacuation region forms in the region where the fluid was originally concentrated. Examination of the conservation variable profiles reveals that $|S| \approx E$, and this observation suggests new variables [33]

$$\Phi \equiv E - S, \qquad \Pi \equiv E + S, \tag{4.20}$$

which loosely represent the in-going (Φ) and out-going (Π) parts of the solution. Thus the new state vector of conservation variables is

$$\mathbf{q} \equiv \begin{bmatrix} \Pi \\ \Phi \end{bmatrix}. \tag{4.21}$$

The $\mathbf{q}$ variables provide a *significant* improvement over the conventional variables, $\mathbf{q}_*$, in spherical symmetry with $\Gamma \gtrsim 1.9$. Not surprisingly, this change of variables does not solve *all* of the numerical problems encountered in the highly relativistic evacuation regions. For example, the new variables do not eliminate the need for a floor when searching for $\Gamma \gtrsim 1.9$ critical solutions.

The equations of motion for the new variables $\mathbf{q}$ can be readily found by adding and subtracting the two components of (4.15), giving

$$\partial_t \mathbf{q} + \frac{1}{r^2}\partial_r\left[r^2 X \mathbf{f}\right] = \mathbf{\Sigma}, \tag{4.22}$$

where the flux and source terms are now given by

$$\mathbf{f} \equiv \begin{bmatrix} \frac{1}{2}(\Pi - \Phi)(1+v) + P \\ \frac{1}{2}(\Pi - \Phi)(1-v) - P \end{bmatrix}, \qquad \mathbf{\Sigma} \equiv \begin{bmatrix} \psi \\ -\psi \end{bmatrix}. \tag{4.23}$$

The transformation from conservative to primitive variables can be found by simply changing variables in (4.17) and (4.18)

$$P = -\beta(\Pi + \Phi) + \left[\beta^2 (\Pi + \Phi)^2 + (\Gamma - 1)\Pi\Phi\right]^{\frac{1}{2}}, \tag{4.24}$$

$$v = \frac{\Pi - \Phi}{\Pi + \Phi + 2P}. \tag{4.25}$$

Given the physical requirement $E > |S|$, the new variables $\mathbf{q}$ are strictly positive: $\Pi > 0$, $\Phi > 0$.

4.3 Characteristic structure

In this section we give the Jacobian matrix $\mathcal{A}$ for the relativistic fluid equations, and then compute the associated eigenvalues and right eigenvectors. The flat-space

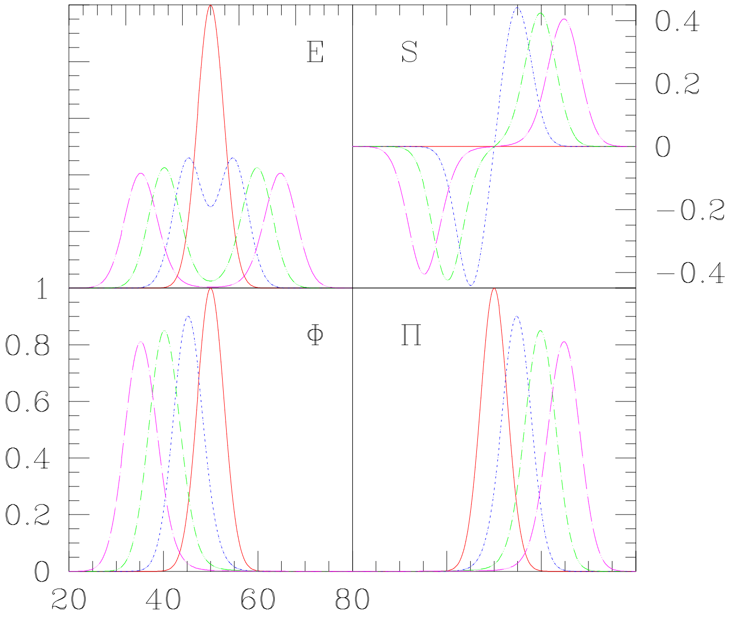

Figure 4.1: These plots show various fluid quantities at four different instances (equally spaced in time) in a flat spacetime, slab-symmetric evolution with $\Gamma = 1.9$. The initial configuration is a time-symmetric Gaussian pulse. The top frames show the evolution of the original conservation variables, E and S. As the evolution proceeds, the pulse separates into left and right-moving halves, and a vacuum region ($E \to 0$) develops between the two sub-pulses. The bottom frames show the evolution of the new conservation variables, Π and Φ, which do not divide into two shells as does E. The correspondence of the new variables to left and right moving "waves" is also evident. Note that the plots of E, Π and Φ have the same vertical scale, while the vertical scale for S is shown separately. The horizontal scale is the same for all of the plots.

components of $\mathcal{A}$ are

$$\begin{aligned}
\mathcal{A}_{11} &= \frac{1}{2}\left(1+2v-v^2\right)+(1-v^2)\frac{\partial P}{\partial \Pi} && (4.26)\\
\mathcal{A}_{12} &= -\frac{1}{2}\left(v+1\right)^2+(1-v^2)\frac{\partial P}{\partial \Phi} && (4.27)\\
\mathcal{A}_{21} &= \frac{1}{2}\left(v-1\right)^2+(v^2-1)\frac{\partial P}{\partial \Pi} && (4.28)\\
\mathcal{A}_{22} &= \frac{1}{2}\left(-1+2v+v^2\right)+(v^2-1)\frac{\partial P}{\partial \Phi}, && (4.29)
\end{aligned}$$

and the partial derivatives of P are easily found from (4.24). The eigenvalues $\lambda_\pm$ of $\mathcal{A}$ are the two roots of the quadratic equation

$$\lambda^2-(\mathcal{A}_{11}+\mathcal{A}_{22})\lambda+\det\mathcal{A}=0, \tag{4.30}$$

and the right eigenvectors are

$$\mathbf{r}_\pm=\begin{pmatrix}1\\ Y_\pm\end{pmatrix}, \tag{4.31}$$

where

$$Y_\pm\equiv\frac{\lambda_\pm-\mathcal{A}_{11}}{\mathcal{A}_{12}}. \tag{4.32}$$

If the eigenvalues are numerically degenerate owing to the limitations of finite precision arithmetic, we set $\lambda_\pm=0$. When $\Gamma=2$, the eigenvalues and eigenvectors become simply

$$\lambda_\pm=\pm1,\quad \mathbf{r}_+=\begin{pmatrix}1\\ 0\end{pmatrix},\quad \mathbf{r}_-=\begin{pmatrix}0\\ 1\end{pmatrix}. \qquad (\Gamma=2) \tag{4.33}$$

4.4 Numerical algorithm

This section discusses the numerical algorithm used to solve the Einstein-fluid system. The fluid equations are discretized using the method of lines (Section 3.7) to consistently incorporate the source term, $\boldsymbol{\Sigma}$. The modified Euler method (also

Section 3.7) is used to integrate the equations in time. The numerical fluxes are constructed using Roe's linearized Riemann solver (Section 3.5.3), and the cells are reconstructed with piece-wise linear functions (Section 3.4) using the minmod limiter (Section 3.4.1).

Particularly in comparison to the treatment of the fluid equations, the numerical solution of the equations governing the geometric quantities α and a is straightforward. As discussed previously, the lapse, α, is fixed by the polar slicing condition (4.9), while a can be found from either the Hamiltonian (4.10) or momentum (4.8) constraints. We have used second-order finite-difference equations for both constraints and have obtained satisfactory results in both cases (the polar slicing equation is likewise solved using a second-order scheme.) In general, however, (and particularly on vector machines) solution via the momentum constraint yields a far more efficient scheme, and we thus generally use the momentum equation to update a.

4.4.1 The floor

A floor, or set minimum values for $\mathbf{q}$, is used in this code as discussed in Section 3.9.1, and is necessary for finding critical solutions with $\Gamma \gtrsim 1.8$. The floor is applied by requiring

$$\Pi \geq \delta, \quad \Phi \geq \delta, \tag{4.34}$$

at each step in the update scheme, where a typical floor magnitude is $\delta = 10^{-10}$. The floor is often applied in regions where Π and Φ differ greatly in magnitude, and discretization errors can easily lead to the calculation of a negative value for either function. For example, the floor may be applied to the "in-going" function in a region where the fluid is overwhelmingly "out-going." In these cases, the effect of the floor is dynamically unimportant. However, the floor may be invoked in other cases, where its effect on the dynamics is less certain.

A crucial question is whether the floor affects the computed solutions in a substantial way. We investigated this question by comparing near-critical solutions for $\Gamma = 2$ (the most extreme case) which were calculated with three distinct floor values: $\delta = 10^{-6}$, $\delta = 10^{-8}$, and the usual $\delta = 10^{-10}$. The solutions appear nearly identical, as judging from residual tests in the strong-field regime, as shown in Figure 4.17. However, we note that the use of a floor makes estimates of the maximum Lorentz factor attained in the critical solutions unreliable because the largest velocities occur in regions where the floor is enforced.

4.4.2 Regularity and boundary conditions

In the polar-areal coordinate system, the lapse "collapses" exponentially near an apparent horizon, preventing the $t =$ constant surfaces from intersecting the physical singularity which must develop interior to a black hole. As the slices "avoid" the singularity, elementary flatness holds at the origin for all times in the evolution, giving

$$a(0,t) = 1. \tag{4.35}$$

At each instant of time, the polar-slicing condition (4.9) determines the lapse only up to an overall multiplicative constant, reflecting the reparameterization invariance, $t \to \tilde{t}(t)$, of the polar slices. We chose to normalize the lapse function so that as $r \to \infty$, coordinate time corresponds to proper time. On a finite computational domain, and provided no matter out-fluxes from the domain, this condition is approximated via

$$\alpha a\Big|_{r_{\max}} = 1. \tag{4.36}$$

In spherical symmetry the fluid flows along radial lines, and given that there are no sources or sinks at the origin, we have that $v(0,t) = S(0,t) = 0$. Thus

$$\Pi(0,t) = \Phi(0,t) = E(0,t). \tag{4.37}$$

Regularity at the origin further requires E, Π and Φ to have even expansions in r as $r \to 0$:

$$E(r,t) = E_0(t) + r^2 E_2(t) + \mathrm{O}(r^4) \tag{4.38}$$

$$\Pi(r,t) = \Pi_0(t) + r^2 \Pi_2(t) + \mathrm{O}(r^4) = E_0(t) + r^2 \Pi_2(t) + \mathrm{O}(r^4) \tag{4.39}$$

$$\Phi(r,t) = \Phi_0(t) + r^2 \Phi_2(t) + \mathrm{O}(r^4) = E_0(t) + r^2 \Phi_2(t) + \mathrm{O}(r^4) \tag{4.40}$$

On our radial grid r_i, $i = 1, 2, \cdots N$, we use these expansions to compute grid-function values defined at $r = r_1 = 0$ in terms of values defined at $r = r_2$ and $r = r_3$. Specifically, once the values Φ_2 and Φ_3 have been updated via the equations of motion, we compute Φ_1 using a "quadratic fit" based on the expansion (4.40):

$$\Phi_1 = \frac{\Phi_2 {r_3}^2 - \Phi_3 {r_2}^2}{{r_3}^2 - {r_2}^2}. \tag{4.41}$$

We then set $\Pi_1 = \Phi_1$.

At the outer boundary we apply out-flow boundary conditions, which in our case are simply first-order extrapolations for Π and Φ:

$$\Phi_N = \Phi_{N-1} \qquad \Pi_N = \Pi_{N-1}. \tag{4.42}$$

The boundary conditions are applied with ghost cells ($r = r_{N+1}, r = r_{N+2}$) as presented in Section 3.8).

4.4.3 Grid

The black-hole-threshold critical solutions—which are our primary focus—are generically self-similar, and as such, require essentially unbounded dynamical range for accurate simulation. Thus, some sort of adaptivity in the construction of the computational domain is crucial, and, indeed, the earliest studies of critical collapse [29] used Berger-Oliger adaptive mesh refinement [9] to great advantage. However, in contrast to the early work, we know (at least schematically) the character of the critical solutions we seek, and thus we can, and have, use this information to construct a simple, yet effective, adaptive grid method. (Our approach is similar in spirit to that adopted by Garfinkle [57] in his study of scalar field collapse.) Specifically, at any time during the integration our spatial grid has three distinct domains: the two regions near $r = 0$ and $r = r_{\max}$ have uniform grid spacings (but the spacing near $r = 0$ is typically *much* smaller than that near the outer edge of the computational domain), and the intermediate region has grid points distributed uniformly in $\log(r)$. As a near-critical solution propagates to smaller spatial scales, additional grid points are added in order to maintain some given number of grid points between $r = 0$ and some identifiable feature of the critical solution. For example, we typically require that at least 300 or so grid points lie between the origin and the maximum of the profile of the metric function a.

As described above, the radial grid is divided into three sections: the first region, $r < r_a$, has uniform spacing between the grid points; the second region, $r_a < r < r_b$, has logarithmic spacing; and the third region, $r > r_b$, also has uniform spacing. The easiest way to construct this grid is to consider an uniform grid in log space, U, ancillary to the radial grid, r. In the second region of the radial grid, the two grids are related by

$$\ln r = U. \tag{4.43}$$

The radial grid has a fixed minimum spacing, $\triangle r_{\min}$, in the first region, $r < r_a$, and a fixed maximum spacing, $\triangle r_{\max}$, in the third region, $r > r_b$. The uniform spacing on the log grid is fixed to be $\triangle U$. (The minimum and maximum values of U are not important, but for simplicity assume $-\infty < U < \infty$.) Figure 4.2 graphically shows how the boundaries r_a and r_b are chosen. Algebraically, we require in the second region that

$$r_{i+1} - r_i \geq \triangle r_{\min}. \tag{4.44}$$

The point U_a is chosen by letting $\triangle r = \triangle r_{\rm min}$ (written now in terms of U)

$$e^{U_1+\triangle U} - e^{U_1} = \triangle r_{\rm min}, \tag{4.45}$$

and solving for U_a

$$U_a = \ln\left(\frac{\triangle r_{\rm min}}{e^{\triangle U}-1}\right). \tag{4.46}$$

U_b can be found by a similar calculation.

The primary advantage of this gridding scheme is that it is simple to implement, and yet allows us to resolve detail over many length scales: the ratio of the grid spacing at the outer edge to the spacing at the origin is typically 10^{10}–10^{13} at the end of an evolution. The primary disadvantage of this scheme is that it is specialized for critical collapse, and cannot be used for more general physical problems.

4.4.4 Details of the integration procedure

The origin in spherical symmetry requires additional care because powers of $1/r$ appear in the flux and source terms. One particular difficulty results from the partial cancellation of the source term, $2\alpha P/(ar)$, with the pressure term in the flux. Numerically this cancellation is not exact, and this non-cancellation can induce large errors near the origin. We therefore modify the difference equations in order to eliminate the offending term. We first decompose the numerical flux into two parts $\mathbf{f}^{(1)}$ and $\mathbf{f}^{(2)}$:

$$\mathbf{f}^{(1)} = \begin{bmatrix} \frac{1}{2}(\Pi-\Phi)(1+v) \\ \frac{1}{2}(\Pi-\Phi)(1-v) \end{bmatrix} \qquad \mathbf{f}^{(2)} = \begin{bmatrix} P \\ -P \end{bmatrix}, \tag{4.47}$$

so that $\mathbf{f} = \mathbf{f}^{(1)} + \mathbf{f}^{(2)}$. We then rewrite the conservation equations (4.15) with these new fluxes as

$$\partial_t \mathbf{q} + \frac{1}{r^2}\partial_r\left(r^2 X\mathbf{f}^{(1)}\right) + \partial_r\left(X\mathbf{f}^{(2)}\right) = \hat{\mathbf{\Sigma}}, \tag{4.48}$$

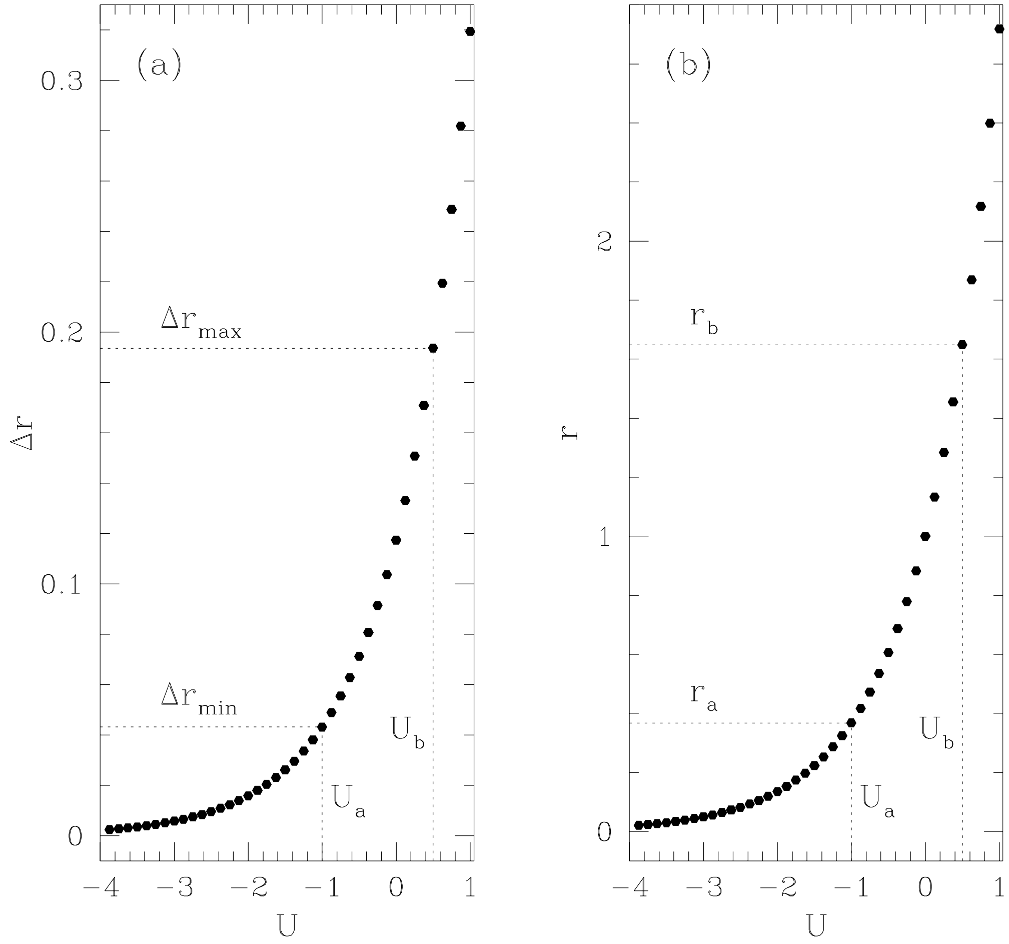

Figure 4.2: The radial grid, r, is created with logarithmic spacing using a uniform grid, U, in log-space. This figure graphically displays the connection between r and U. The uniform spacing of the log grid, $\triangle U$, and the minimum and maximum spacings on the radial grid, $\triangle r_{\rm min}$ and $\triangle r_{\rm max}$, respectively, are fixed in advance. The radial grid has logarithmic spacing when $\triangle r_{\rm min} \leq r(U_{i+1}) - r(U_i) \leq \triangle r_{\rm max}$. Frame (a), shows $\triangle r_i \equiv r(U_i) - r(U_{i-1})$ vs. U. The boundaries U_a and U_b are found from $\triangle r_{\rm min}$ and $\triangle r_{\rm max}$, respectively. Frame (b) plots r vs. U, giving the boundaries on the radial grid, r_a and r_b.

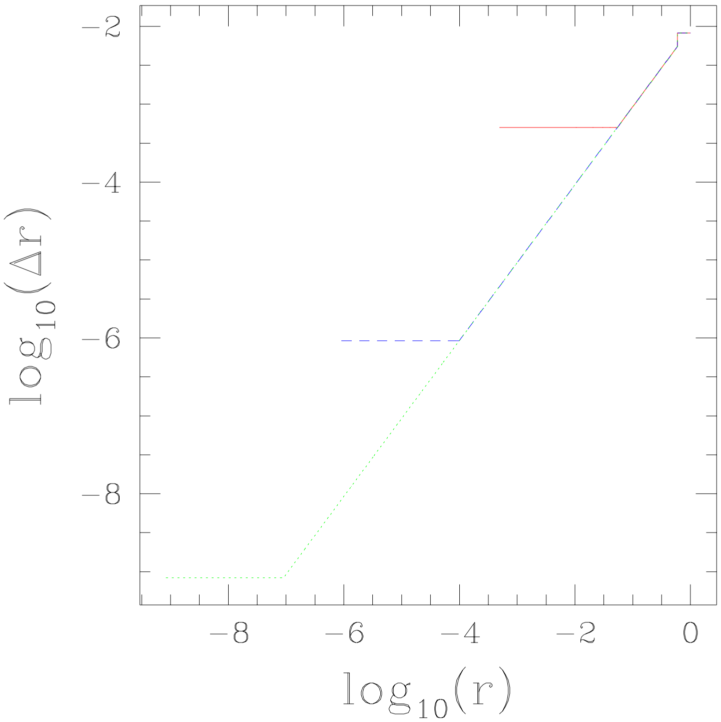

Figure 4.3: Illustration of the re-meshing algorithm used in investigations of critical collapse. The grid spacing $\triangle r$ is shown as a function of r on a log-log plot. The solid line represents the initial grid, the dotted line shows the grid spacing after the first addition of points near the origin, and the dashed line shows the grid spacing after the second regridding. Note that the grid spacings near the origin, and near the outer edge of the computational domain are uniform (horizontal lines). At each regridding cycle, the grid spacing near the origin is halved, and the new points are matched smoothly onto the previous grid. A critical evolution may involve more than 20 regriddings, although only a small number of points (50–150) may be added at a time.

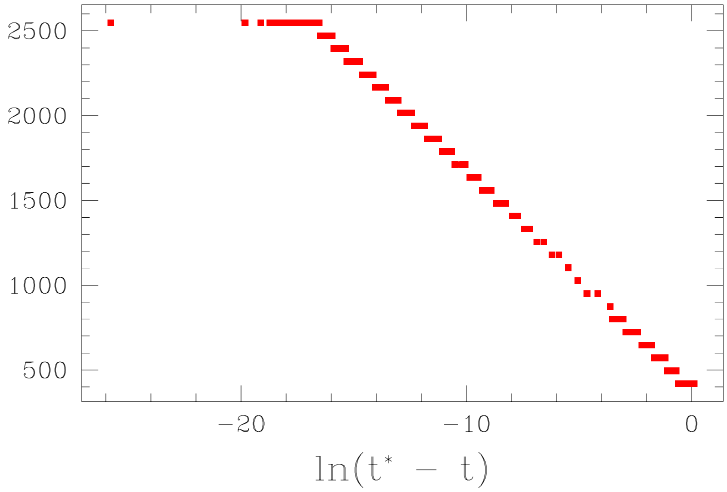

Figure 4.4: The number of grid points as a function of time for a $\Gamma = 2$ near critical evolution. The mesh refinement terminates when a maximum resolution limit is reached, which occurs here around $\ln(t^\star - t) \approx -18$.

where the new source term $\hat{\mathbf{\Sigma}}$ is

$$\hat{\mathbf{\Sigma}} = \begin{bmatrix} \Theta \\ -\Theta \end{bmatrix}. \tag{4.49}$$

The numerical flux function $\mathbf{F}$ is similarly decomposed: $\mathbf{F} = \mathbf{F}^{(1)} + \mathbf{F}^{(2)}$, with

$$\mathbf{F}^{(1)}_{i+1/2} = \frac{1}{2}\left[\mathbf{f}^{(1)}(\tilde{\mathbf{q}}^{\ell}_{i+1/2}) + \mathbf{f}^{(1)}(\tilde{\mathbf{q}}^{r}_{i+1/2}) - \sum_{\mu} |\lambda_\mu| \triangle \boldsymbol{\omega}_\mu \mathbf{r}_\mu\right], \tag{4.50}$$

$$\mathbf{F}^{(2)}_{i+1/2} = \frac{1}{2}\left[\mathbf{f}^{(2)}(\tilde{\mathbf{q}}^{\ell}_{i+1/2}) + \mathbf{f}^{(2)}(\tilde{\mathbf{q}}^{r}_{i+1/2})\right]. \tag{4.51}$$

The finite-differencing of the flux terms is adapted so that the derivatives have the correct leading order behavior near the origin. From the regularity conditions discussed in Section 4.4.2 we have

$$\lim_{r\to 0} r^2 X \mathbf{f}^{(1)} \propto r^3, \qquad \lim_{r\to 0} X \mathbf{f}^{(2)} \propto \text{constant}, \tag{4.52}$$

and we thus write the discretized equations of motion as

$$\begin{aligned}\frac{\mathrm{d}\bar{\mathbf{q}}_i}{\mathrm{d}t} &= -\frac{3\left[\left(r^2X\mathbf{F}^{(1)}\right)_{i+1/2}-\left(r^2X\mathbf{F}^{(1)}\right)_{i-1/2}\right]}{r^3_{i+1/2}-r^3_{i-1/2}} \\ &\quad -\frac{\left(X\mathbf{F}^{(2)}\right)_{i+1/2}-\left(X\mathbf{F}^{(2)}\right)_{i-1/2}}{r_{i+1/2}-r_{i-1/2}}+\hat{\mathbf{\Sigma}}_i. \qquad (4.53)\end{aligned}$$

The geometric equations are differenced using standard second-order finite-difference techniques. The momentum constraint is

$$\frac{\mathrm{d}a_i}{\mathrm{d}t}=2\pi r_i\alpha_i a_i^2\left(\Pi_i-\Phi_i\right), \qquad (4.54)$$

and is integrated using the modified Euler method described in Section 3.7. The discretized polar slicing condition (4.9) in discrete form is

$$\begin{aligned}(\ln\alpha)^n_{i+1} &= (\ln\alpha)^n_i \\ &\quad +\triangle r\left\{a\left[2\pi r((\Pi-\Phi)v+P)+\frac{1}{2r}\left(1-\frac{1}{a^2}\right)\right]\right\}^n_{i+1/2}, \qquad (4.55)\end{aligned}$$

where all of the basic variables—a, Π, Φ, v and P—in the $\{\}$ braces are evaluated at $r_{i+1/2}$ using an arithmetic average.

Finally, the overall flow of an integration step is as follows:

1. Begin with the data for time $t=t^n$: $\{\Pi^n, \Phi^n, P^n, v^n, \alpha^n, a^n\}$.

2. Reconstruct the conservation variables using (3.44)–(3.45)to obtain values at the cell interfaces for $\{\tilde{\mathbf{q}}^\ell, \tilde{\mathbf{q}}^r\}$, and calculate the corresponding primitive values, $\{\tilde{\mathbf{w}}^\ell, \tilde{\mathbf{w}}^r\}$, using (4.24) and (3.117). Using the characteristic information in 4.3, calculate the numerical fluxes $\mathbf{F}(\tilde{\mathbf{q}}^\ell, \tilde{\mathbf{q}}^r)$ using (4.50) and (4.51).

3. Begin integrating the equations of motion, (4.53), and the momentum constraint, (4.54), by perform the predictor step of the modified Euler method (3.102) , obtaining $\{\Pi^{(1)}, \Phi^{(1)}, a^{(1)}\}$, then calculate $\{P^{(1)}, v^{(1)}\}$ using (4.24) and (3.117). Integrate the slicing condition (4.55) to determine $\alpha^{(1)}$.

4. Reconstruct cells for $\{\tilde{\mathbf{q}}_\ell^{(1)}, \tilde{\mathbf{q}}_r^{(1)}\}$, and $\{\tilde{\mathbf{w}}_\ell^{(1)}, \tilde{\mathbf{w}}_r^{(1)}\}$, and calculate the numerical fluxes $\mathbf{F}(\tilde{\mathbf{q}}_\ell^{(1)}, \tilde{\mathbf{q}}_r^{(1)})$.

5. The update is completed by performing the corrector step of the modified Euler method (3.103), giving $\{\Pi^{n+1}, \Phi^{n+1}, a^{n+1}\}$ and $\{P^{n+1}, v^{n+1}\}$. The slicing condition is then integrated to determine α^{n+1}.

6. Check the regridding criteria, and regrid if necessary.

4.5 Tests

When developing a code such as the one described here, a variety of tests can verify that the code is producing reliable results. For example, independent residual tests and comparisons with exact solutions can be used to ensure that the code is solving the correct differential equations, and producing “physical” solutions. Perhaps most fundamental is the convergence test, which generally demonstrates that the numerical method is consistent and has been correctly implemented, but which also provides an *intrinsic* method for estimating the level of error in a given numerical solution. This section discusses the convergence properties of our code, focusing especially on convergence in the critical regime of a collapsing fluid. Additional tests are also presented.

For our high-resolution shock-capturing scheme, a general rule-of-thumb is that the convergence should be (apparently) second order where the flow is smooth, and first order at discontinuities, where the effects of the slope limiter become important. In addition, we can also expect first order convergence near extrema of $\bar{\mathbf{q}}$, since at these points, the slope, $\mathbf{s}$, changes sign, and the minmod limiter gives a piece-wise constant reconstruction for $\tilde{\mathbf{q}}$. A convergence test where these effects are apparent is shown in Figure 4.5.

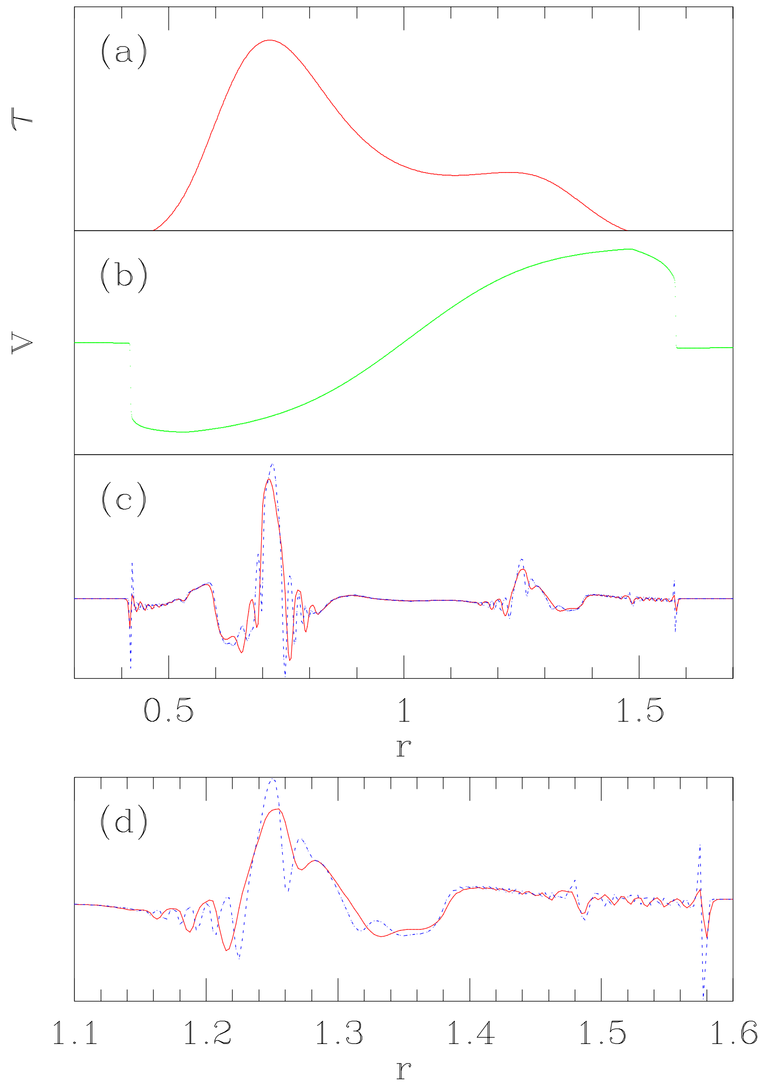

Figure 4.5: Illustration of some of the convergence properties of the solution algorithm discussed in the text. This figure's caption is continued on the next page.

Caption for Figure 4.5 (continued): Here we evolved a time-symmetric shell of fluid ($\Gamma = 1.3$) using uniform grids with three different resolutions: $\triangle r = h, 2h$ and $4h$. Convergence is investigated by comparing the solutions obtained using the three distinct discretization scales. In frame (c), the solid line is $(E_{2h} - E_{4h})$ and the dotted line is $4\,(E_h - E_{2h})$, where the subscript on E indicates the grid spacing for a particular solution. When the convergence is second order, the two lines should (roughly) coincide, while when the convergence is first order, the amplitude of the dotted line should be twice that of the solid line. As expected, we see that the convergence is not second order at the shock. (Of course the whole notion of convergence at a discontinuity fails, as the notion of Richardson expansion requires smooth functions.) However, we also can see that the convergence is only first order at the extrema of $\mathbf{q}$—at these points, the slope changes sign, and the minmod limiter produces a first-order reconstruction. Frame (d) shows a more detailed view of a portion of the data displayed in (c). For context, we also show E in frame (a) and v in frame (b).

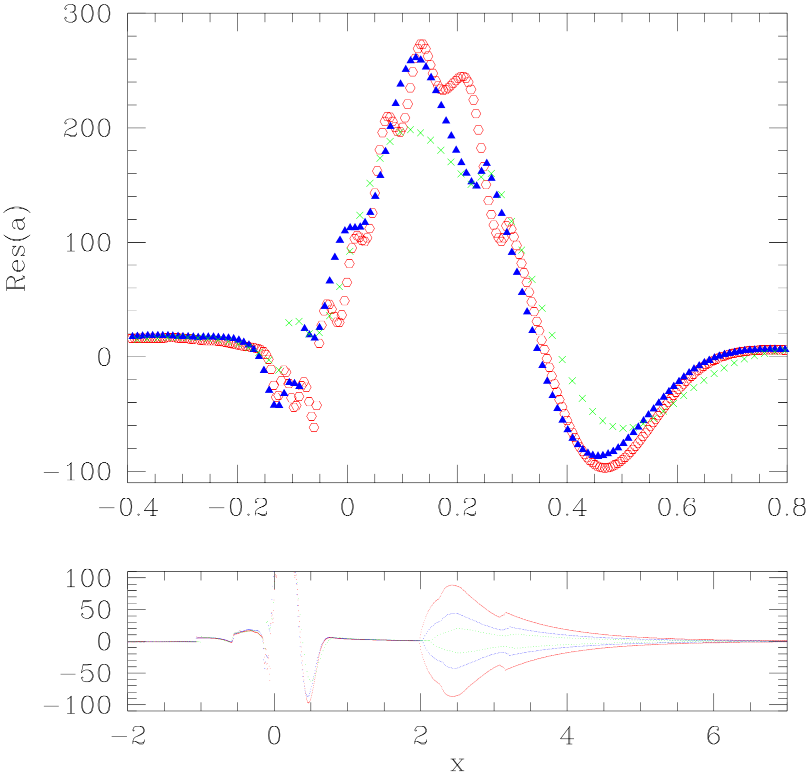

Figure 4.6: The residual of the Hamiltonian constraint, Res(a), for a $\Gamma = 1.9$ sub-critical evolution near the threshold of black hole formation. The residual is calculated at three different resolutions on the adaptive log grid, and this figure shows the residual just before the fluid disperses from the origin. The top frame shows the residuals in the neighborhood of the critical solution, and the lower frame shows the residuals for the entire grid. The crosses show Res(a) for a low resolution run, the triangles show 4Res(a) for a medium resolution run, and the circles show 16Res(a) for a high resolution run. The resolution differs approximately by factors of 2 for each grid. The overlap of these functions indicates that the fluid in the region of interest converges quadratically (see the top frame). A region of first order convergence is apparent in the bottom frame. This appears to be a transition region between a region of the grid where the floor is inactive, in this frame $x < 2$, and a region where the floor is continuously applied, at this time $x > 3.5$. In this transition region, the floor is active every second grid point. The x coordinate is a logarithmic coordinate proportional to $\ln r$, and is defined in Section 5.2.

Our fluid code has been primarily optimized for studying perfect fluid critical solutions. These solutions are continuously self-similar, smooth, very dynamic, and exist in the strong field limit of general relativity. Thus the most important test is a convergence test of a near critical solution at the verge of black hole formation. We found the critical solutions for a $\Gamma = 1.9$ fluid at three different resolutions, and plotted the residual of the Hamiltonian constraint in Figure 4.6. While the convergence of our scheme reverts to first order at the extrema of $\{\Pi, \Phi\}$, which occur at $r = 0$ for a collapsing perfect fluid, the region most interesting for studying critical solutions is near the maximum of r^2E. Thus the maximum of r^2E occurs away from the origin where the convergence is second order.

The Riemann problem is an exact solution for two discontinuous initial states separated by a divider at $t = 0$,

$$\mathbf{q}(x,0) = \begin{cases} \mathbf{q}_\ell & \text{if } x < 0, \\ \mathbf{q}_r & \text{if } x > 0. \end{cases} \tag{4.56}$$

This solution can be used to test the shock-capturing algorithm, checking that the code calculates the shock jumps and velocities correctly. We show five shock tube PDE solutions plotted together with the analytic solutions in Figures 4.7 and 4.11.

While the shock-tube provides a good test of the fluid solver, the test is done in Minkowski space with slab symmetry, and can probe neither the implementation of the geometric factors in the fluid equations, nor the discretized Einstein equations. A few general relativistic fluid systems *can* be solved exactly, and have traditionally been used to test new codes, including static, spherical stars (Tolman-Oppenheimer-Volkoff), and spherical dust collapse (Oppenheimer-Synder). (The TOV solutions for the ultrarelativistic equation of state have the form $\rho \propto 1/r^2$ [116]; this code requires regularity at the origin, precluding the TOV solution as a possible test.)

In the residual test, we discretize the PDEs using the leap-frog scheme, and evaluate the discretized equations with the high-resolution shock-capturing solution.

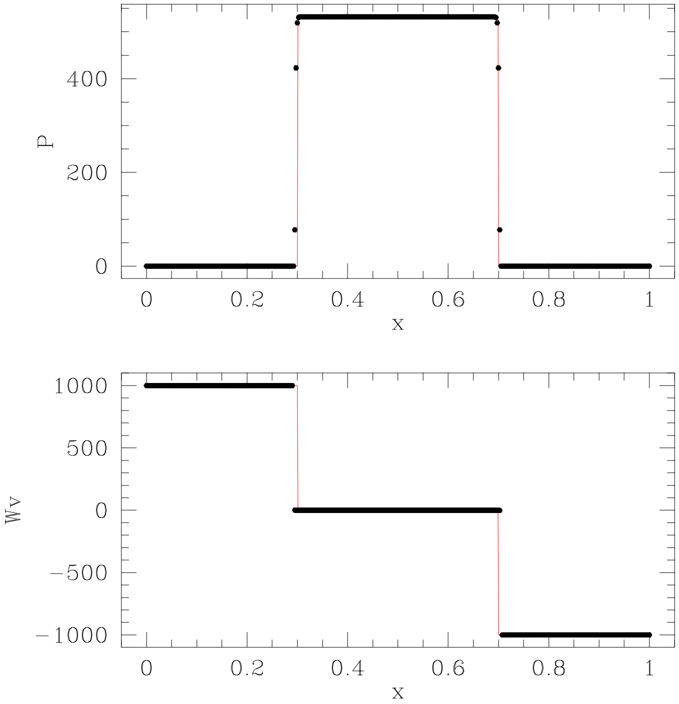

Figure 4.7: The shock compression of a diffuse relativistic gas is demonstrated in this shock tube test of a $\Gamma = 4/3$ fluid. The solid lines show the exact solution, and the points correspond to the PDE solution. The top frame shows the pressure at $t = 0.6$, and the bottom frame shows the product of the Lorentz factor and the velocity. The initial left state is $P_\ell = 10^{-4}$, $v_\ell = 0.9999995$, and the initial right state is $P_r = 10^{-4}$, $v_r = -0.9999995$. The solution is calculated with 400 cells.

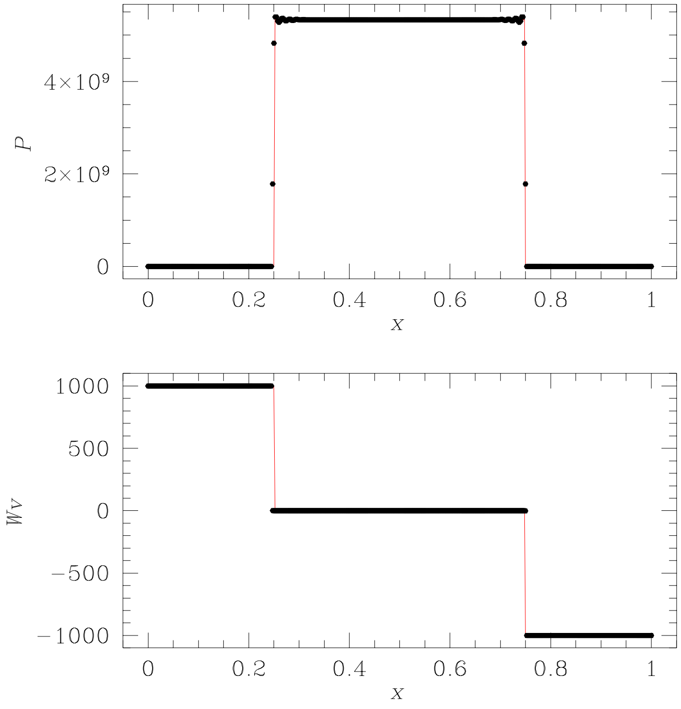

Figure 4.8: The shock compression of a relativistic fluid is shown in this shock tube test for $\Gamma = 4/3$. The top frame shows the pressure, and the bottom frame shows the product of the Lorentz factor and the velocity. The initial left state is $P_\ell = 10^3$, $v_\ell = 0.9999995$, and the initial right state is $P_r = 10^3$, $v_r = -0.9999995$. The solution is calculated with 400 cells using the monotonized central-difference limiter.

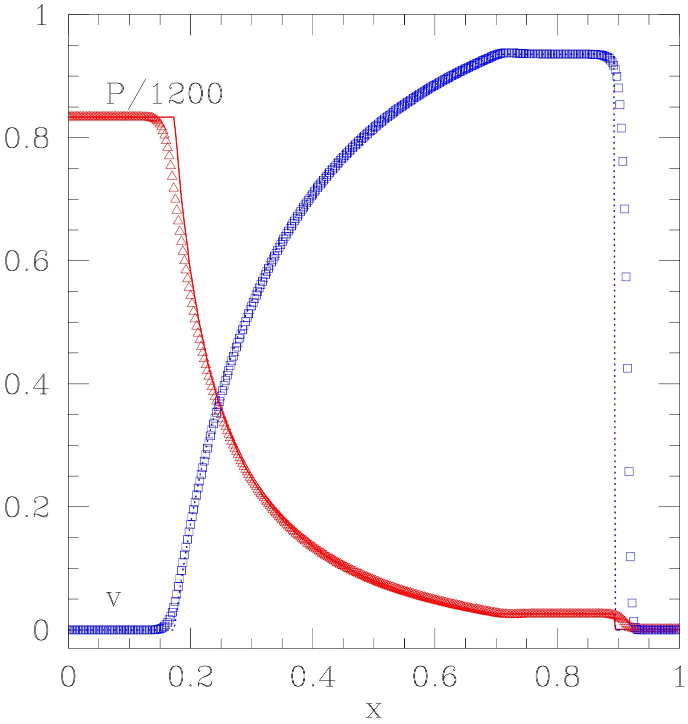

Figure 4.9: The lines show the exact solution for this shock tube test with a $\Gamma = 5/3$ fluid at $t = 0.4$. The triangles and squares show the pressure and velocity of the PDE solution, respectively. The initial left state is $P_\ell = 10^3$, $v_\ell = 0$, and the initial right state is $P_r = 1$, $v_r = 0$. The solution is calculated with 400 cells.

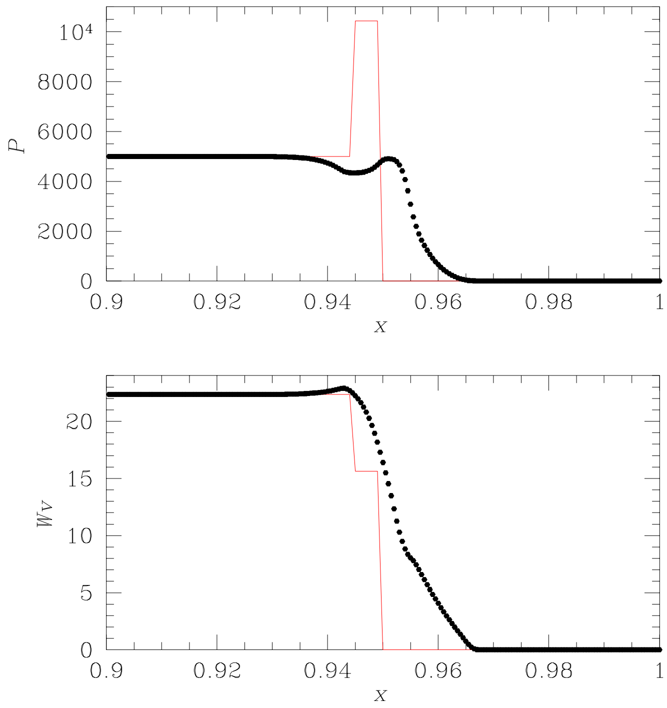

Figure 4.10: A relativistic shock tube test of a $\Gamma = 1.6$ fluid using the minmod limiter. The same test using the MC-limiter is shown in Figure 4.11. The initial left state is $P_\ell = 5000$, $v_\ell = 0.999$, and the initial right state is $P_r = 10$, $v_r = 0$. The solution is plotted at $t = 0.45$, and the test was performed with 1000 computational cells and a Courant number of 0.5. The limiters are defined in Section 3.4.1.

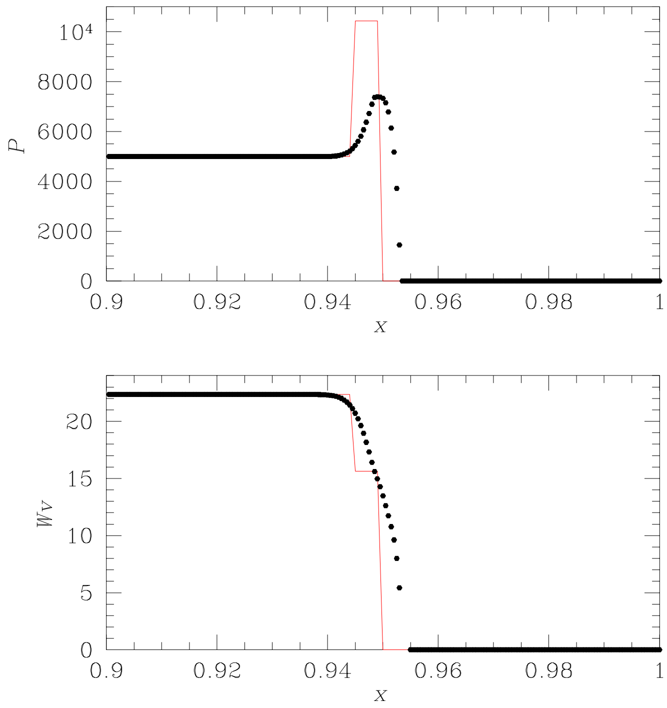

Figure 4.11: A relativistic shock tube test of a $\Gamma = 1.6$ fluid using the MC-limiter. The same test using the minmod limiter is shown in Figure 4.10. The initial left state is $P_\ell = 5000$, $v_\ell = 0.999$, and the initial right state is $P_r = 10$, $v_r = 0$. The solution is plotted at $t = 0.45$, and the test was performed with 1000 computational cells and a Courant number of 0.5. The limiters are defined in Section 3.4.1.

Using an uniform grid and a $\Gamma = 2$ fluid, we performed the residual test of the fluid equations of motion using the variables $\{E, S\}$ (4.15), and the Hamiltonian constraint (4.10). Figure 4.12 shows the residuals at a given time, plotted along with E and S for reference. The ℓ_2 norms of the residuals for the E equation of motion and Hamiltonian constraint as functions of time are plotted in Figures 4.14 and 4.15. These plots show that the largest errors occur when the fluid is at the origin, and this error also contributes to the difficulty in experimentally measuring the black hole mass-scaling parameter via supercritical evolutions. Finally, we find a remnant at the floor level in E at the origin after the pulse rebounds from the center, causing a large residual in the Hamiltonian constraint. Figure 4.16 shows this effect at different resolutions.

A test for the effect of the floor on the $\Gamma = 2$ critical solution is included here. This test, shown in Figure 4.17, indicates that the magnitude of the floor has very little effect on the near-critical solution. However, the mere presence of a non-zero floor may affect the solution. A test for the floor's effect on the mass scaling exponents calculated for critical solutions is included in Section 5.3.4 of the next chapter.

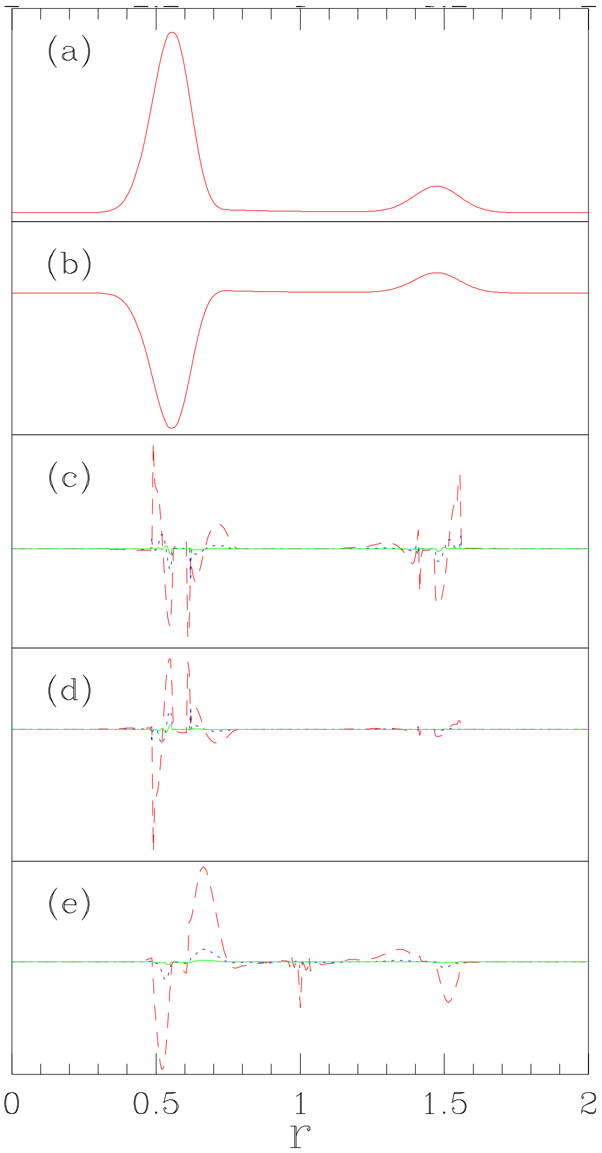

Figure 4.12: This figure shows the independent residual test for a subcritical evolution of a $\Gamma = 2$ fluid at $t = 0.62$. This caption is continued on the following page.

Caption for Figure 4.12 (continued): The fluid equations of motion and the Hamiltonian constraint are discretized independently using centered differences (in time and space). These equations are evaluated with the HRSC solution, and the residuals are shown here. The top two frames show the fluid variables E and S in frames (a) and (b), respectively. The next two frames show the residuals of the equations of motion, the E equation in frame (c), and the S equation in frame (d). The residual of the Hamiltonian constraint is shown in frame (e). The initial data are for a time-symmetric Gaussian pulse centered on the grid. The grid is uniform, and the residuals are shown at three different resolutions: $\triangle r = h$ (solid line), $\triangle r = 2h$ (dotted), and $\triangle r = 4h$ (dashed). The residuals decrease quadratically as the resolution is doubled, indicating a quadratic convergence to the correct solution. A detail of this plot is in Figure 4.13. The behavior of the residuals as a function of time is shown in Figures 4.14 and 4.15.

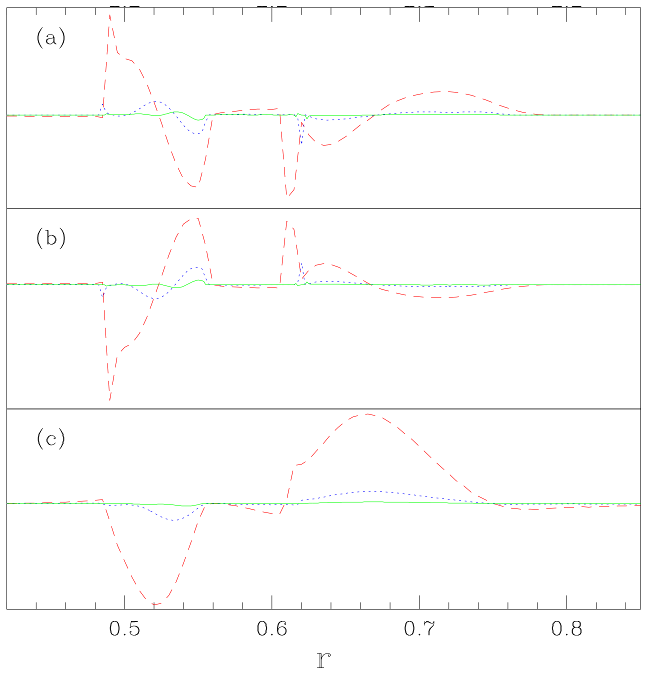

Figure 4.13: Detail near the origin of the independent residual test for a subcritical evolution of a $\Gamma = 2$ fluid at $t = 0.62$ shown in Figure 4.12. Frame (a) shows the residual of the E equation, frame (b) the residual of the S equation, and frame (c) shows the residual of the Hamiltonian constraint. See Figure 4.12 for further information and discussion.

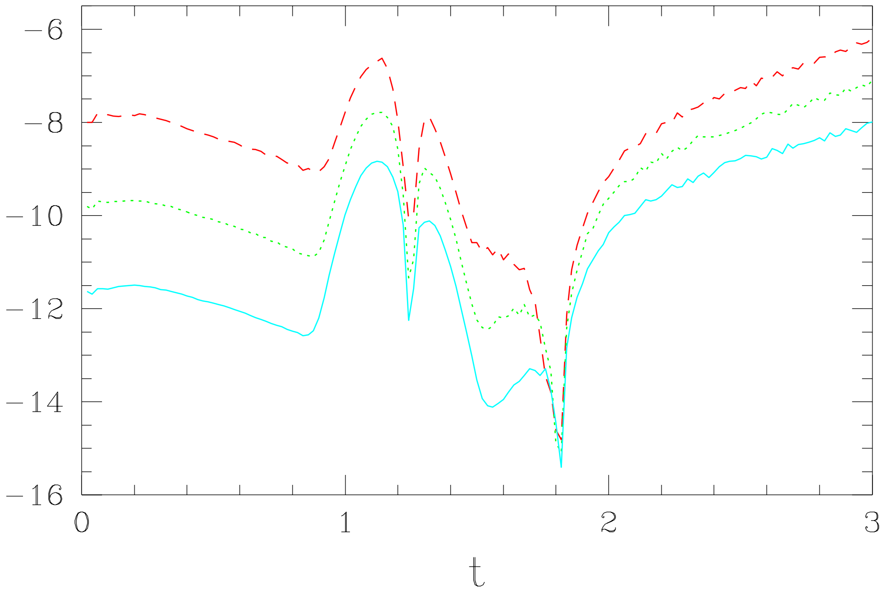

Figure 4.14: A plot of $\ln ||\mathrm{Res}(E)||_2 / \ln ||E||_2$ as a function of time for a subcritical evolution at three different resolutions, where $\mathrm{Res}(E)$ is the residual of the E equation of motion, and $|| \cdot ||_2$ is the ℓ_2 norm. The evolutions were performed on an uniform grid with spacings $\triangle r = h$ (solid line), $\triangle r = 2h$ (dotted), and $\triangle r = 4h$ (dashed), and the residual is evaluated independently with centered finite difference operators. The initial data are for a time-symmetric Gaussian pulse centered on the grid, and $\Gamma = 2$. Initially, the lines differ by 2 on the vertical scale, indicating that the residual converges quadratically to zero. When the bulk of the fluid reaches the origin, the convergence decreases, until the pulse reaches its maximum compression $t \approx 1.82$. The pulse then moves outward from the origin.

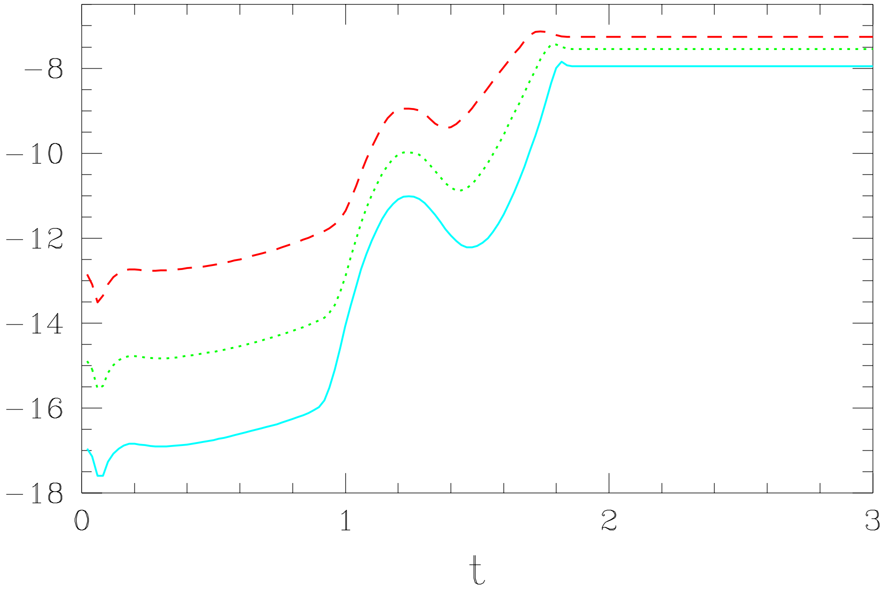

Figure 4.15: A plot of $\ln ||\mathrm{Res}(a)||_2$ as a function of time for a subcritical evolution at three different resolutions, where $\mathrm{Res}(a)$ is the residual of the Hamiltonian constraint. We solve the momentum constraint for the metric function a, thus the Hamiltonian constraint provides an independent check that the Einstein equations are solved correctly. The residual is evaluated with centered finite difference operators. See Figure 4.14 for further information on the resolution and initial data.

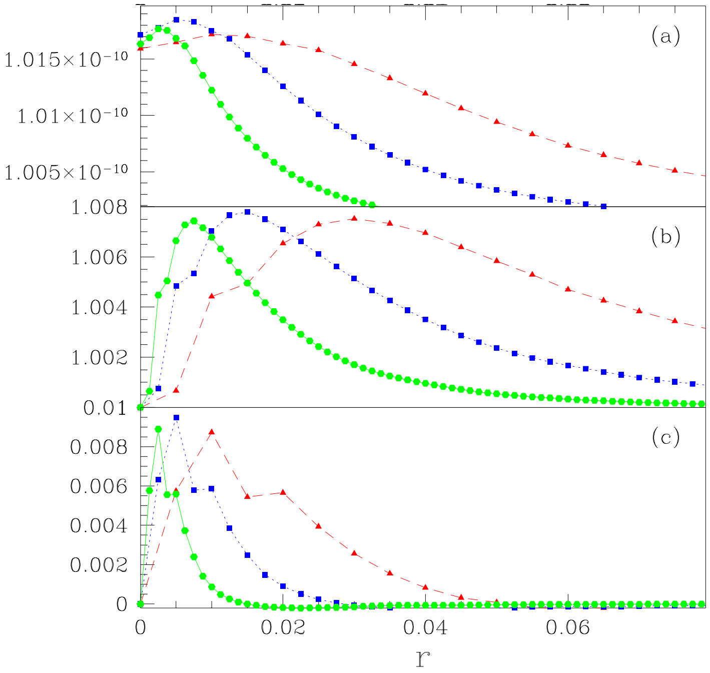

Figure 4.16: This figure shows a small "glitch" in E that develops at the floor level after the fluid rebounds from the origin in the subcritical evolution of Figure 4.12. Frame (a) shows E at the origin at $t = 3$, long after the bulk of the fluid has left the origin. Frame (b) shows the metric function a, and frame (c) shows the residual of the Hamiltonian constraint. Each frame shows the solution plotted at three resolutions, the hexagons at $\triangle r = h$, the squares at $\triangle r = 2h$, and the triangles at $\triangle r = 4h$. The floor in this test is $\delta = 10^{-10}$. While the error in E is at the floor level, the corresponding residual of the Hamiltonian constraint is relatively large, thus explaining the apparent loss of convergence in the Hamiltonian constraint after the fluid leaves the origin, as shown in Figure 4.15.

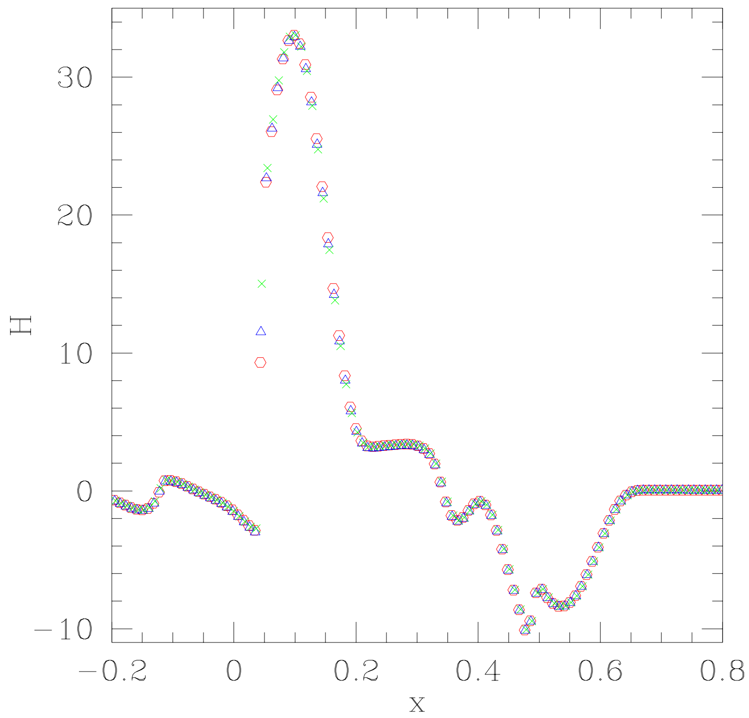

Figure 4.17: The residual of the Hamiltonian constraint for a $\Gamma = 2$ sub-critical solution calculated with three different floors at the same resolution. The crosses show the residual for $\delta = 10^{-6}$, the triangles for $\delta = 10^{-8}$, and the circles for $\delta = 10^{-10}$. The residuals provide an independent check of the truncation error, and are directly a function of the resolution used to calculate the solution. As illustrated in this figure, the residuals are not a function of the floor, indicating that the magnitude of the floor does not strongly affect the solution. However, the mere presence of a non-zero floor may affect the solution. For a further test of the floor's effects on the mass-scaling exponents calculated for critical solutions, see Figure 5.11.

Chapter 5

Critical phenomena (Type II)

The chapter is a study of spherically symmetric critical solutions for the Einstein-fluid system, using the computer code described in Chapter 4. This work has been previously reported in Neilsen and Choptuik [97].

5.1 Introduction to critical phenomena

The formation of black holes is an exciting topic in general relativity, and a class of solutions which exists precisely at the threshold of black hole formation has recently generated considerable interest. These solutions have surprising properties, reminiscent of some thermodynamic systems near phase transitions, and, by analogy, have been called critical solutions. Critical phenomena in gravitational collapse were first discovered empirically in simulations of the massless Klein-Gordon field minimally coupled to gravity (EMKG) [29]. Subsequent studies have shown that critical behavior is present in a variety of physical systems, and indicate that the phenomena are generic features of gravitational collapse in general relativity. In this section we focus on the critical solutions for a spherically symmetric perfect fluid with equation of state $P = (\Gamma - 1)\rho$, where ρ is the total energy density and Γ is constant, and present new solutions for $\Gamma \gtrsim 1.89$. While a brief introduction to critical solutions is included here, the review by Gundlach is an excellent introduction to critical phenomena [63], and additional information can be found in the review by Choptuik [32].

5.1.1 Basic properties of critical solutions

Imagine an experiment to investigate the details of gravitational collapse and black hole formation by imploding shells of fluid with a fixed equation of state. The initial energy density in the shell might be

$$\rho = A_0 \exp\left[-\left(r - r_0\right)^2 / \Delta^2\right] , \tag{5.1}$$

where A_0, r_0, and Δ are parameters. In the course of the experiment we fix two of the three parameters, and allow only one of them, which we label p, to vary. For small p (assuming the fluid's initial kinetic energy is sufficiently large—i.e., in what one might call the ultrarelativistic limit), the fluid implodes through the origin and completely disperses. However, for p sufficiently large, in particular for p larger than some critical value $p^\star$, a black hole forms during the implosion, trapping some of the matter/energy within a finite radius. In the exactly critical case, $p = p^\star$, which represents the threshold of black hole formation, the evolution temporarily asymptotes to a special critical solution, $Z^\star$, which has a number of interesting properties, including scale invariance (self-similarity) and universality. The critical solution is universal in the sense that if we now use different "interpolating families" to probe the threshold of black hole formation, we will generically find the same critical solution (provided we remain in the ultrarelativistic regime). Additionally, in the super-critical regime $p > p^\star$, the black hole masses are well described by a scaling law

$$M_{\mathrm{BH}}(p) \propto |p - p^\star|^\gamma . \tag{5.2}$$

Here the mass-scaling exponent γ is *also* universal in the sense that it is independent of the particular choice of initial data family. (However, as first predicted by

Maison [86], and Hara, Koike and Adachi [68, 74], and as discussed in detail below, γ *is* a function of the adiabatic index Γ.)

One of the most profound consequences of the self-similar nature of critical collapse is that black hole formation in the ultrarelativistic limit turns on at *infinitesimal* mass. In analogy with second-order phase transitions in statistical mechanics, we refer to this behavior as Type II. As we will discuss shortly, Type I behavior, wherein black hole formation turns on with *finite* mass in interpolating families, has also been seen in various models of collapse and it is undoubtedly present in at least some of the perfect fluid models considered here.

5.1.2 Critical solutions and one-mode instability

A crucial feature of the critical solutions sketched above is that they are, *by construction*, unstable. If this is not obvious, one should observe that the critical solution is *not* a long-time ($t \to \infty$) solution of the equations of motion. Indeed, as sketched above, the only long-time stable "states" one finds from evolutions of a generic ultrarelativistic family of initial data either have (i) all of the fluid dissipated to arbitrarily large radii, with (essentially) flat spacetime in the interior, or (ii) some fluid dissipated to arbitrarily large radii, with a black-hole in the interior. The critical solution, $Z^\star$, on the other hand, exists just at the threshold of black hole formation, and, in near-critical evolutions, the dynamics asymptotes to $Z^\star$ *only* during the strong-field dynamical epoch. For any given initial data, this strong-field regime persists for a *finite* amount of time (as measured, for example, by an observer at infinity). Eventually (and in fact, on a dynamical time scale) any non-critical data will evolve into one of the two stable end states.

Although the unstable nature of critical solutions was clear from the earliest phenomenological studies, considerable insight has been gained from the observation by Koike, Hara and Adachi [73] that the "sharpness" of the critical behavior seen in

Type II collapse suggests that the critical solutions have *exactly one* unstable mode in perturbation theory. This *ansatz* immediately explains the universality of the critical solution: as $p \to p^\star$, one is effectively directly tuning out the single unstable mode from the initial data. Furthermore, using the self-similarity of the dynamics in the near-critical regime and a little dimensional analysis, it is an easy matter to relate the mass-scaling exponent to the Lyapunov exponent associated with the single mode. In fact, since the pioneering work by Koike *et al.*, this picture of Type II critical solutions as one-mode unstable, self-similar "intermediate attractors" has been validated for essentially every spherically-symmetric model where Type II behavior has been observed in the solution of the full equations of motion.

Moreover, the perturbative analysis applies equally well to Type I critical solutions which, arguably, have been well known to relativists and astrophysicists for decades, although perhaps not in the context of interpolating families. In this case, the critical solution is an unstable *static* or *periodic* configuration which, depending on how it is perturbed, will either completely disperse, or collapse to a finite-mass black hole. Once again, one generically finds that such solutions have a *single* unstable eigenmode, whose Lyapunov exponent is now a measure of the increase in lifetime of the unstable configuration as one tunes $p \to p^\star$. Type I behavior has been observed in the collapse of Yang-Mills [30, 35] and massive scalar fields [15]. As discussed in Section 2.8.2 and illustrated in Figures 2.7–2.10, a family of static solutions parameterized by the central energy density can be generated, which contains both stable *and* unstable solutions. There is every reason to expect that these unstables solutions are Type I critical solutions.

5.1.3 Critical solutions and self-similarity

Heuristically, systems exhibiting self-similarity appear identical over many different spatial and/or temporal scales, and generally arise in physical situations in which

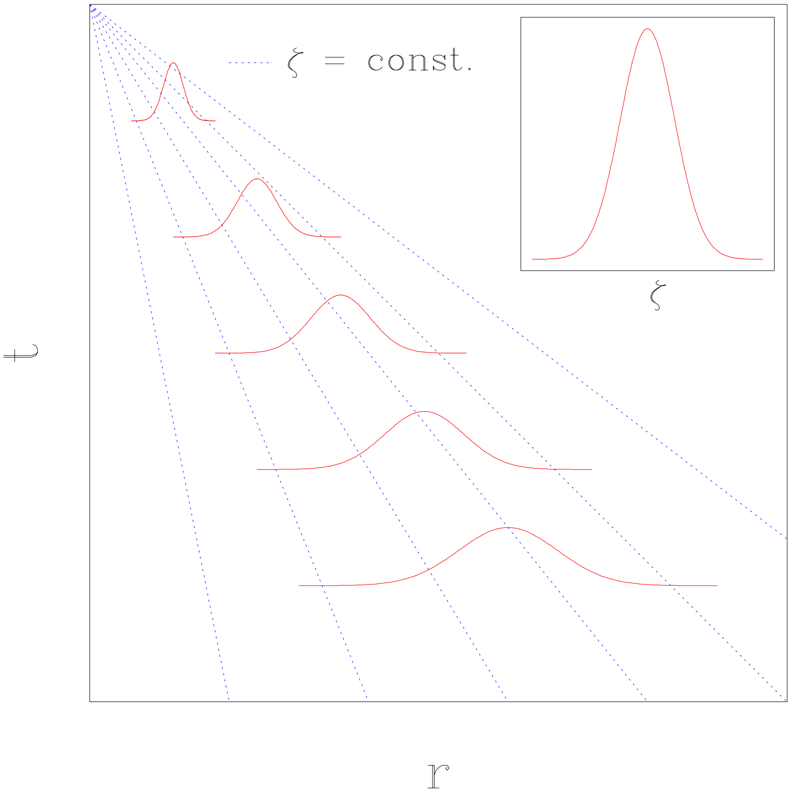

Figure 5.1: A schematic diagram showing a continuously self-similar (CSS) pulse at five different times as it moves toward the origin $r = 0$. The dotted lines are lines of constant $\zeta = r/t$, the similarity variable. These lines converge at the space-time origin $(r, t) = (0, 0)$ in the upper left-hand corner of the plot, and the inset shows the pulse as a function of ζ. As the pulse moves toward the origin, it appears the same on smaller and smaller length scales.

there are no natural length scales. Here it is important to note that a scale-free solution can be generated from a model which *does* have specific length scales, provided that the scaling solution represents a "self-consistent" limit. The current case of fluid collapse provides a perfect example. The rest mass of the fluid *does* set a length-scale, but the Type II critical solutions describe an ultrarelativistic limit wherein the rest-mass of the solution is irrelevant. To put this another way, we can have *solutions* of the equations of motion which have greater symmetry (scale symmetry in this case) than the equations of motion themselves.

Self-similarity can be either continuous (CSS) or discrete (DSS), and both types have been observed in critical gravitational collapse. The perfect fluid critical solutions have continuous self-similarity of the *first* kind, a particularly simple self-similarity wherein the solutions can be written solely as functions of dimensionless variables, such as $\zeta = r/t$, where r is the radial coordinate in spherical symmetry and t is the coordinate time. An example of a CSS function of the first kind is shown schematically on a spacetime diagram in Figure 5.1.

At this point we should also note that the self-similar nature of Type II critical solutions provides a link between work on black-hole critical phenomena and the large body of literature dealing with self-similarity in the context of Einstein gravity (see Carr and Coley [23] for a recent, extensive review). The self-similar *ansatz* has been widely employed, not only to produce more tractable problems, but also in investigations of possible mechanisms to generate counter-examples to the cosmic censorship conjecture. However, it is clear that not all self-similar solutions will be relevant to critical collapse, particularly if we restrict the definition of critical to "one-mode unstable". Moreover, because most studies which are based on the self-similar *ansatz* have only considered the solutions themselves, and not perturbations thereof, it has proven non-trivial to identify which self-similar perfect-fluid solutions previously discussed in the literature are relevant to critical collapse [23, 60, 25].

5.1.4 Review of previous perfect-fluid studies

Shortly after the discovery of Type II behavior in scalar field collapse [29], Evans, having been frustrated in attempts to "analytically" understand the massless-scalar critical solutions, turned his attention to perfect-fluid collapse. Armed with the intuition that the self-similarity of critical collapse was a defining characteristic, and aware of the existence of continuously self-similar relativistic fluid flows, he and Coleman [52] considered collapse in the context of the specific equation of state, $P = \frac{1}{3}\rho$. Significantly, they were able to construct a single critical solution, both from the self-similar *ansatz* (i.e., by solving ODEs), and by tuning the initial data used in solution of the full partial differential equations of motion. Moreover, they noted that a perturbation analysis about the inherently unstable critical solution would provide an accurate description of the near-critical dynamics, including the calculation of the mass-scaling exponent γ.

Such a perturbation analysis was quickly carried out (again for the case $P = \frac{1}{3}\rho$) by Koike *et al.* [73], who, as mentioned above, made the crucial additional observation that the "sharp" transition in the mass scaling suggested that there was only *one* growing unstable mode associated with the critical solution, and that the Lyapunov exponent of the mode was simply the reciprocal of the mass-scaling exponent γ. Their analysis fully validated this conjecture—in particular, they found strong evidence for a single unstable mode with Lyapunov exponent $2.81055\ldots$, corresponding to $\gamma = 0.3558019\ldots$, in excellent agreement with Coleman and Evans' "measured" value, $\gamma \approx 0.36$.

At about the same time, Maison [86]—assuming that the critical solutions would be continuously self-similar for other values of Γ—adopted the CSS *ansatz* for the more general equation of state $P = (\Gamma - 1)\rho$. He was able to construct CSS solutions for $1.01 \leq \Gamma \leq 1.888$, and additionally presented strong evidence that all of the solutions were one-mode unstable. Furthermore, the Lyapunov exponents, and hence the mass-scaling exponents were found to be Γ-dependent, with, γ, for example, varying from $\gamma = 0.1143$ for $\Gamma = 1.01$ to $\gamma = 0.8157$ for $\Gamma = 1.888$. These calculations were particularly notable for providing early evidence that γ was not a "truly" universal exponent, in the sense of having the same value across *all* possible models of collapse.

One interesting outcome of Maison's linearized analysis of the equations of motion about the sonic point, was that at $\Gamma \simeq 1.888$, two of the eigenvalues of the linearized problem degenerated, and the sonic point apparently changed from a node to a focus. This led Maison to conclude that regular self-similar solutions did not exist for $\Gamma \gtrsim 1.89$. A similar analysis by Hara, Koike and Adachi [68, 74] (expanding on their previous work) again suggested a change in solution behavior at $\Gamma \approx 1.89$. Those authors computed the CSS solutions, unstable eigenmodes, and eigenvalues for $1 < \Gamma \leq 1.889$, with results essentially identical to Maison's. Evans and Perkins [101] also performed the linear stability analysis for $\Gamma \leq 1.888$, finding the same results reported by Maison. In addition, they performed the first critical solution searches using the full set of PDEs for $1.05 \leq \Gamma \leq 1.5$, confirming that the CSS solutions are the unique critical solutions for Γ is this range. Goliath *et al.* [60] discussed, in the wider context of time-like self-similar fluid solutions, the mode structure of the $P = (\Gamma - 1)\rho$ CSS solutions, and reported that physical solutions do not exist for $\Gamma \gtrsim 1.89$.

Furthermore, the conclusion of these linear perturbation analyses—that regular critical solutions for $\Gamma \gtrsim 1.89$ do not exist—has inspired various proposals regarding the nature of $\Gamma \gtrsim 1.89$ critical solutions [63, 23, 16]. (Recall that as long as we can set up interpolating data, there *will* be a critical solution, virtually by definition). One proposal is that a loss of analyticity at the sonic point for $\Gamma \gtrsim 1.89$ violates a condition required to find the ODE solutions. Other proposals have suggested that the solution might become Type I, discretely self-similar, or display a mixture of DSS and CSS behavior. Some of these conjectures were evidently based on the fact that, under certain conditions, a stiff ($P = \rho$) perfect fluid can be formally identified with the EMKG system [127, 84, 85]. For example, it has been conjectured [63, 23, 16] that at some point as $\Gamma \to 2$, the critical solution might begin to display the discrete self-similarity characteristic of the EMKG critical solution. Brady and Cai [16] computed threshold solutions for $\Gamma \leq 1.98$ using the full fluid equations of motion, finding—in all cases examined—evidence that the critical solutions are both CSS and Type II. Using a two-step Lax-Wendroff numerical scheme to integrate the fluid equations, they calculated mass-scaling exponents by evolving supercritical initial data. However their code has severe resolution limitations, being able to observe scaling only over two orders of magnitude in $|p - p^\star|$.

Yet, lacking solutions for $\Gamma = 2$, and high resolution solutions near $\Gamma \simeq 1.89$, it was still expected that the perfect fluid critical solution changed its character as $\Gamma \to 2$. As we will discuss below, this does not seem to be the case, and in fact, $\Gamma \simeq 1.89$ seems problematic only in the context of the the precisely self-similar *ansatz.* Specifically, we have strong evidence that the CSS *ansatz* generates an increasingly ill-conditioned problem as $\Gamma \to 1.8896244\ldots$, but that the PDEs remain perfectly well-behaved there.

More recently, after the results presented in this chapter appeared in pre-print form, the existence of (globally regular) CSS solutions for $\Gamma \gtrsim 1.89$ has been confirmed by Carr *et al.* [24], and Gundlach [67]. These solutions have been studied using analytical techniques by Carr *et al.* [24, 25, 26], who claim that these solutions “are associated with a new class of asymptotically Minkowski self-similar spacetimes” [24]. Finally, motivated by this research, Brady and Gundlach [17] have found a CSS massless scalar field solution that essentially matches the $\Gamma = 2$ perfect fluid critical solution found here. Preliminary results from a perturbation analysis of this solution indicate that this solution’s mass-scaling exponent is $\gamma \approx 0.94$, in agreement with our results with limited precision.

5.2 Fluid equations

Continuous self-similar solutions for spherically symmetric relativistic fluids have been studied since the work of Bogoyavlenskii [14], however their stability—a defining property for criticality—properties were largely ignored. Evans and Coleman [52] found that the critical solution ($\Gamma = 4/3$) could be constructed with the CSS *ansatz* by requiring the solutions to be globally regular. In this section we construct the critical solutions following the conditions used by Evans and Coleman. First the fluid equations are written in terms of the primitive variables, and then they are reduced to ordinary differential equations by introducing a similarity variable. Methods for solving these equations are given, along with sample solutions.

We write the spherically symmetric line element in polar-areal coordinates as

$$\mathrm{d}s^2 = -\alpha(r,t_*)^2\,\mathrm{d}t_*^2 + a(r,t_*)^2\,\mathrm{d}r^2 + r^2\,\left(\mathrm{d}\theta^2 + \sin^2\theta\,\mathrm{d}\phi^2\right), \tag{5.3}$$

where the radial coordinate, r, directly measures the proper surface area. The time coordinate is introduced with an asterisk ($*$) to differentiate it from the time coordinate used in the evolution codes. The latter coordinates are chosen to be the proper time for an observer at infinity (see Section 4.4.2). The coordinate t_* is determined by reference to the fluid's sonic point, as discussed below. The Einstein equations give three relations for the metric quantities α and a, equations (4.8)–(4.10), and there are two fluid equations of motion (4.15). These equations are

$$\partial_r \ln(a) = \frac{1-a^2}{2r} + 4\pi r a^2\left(\rho W^2 + P W^2 v^2\right) \tag{5.4}$$

$$\partial_r \ln(\alpha) = \frac{a^2-1}{2r} + 4\pi r a^2\left(\rho W^2 v^2 + P W^2\right) \tag{5.5}$$

$$\partial_{t*} \ln(a) = -4\pi r a \alpha(\rho + P) W^2 v \tag{5.6}$$

$$\partial_{t*}(a\rho W) + P\partial_{t*}(aW) + \frac{1}{r^2}\left[\partial_r(r^2\alpha\rho W v) + P\partial_r(r^2\alpha W v)\right] = 0 \tag{5.7}$$

$$\partial_{t*}(aPWv) + \partial_{t*}(aWv) + \partial_r(\alpha PW) + \rho\partial_r(\alpha W) = 0. \tag{5.8}$$

A continuously self-similar spacetime is generated by a homothetic Killing vector ξ [22],

$$\pounds_\xi g_{\mu\nu} = 2g_{\mu\nu}. \tag{5.9}$$

To simplify the fluid equations, we introduce new independent variables, s and x, adapted to this symmetry

$$s \equiv -\ln(-t_*), \tag{5.10}$$

$$x \equiv \ln(-\frac{r}{t_*}). \tag{5.11}$$

The time coordinate t_* is chosen such that a collapsing, self-similar solution reaches the origin at $t_* = 0$, *and* the sonic point is at $x = 0$. To simplify and reduce the fluid equations (5.4)–(5.8) to ordinary differential equations, we define the following dimensionless quantities

$$N \equiv \frac{\alpha}{a\mathrm{e}^x}, \tag{5.12}$$

$$A \equiv a^2, \tag{5.13}$$

$$\omega \equiv 4\pi r^2 a^2 \rho. \tag{5.14}$$

In terms of these new dimensionless variables, the fluid equations become

$$\frac{1}{A}\partial_x A = 1 - A + \frac{2\omega\left(1 + (\Gamma - 1)\,v^2\right)}{1 - v^2} \tag{5.15}$$

$$\frac{1}{N}\partial_x N = -2 + A - (2 - \Gamma)\omega \tag{5.16}$$

$$\frac{1}{A}\partial_s A + \frac{1}{A}\partial_x A = -\frac{2\Gamma N v\omega}{1 - v^2} \tag{5.17}$$

$$
\begin{aligned}
&(\Gamma-1)\frac{v}{\omega}\partial_s\omega+\frac{(1+Nv)}{\omega}\partial_x\omega+\frac{\Gamma(N+v)}{1-v^2}\partial_x v \\
&\quad=\frac{3(2-\Gamma)}{2}Nv-\frac{2+\Gamma}{2}ANv+(2-\Gamma)Nv\omega
\end{aligned}
\tag{5.18}
$$

$$
\begin{aligned}
&(\Gamma-1)\frac{v}{\omega}\partial_s\omega+\frac{\Gamma}{1-v^2}\partial_s v+(\Gamma-1)\frac{N+v}{\omega}\partial_x\omega+\frac{\Gamma(1+Nv)}{1-v^2}\partial_x v \\
&\quad=(2-\Gamma)(\Gamma-1)N\omega+\frac{7\Gamma-6}{2}N+\frac{2-3\Gamma}{2}AN.
\end{aligned}
\tag{5.19}
$$

The self-similarity *ansatz* requires that all derivatives with respect to s vanish, thus reducing the system to autonomous, first order ordinary differential equations [68].

$$
\frac{A'}{A}=1-A+\frac{2\omega\left(1+(\Gamma-1)\,v^2\right)}{1-v^2}
\tag{5.20}
$$

$$
\frac{N'}{N}=-2+A-(2-\Gamma)\,\omega
\tag{5.21}
$$

$$
\frac{A'}{A}=-\frac{2\Gamma Nv\omega}{1-v^2}
\tag{5.22}
$$

$$
\begin{aligned}
&(1+Nv)\,\frac{\omega'}{\omega}+\frac{\Gamma\,(N+v)\,v'}{1-v^2} \\
&\qquad=\frac{3}{2}(2-\Gamma)Nv-\frac{2+\Gamma}{2}ANv+(2-\Gamma)Nv\omega
\end{aligned}
\tag{5.23}
$$

$$
\begin{aligned}
&(\Gamma-1)(N+v)\frac{\omega'}{\omega}+\frac{\Gamma(1+Nv)v'}{1-v^2} \\
&\qquad=(2-\Gamma)(\Gamma-1)N\omega+\frac{7\Gamma-6}{2}N+\frac{2-3\Gamma}{2}AN.
\end{aligned}
\tag{5.24}
$$

This system is overdetermined, as there are five equations for four unknowns: A, N, v, and ω. (The equations are overdetermined because solutions of the Einstein equations also must satisfy the contracted Bianchi identities, or equivalently, because the solution must satisfy both evolution *and* constraint equations.) Both equations

(5.20) and (5.22) contain only a single derivative, A', and can be combined into the algebraic equation

$$(1-A)(1-v^2) + 2\omega\left(1+(\Gamma-1)v^2\right) + 2\Gamma N v\omega = 0. \tag{5.25}$$

This equation could be used to eliminate one of the unknowns. However, we solve four equations, and use the algebraic constraint to monitor the error in our solutions. The equations (5.21)–(5.24) are integrated to find the self-similar solutions. We write these equations formally as

$$\boldsymbol{M}(\boldsymbol{y})\,\boldsymbol{y}' = \boldsymbol{f}(\boldsymbol{y}), \tag{5.26}$$

where $\boldsymbol{y}$ is a "state vector" containing the four dependent variables A, N, v, and ω, i.e.,

$$\boldsymbol{y} \equiv \begin{bmatrix} A \\ N \\ v \\ \omega \end{bmatrix}. \tag{5.27}$$

5.2.1 The sonic point

The system of ODEs (5.26) can be solved provided that the inverse matrix $\boldsymbol{M}^{-1}$ exists. When $\det \boldsymbol{M} = 0$—a condition occurring at a sonic Cauchy horizon or sonic point—the ODEs cannot be integrated without further assumptions. In particular, if $\det \boldsymbol{M} = 0$, the derivatives, $\boldsymbol{y}'$, may either (i) not exist or (ii) be undefined. In the former case, the functions may be continuous but not differentiable, or a shock may form (discontinuous functions) at the sonic point; the latter case corresponds to the physically-relevant regular solutions in which we are interested. By definition, the sonic point is the position where the magnitude of the fluid velocity, as measured by an observer at constant $x = \ln(-r/t_*)$, is equal to the fluid sound speed

$$c_s = \sqrt{\Gamma - 1}. \tag{5.28}$$

All CSS perfect fluid solutions that are regular at the origin have at least one sonic point [100].

The requirement that $\boldsymbol{y}$ be differentiable at the sonic point allows one to find additional relations which hold only at the sonic point. At this point, it is convenient to consider only the fluid equations. Let $\boldsymbol{z}$ be the state vector of fluid variables

$$\boldsymbol{z} \equiv \begin{bmatrix} v \\ \omega \end{bmatrix}, \tag{5.29}$$

and write the fluid equations (5.23)–(5.24) as

$$\boldsymbol{J}\boldsymbol{z}' = \boldsymbol{b}. \tag{5.30}$$

where $\boldsymbol{J}$ is a 2×2 matrix containing no derivatives of $\boldsymbol{z}$, and $\boldsymbol{b}$ is a two-component state vector consisting of the right-hand sides of (5.23)–(5.24). To solve the ODE system (5.30), we isolate $\boldsymbol{z}$ by writing (5.30) as

$$\boldsymbol{z}' = \boldsymbol{J}^{-1}\boldsymbol{b}. \tag{5.31}$$

The inverse of $\boldsymbol{J}$ is

$$\boldsymbol{J}^{-1} = \frac{1}{\det \boldsymbol{J}}\boldsymbol{K}, \tag{5.32}$$

where $\boldsymbol{K}$ is the matrix

$$\boldsymbol{K} = \begin{pmatrix} J_{22} & -J_{12} \\ -J_{21} & J_{11} \end{pmatrix}, \tag{5.33}$$

and

$$\det \boldsymbol{J} \propto \frac{(1+Nv)^2 - (\Gamma - 1)(N+v)^2}{1-v^2}. \tag{5.34}$$

If $\boldsymbol{z}$ is regular at the sonic point, then the rows of $\boldsymbol{J}$ must be linearly dependent so that $\det \boldsymbol{J} = 0$. This can be seen by expanding $\boldsymbol{J}^{-1}$ in (5.31) as

$$(\det \boldsymbol{J})\, \boldsymbol{z}' = \boldsymbol{K}\boldsymbol{b}. \tag{5.35}$$

As $\det \boldsymbol{J} = 0$ at the sonic point, and if $\boldsymbol{z}$ is regular, then (5.35) requires that

$$\boldsymbol{K}\boldsymbol{b} = \boldsymbol{0}. \tag{5.36}$$

This condition allows one to parameterize the CSS solutions with a *single* parameter, $v_{\rm sp}$, which is the fluid velocity at the sonic point. Setting $\det \boldsymbol{J} = 0$ in (5.34) gives N at the sonic point

$$N_{\rm sp} = \frac{1 - v_{\rm sp}\sqrt{\Gamma - 1}}{\sqrt{\Gamma - 1} - v_{\rm sp}}. \tag{5.37}$$

Requiring rows of $\boldsymbol{K}$ to be proportional (5.36), combined with (5.25) gives A and ω at the sonic point

$$\begin{aligned} A_{\rm sp} &= \frac{1}{\Gamma^2(1 - v_{\rm sp}^2)} \\ &\qquad \times \left[\Gamma^2 + 4\Gamma - 4 + 8(\Gamma - 1)^{3/2} v_{\rm sp} - (3\Gamma - 2)(2 - \Gamma) v_{\rm sp}^2\right], \end{aligned} \tag{5.38}$$

$$\omega_{\rm sp} = \frac{1}{\Gamma^2(1 - v_{\rm sp}^2)} \left[2\sqrt{\Gamma - 1}\left(\sqrt{\Gamma - 1} - v_{\rm sp}\right)\left(1 + \sqrt{\Gamma - 1} v_{\rm sp}\right)\right]. \tag{5.39}$$

Furthermore, this regularity condition fixes not only $\boldsymbol{y}$ at the sonic point in terms of $v_{\rm sp}$, but also determines its derivative, $\boldsymbol{y}'_{\rm sp}$, in terms of $v_{\rm sp}$ and $v'_{\rm sp}$. Taking the first derivative of (5.35) gives the condition on $\boldsymbol{y}'_{\rm sp}$

$$(\det \boldsymbol{J})' \boldsymbol{z}' = (\boldsymbol{K}\boldsymbol{b})' \tag{5.40}$$

Substituting $A'_{\rm sp}$ and $N'_{\rm sp}$ from equations (5.21) and (5.22) into (5.40), we combine both equations into one equation for $v'_{\rm sp}$, yielding a quadratic condition on $v'_{\rm sp}$ which we schematically write as

$$c_2 {v'_{\rm sp}}^2 + c_1 v'_{\rm sp} + c_0 = 0. \tag{5.41}$$

Here, the coefficients, c_0, c_1 and c_2, are complicated functions of $\boldsymbol{y}_{\rm sp}$. This expression is not given explicitly here because we actually only calculate this equation using the symbolic manipulation program *Maple V*. In our implementation, (5.41) is actually expressed in terms of a cubic equation. The additional root is eliminated by requiring $v'_{\rm sp} > 0$.

The key point is that this constraint—that the critical solutions are regular at the sonic point—limits the number of solutions to discrete values of $v_{\rm sp}$, and virtually eliminates the possibility that globally regular solutions with more than one sonic point exist [100, 53]. Indeed, all of the $\Gamma \leq 2$ critical solutions we have found, either from a CSS *ansatz,* or by solving the full Einstein/fluid equations, have only one sonic point.

5.2.2 Solving the ordinary differential equations

The system of ordinary differential equations (5.26) is solved by choosing a candidate fluid velocity, $v_{\rm sp}$, at the sonic point, and integrating numerically from the sonic point toward the origin. The inward integration is halted when either

$$A < 1 \qquad \text{or} \qquad \det \boldsymbol{J} = 0, \tag{5.42}$$

and these generic stopping criteria allow one to determine the parameter $v_{\rm sp}$ by a standard "shooting" procedure. (If $A < 1$ signals that $v_{\rm sp}$ is too small, then $\det \boldsymbol{J} = 0$ indicates that $v_{\rm sp}$ is too large, and vice versa). Once $v_{\rm sp}$ has been determined from the inward integration, the solution can be completed by integrating outwards from the sonic point. The entire solution process is complicated by the fact that the integration can not actually begin at the sonic point, since $\det \boldsymbol{J} = 0$ there. Therefore, we first expand the dependent variables $\boldsymbol{y}$ about the sonic point to first order

$$\boldsymbol{y}_o \approx \boldsymbol{y}_{\rm sp} + \boldsymbol{y}'_{\rm sp} \triangle x, \tag{5.43}$$

where $\triangle x \equiv x_o - x_{\rm sp}$, and actually begin the integration from x_o. $\triangle x$ is chosen so that the $\mathrm{O}((\triangle x)^2)$ error terms in the expansion, are smaller than the error tolerance allowed in the solution. We obtain $\boldsymbol{y}'_{\rm sp}$ by solving (5.41) for $v'_{\rm sp}$ and integrate the ODEs for both roots.

The ODEs are integrated using `LSODE`, a robust numerical routine for integrating ordinary differential equations [70, 103], and *all* of the critical solutions can be found using double precision arithmetic, *except* those solutions for $\Gamma \approx 1.89$. These $\Gamma \approx 1.89$ solutions require greater precision, and can be found using the arbitrary precision implementation of `LSODE` in *Maple V* [34], which also proved invaluable for convergence testing the solutions. In the convergence tests we vary $\triangle x$, the `LSODE` absolute error tolerance ε (the relative error tolerance is set to zero), and the number of digits used in the calculation, while monitoring the residual of the algebraic constraint (5.25) as an indication of the error in the solution. For example, we calculated the critical solution for $\Gamma = 1.99$ using 40 digits and error tolerances $\varepsilon = 10^{-10}$, 10^{-15}, 10^{-20} and 10^{-25}, and then performed similar tests using 30 and 35 digits. In all cases the solutions converge, and the residual of (5.25) is $\mathrm{O}(\varepsilon)$.

Sample solutions are plotted in Figures 5.2–5.5. These solutions were found using the `LSODE` integrator in *Maple* with 30 precision digits, and an `LSODE` error tolerance, $\varepsilon = 10^{-18}$. These continuously self-similar solutions are compared with the dynamically calculated critical solutions in Section 5.3.3, demonstrating that these CSS solutions *are* the spherically symmetric critical solutions.

5.2.3 Degenerate node

Although nonlinear systems of ODEs are often impossible to solve in closed-form, qualitative features of their solutions can frequently be deduced by linearizing the equations about "critical" points. Perfect fluid CSS solutions have often been studied using this type of analysis [86, 68, 60, 100, 14, 12, 13, 53], and here we discuss some of these results in the context of our work. We emphasize, however, that we have *not* performed perturbation analyses in our current work.

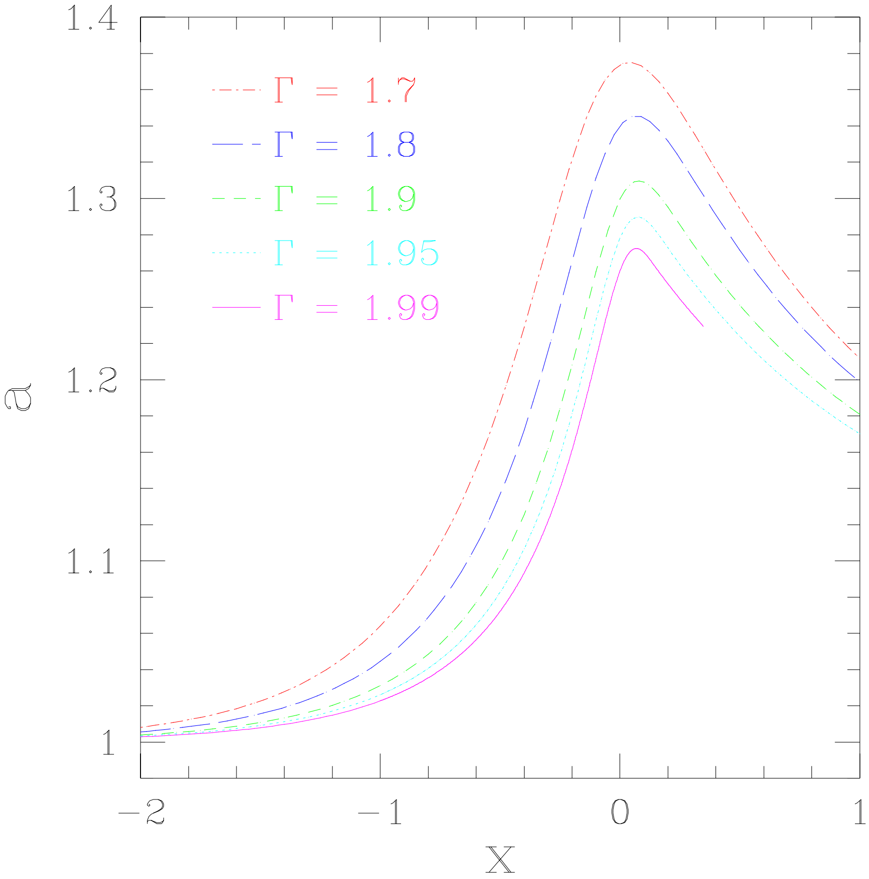

Figure 5.2: The geometric variable a of the critical solution for several values of Γ. The sonic point is at $x = 0$. The ODEs were integrated using the *Maple V* implementation of `LSODE` with 30 digits and an absolute error tolerance $\varepsilon = 10^{-18}$. We are increasingly unable to integrate these solutions outwards as $\Gamma \to 2$. This often occurs owing to a loss of numerical precision as $\omega \to 0$, and the Lorentz factor, $W = 1/\sqrt{1-v^2}$, becomes large (see Figure 5.5).

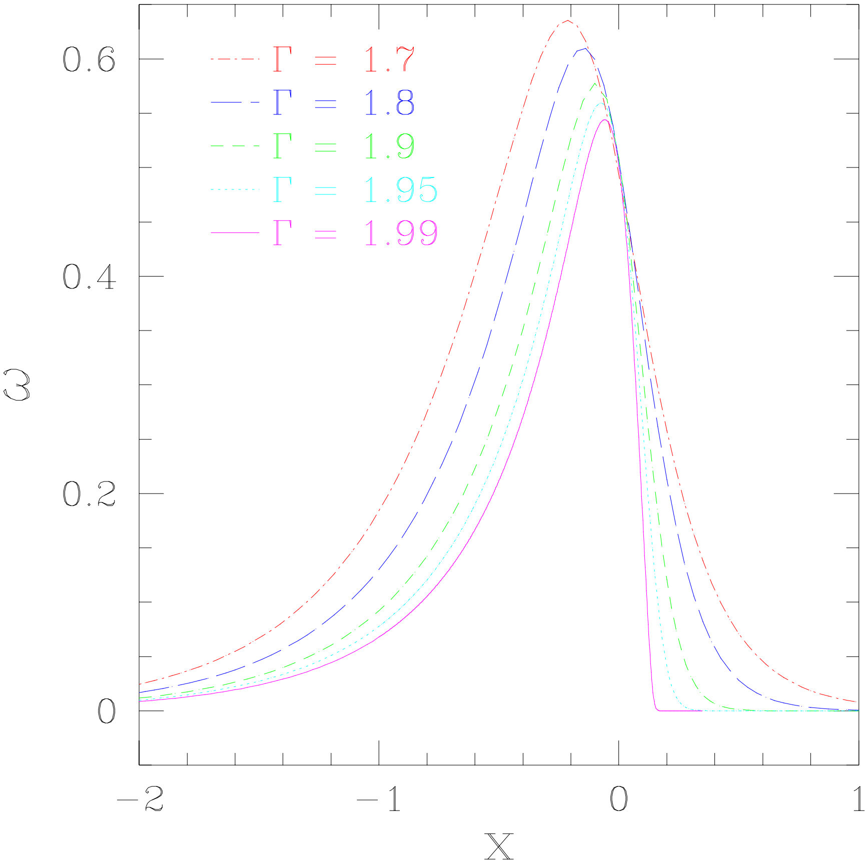

Figure 5.3: The fluid variable ω of the critical solution for several values of Γ. The sonic point is at $x = 0$.

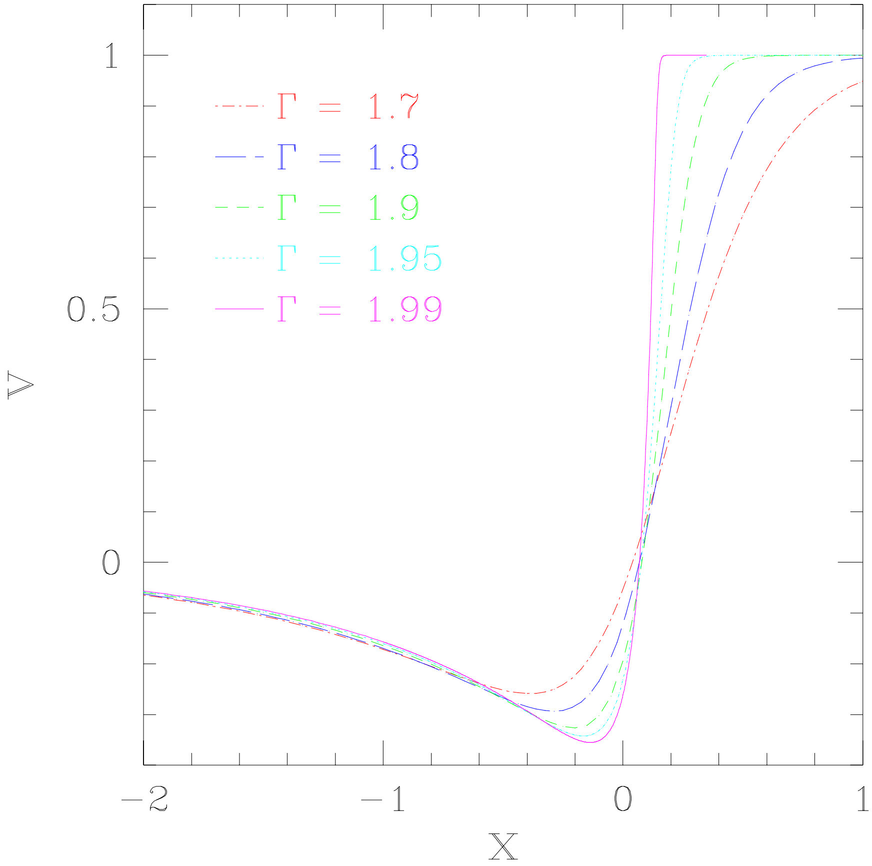

Figure 5.4: The fluid velocity v of the critical solution for several values of Γ. The sonic point is at $x = 0$.

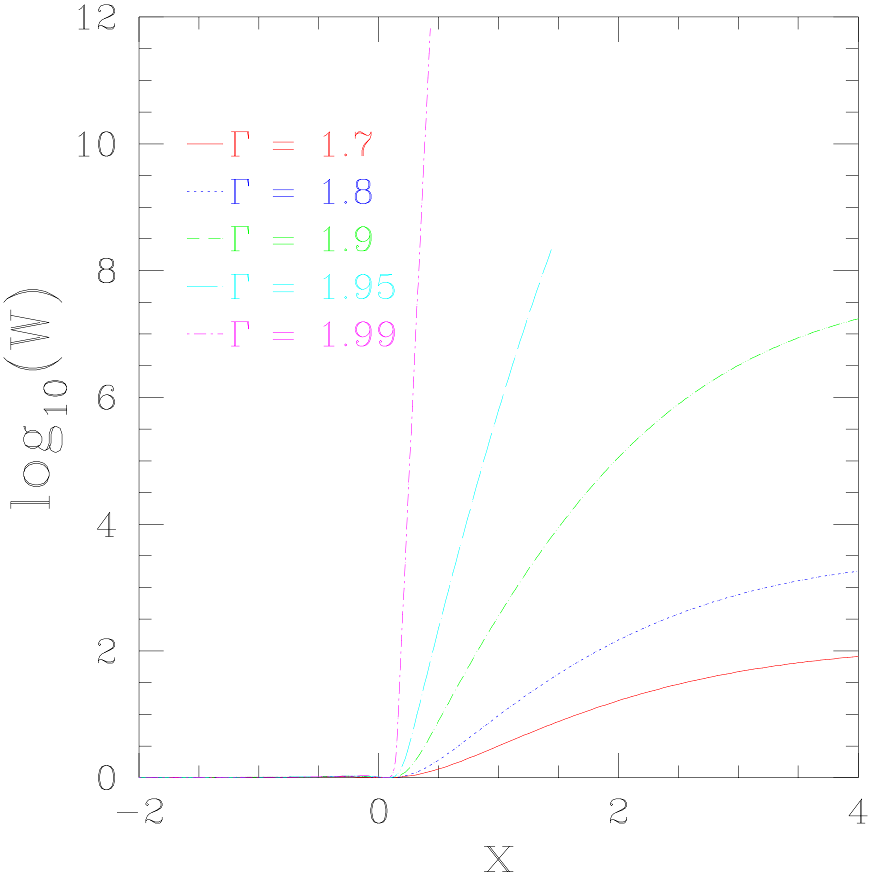

Figure 5.5: The logarithm of the Lorentz factor for the fluid velocity, $W = 1/\sqrt{1-v^2}$, of the critical solution for several values of Γ. Notice the exponential growth in the Lorentz factor for larger values of Γ. The sonic point is at $x = 0$.

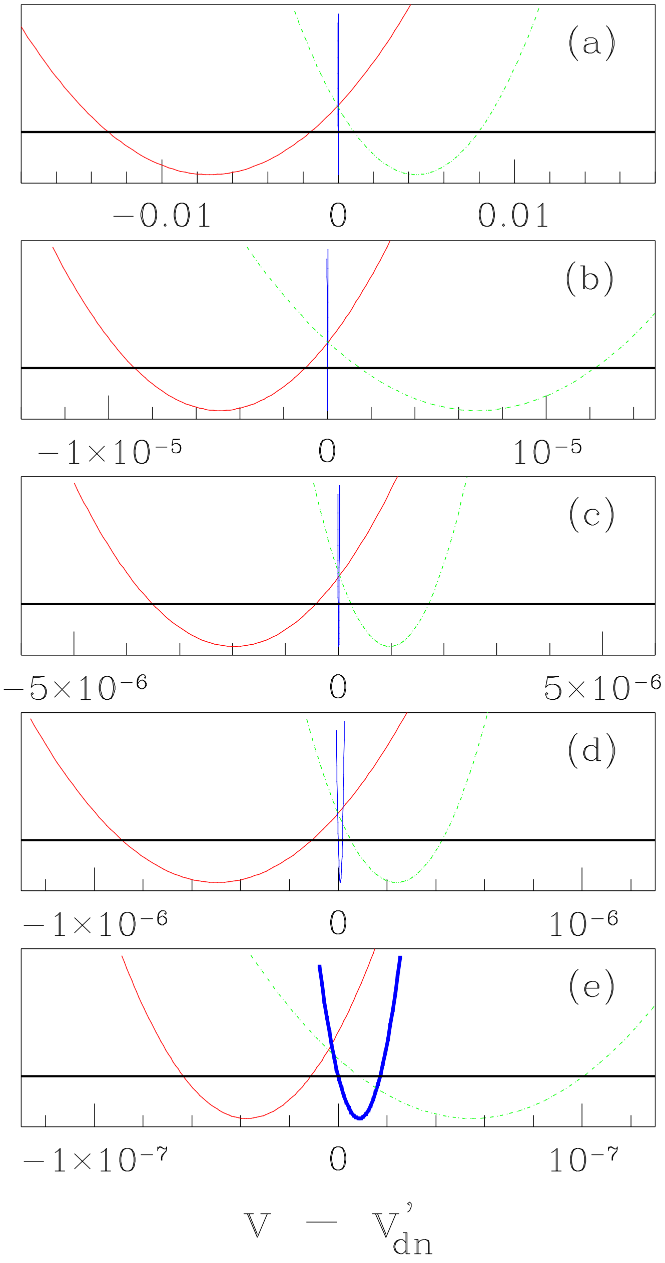

Figure 5.6: The degeneracy of the eigenvalues in the perfect fluid critical solution as $\Gamma \to \Gamma_{\rm dn}$. This figure's caption is continued on the next page.

Caption for Figure 5.6 (continued): The sonic point of the $\Gamma_{\rm dn} \simeq 1.8896244$ critical solution is a degenerate node, and this figure shows the approach to degeneracy by plotting the quadratic function in (5.41) as $\Gamma \to \Gamma_{\rm dn}$. The roots of (5.41) are possible values for v' at the sonic point, and when $\Gamma = \Gamma_{\rm dn}$ these roots are equal, $v'_{\rm dn}$. Each frame shows a parabola for three values of Γ. The parabolas on the left are for Γ less than $\Gamma_{\rm dn}$ ($\Gamma_<$), and the parabolas on the right are for Γ greater than $\Gamma_{\rm dn}$ ($\Gamma_>$). The center parabola has the same Γ in all five frames, namely $\Gamma_C \simeq \Gamma_{\rm dn}$ ($\Gamma_C = 1.88962441796875$), and one must be careful not to mistake it for a vertical axis in frames (a)–(c). For all Γ, the critical solution's $v'_{\rm sp}$ is the root closest to the center ($v'_{\rm dn}$). We estimate $\Gamma_{\rm dn} \simeq 1.8896244169921874$ ($v_{\rm sp} = -0.18696\ldots$, $v'_{\rm sp} = 1.7385\ldots$, and $\vartheta_{\rm sp} = 1.0000000002$), and for clarity, we use $v'_{\rm dn}$ to translate the horizontal axis such that the parabolas cluster around zero, and normalize the parabolas. In frame (a), $\Gamma_< = 1.889$ and $\Gamma_> = 1.890$. In (b), $\Gamma_< = 1.889624$ and $\Gamma_> = 1.889625$. In (c), $\Gamma_< = 1.88962425$ and $\Gamma_> = 1.8896245$. In (d), $\Gamma_< = 1.889624375$ and $\Gamma_> = 1.8896244375$. In (e), $\Gamma_< = 1.8896244140625$ and $\Gamma_> = 1.889624421875$. These calculations were done with *Maple V* using 30 digits and $\varepsilon = 10^{-18}$.

The CSS perfect fluid equations (5.26) can be linearized about the sonic point, resulting in a system we can write in the form

$$\boldsymbol{y}' = \mathcal{B}\,\boldsymbol{y}, \tag{5.44}$$

where $\mathcal{B}$ is a matrix which, generically, has two non-zero eigenvalues, which we label κ_1 and κ_2 (or simply κ when the distinction is irrelevant), with corresponding eigenvectors $\boldsymbol{V}_1$ and $\boldsymbol{V}_2$. Near the sonic point, the solution of the linear equations (5.44) can be written [12]

$$\boldsymbol{y} = \boldsymbol{y}_{\text{sp}} + k_1 \boldsymbol{V}_1\, \mathrm{e}^{\kappa_1 x} + k_2 \boldsymbol{V}_2\, \mathrm{e}^{\kappa_2 x}, \tag{5.45}$$

where k_1 and k_2 are arbitrary constants. The eigenvalues κ provide important information about the solutions near the sonic point, and we classify the sonic point according to the relative values of κ, as given by the quantity ϑ [100]

$$\vartheta = \frac{\Gamma + \sqrt{\eta}}{\Gamma - \sqrt{\eta}}. \tag{5.46}$$

Here,

$$\eta \equiv 4(3\Gamma - 2)U^2 - (3\Gamma^2 - 12\Gamma + 8)(1 - 4U), \tag{5.47}$$

and

$$U \equiv \frac{A - 1}{2\omega}. \tag{5.48}$$

The sonic point classification in terms of ϑ is shown in Table 5.1. Due to the facts that (i) ϑ is only a function of $\boldsymbol{y}_{\text{sp}}$, and (ii) the eigenvalues κ are related to v'_{sp} [53], we can make a connection to the linearized theory without explicit calculation of the eigenvalues.

Maison [86] and Goliath *et al.* [60] have previously concluded that the sonic points for $\Gamma \gtrsim 1.89$ are foci, with complex κ and v'_{sp}, and hence have suggested that physical self-similar solutions do not exist for $\Gamma \gtrsim 1.89$. (Hara *et al.* did not address the existence of solutions for $\Gamma \gtrsim 1.89$, but presumably also encountered

$\vartheta < 0$	saddle point
$\vartheta > 0$	nodal point
$\vartheta \in \mathbb{C}$	focal point
$\vartheta = 1$	degenerate nodal point

Table 5.1: Classifications of the sonic point using ϑ.

problems with their numerical analysis in that regime.) However, we find that $\vartheta > 0$ for *all* $\Gamma \gtrsim 1.89$ critical solutions, and thus conclude that the sonic-points for those solutions are nodes rather than foci. It seems plausible that this apparent contradiction stems from insufficient numerical precision in the earlier studies. To provide some specific evidence to back this claim, we have used *Maple* with 30 digits to find a critical solution for $\Gamma \simeq \Gamma_{\mathrm{dn}}$. Then, taking v_{sp} from this solution, we have calculated ϑ using both 30 digits in *Maple* and `FORTRAN` double precision. The `FORTRAN` calculation gave a complex ϑ—which would support the erroneous (we claim) conclusion that the sonic point is a focus. The same calculation done with greater precision using *Maple* shows that the sonic point is actually a node. In addition, we find that for $\Gamma < \Gamma_{\mathrm{dn}}$ (with Γ restricted to $\Gamma > 1.8$ for simplicity, and Γ_{dn} defined below), the critical solution's v'_{sp} is the maximum root of (5.41), while for $\Gamma > \Gamma_{\mathrm{dn}}$, the critical solution's v'_{sp} is the minimum root. As $\Gamma \to \Gamma_{\mathrm{dn}}$, the two roots v'_{sp} come closer together until they are equal for Γ_{dn}, as shown in Figure 5.6. Here the sonic point is a degenerate node with $\Gamma_{\mathrm{dn}} \simeq 1.8896244$ ($\eta_{\mathrm{dn}} = \mathrm{O}(\varepsilon)$, and $\vartheta_{\mathrm{dn}} = 1 + \mathrm{O}(\sqrt{\varepsilon})$).

5.2.4 $\Gamma = 2$

A continuously self-similar solution can also be found for $\Gamma = 2$ by following the same prescription for the $\Gamma < 2$ solutions. A solution by this method was unexpected because the sound speed for the $P = \rho$ fluid is equal to the speed of light, and the definition of sonic point does not seem to apply. However, a point where $\det \boldsymbol{J} = 0$ exists, and the solution can be found by demanding regularity at this point. This solution, shown in Figure 5.9 is qualitatively different from the $\Gamma < 2$ solutions, as this solution, for $x > 0$, violates the physical fluid properties as $\rho < 0$ and $|v| > 1$. However, this solution does match the dynamically calculated critical solution for $x \lesssim 0$. Using these results, Brady and Gundlach [17] have identified a continuously self-similar EMKG solution which matches the CSS prefect fluid solution. Further discussion is included in Section 5.3.3.

5.3 The full PDE critical solutions

A crucial check that the CSS solutions of the reduced fluid equations are indeed the unique critical solutions involves a comparison with the solutions of the full Einstein-fluid equations. Using the relativistic fluid code described in Chapter 4, we have found the critical solutions for $1.05 \leq \Gamma \leq 2$ by evolving parameterized families of initial data. The greatest computational challenge in finding these solutions—especially as $\Gamma \to 2$—is the accurate treatment of flows with very large Lorentz factors. All of these solutions are continuously self-similar (CSS) and black hole formation for near-critical initial data begins with infinitesimal mass (Type II). This section compares the critical solutions calculated from the full Einstein-fluid equations with the ODE solutions found using the continuously self-similar *ansatz*. The calculation of the mass-scaling exponents is then discussed, followed by a brief consideration of critical solutions for the ideal-gas equation of state.

5.3.1 Initial data

We expect that the critical solutions in fluid collapse will be universal, in the sense that *any* family of initial data which generates families that "interpolate" between complete dispersal and black hole formation, should exhibit the same solution at the black hole threshold. We have thus focused attention on a specific form of initial data, which generates initially imploding (or imploding/exploding) shells of fluid.

Specifically, the energy density in the shells has a Gaussian profile,

$$\tau = \tau_o \exp\left[-(r - r_o)^2/\Delta^2\right] + K, \tag{5.49}$$

where the constant K—typically of magnitude $10^{-6}\tau_o$—represents a constant "background". It should be note that this background is used only in setting the initial data, and is not held fixed during the evolution—in particular K is *not* a floor as discussed in Section 3.9.1. The shells are either time-symmetric, or have an initial inward velocity which is proportional to r. Critical solutions were found by fixing r_o and Δ, and then tuning the pulse amplitude τ_o.

5.3.2 The transformation from r to x

The dynamic Einstein-fluid partial differential equations are solved with the code described in Chapter 4, using the areal coordinate r, and the proper time for an observer at infinity, t. To compare the dynamic critical solutions with the ODE solutions, which define the time s in terms of the sonic point, it is necessary to transform the solutions from one coordinate frame to another.

Let $t^\star$ be the coordinate time at which a near-critical solution reaches the origin in the evolution code. Then estimate the time

$$s = \ln(t^\star - t). \tag{5.50}$$

The sonic point is found by searching the solution for $\det \boldsymbol{J} = 0$, r_{sp}. The transformation to the logrithmic coordinate x is then

$$x = \ln\left(\frac{r}{r_{\text{sp}}}\right). \tag{5.51}$$

The time $t^\star$ can be found after by evolving the solution until it reaches the origin, or it can be estimated during the evolution by tracking a unique feature of the solution, e.g., the maximum of a.

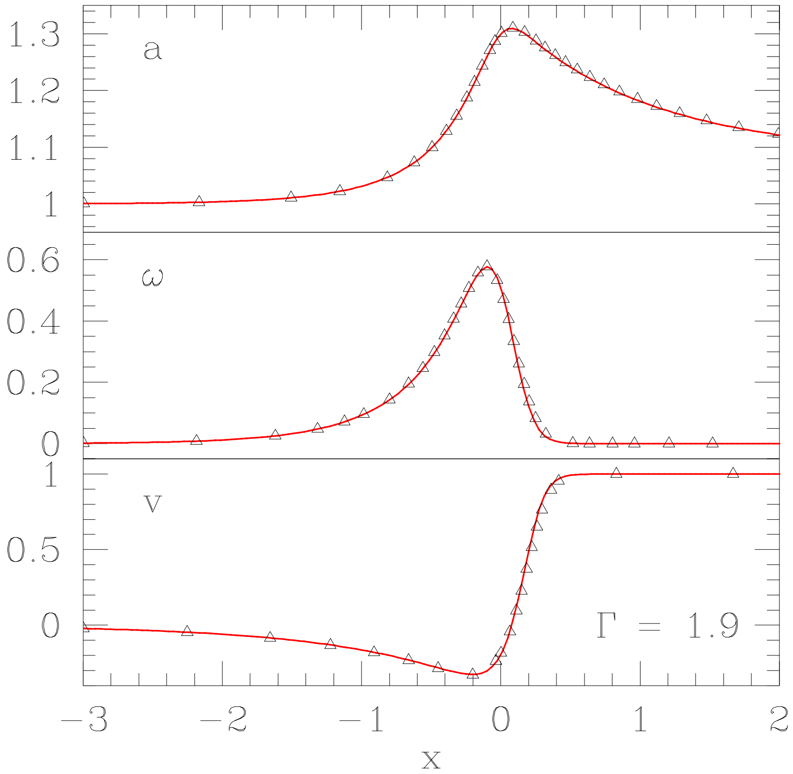

Figure 5.7: The $\Gamma = 1.9$ critical solution. The solid lines are the solution obtained by solving the ODEs, and the triangles indicate selected points from the solution of the PDEs.

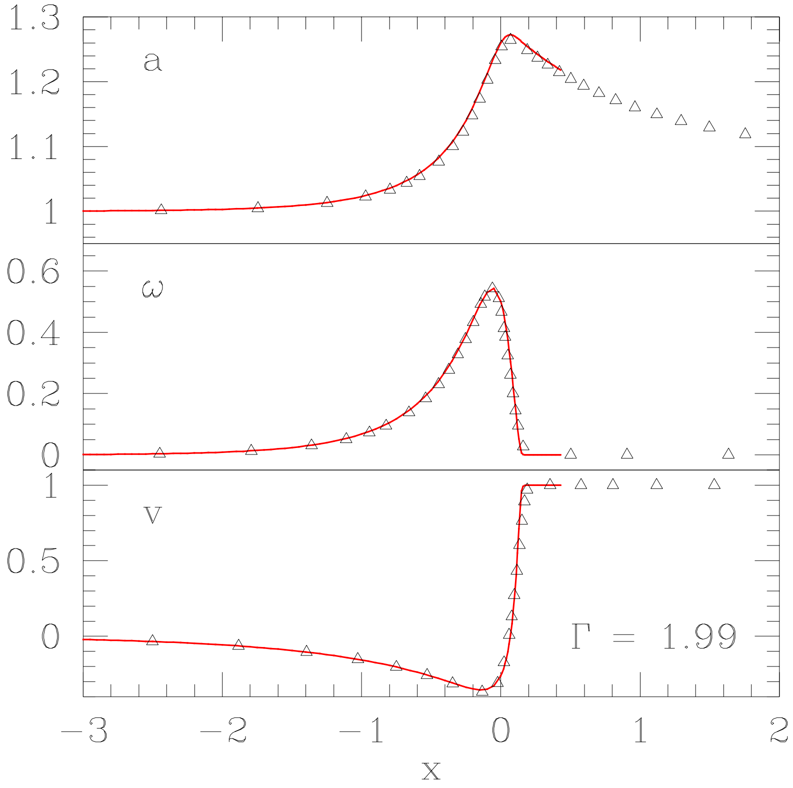

Figure 5.8: The $\Gamma = 1.99$ critical solution. The solid lines are the solution obtained by solving the ODEs, and the triangles are selected points from the PDE solution. The PDE solution underestimates the fluid density in the pulse leading to a corresponding error in a. This problem stems from a lack of resolution in the computational grid.

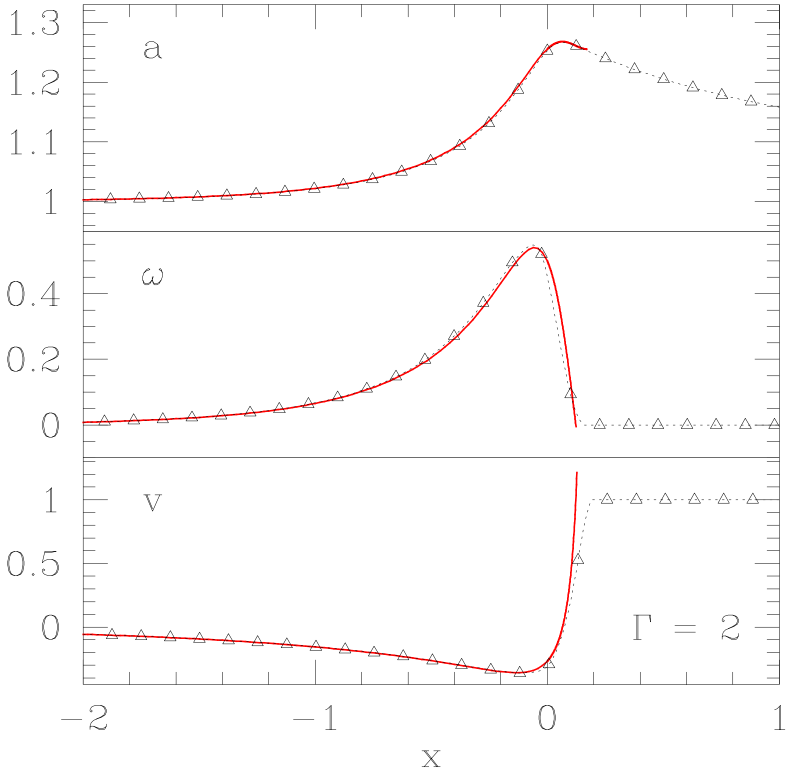

Figure 5.9: The $\Gamma = 2$ critical solution. The solid lines show the solution obtained from the ODEs, and the dotted lines with triangles show the solution obtained by solving the PDEs. Here some divergence between the PDE and ODE solutions can be seen. The PDE solution for ω lies *above* the ODE solution for $x < 0$, behavior opposite from that observed in the $\Gamma = 1.99$ solution. Beyond the sonic point, $x = 0$, the solutions become very different. Here the ODE solution becomes unphysical—in the traditional understanding of a perfect fluid—with $\omega < 0$ and $v > 1$. The PDE solution retains physical values for v and ω—$v < 1$ and $\omega > 0$—because these values are constrained to the physical regime in the evolution code [97].

5.3.3 Results

Figures 5.7–5.8 show the PDE critical solutions for $\Gamma = 1.9$ and $\Gamma = 1.99$ respectively, and include the ODE solutions for comparison. The $\Gamma = 1.9$ PDE and ODE solutions compare well, while Figure 5.8 indicates that the $\Gamma = 1.99$ PDE solution underestimates a and ω. From our experience with other critical solution searches, we feel that this discrepancy is the result of insufficient (spatial) resolution. As $\Gamma \to 2$, the fluid becomes increasingly dynamic, requiring greater precision to resolve the solution's relevant features, and it becomes increasingly expensive to calculate the critical solutions. The mass-scaling exponents γ shown in Table 5.2 provide a quick guide to the requisite dynamical range for a critical evolution as $\Gamma \to 2$. As $(p - p^\star)$ changes by n orders of magnitude, the relevant length scales in the solution, such as the radius of a black hole R_{BH}, change by γn orders of magnitude. The mass-scaling exponent for the stiff fluid, $\gamma \approx 1$, is almost three times larger than the scaling exponents for a radiation fluid ($\gamma \approx 0.36$) or massless scalar field ($\gamma_{\mathrm{SF}} \approx 0.37$), and simulations of the stiff fluid critical solutions require correspondingly more resolution.

The critical solutions for $\Gamma < 2$ all appear very similar; indeed one can imagine that one could smoothly transform a solution for a given Γ into a solution for a different Γ. At first glance, the $\Gamma = 2$ solution seems to fit nicely into this "family" of critical solutions parameterized by Γ—it is CSS, Type II, and differs only slightly from the $\Gamma = 1.99$ critical solution. However, the ODE solution (obtained by solving ODEs with the CSS *ansatz*) indicates that important differences may exist between the $\Gamma = 2$ and $\Gamma < 2$ critical solutions. As noted previously, we are unable to integrate the ODEs for Γ near 2 to arbitrarily large x. In these cases, we observe that the Lorentz factor, W, grows exponentially (see Figure 5.5), with a corresponding exponential decrease in ω, until `LSODE` is unable to satisfy the required error tolerances. We emphasize that in these $\Gamma < 2$ solutions, the fluid velocity and density retains its expected "physical" properties: $\omega > 0$, and $|v| < 1$. The $\Gamma = 2$ solution (see Figure 5.9), on the other hand, displays very different behavior. Instead of the exponential approach of $v \to 1$ and $\omega \to 0$, we find that ω and v pass through their expected physical bounds, giving $\omega < 0$ and $v > 1$.

The $\Gamma = 2$ PDE solution is also shown in Figure 5.9, and in contrast to the ODE solution, this solution retains "physical" values for the fluid variables. However, this property of the PDE solution is achieved by *fiat:* we impose a "floor" on the fluid variables such that $\rho > 0$ and $|v| < 1$ [97]. While the floor is used generally for $\Gamma \gtrsim 1.8$ without noticeable ill effect for $\Gamma < 2$, it is clear that the floor affects the $\Gamma = 2$ solution (as compared to the ODE solution) even in the regime where $\omega > 0$ and $|v| < 1$. The mathematical and physical significance of this observation is clearly an issue which requires more study—for example, can a vacuum region be matched to the $\Gamma = 2$ fluid in such a way that the fluid remains equivalent to a EMKG field [66]?

As is generally known, the stiff perfect fluid can be related to a scalar field. Motivated by the current results, a CSS scalar field solution has been found by Brady and Gundlach which matches the ODE $\Gamma = 2$ fluid solution [17]. A perturbation study of this EMKG solution gives that the mass-scaling exponent for this solution should be $\gamma \approx 0.94$, in good agreement with the "measured" value of $\gamma \approx 1$ using our evolution code. (See the discussion in Section 5.3.4 regarding the calculation of mass-scaling exponents by evolving initial data, and the limited precision we encounter as $\Gamma \to 2$.)

Finally, we note that the $\Gamma = 2$ critical solution is not related to other familiar EMKG solutions, such as the Roberts solution [108, 109], or the EMKG critical solution [29]. Both of these solutions have space-like gradients of the scalar field. Extracting data from a near-critical $\Gamma = 2$ solution, we have set equivalent initial data for an EMKG evolution and then have evolved the data with the Einstein/scalar equations of motion. However, the evolution of the scalar field does *not* seem to match the $\Gamma = 2$ perfect-fluid critical solution for any appreciable length of time, and naïve variations of the initial data apparently produce the usual DSS scalar field critical solution at the black-hole threshold.

5.3.4 Mass scaling

Mass-scaling exponents γ are found by evolving near-critical initial data sets which lead to the formation of black holes. In our coordinate system, black hole formation is signaled by

$$\left.\frac{2m(r,t)}{r}\right|_{R_{\mathrm{BH}}} \to 1, \tag{5.52}$$

where R_{BH} is the (areal) radius of the black hole. The black hole mass is then simply given by

$$M_{\mathrm{BH}} = \frac{R_{\mathrm{BH}}}{2}. \tag{5.53}$$

As mentioned earlier, all of the critical solutions discussed here are Type II, meaning that the associated black-hole transition begins with infinitesimal mass holes. As a typical example of our results, the mass-scaling of near-critical solutions for $\Gamma = 2$ is shown in Figure 5.10.

The simple adaptive grid that we use [97] did not allow us to calculate M_{BH} with sufficient accuracy to justify searching for $p^\star$ to the limit of machine precision in a reasonable amount of time. We therefore estimated $p^\star$ by searching for the best linear fit to

$$\ln M_{\mathrm{BH}} \propto \gamma \ln |p - p^\star| \,. \tag{5.54}$$

The totality of mass-scaling exponents γ calculated from our simulation data are shown in Table 5.2, along with the values predicted from Maison's perturbative calculations [86]. (These exponents for $\Gamma \leq 1.98$ are similar to those found independently by Brady and Cai [16].) For a variety of reasons, estimation of the error (no doubt overwhelmingly "systematic") in the mass-scaling exponents is not an easy task, and we therefore have provided estimates of γ which are conservative in their use of "significant" digits. One notes that as $\Gamma \to 2$, the mass-scaling exponent $\gamma \to 1$.

One possible source of error in the measurements of γ is the floor (δ) used in the fluid code (see Section 3.9.1 and Section 4.4.1). The effect of the floor's magnitude was tested for $\Gamma = 2$ by measuring γ for different values of δ, specifically, $\delta = 10^{-6}$, $\delta = 10^{-8}$, and $\delta = 10^{-10}$. In this test the magnitude of δ did not strongly affect γ, as shown in Figure 5.11. Although γ appears to be insensitive to $||\delta||$, the mere existence of an enforced floor could significantly modify a solution, but this is something which needs further study. As a possible example, consider the critical solutions for $\Gamma = 2$ shown in Figure 5.9 above. These two solutions differ essentially where the ODE solution becomes unphysical with $v > 1$ and $\rho < 0$.

5.3.5 Ideal gas equation of state

The equation of state $P = (\Gamma - 1)\rho$ can be interpreted as the ultrarelativistic limit of the ideal-gas state equation

$$P = (\Gamma - 1)\rho_o \epsilon, \tag{5.55}$$

where ρ_o is the rest energy density and ϵ is the specific internal energy density. Following Ori and Piran [100], Evans [51] (and others), we have argued [97] that self-similar perfect fluid solutions *require* the ultrarelativistic equation of state. Let us now consider searching for critical solutions with the ideal-gas equation of state. Heuristically, one can describe critical behavior in terms of competition between the fluid's kinetic energy and gravitational potential energy. One might expect that in the critical solution, which stands just on the verge of black-hole formation, $P \gg \rho_o$, and that the critical solutions for the ideal-gas state equation would correspond to the ultrarelativistic equation of state solutions. Using an evolution code, we

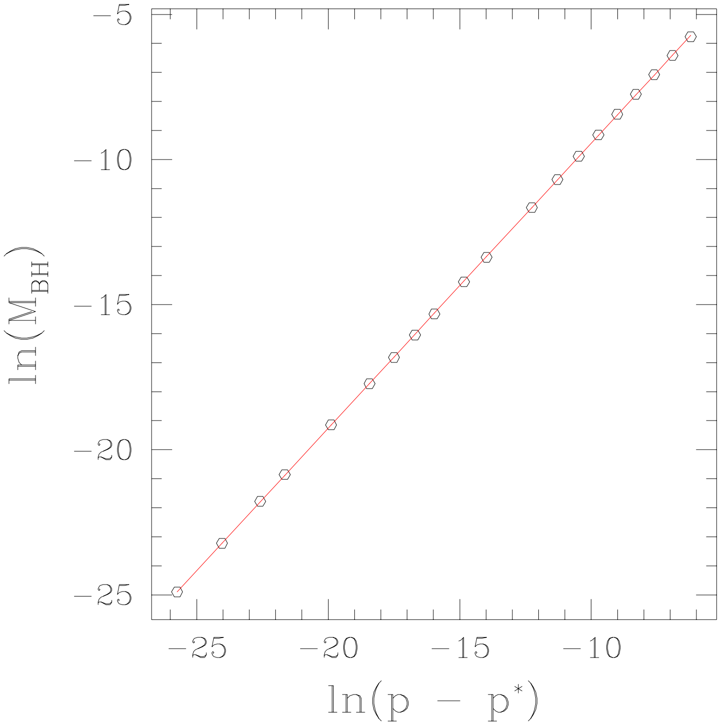

Figure 5.10: Illustration of black-hole mass scaling for the case $\Gamma = 2$. In this instance—as for all values of Γ considered here—the critical behavior is Type II, allowing one to create arbitrarily small black holes through sufficient fine-tuning of initial data.

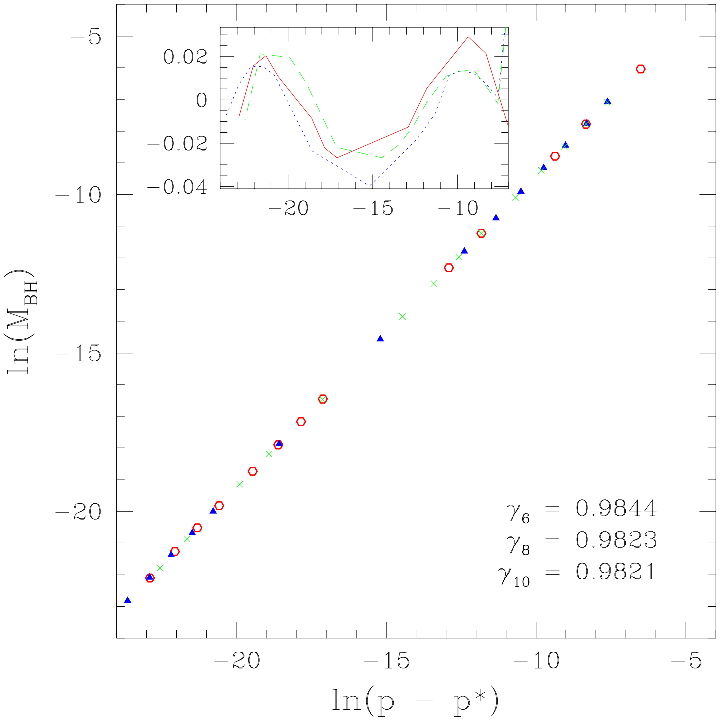

Figure 5.11: The black hole mass as a function of critical parameter for $\Gamma = 2$ super-critical evolutions with three different floors with the same resolution. The crosses show the black hole masses calculated when $\delta = 10^{-6}$, the triangles when $\delta = 10^{-8}$, and the circles when $\delta = 10^{-10}$. The black-hole mass is a simple function of the critical parameter (Section 5.1.1), and this figure shows that floor does not strongly affect measurements of the mass-scaling parameter from super-critical evolutions. In the lower right corner, we show the mass-scaling coefficients obtained from a least-squares fit of the data, the subscript on γ indicating the floor. Note that these coefficients are indicative only of the insensitivity to the floor. In particular, they do not constitute our best measurement of γ for $\Gamma = 2$, which is obtained from a higher-resolution solution. The inset in the upper left corner shows the deviation of the data points from the least squares fit. The solid line when $\delta = 10^{-10}$, the dotted line when $\delta = 10^{-8}$, and the dashed line when $\delta = 10^{-6}$. Again this deviation shows no dependence on the floor magnitude.

Γ	measured γ	calculated γ
1.05	0.15	0.1478
1.1	0.19	0.1875
1.2	0.26	0.2614
1.3	0.33	0.3322
4/3	0.36	0.3558
1.4	0.40	0.4035
1.5	0.48	0.4774
1.6	0.56	0.5556
1.7	0.64	0.6392
1.8	0.73	0.7294
1.888	0.82	0.8157
1.89	0.82	—
1.9	0.83	—
1.92	0.86	—
1.95	0.9	—
1.99	1	—
2	1	—

Table 5.2: The mass-scaling exponent γ as a function of the adiabatic constant Γ. The second column shows the mass-scaling exponents estimated from $M_{\mathrm{BH}}(p)$ by evolving near-critical ($p \to p^\star$) initial data. For comparison, “calculated” exponents—computed from perturbative calculations—are also listed.

have found critical solutions for the ideal-gas state equation, and these solutions *do* match the corresponding solutions with the ultrarelativistic equation of state. As an example, the critical solution for a $\Gamma = 1.4$ ideal gas is compared with the precisely CSS ultrarelativistic $\Gamma = 1.4$ solution in Figure 5.12. Additional evidence that near-critical ideal gas solutions are ultrarelativistic is shown in Figure 5.13.

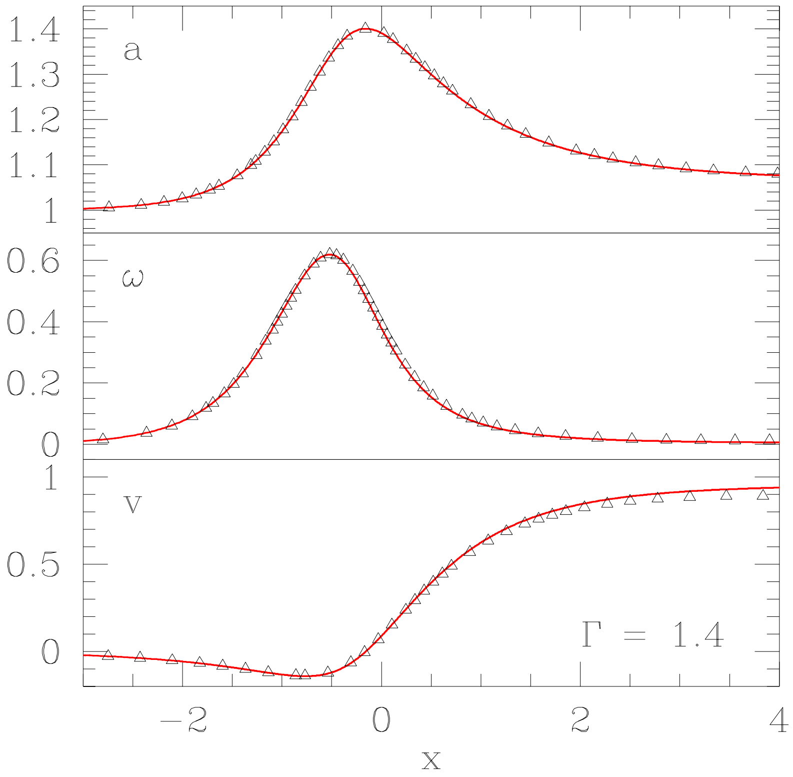

Figure 5.12: A comparison of the critical solutions for the ideal-gas and ultrarelativistic equations of state for $\Gamma = 1.4$. The solid lines are solutions obtained by solving the ODEs with the ultrarelativistic equation of state, and the triangles are selected points from the PDE solution which uses the ideal-gas equation of state. The ideal gas is in the ultrarelativistic limit near the infalling matter (see Figure 5.13), and the two solutions correspond in this region. At large r the ultrarelativistic approximation breaks down, and the solutions differ. The ideal-gas equation of state solution was computed using a code similar to the one described in [97].

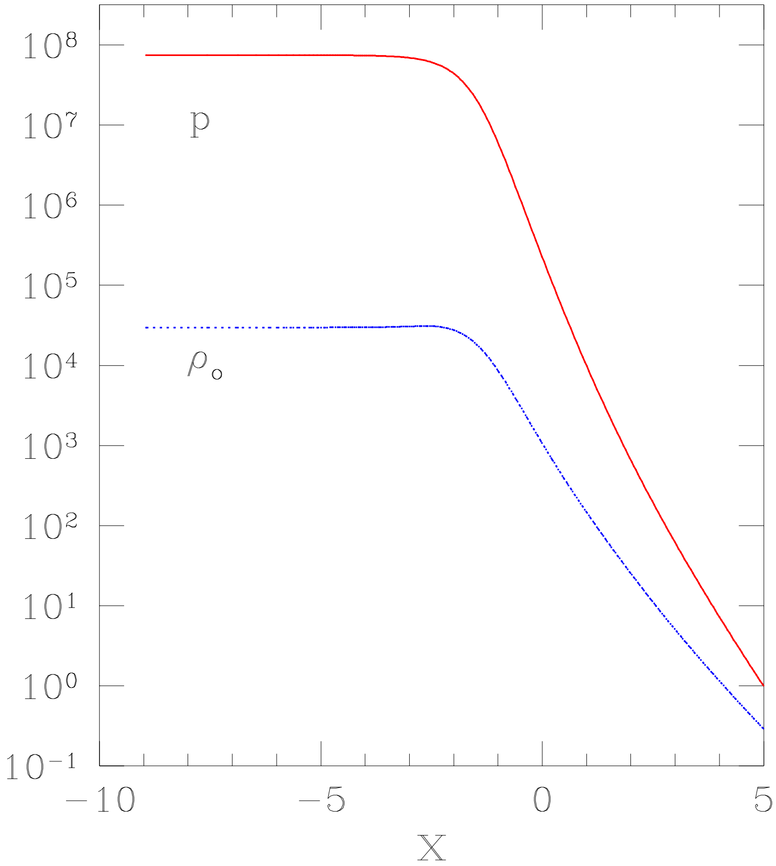

Figure 5.13: P and ρ_o are shown at the moment of maximum compression in this log-log plot of a marginally subcritical evolution of a $\Gamma = 1.4$ ideal gas. Note that near the origin, the ideal gas is clearly in the ultrarelativistic limit where $P \gg \rho_o$. At large r (X), the ultrarelativistic limit no longer holds, and the solution does not match one computed using the ultrarelativistic equation of state.

Chapter 6

A two-dimensional fluid code

The previous chapter described the critical solutions for a scale-free perfect fluid in spherical symmetry. While this work essentially completes our understanding of perfect fluid critical phenomena in spherical symmetry, research on critical collapse in axial symmetry, including angular momentum, is just beginning. Gundlach [67, 64] has examined the stability properties of the spherically symmetric, continuously self-similar solutions to axisymmetric perturbations. He found that the spherically symmetric solutions constructed with the CSS *ansatz* have a single unstable mode, which is spherically symmetric, for $1.123 \lesssim \Gamma \lesssim 1.446$. Therefore, these solutions are presumably the critical solutions for parameterized families of axisymmetric initial data. However, the spherically symmetric CSS solutions for $\Gamma \lesssim 1.123$ and $\Gamma \gtrsim 1.446$ apparently have additional, non-spherical growing modes, and thus are not expected to be critical solutions for general, axisymmetric initial data. By definition, a critical solution—that solutions separates dispersing solutions from those with a black hole—exists as long as interpolating families of initial data can be generated. However, the characteristics of these solutions for generic, axisymmetric initial data are unknown at this time.

The sure way to learn about the critical solutions for axisymmetric systems is to study the full dynamical equations. The computational demands of such a project are very high, requiring adaptive mesh refinement on parallel computational platforms. Choptuik and collaborators are beginning to develop the computational framework for this ambitious project. (Marsa [88] developed a high-level numerical language, RNPL, for efficiently describing finite difference equations. The RNPL compiler generates either FORTRAN 77 or C computer code to solve the difference equations. Liebling [83] reported on preliminary efforts to solve the general relativistic constraint equations for axisymmetric systems using multi-grid methods.) The study of dynamic critical phenomena will involve various models, such as the massless Klein-Gordon field that was pivotal in the discovery of critical phenomena in gravitational collapse [29]. As a step towards including the perfect fluid model in these studies, I have written a new two-dimensional perfect fluid code. This code builds on the same techniques used for the spherically symmetric codes, and preliminary tests, included here, indicate that it will accurately solve highly relativistic fluid systems, and maintain regularity along the symmetry axis of cylindrical coordinates. The code uses the full ADM metric, thus allowing an arbitrary geometry whose equations of motion are two-dimensional. Godunov-type numerical methods are incorporated with *dimensional splitting,* where the equations are solved alternately along one dimension then the other. This chapter reports the current status of the two-dimensional code, and presents some preliminary shock tube tests.

While a study of axisymmetric critical phenomena provides one motivation for pursuing this research, many other outstanding problems involving general relativistic, axisymmetric fluids remain. For example, open questions remain in estimating the gravitational waves emitted in the head-on collision of neutron stars [94, 120].

A similar effort to develop an axisymmetric perfect fluid code using Godunov-type numerical methods was begun by Brandt *et al.* [21]. The geometric equations were solved using an earlier code of Brandt and Seidel, which treated the vacuum Einstein equations in scenarios involving a central black hole [18, 19, 20]. Recently, Alcubierre *et al.* [1] developed a new regularization technique for the axis in cylindrical coordinates, where region near the axis is differenced in Cartesian coordinates.

6.1 The fluid equations for the two-dimensional code

The perfect fluid equations of motion were written in conservative form compatible with the ADM Einstein equations in Section 2.5. These equations are

$$\frac{1}{\sqrt{-g}}\left[\partial_t\sqrt{\gamma}\,\mathbf{q}+\partial_i\sqrt{-g}\,\mathbf{f}^i\right]=\mathbf{\Sigma}(\mathbf{q}), \tag{6.1}$$

where

$$\mathbf{q}=\begin{bmatrix} D \\ S_j \\ \tau \end{bmatrix}. \tag{6.2}$$

Before beginning developing a numerical algorithm to solve these equations, the leading $(-g)^{-1/2}$ factor, one the left hand side of the equations, must give us pause. This term may become singular in some coordinate systems, such as spherical symmetry, where $(-g)^{-1/2} \propto 1/r^2$. In such cases, errors in a naïve finite difference scheme are amplified near the singularity of the coordinate system, causing the scheme to become unstable. For the spherically symmetric code described in Chapter 4, the difference equations were rewritten to alleviate this problem (see Section 4.4.4). Ideally, the two-dimensional code would be somewhat generic, allowing different coordinate systems to be used with a minimum of effort. This requires coordinate-specific fixes of the discretized equations to be kept to a minimum. An alternate strategy [55], is to incorporate the leading $(-g)^{-1/2}$ term into the source, $\mathbf{\Sigma}$, and to adopt "densitized" conservative variables

$$\hat{\mathbf{q}} \equiv \sqrt{\gamma}\mathbf{q}, \tag{6.3}$$

and similar definitions of the flux and source

$$\hat{\mathbf{f}}^i \equiv \sqrt{\gamma}\,\mathbf{f}^i, \tag{6.4}$$

$$\hat{\mathbf{\Sigma}} \equiv \sqrt{-g}\,\mathbf{\Sigma}. \tag{6.5}$$

The densitized quantities are thus

$$\hat{\mathbf{q}} = \begin{bmatrix} \sqrt{\gamma}D \\ \sqrt{\gamma}S_j \\ \sqrt{\gamma}\tau \end{bmatrix}, \tag{6.6}$$

$$\hat{\mathbf{f}}^j = \begin{bmatrix} \hat{D}\left(v^i - \dfrac{\beta^i}{\alpha}\right) \\ \hat{S}_j\left(v^i - \dfrac{\beta^i}{\alpha}\right) + \sqrt{\gamma}\,P{\delta^i}_j \\ \hat{\tau}\left(v^i - \dfrac{\beta^i}{\alpha}\right) + \sqrt{\gamma}\,Pv^i \end{bmatrix}, \tag{6.7}$$

and

$$\hat{\mathbf{\Sigma}} = \begin{bmatrix} 0 \\ \sqrt{\gamma}\,T^{\mu\nu}\left(\partial_\mu g_{\nu j} - {\Gamma^\delta}_{\nu\mu} g_{\delta j}\right) \\ \sqrt{-g}\,\left(T^{\mu 0}\partial_\mu \ln\alpha - T^{\mu\nu}{\Gamma^0}_{\nu\mu}\right) \end{bmatrix}. \tag{6.8}$$

With this change to densitized variables, the fluid equations can generally be written

$$\partial_t\hat{\mathbf{q}} + \partial_1\left(\alpha\hat{\mathbf{f}}^1\right) + \partial_2\left(\alpha\hat{\mathbf{f}}^2\right) = \hat{\mathbf{\Sigma}}(\hat{\mathbf{q}}). \tag{6.9}$$

These are the equations solved by the two-dimensional code. As with the spherical code, we also remove the pressure term from $\hat{\mathbf{f}}$, and add it to the source term.

6.2 Numerical methods

The fluid equations are solved using a second-order Gudonov method for conservation laws, as described in Chapter 3. The development of multi-dimensional numerical schemes for conservation laws is still an area of active research. However, for simplicity we employ a relatively simple method known as dimensional splitting, wherein we calculate the numerical fluxes along each coordinate direction independently. A more elaborate method would also include dimensional coupling terms, which we ignore in dimensional splitting. Our scheme is improved by using a two-step, predictor-corrector method to integrate the equations in time. Thus information from both coordinate directions is included in the final corrector step. As before with the spherically symmetric codes, a linearized Riemann solver is used to calculate the numerical flux functions, and we discretize the equations using the method of lines. The equations are then time-integrated using the second-order modified Euler method.

While the code is currently implemented in Minkowski space, the future coupling with general relativistic code guides many of the design decisions. The code is being developed using the RNPL numerical programming language [88]. RNPL handles all memory management, I/O, and generates the driver routines. The fluid updates and associated utilities are written by hand.

The fluid equations are evolved on a static background, and when solving a dynamic system, the fluid equations and geometric equations will be successively solved. Although the code is written for a general metric, currently only diagonal submetrics are supported: $\gamma_{ij} = 0$ for $i \neq j$. This is primarily to conserve memory during the initial testing stages, allowing the code to be run more efficiently on workstations. The boundary and regularity conditions are implemented via ghost cells along all four boundaries. Currently outflow, fixed, and reflection boundary conditions are available.

6.2.1 Calculating the primitive variables

The specializations for ultrarelativistic flow discussed for spherical codes (see Section 3.9), where the transformation from conservation to primitive variables is carefully constructed to minimize round-off error, have not been completed in the two-dimensional code. Here, the primitive variables $\mathbf{w}$ are found by solving a transcendental equation for P, using an iterative Newton root finder. The algorithm is shown in Figure 6.1.

6.2.2 Riemann initial value problem tests

The first real tests of a fluid code are generally Riemann shock tube tests in flat space. The metric in Cartesian coordinates is

$$\mathrm{d}s^2 = -\mathrm{d}t^2 + \mathrm{d}x^2 + \mathrm{d}y^2 + \mathrm{d}z^2 \tag{6.10}$$

The fluid source terms are zero

$$\mathbf{\Sigma} = \mathbf{0}. \tag{6.11}$$

Shock tube tests are shown in Figures 6.2–6.4. In the tests, the initial discontinuity is placed along a diagonal of a square grid, and the solution is examined along the opposite diagonal.

6.3 Axial symmetry

In this section the fluid equations are written for the axisymmetric systems in canonical cylindrical coordinates, with the line element

$$\mathrm{d}s^2 = -\mathrm{d}t^2 + \mathrm{d}R^2 + \mathrm{d}z^2 + R^2\mathrm{d}\phi^2. \tag{6.12}$$

All variables are assumed to be functions of t, R, and z: $f = f(R, z, t)$. A test of the fluid code using cylindrical coordinates is given in Chapter 7 for a fluid coupled to scalar gravity.

The only non-zero Christoffel symbols for this metric are

$$\Gamma^{\phi}{}_{\phi R} = \frac{1}{R}, \tag{6.13}$$

$$\Gamma^{R}{}_{\phi\phi} = -R. \tag{6.14}$$

```
$\hat{P}_{\mathrm{new}} = \sqrt{\gamma}\,P^{n}$ (the initial guess)

do

    $\hat{P} = \hat{P}_{\mathrm{new}}$

    $\left\{ v^{i} = \dfrac{\hat{S}^{i}}{\hat{\tau} + \hat{D} + \hat{P}} \right\}$

    $W^{2}(\hat{P}) = \dfrac{(\hat{\tau} + \hat{D} + \hat{P})^{2}}{(\hat{\tau} + \hat{D} + \hat{P})^{2} - \hat{S}_{i}\hat{S}^{i}}$

    $W'(\hat{P}) = \left(1 - W^{2}\right) \left[ \left( \hat{\tau} + \hat{D} + \hat{P} \right)^{2} - \hat{S}_{i}\hat{S}^{i} \right]^{1/2}$

    $\left\{ \rho_{o} = \dfrac{\hat{D}}{\sqrt{\gamma}\,W} \right\}$

    $f(\hat{P}) = \hat{D}W + \dfrac{\Gamma}{\Gamma - 1}\hat{P}W^{2} - \hat{P} - \hat{\tau}$

    $f'(\hat{P}) = \left( \hat{D} + \dfrac{2\Gamma}{\Gamma - 1}\hat{P}W \right) W' + \dfrac{\Gamma}{\Gamma - 1}W^{2} - 1$

    $\hat{P}_{\mathrm{new}} = \hat{P} - \dfrac{f}{f'}$

while ( $|\hat{P}_{\mathrm{new}} - \hat{P}| < \epsilon$ )

$P^{n+1} = (\gamma)^{-1/2}\,\hat{P}_{\mathrm{new}}$
```

Figure 6.1: Pseudo-code for the primitive variable solver using Newton's method in the two-dimensional code for the ideal-gas equation of state. A prime indicates differentiation with respect to $\hat{P}$. The updates for v_i and ρ_o are indicated by the quantities in braces, $\{\cdot\}$, and are not actually calculated in the Newton solver loop.

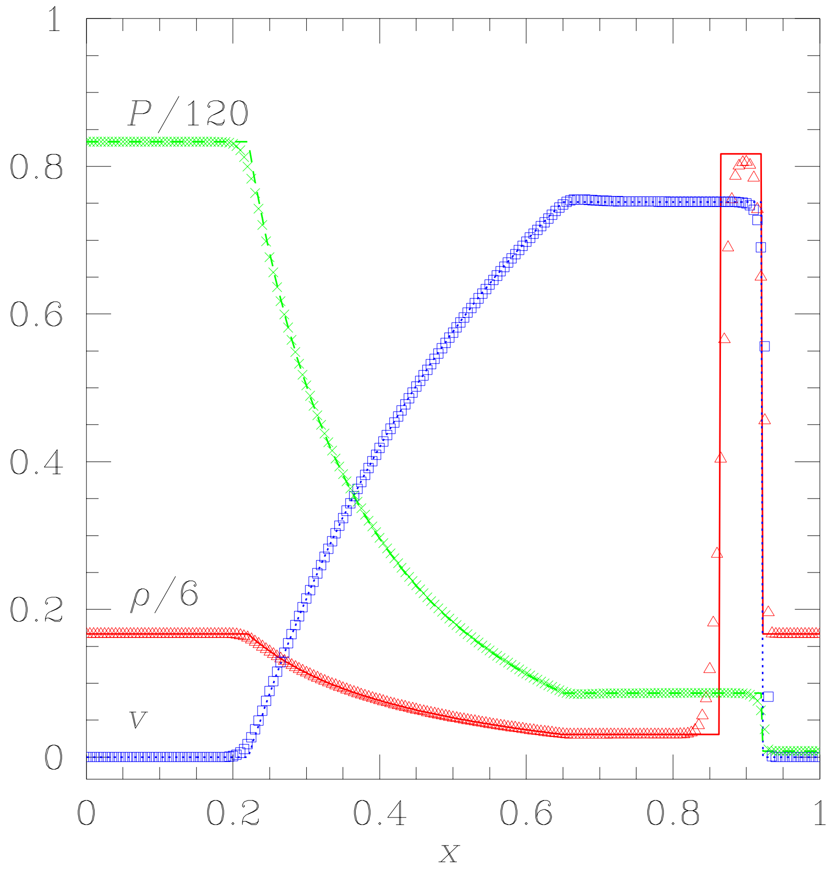

Figure 6.2: A Riemann shock tube test performed with the 2D code with a $\Gamma = 4/3$ fluid. The initial left state is $\rho_\ell = 1$, $v^i_\ell = 0$, $P_\ell = 100$; the initial right state is $\rho_r = 1$, $v^i_r = 0$, $P_r = 1$. The initial discontinuity is placed along one diagonal, and the 1-dimensional solution is viewed along the opposite diagonal. The solid lines show the exact solution, and the evolution solution is indicated by triangles (ρ), squares ($v = \sqrt{(v^x)^2 + (v^y)^2}$), and crosses ($P$). The evolution solution is calculated with 200×200 zones on $x \in [0, \sqrt{2}/2]$ and $y \in [0, \sqrt{2}/2]$, with a Courant number of $1/2$.

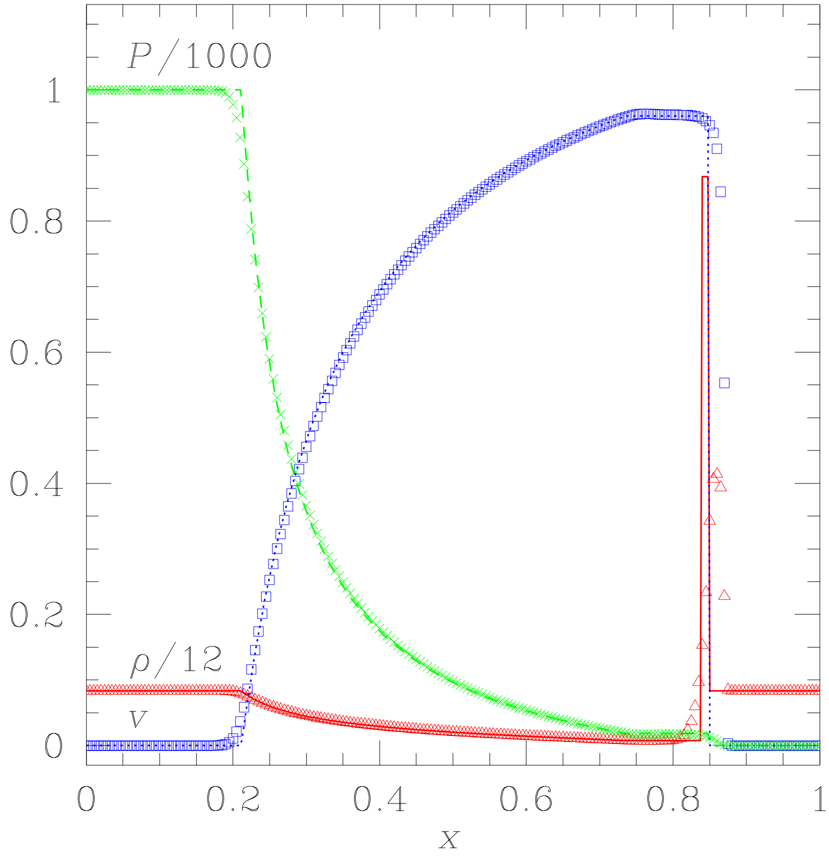

Figure 6.3: A Riemann shock tube test performed with the 2D code with a $\Gamma = 4/3$ fluid. The initial left state is $\rho_\ell = 1$, $v^i_\ell = 0$, $P_\ell = 1000$; the initial right state is $\rho_r = 1$, $v^i_r = 0$, $P_r = 0.01$. The initial discontinuity is placed along one diagonal, and the 1-dimensional solution is viewed along the opposite diagonal. The solid lines show the exact solution at $t = 0.353553391$, and the evolution solution is indicated by triangles (ρ), squares ($v = \sqrt{(v^x)^2 + (v^y)^2}$), and crosses ($P$). The evolution solution is calculated with 200×200 zones on $x \in [0, \sqrt{2}/2]$ and $y \in [0, \sqrt{2}/2]$, with a Courant number of $1/2$.

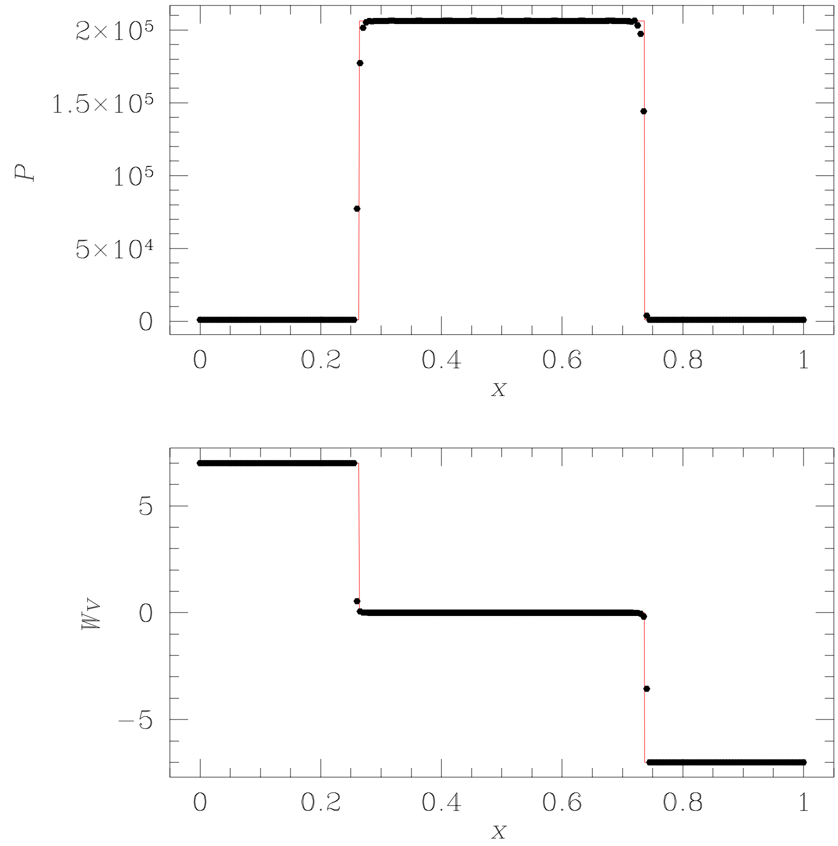

Figure 6.4: Shock heating of a $\Gamma = 5/3$ fluid calculated with the 2D code. The initial left state is $\rho_\ell = 1$, $v^x_\ell = 0.7$, $v^y_\ell = 0.7$, $v^z_\ell = 0$, and $P_\ell = 1000$; the initial right state is $\rho_r = 1$, $v^x_r = -0.7$, $v^y_r = -0.7$, $v^z_r = 0$, and $P_r = 1000$. The initial discontinuity is placed along one diagonal, and the 1-dimensional solution is viewed along the opposite diagonal. The solid lines show the exact solution at $t = 0.353553391$, and the evolution solution is indicated by triangles (ρ), squares ($v = \sqrt{(v^x)^2 + (v^y)^2}$), and crosses ($P$). The evolution solution is calculated with 200×200 zones on $x \in [0, \sqrt{2}/2]$ and $y \in [0, \sqrt{2}/2]$, with a Courant number of 1/2. My exact Riemann solver for the ideal gas equation of state was unable to find the solution for this initial data, so the exact solution shown here is for the ultrarelativistic state equation.

The densitized conservation variables are

$$\hat{\mathbf{q}} = \begin{bmatrix} RD \\ RS_R \\ RS_z \\ RS_\phi \\ R\tau \end{bmatrix}. \tag{6.15}$$

The numerical fluxes are

$$\hat{\mathbf{f}}^R = \begin{bmatrix} \hat{D}v^R \\ \hat{S}_R v^R + RP \\ \hat{S}_z v^R \\ \hat{S}_\phi v^R \\ (\hat{\tau} + RP)v^R \end{bmatrix}, \tag{6.16}$$

and

$$\hat{\mathbf{f}}^z = \begin{bmatrix} \hat{D}v^z \\ \hat{S}_R v^z \\ \hat{S}_z v^z + RP \\ \hat{S}_\phi v^z \\ (\hat{\tau} + RP)v^z \end{bmatrix}, \tag{6.17}$$

and the source term is

$$\hat{\mathbf{\Sigma}} = \begin{bmatrix} 0 \\ \frac{1}{R}\hat{S}_\phi v^\phi + P \\ 0 \\ -R\hat{S}_R v^\phi \end{bmatrix}. \tag{6.18}$$

$$\partial_t \hat{\mathbf{q}} + \partial_R \hat{\mathbf{f}}^R + \partial_z \hat{\mathbf{f}}^z = \hat{\mathbf{\Sigma}} \tag{6.19}$$

The regularity conditions for the conservation variables can be derived by using the method of Bardeen and Piran [8]. Regularity is ensured by requiring that all Cartesian tensor components can be expanded in non-negative powers of the Cartesian coordinates x, y, and z. In cylindrical coordinates, we label the N_R grid points along R with R_i, where $i = 1, \ldots, N_R$. The symmetry axis coincides with the second cell, $R_2 = 0$. The $i = 1$ and $i = 2$ cells are treated as ghost cells in the update routines (see Section 3.8). The regularity conditions in discrete form are

$$\begin{aligned}
&\hat{D}_1 = \hat{D}_3 && \hat{D}_2 = 0 \\
&(\hat{S}_R)_1 = -(\hat{S}_R)_3 && (\hat{S}_R)_2 = 0 \\
&(\hat{S}_z)_1 = (\hat{S}_z)_3 && (\hat{S}_z)_2 = 0 \\
&(\hat{S}_\phi)_1 = (\hat{S}_\phi)_3 && (\hat{S}_\phi)_2 = 0 \\
&\hat{\tau}_1 = \hat{\tau}_3 && \hat{\tau}_2 = 0.
\end{aligned} \tag{6.20}$$

The outflow boundary conditions described in Section 3.8 are used on the other grid boundaries, and are also implemented with ghost cells.

6.4 Conclusion

The two-dimensional fluid code of this chapter was tested in slab symmetry (Cartesian coordinates) with the Riemann initial value problem. While the code can also use cylindrical coordinates, there are no exact solutions for an axially symmetric perfect fluid in flat space for direct comparison. In the following chapter, we introduce scalar gravity, a simplified model for gravity using a single scalar field. This model is simple to implement, and allows us to test the performance of the two-dimensional code in cylindrical coordinates for problems with significant “self-gravitation.”

Chapter 7

Scalar gravity

Eventually, the two-dimensional fluid code described in Chapter 6 will be used to study the fully general relativistic problems mentioned in the introduction, such as the critical behavior of axisymmetric fluids, and neutron star systems. However, solvers for the Einstein equations are just now being written, and will not be finished for some time. To sample the physics we wish to address, we turn now to a simple gravitation model known as *scalar gravity.* However, it must be stressed at the outset that the results presented here are *preliminary,* and additional study is required for a complete understanding.

Before choosing a new gravitational model, we might first consider Newtonian gravity. Newtonian gravity is completely described by a scalar field, φ, which satisfies

$$\nabla^2\varphi = 4\pi G\rho_o. \tag{7.1}$$

The gravitational force is proportional to $\vec{\nabla}\varphi$, and the acceleration of a test-body due to the field φ is

$$\frac{\mathrm{d}^2\vec{\boldsymbol{x}}}{\mathrm{d}t^2} = -\vec{\nabla}\varphi. \tag{7.2}$$

Equation (7.1) for φ is an elliptic equation, and thus any change in the matter distribution is communicated instantaneously throughout space, a result directly at odds with the fundamental assumptions of special relativity. Thus, Newtonian gravity can not be self-consistently combined with a relativistic fluid. Perhaps the obvious way to modify (7.1) such that it is consistent with special relativity is

$$\Box\varphi = 4\pi G\, T_{\text{total}}, \tag{7.3}$$

where the elliptic Laplacian operator is replaced by the hyperbolic D'Alembertian operator

$$\Box \equiv \nabla_\mu \nabla^\mu, \tag{7.4}$$

and T_{total} is the trace of the stress-energy tensor. To be consistent with the equivalence of mass and energy in special relativity, φ now couples to the total stress-energy—including the contribution of φ)—in the space-time [75]. While this approach is not adopted here, the scalar gravity model is very similar in spirit.

Scalar gravity is introduced in Exercise 7.1 of Misner, Thorne and Wheeler [95], as the first of a series of three exercises illustrating the incompatibility of special relativity and gravitation (as either a scalar, vector, or tensor field). Like Newtonian gravity, scalar gravity is a flat spacetime theory, i.e., the *geometry* of space-time is fixed *a priori,* and the gravitational force is given as the gradient of a scalar potential, Ψ. Whereas the Newtonian potential satisfies the Poisson equation, scalar gravity obeys a nonlinear wave equation. An immediate consequence of the scalar gravity equation of motion is that scalar gravity contains "gravitational waves," even in spherical symmetry.

Scalar gravity was first investigated as a laboratory for numerical relativity by Shapiro, Teukolsky, and Scheel [118, 119, 113]. They examined spherical and axisymmetric systems for a collection of massive point particles, or dust, and were especially interested in extracting the gravitational waves from these distributions.

7.1 The scalar gravity model

Scalar gravity and its coupling with other matter is described by a Lagrangian. Although the perfect fluid equations can be derived using a variational principle, the method requires considerable effort (using four pseudo-potentials) [115]. For simplicity, we will first derive the scalar gravity equations for a point particle, and then simply extend the results to the known perfect fluid stress-energy tensor.

Let $z^{\alpha}(t_o)$ be the world line of a particle parameterized by the proper time, t_o. The particle has mass m and interacts with a field, Ψ, according to the action

$$I = \int \mathrm{d}^4 x \sqrt{-g}\, \mathcal{L}, \tag{7.5}$$

where the Lagrangian density, $\mathcal{L}$, is

$$\mathcal{L} = -\frac{1}{8\pi G} g^{\mu\nu} \nabla_\mu \Psi \nabla_\nu \Psi - e^{\Psi} \rho, \tag{7.6}$$

and G is the Newtonian gravitation constant, which we explicitly re-introduce. The comoving density is

$$\rho = m \int \mathrm{d}t_o \sqrt{-g}\, \delta^4 \left[x - z(x)\right]. \tag{7.7}$$

The field equation for Ψ can be found by varying the action with respect to Ψ,

$$\Box \Psi = 4\pi G e^{\Psi} \rho, \tag{7.8}$$

and the stress-energy of the particle-field system can be found by varying the action with respect to $g_{\mu\nu}$

$$T^{\mu\nu}_{\text{total}} = \frac{2}{(-g)^{1/2}} \frac{\delta[\mathcal{L}\sqrt{-g}]}{\delta g_{\mu\nu}}. \tag{7.9}$$

We find that the total stress-energy can be written

$$T^{\mu\nu}_{\text{total}} = \mathcal{S}^{\mu\nu} + \mathcal{T}^{\mu\nu}_{\text{dust}}, \tag{7.10}$$

where $\mathcal{S}^{\mu\nu}$ is the stress-energy of the scalar gravity field

$$\mathcal{S}_{\mu\nu} = \frac{1}{4\pi G} \left[\nabla_\mu \Psi \nabla_\nu \Psi - \frac{1}{2} g_{\mu\nu} \nabla^{\epsilon} \Psi \nabla_{\epsilon} \Psi \right], \tag{7.11}$$

and $\mathcal{T}^{\mu\nu}_{\rm dust}$ is the stress-energy of the particles

$$\mathcal{T}^{\mu\nu}_{\rm dust} = e^{\Psi}\left(\rho u^{\mu} u^{\nu}\right). \tag{7.12}$$

We define the trace of $\mathcal{T}^{\mu\nu}$,

$$\mathcal{T} \equiv \mathcal{T}^{\mu}{}_{\mu}, \tag{7.13}$$

and note that (7.8) can be written

$$\Box\Psi = -4\pi G \mathcal{T}_{\rm dust}. \tag{7.14}$$

This final equation gives the scalar gravity field equation in terms of an invariant, tensor quantity, and provides one method for extending this model to systems other than dust. Shapiro and Teukolsky [118] use (7.14) to couple the perfect fluid to scalar gravity without employing a variational principle, and we follow suit here.

In analogy with (7.12), we write the perfect fluid stress-energy as

$$\mathcal{T}_{\mu\nu} = e^{\Psi}\left[(\rho + P) u_{\mu} u_{\nu} + g_{\mu\nu} P\right], \tag{7.15}$$

using the previous definition for ρ as the *total* fluid energy density. The scalar gravity field equation when coupled to a perfect fluid becomes

$$\Box\Psi = 4\pi e^{\Psi}(\rho - 3P), \tag{7.16}$$

since we have from (7.15) that

$$\mathcal{T} = -e^{\Psi}(\rho - 3P). \tag{7.17}$$

The fluid equations of motion can be found in the standard way by considering projections of $\nabla \cdot \boldsymbol{\mathcal{T}} = 0$ which are parallel and perpendicular to the four-velocity. As usual, the parallel projection yields the energy equation The energy equation is

$$u_{\mu} \nabla_{\nu} T^{\mu\nu} = 0, \tag{7.18}$$

which can be written as an evolution equation for ρ

$$\frac{\mathrm{d}\rho}{\mathrm{d}t} = -(\rho + P)\nabla_a u^\mu - 3Pu^\mu \nabla_\mu \Psi \tag{7.19}$$

The perpendicular projection yields the Euler equation

$$h_{\mu\lambda}\nabla_\lambda T^{\mu\lambda} = 0, \tag{7.20}$$

which can be written as

$$(\rho + P)u^\nu \nabla_\nu u_\mu = h^\nu{}_\mu \left[\nabla_\nu P + \nabla_\nu \Psi(\rho - 2P)\right]. \tag{7.21}$$

Finally, the continuity equation retains its Minkowski form:

$$\nabla_\mu(\rho_o u^\mu) = 0. \tag{7.22}$$

Before continuing, we note one immediate difficulty with this coupling of scalar gravity to a perfect fluid. While the trace $\mathcal{T}_{\text{dust}}$ is negative definite, the trace $\mathcal{T}_{\text{fluid}}$ is *not,* and may be either positive or negative, depending on the relative magnitudes of ρ and P. When $\mathcal{T} > 0$, Ψ essentially couples to "negative matter." This possibility is considered more fully in the next section.

7.2 Potentially "negative" matter?

The perfect fluid was coupled to scalar gravity in the previous section by first considering dust, where the scalar field Ψ couples to the trace of the dust stress-energy tensor

$$\Box\Psi = 4\pi e^\Psi \rho = -4\pi \mathcal{T}_{\text{dust}}. \tag{7.23}$$

The fluid coupling proceeds simply by analogy,

$$\Box\Psi = -4\pi \mathcal{T}_{\text{fluid}}. \tag{7.24}$$

$\mathcal{T}_{\text{dust}}$ is a negative definite quantity, and $\Box\Psi$ thus couples to a positive definite source term. For the perfect fluid,

$$\mathcal{T}_{\text{fluid}} = -e^{\Psi}(\rho - 3P), \tag{7.25}$$

and the difference in sign between ρ and P opens the possibility that $\mathcal{T}$ may become positive, effectively coupling Ψ to negative matter.

Consider now the ideal-gas equation of state

$$P = (\Gamma - 1)\rho_o\epsilon, \tag{7.26}$$

and use the state equation to rewrite (7.25) as

$$\mathcal{T} = -e^{\Psi}\left(\rho_o + \frac{4-3\Gamma}{\Gamma-1}P\right). \tag{7.27}$$

The sign of $\mathcal{T}$ is a function of ρ_o, P, and most importantly, Γ. $\mathcal{T}$ is negative definite, as for dust, only for $\Gamma \leq 4/3$. For $\Gamma > 4/3$, the sign of $\mathcal{T}$ depends on the relative magnitude of ρ_o and P. In particular, the negative energy problem occurs more readily when the fluid is "hot" ($P \gg \rho_o$), and may not appear at all for "cold" fluids ($P \ll \rho_o$). $\Gamma = 4/3$ is a special case because the second term of (7.27) is identically zero, and Ψ couples only to the rest mass ρ_o.

The consequences of the indeterminate sign for $\mathcal{T}$ are dramatic, as the gravitational force changes from an attractive force to a repulsive force. We have investigated this change in behavior for static, spherically symmetric "star" solutions for $\Gamma = 1.35$—a Γ slightly greater than the $\Gamma = 4/3$ limit for a negative-definite $\mathcal{T}$—with the isentropic equation of state and a varying k (see Section 7.5). The effect produces increasingly strange solutions as k increases, and similar effects are seen in dynamic fluid solutions, as the relativistic shocks easily impart large amounts of kinetic energy (heat) to the diffuse outer medium. To avoid this problem we fix $\Gamma = 4/3$ in the following.

7.3 Conserved quantities: the tale of three masses

Scalar gravity unfolds in Minkowski space, and thus allows the definition of *globally* exact conservation laws [118]. The first two conserved quantities come from applying Gauss' law to $\nabla \cdot \mathbf{J} = 0$ and $\nabla \cdot \mathbf{T} = 0$. The first of these defines a conserved *rest* mass

$$M_o = \int \mathrm{d}^3x\, J^0 = \int \mathrm{d}^3x (\rho_o W) \tag{7.28}$$

The second defines the total energy

$$M = \int \mathrm{d}^3x\, T^{00}_{\text{total}}, \tag{7.29}$$

which, using (7.15), becomes

$$M = \int \mathrm{d}^3x \left[\frac{1}{8\pi G} \left[(\nabla_0 \Psi)^2 + \nabla_i \Psi \nabla^i \Psi \right] + e^{\psi} \left((\rho + P) W^2 - P \right) \right]. \tag{7.30}$$

M is conserved outside of the matter source and gravitational waves. The third conserved quantity is

$$M_{\mathrm{C}} = -\int \mathrm{d}^3x\, \mathcal{T}. \tag{7.31}$$

Shapiro and Teukolsky [118] call this the "Coulomb" mass because, in the limits $\Psi \to 0$ as $r \to \infty$, this mass becomes

$$M_{\mathrm{C}} = -\frac{1}{G} \lim_{r \to \infty} r\Psi. \tag{7.32}$$

7.4 Gravitational radiation

One of the most exciting aspects of the scalar gravity model is the existence of gravitational waves—even in spherical symmetry. Shapiro and Teukolsky [118, 113] analyzed the gravitational radiation in the weak-field, slow-motion limit, finding that the (spherically symmetric) monopole radiation and the quadrupole contribution both fall off like $1/r$. In spherical symmetry, where only monopole radiation exists, the wave extraction is very simple. In axisymmetric systems, the analysis is slightly more complicated. As time constraints prevented a detailed examination of gravitational radiation in this work, a more complete discussion is not given here.

7.5 The spherically symmetric static solution

This section presents the static, spherically symmetric solutions in scalar gravity which are analogous to the TOV solutions of general relativity. The Minkowski spherically symmetric line element is

$$\mathrm{d}^2 s = -\mathrm{d}t^2 + \mathrm{d}r^2 + r^2 \mathrm{d}\theta^2 + r^2 \sin^2\theta \, \mathrm{d}\phi^2. \tag{7.33}$$

To find static solutions we set the time derivatives in the Euler equations to zero and the four-velocity to $u^\nu = (1, 0, 0, 0)$. The energy equation is trivially satisfied, and the only non-trivial Euler equation is

$$\frac{\mathrm{d}P}{\mathrm{d}r} = -(\rho - 2P)\frac{\mathrm{d}\Psi}{\mathrm{d}r} \tag{7.34}$$

The scalar gravity field equation is

$$\nabla^2 \Psi = \frac{1}{r^2}\partial_r \left(r^2 \partial_r \Psi\right) = 4\pi e^{\Psi}(\rho - 3P). \tag{7.35}$$

Let

$$\Upsilon \equiv \partial_r \Psi, \tag{7.36}$$

and write (7.35) as a first order system

$$\partial_r \Psi = \Upsilon \tag{7.37}$$

$$\partial_r \Upsilon = -\frac{2}{r}\Upsilon + 4\pi e^{\Psi}(\rho - 3P). \tag{7.38}$$

The symmetry conditions require that $\mathrm{d}\Psi/\mathrm{d}r = 0$ at the origin. Solutions can be found by choosing the central pressure, P_o, and the central value of the scalar field, Ψ_o, and then integrating equations (7.34), (7.37), and (7.38) until $P \leq 0$.

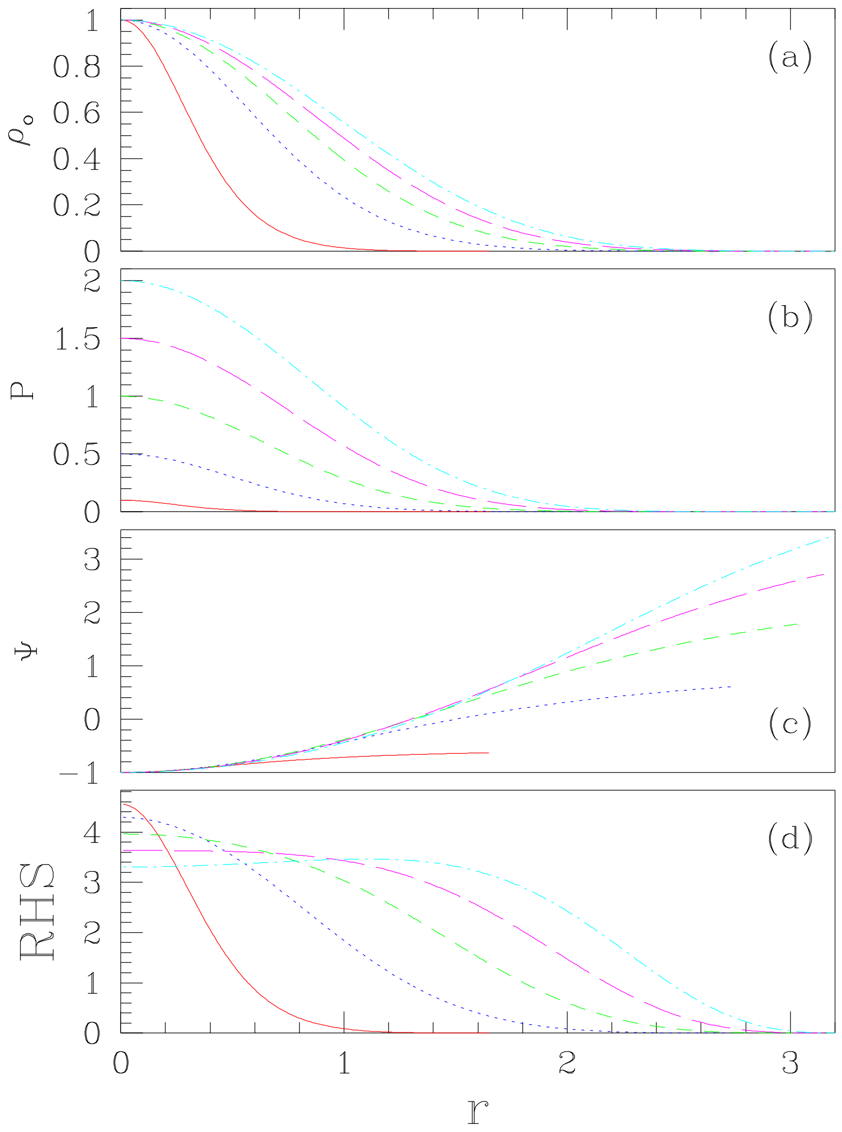

Figure 7.1: Spherically symmetric, static "star" solutions in scalar gravity for $\Gamma = 1.35$ for varying values of k, where we use the isentropic equation of state $P = k\rho_o^\Gamma$. Frame (a) shows ρ_o, frame (b) shows P, frame (c) shows Ψ, and frame (d) shows the scalar gravity coupling term, $4\pi e^\Psi(\rho - 3P)$. In all of these solutions we set $\Psi(0,t) = -1$, $\rho_o(0,t) = 1$, and vary k. The outward integration is halted when $P \leq 0$. The solid line shows the solutions for $k = 0.1$, the dotted line for $k = 0.5$, the short-dashed line for $k = 1$, the long-dashed line for $k = 1.5$, and the dot-dashed line for $k = 2$. As $\Gamma > 4/3$, the coupling term plotted in frame (d) is not positive definite. When $k = 0.1$, Ψ essentially couples to the rest mass, ρ_o. As k increases, the coupling to ρ_o becomes increasingly weaker, as can be seen in frame (d).

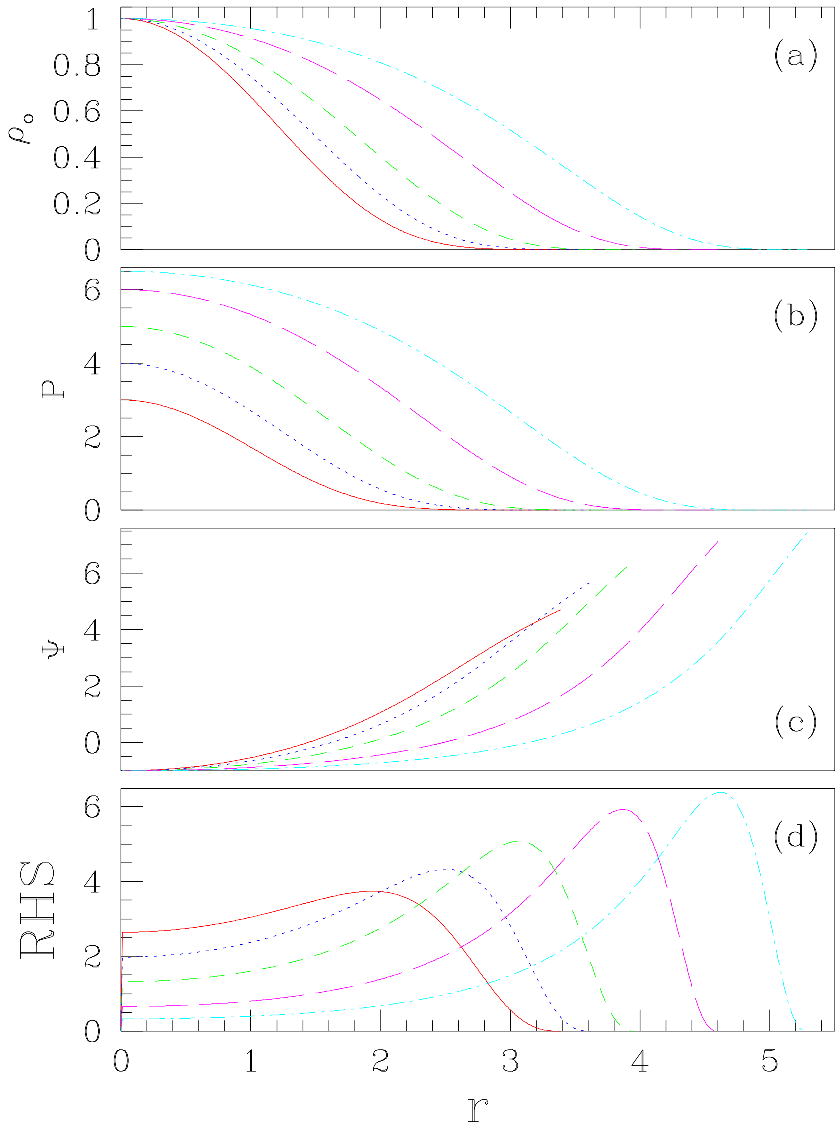

Figure 7.2: A continuation of the solutions plotted in Figure 7.1 for $3 \leq k \leq 6.5$. Frame (a) shows ρ_o, frame (b) shows P, frame (c) shows Ψ, and frame (d) shows the scalar gravity coupling term, $4\pi e^{\Psi}(\rho - 3P)$. The solid line shows the solutions for $k = 3$, the dotted line for $k = 4$, the short-dashed line for $k = 5$, the long-dashed line for $k = 6$, and the dot-dashed line for $k = 6.5$. The coupling between Ψ and ρ_o (or indeed ρ!) continues to weaken, while the gravitational force, $\nabla_r \Psi$, tends to zero near the origin.

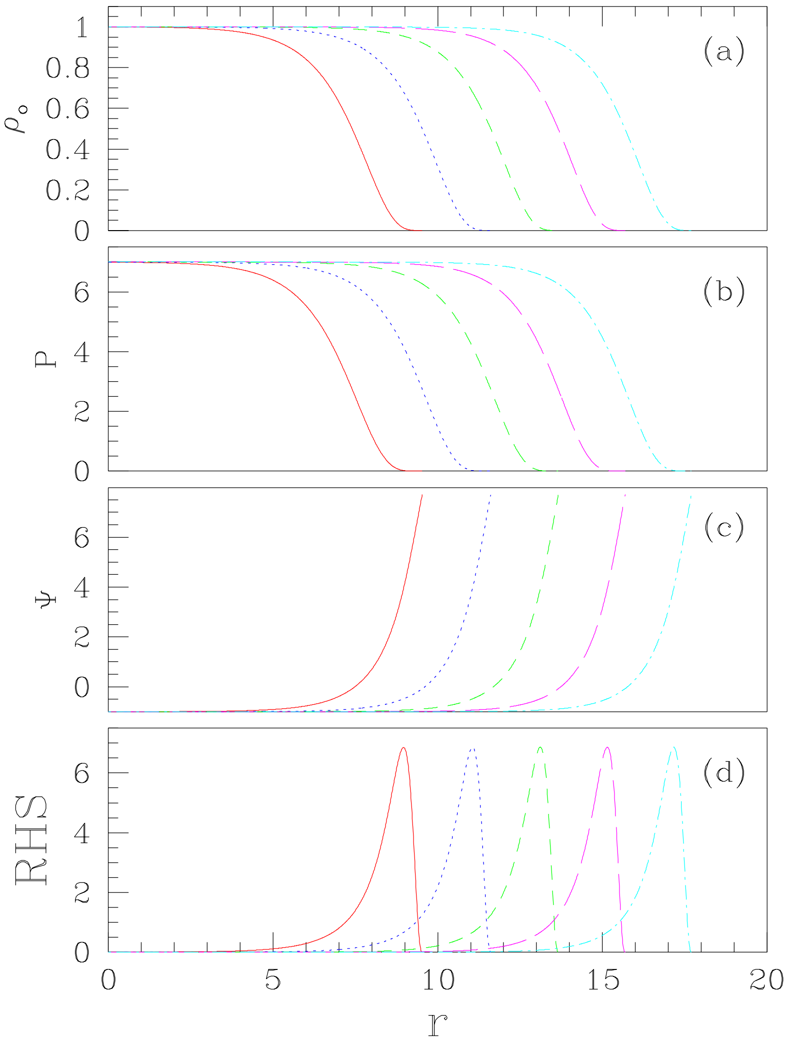

Figure 7.3: A continuation of the solutions plotted in Figure 7.1 for $6.9921875 \leq k \leq 6.999998092651367$. (These results, and others in this chapter are preliminary. Although the values for k reported here are given with 16 digits, not all of these digits are "significant." No attempt has been made rigorously determine the proper level of precision.) Frame (a) shows ρ_o, frame (b) shows P, frame (c) shows Ψ, and frame (d) shows the scalar gravity coupling term, $4\pi e^{\Psi}(\rho - 3P)$. The solid line shows the solutions for $k = 6.9921875$, the dotted line for $k = 6.9990234375$, the short-dashed line for $k = 6.9998779296875$, the long-dashed line for $k = 6.999984741210938$, and the dot-dashed line for $k = 6.999998092651367$. These solutions represent the extreme limiting solutions before $\mathcal{T}$ changes sign near the origin. The effects noted in the previous two figures are greatly exaggerated in these solutions.

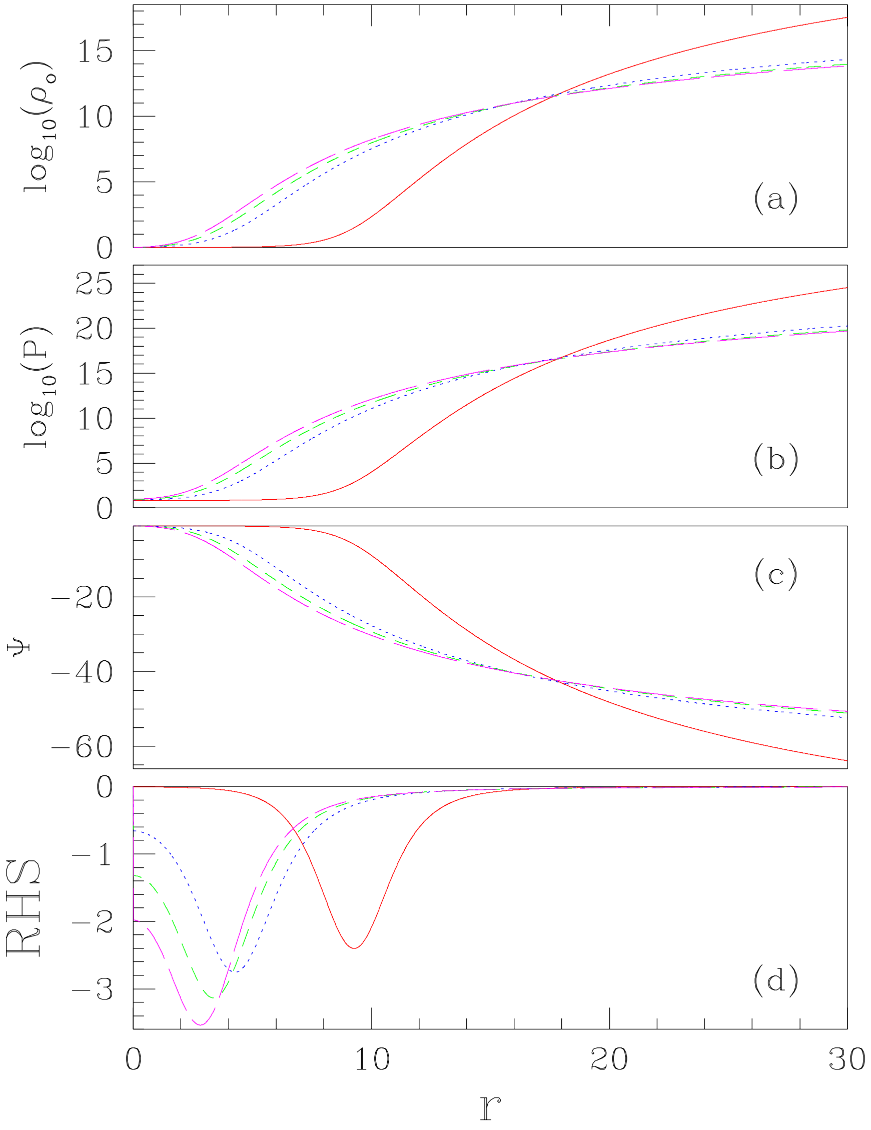

Figure 7.4: A continuation of the solutions plotted in Figure 7.1 for $7.01 \leq k \leq 10$. The coupling term $\mathcal{T}$ has now changed sign near the origin, and the scalar gravity has changed from an attractive, to a repulsive force. Frame (a) *now* shows $\log_{10} \rho_o$, frame (b) *now* shows $\log_{10} P$, frame (c) shows Ψ, and frame (d) shows the scalar gravity coupling term, $4\pi e^{\Psi}(\rho - 3P)$. The solid line shows the solutions for $k = 7.01$, the dotted line for $k = 8$, the short-dashed line for $k = 9$, and the long-dashed line for $k = 10$. (Note that the vertical scales in these plots are very different from the others in the series, especially the logarithmic scale in (a) and (b).)

As discussed in Section 7.2 above, the perfect-fluid/scalar-gravity coupling is problematic for $\Gamma > 4/3$, because $\mathcal{T}$ is no longer negative definite. Figures 7.1–7.4, present a series of spherically symmetric, static solutions for $\Gamma = 1.35$ with the isentropic equation of state

$$P = k\rho_o^{\Gamma}. \tag{7.39}$$

The figures begin with $k = 0.1$, gradually increasing k to $k \approx 7$, where $\mathcal{T}$ first becomes positive. Figure 7.4 shows four solutions with $k > 7$, all of which have "repulsive" gravity with $\mathcal{T} > 0$.

7.6 Axisymmetric scalar gravity

As mentioned previously, the motivation for introducing the scalar gravity model is to create simple, axisymmetric test problems for the two-dimensional code. The first "test" is merely to see if the solutions remain stable and regular along the symmetry axis ($R = 0$) of cylindrical coordinates. Secondly, we can create "toy" problems that mimic the physical problems of interest, such as the collision of two objects shown below. Finally, the static, spherically symmetric solution of Section 7.5 tests that the coupled fluid and scalar gravity equations are solved correctly. This section writes the scalar gravity equations for axisymmetric systems using cylindrical coordinates, and briefly discusses methods for solving them numerically. The static star solution is used as initial data for the two-dimensional code, and the results indicate that that the equations are being solved correctly. Finally, we set initial data for two objects along the symmetry axis, which collide to form a single object. Several frames from this evolution are included here.

In axial symmetry we adopt the canonical cylindrical coordinates, and write the Minkowski line element as

$$\mathrm{d}s^2 = -\mathrm{d}t^2 + \mathrm{d}R^2 + \mathrm{d}z^2 + R^2\mathrm{d}\theta^2. \tag{7.40}$$

The fluid equations of motion in this coordinate system are

$$\partial_t \mathbf{q} + \frac{1}{R}\partial_R \mathbf{f}_R + \partial_z \mathbf{f}_z = \mathbf{\Sigma} - \mathbf{\Sigma}_\psi, \tag{7.41}$$

where $\mathbf{\Sigma}_\psi$ contains the coupling terms to scalar gravity

$$\mathbf{\Sigma}_\psi = \begin{bmatrix} 0 \\ S_R \Xi + (\tau + D - S_z v^z - S\phi v^\phi - 2P)\Upsilon_R + S_R v^z \Upsilon_z \\ S_z \Xi + S_z v^R \Upsilon_R + (\tau + D - S_R v^R - S_\phi v^\phi - 2P)\Upsilon_z \\ S_\phi \Xi + S_\phi v^R \Upsilon_R + S_\phi v^z \Upsilon_z \end{bmatrix}. \tag{7.42}$$

These equations are now written with the "densitized" variables of Section 6.3, $\hat{\mathbf{q}}$. The fluid equations are now

$$\partial_t \hat{\mathbf{q}} + \partial_R \hat{\mathbf{f}}^R + \partial_z \hat{\mathbf{f}}^z = \hat{\mathbf{\Sigma}} - \hat{\mathbf{\Sigma}}_\psi, \tag{7.43}$$

where

$$\hat{\mathbf{\Sigma}}_\psi = \begin{bmatrix} 0 \\ \hat{S}_R \Xi + (\hat{\tau} + \hat{D} - \hat{S}_z v^z - \hat{S}\phi v^\phi - 2RP)\Upsilon_R + \hat{S}_R v^z \Upsilon_z \\ \hat{S}_z \Xi + \hat{S}_z v^R \Upsilon_R + (\hat{\tau} + \hat{D} - \hat{S}_R v^R - \hat{S}_\phi v^\phi - 2RP)\Upsilon_z \\ \hat{S}_\phi \Xi + \hat{S}_\phi v^R \Upsilon_R + \hat{S}_\phi v^z \Upsilon_z \end{bmatrix}. \tag{7.44}$$

As in the spherically symmetric case, we write the scalar gravity evolution equation in first order form, defining new variables

$$\Xi \equiv \partial_t \Psi \tag{7.45}$$

$$\Upsilon_R \equiv \partial_R \Psi, \tag{7.46}$$

$$\Upsilon_z \equiv \partial_z \Psi. \tag{7.47}$$

The equations of motion for Ψ are then

$$\partial_t \Psi = \Xi, \tag{7.48}$$

$$\partial_t \Upsilon_R = \partial_R \Xi, \tag{7.49}$$

$$\partial_t \Upsilon_z = \partial_z \Xi, \tag{7.50}$$

$$\partial_t \Xi = \frac{1}{R}\partial_R \left(R\Upsilon_R\right) + \partial_z \Upsilon_z + 4\pi\mathfrak{T}. \tag{7.51}$$

The fluid equations and the scalar gravity evolution equations are updated sequentially, with the fluid updated first. The fluid update consists of solving the fluid equations in cylindrical coordinates coupled to scalar gravity (7.43) with the high-resolution Godunov scheme described in Chapter 6. Then the scalar gravity equations are evolved to the advanced time using the Crank-Nicholson method (Section 3.1.1). We apply Kreiss-Oliger [76] dissipation to the scalar gravity equations, (7.48)–(7.51), on the interior of the grid, as well as outer grid boundaries.

The out-going radiation boundary condition for spherically symmetric systems is applied to Ξ. In spherical symmetry this condition is

$$\partial_t \Xi + \frac{1}{r}\partial_r \left(r\Xi\right) = 0. \tag{7.52}$$

The spherical radial coordinate, r, is related to the cylindrical coordinates by

$$r^2 = R^2 + z^2. \tag{7.53}$$

Changing to the cylindrical variables, the out-going radiation condition becomes

$$\partial_t \Xi + \left(R^2 + z^2\right)^{-1/2} \left[\, R\,\partial_R\,\Xi + z\,\partial_z\,\Xi + \Xi\,\right] = 0. \tag{7.54}$$

Boundary conditions are not applied to Υ_R, Υ_z, or Ψ, but equations (7.48)–(7.50) are integrated here with backwards or forward differences, as required.

Time symmetric initial data is used for the fluid variables, and Ξ is also assumed to be time symmetric. The scalar gravity initial data is set by solving

$$\nabla^2 \Psi = -4\pi\mathfrak{T}. \tag{7.55}$$

To test the two dimensional scalar-gravity/perfect-fluid code we first set initial data for a spherically symmetric, static solution (Section 7.5). We use fixed boundary conditions for the outer boundaries, and require that the axis, $R = 0$, remain regular. We computed this solution on a rectangular grid with 401×801 cells, and the solution is discussed in Figures 7.5–7.7.

As a demonstration of the code's ability to evolve dynamic configurations, we present *very* preliminary results of a two-body collision in scalar gravity. The initial data consist of two spherically symmetric objects of equal mass on axis, initially positioned at $R = 0$ and $z = \pm z_c$. The initial data is time symmetric, and Dirichlet boundary conditions, $\Psi = 1$, are set on the outer boundaries. The solution is calculated on a square grid with 201×201 grid points. The variables ρ_o, v^z, v^R, Ψ, and Ξ are plotted at eight representative times in Figures 7.8–7.17

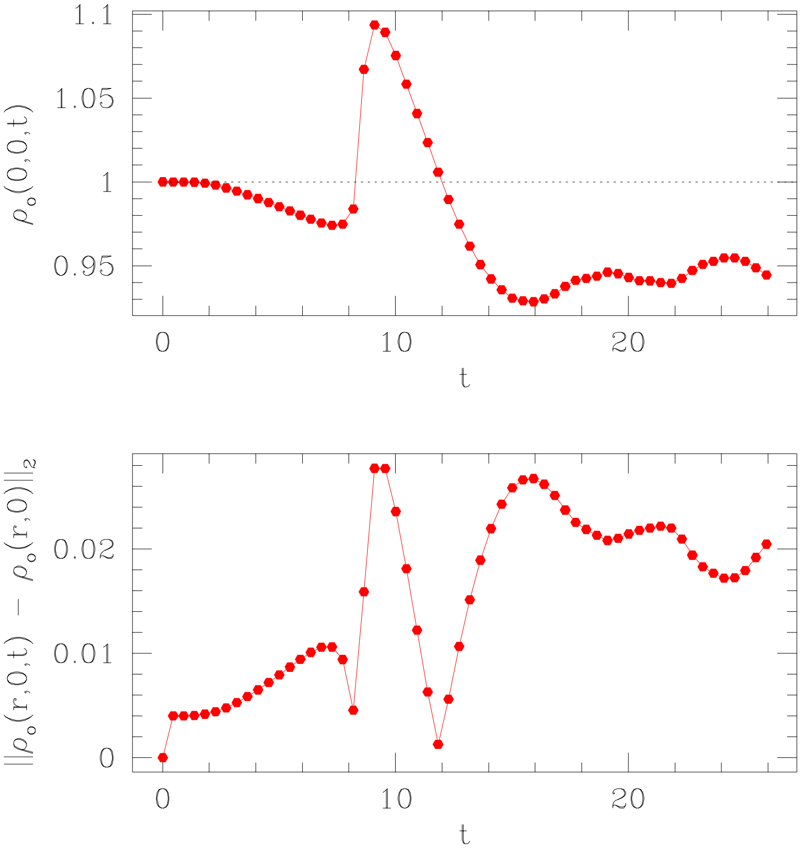

Figure 7.5: The top frame shows the central density $\rho_o(R,z,t) = \rho_o(0,0,t)$ of a "star" in scalar gravity from a two-dimensional evolution. The bottom frame shows the ℓ_2 norm of the error along the line $z=0$, as defined to be the difference of the evolved solution, $\rho_o(R,0,t)$, and the exact solution, $\rho_o(R,0)$. The evolution used $\{\, (R,z) \,|\, R \in [0,1.82], z \in [-1.82, 1.82] \,\}$ with 401 × 801 grid points. The static solution is generated using the isentropic equation of state, $P = k\rho_o^\Gamma$, with $k = 0.1$ and $\Gamma = 4/3$, with $\rho_o(0,0) = 1$ and $\Psi(0,0) = -1$. The star radius is $r_{\rm star} = 1.81$. The evolution continued for approximately 4.75 "sound-crossing times," as estimated by $c/3$ along the R-direction, and then crashed owing to noise generated by the interaction of the background fluid with the star and the outer boundary conditions. This noise is apparent in the two-dimensional plots of v^R of Figure 7.7. This solution required approximately one week of computer time on a dedicated, single processor (R10000) Silicon Graphics work station.

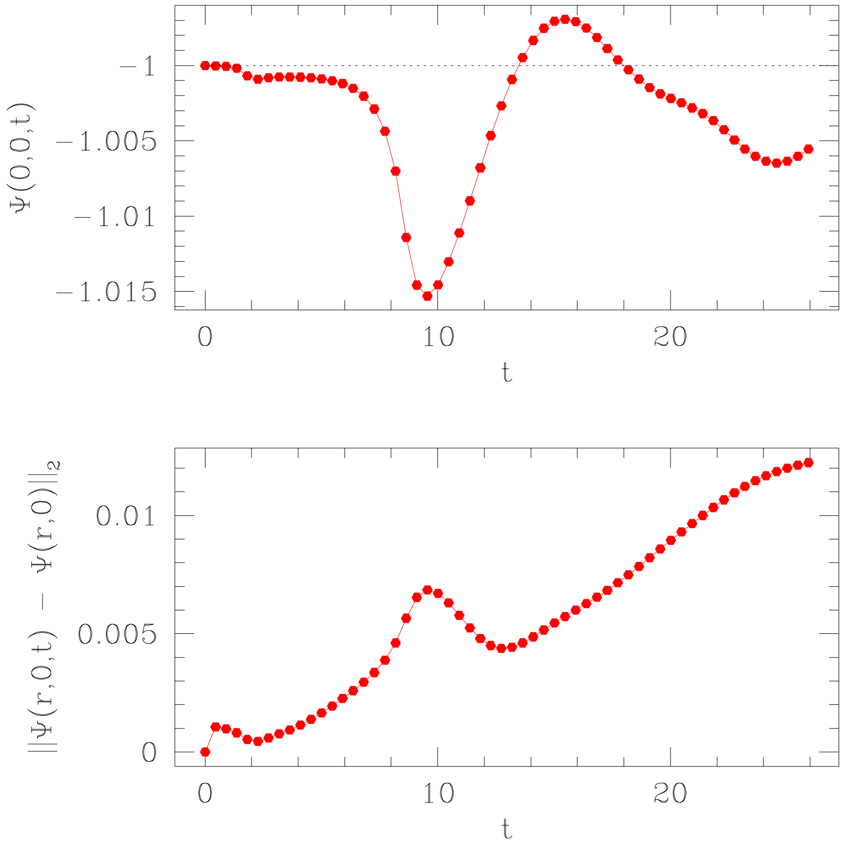

Figure 7.6: The top frame shows the central value of the scalar gravity field $\Psi(R, z, t) = \Psi(0, 0, t)$ for a "star" in a two-dimensional evolution. The bottom frame shows the ℓ_2 norm of the error along the line $z = 0$, as defined to be the difference of the evolved solution, $\Psi(R, 0, t)$, and the exact solution, $\Psi(R, 0)$. See Figure 7.5 for additional information.

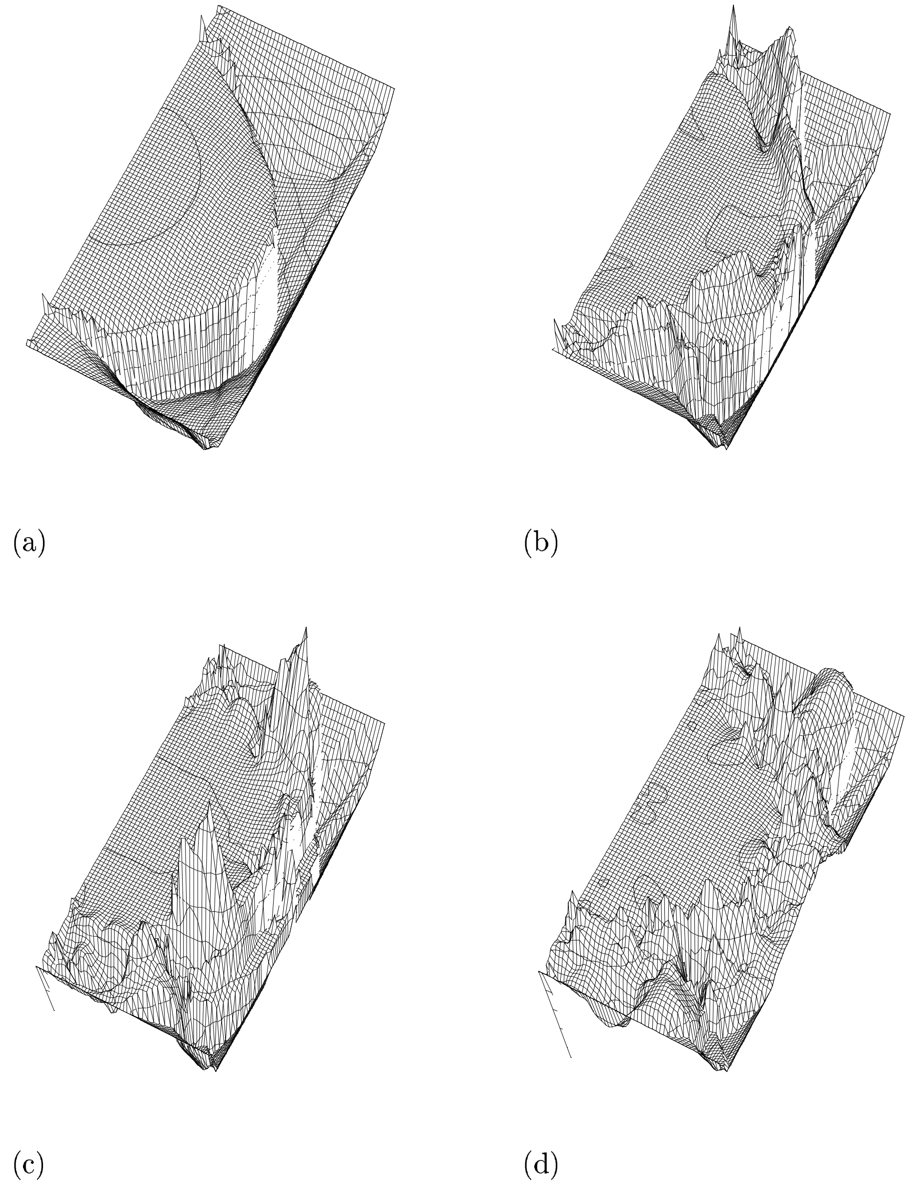

(a) (b) (c) (d)

Figure 7.7: A time series showing v^R for a scalar gravity static star. These frames are shown at approximately one sound-crossing-time intervals, as estimated by $c/3$ along the R-direction. Frame (a) is shown at $t = 5.46$, frame (b) at $t = 10.92$, frame (c) at $t = 16.38$, and frame (d) at $t = 21.84$. The interaction of the background fluid with the star and the outer boundary conditions causes a substantial amount of noise in the solution. The boundary conditions, which are applied along the edges of the rectangular grid, cause the star to loose its initial spherical symmetry.

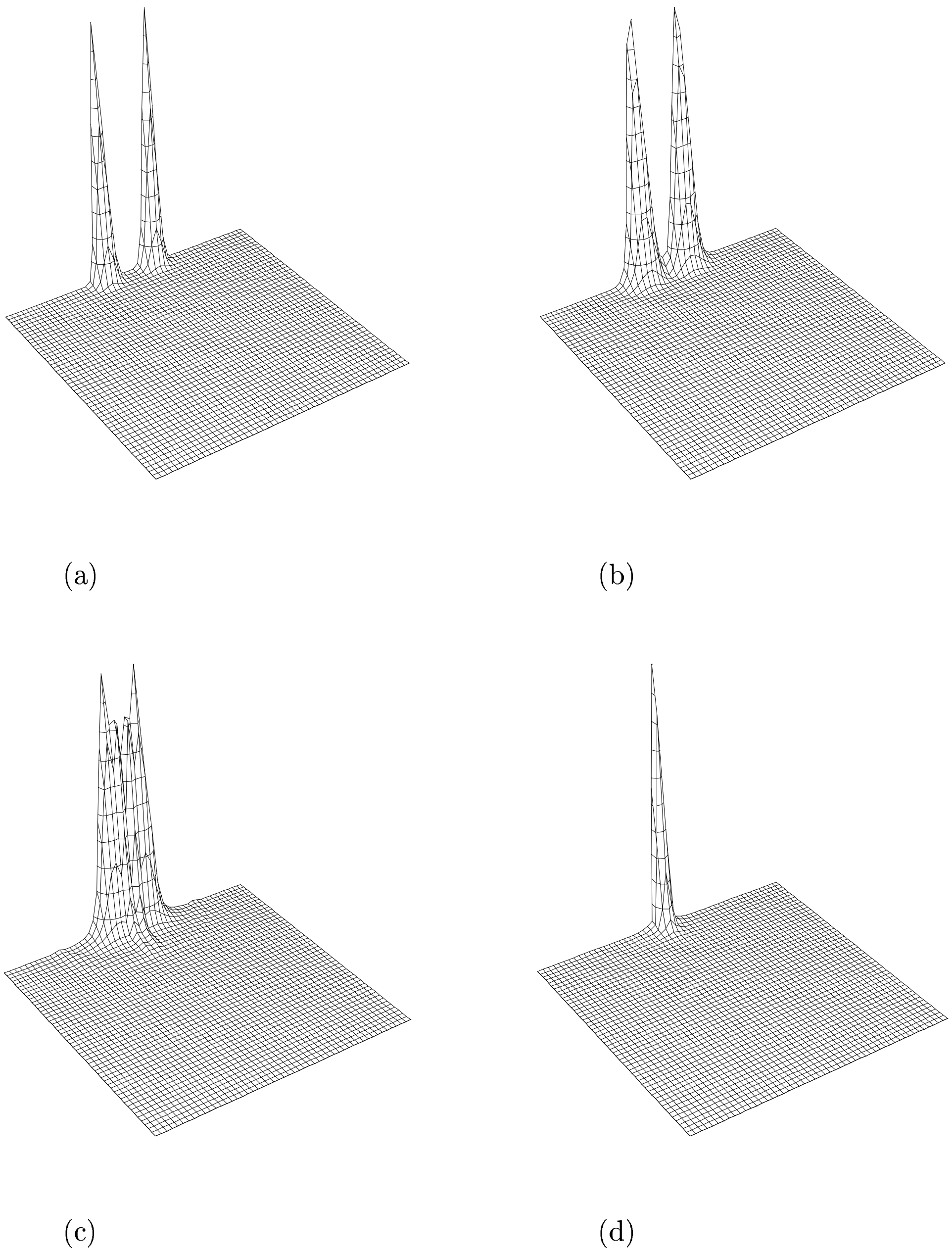

(a) (b)

(c) (d)

Figure 7.8: A time series showing ρ_o for a two-body collision. The two objects are initially of equal mass and centered on the axis. Frame (a) shows the initial configuration, and the remaining frames are at equal intervals. The data are scaled in each frame individually, unfortunately masking the large dynamic range of the data.

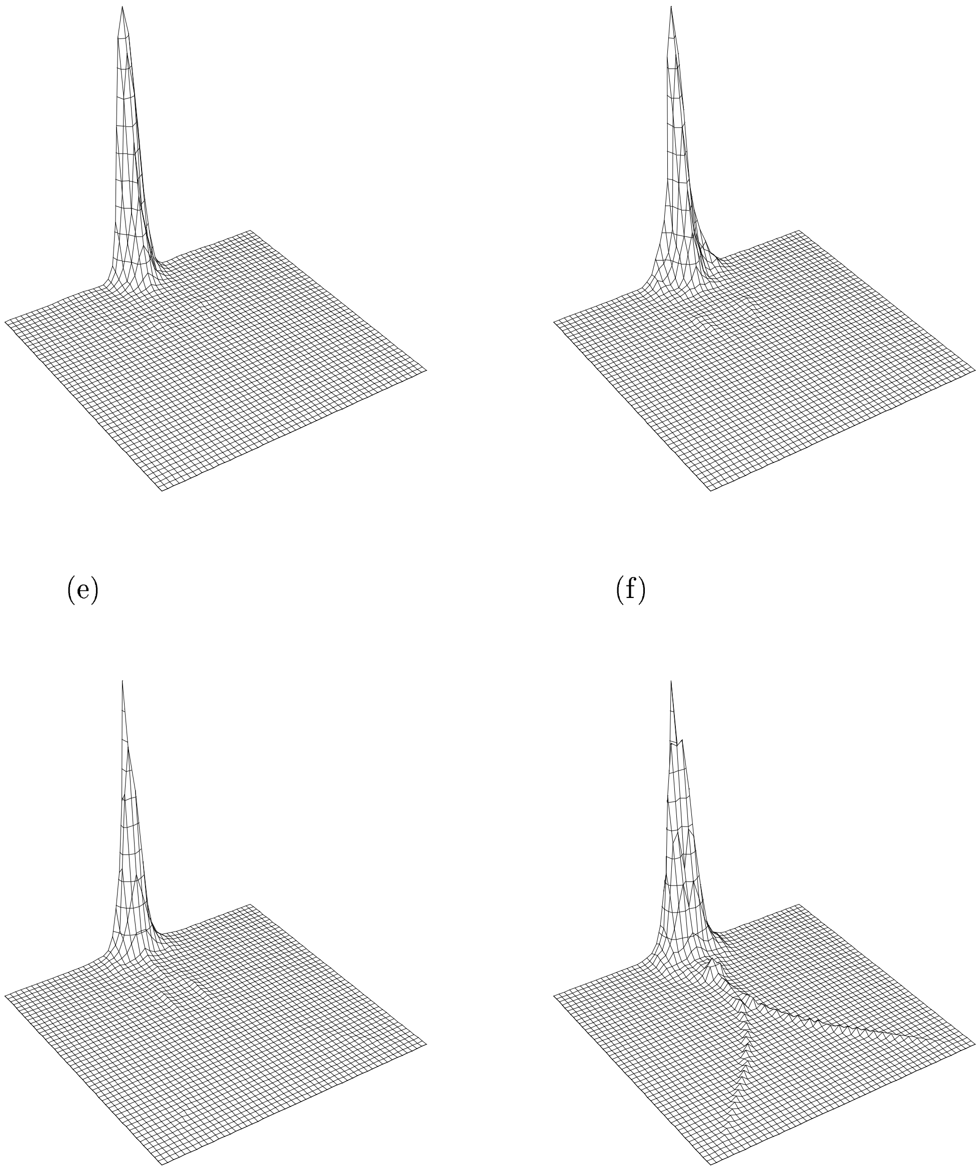

(e)

(f)

(g)

(h)

Figure 7.9: A time series showing ρ_o for a two-body collision (continued).

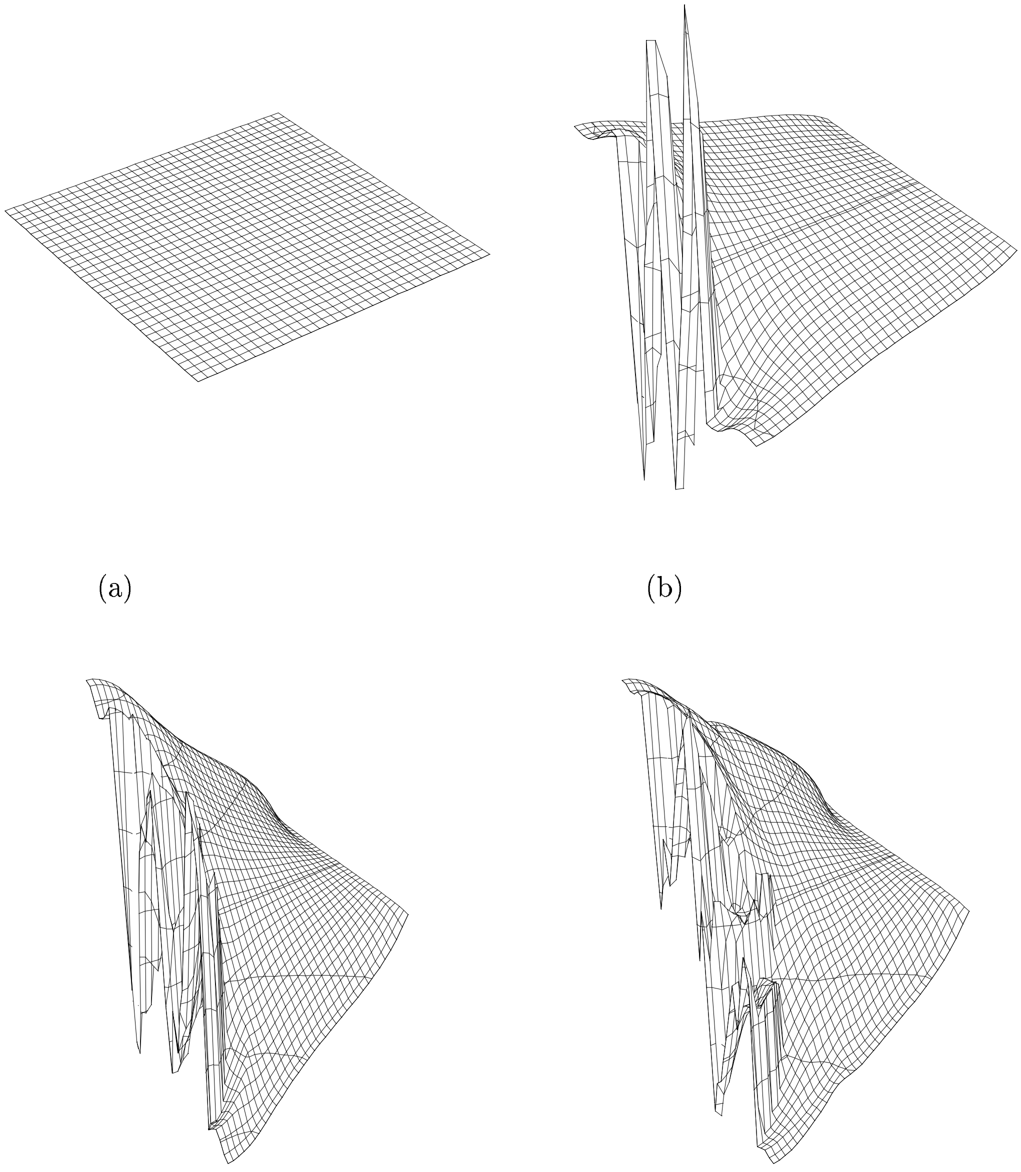

(a) (b)

(c) (d)

Figure 7.10: A time series showing v^z for a two-body collision.

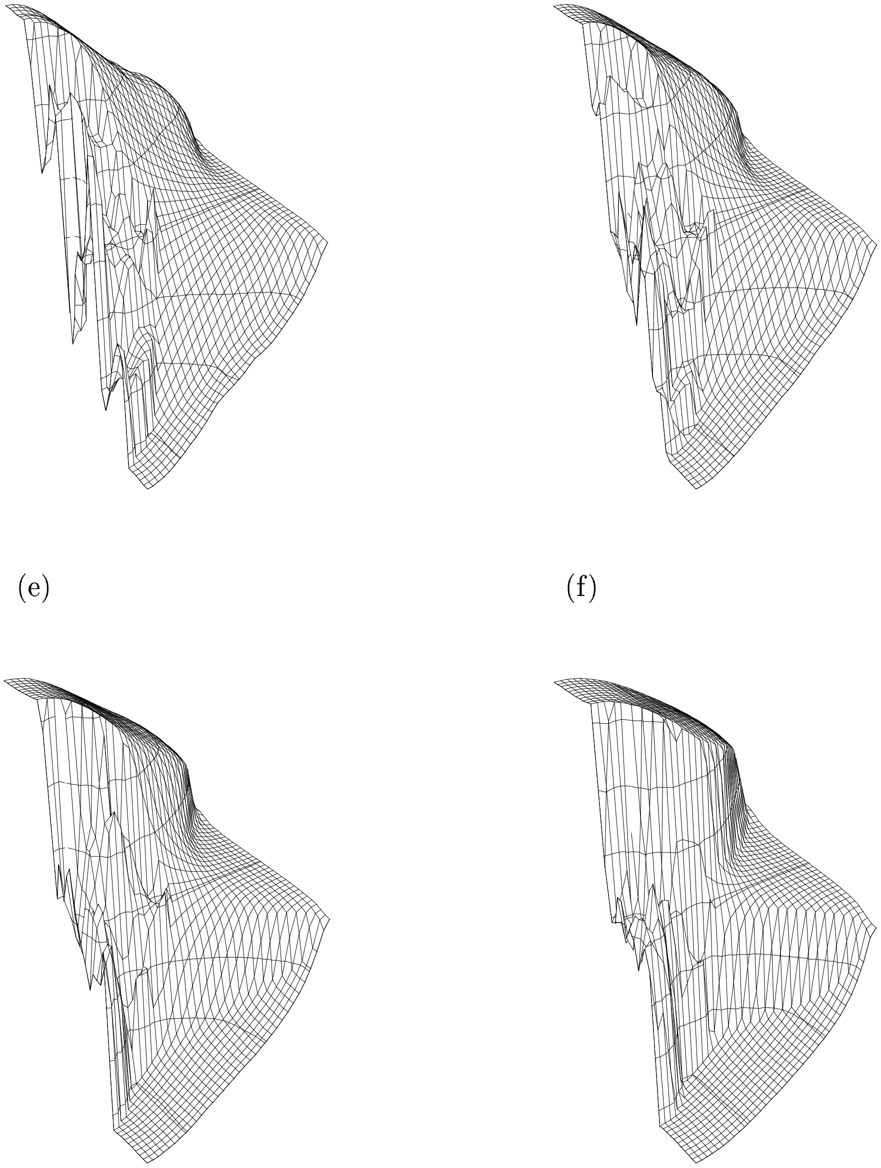

(e) (f)

(g) (h)

Figure 7.11: A time series showing v^z for a two-body collision (continued).

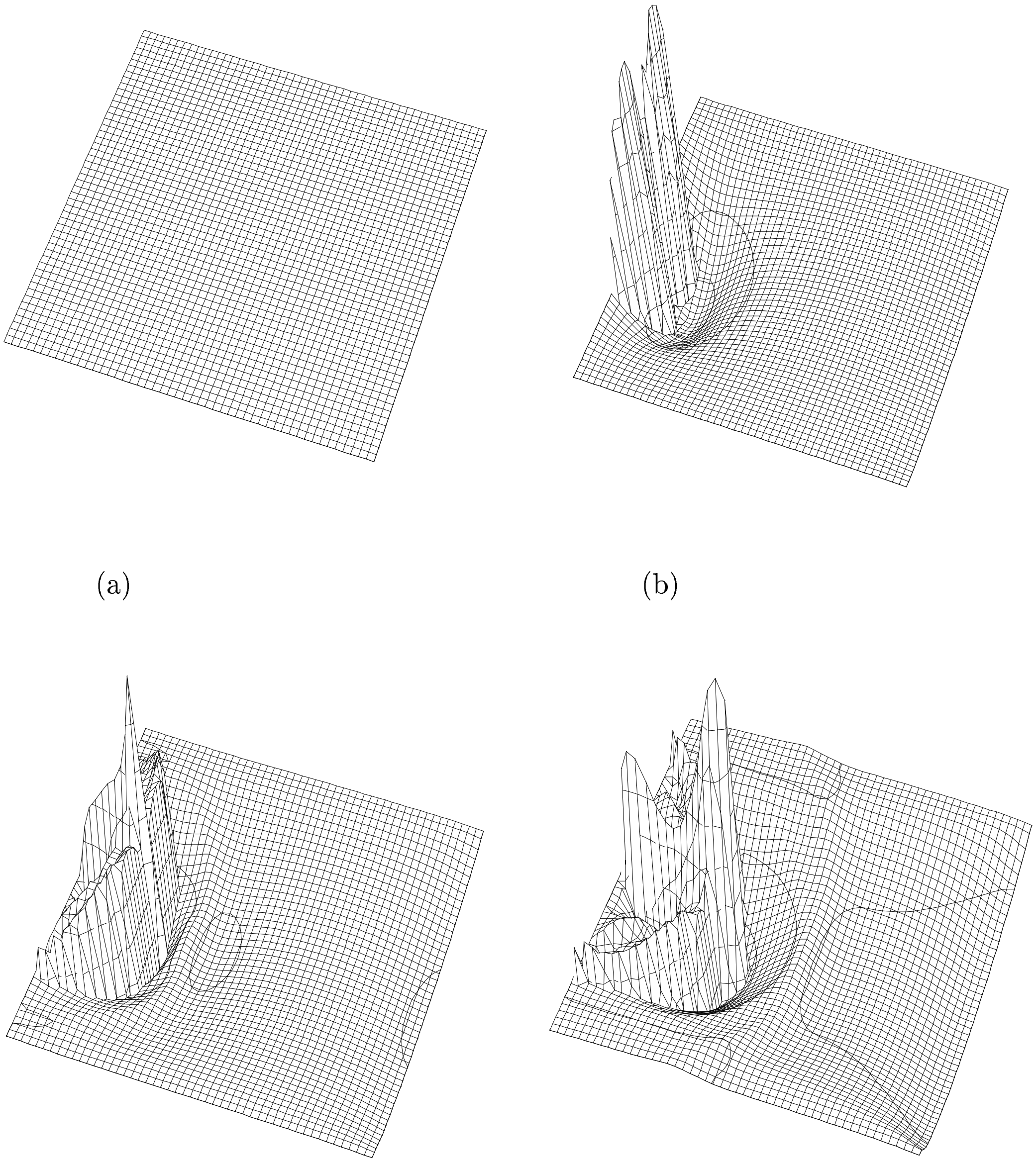

(a) (b)

(c) (d)

Figure 7.12: A time series showing v^R for a two-body collision.

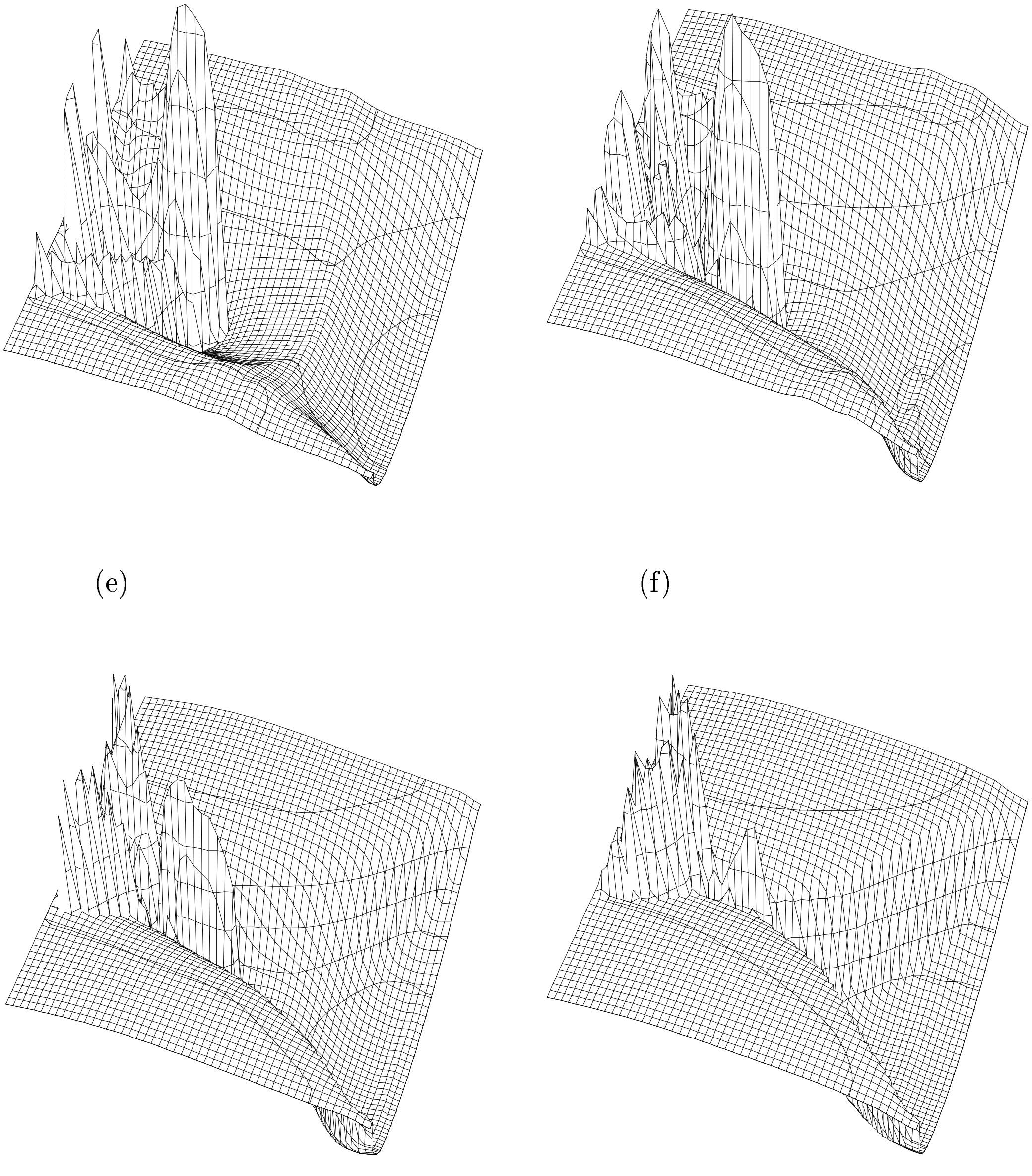

(e) (f)

(g) (h)

Figure 7.13: A time series showing v^R for a two-body collision (continued).

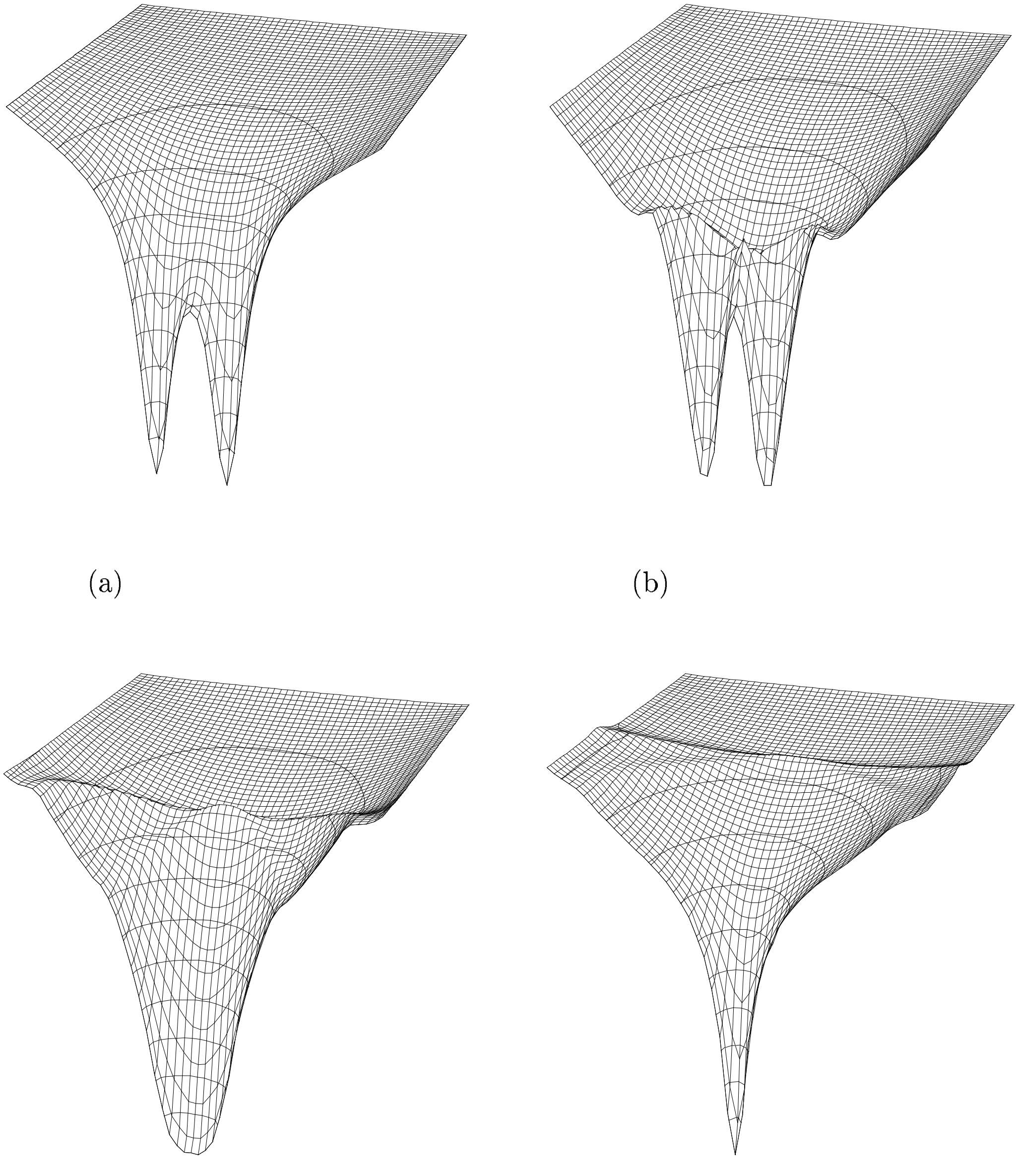

(a) (b)

(c) (d)

Figure 7.14: A time series showing Ψ for a two-body collision.

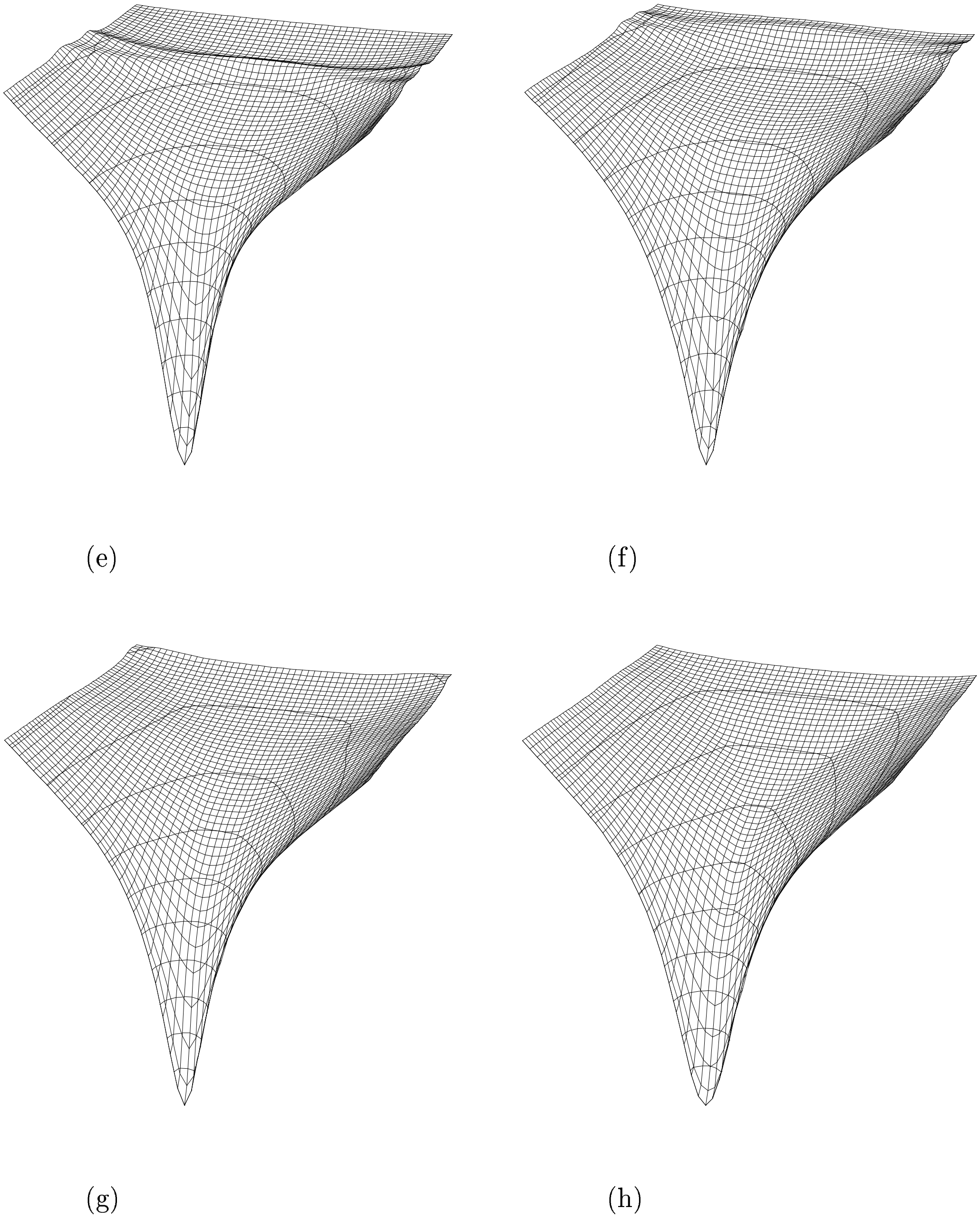

(e) (f)

(g) (h)

Figure 7.15: A time series showing Ψ for a two-body collision (continued).

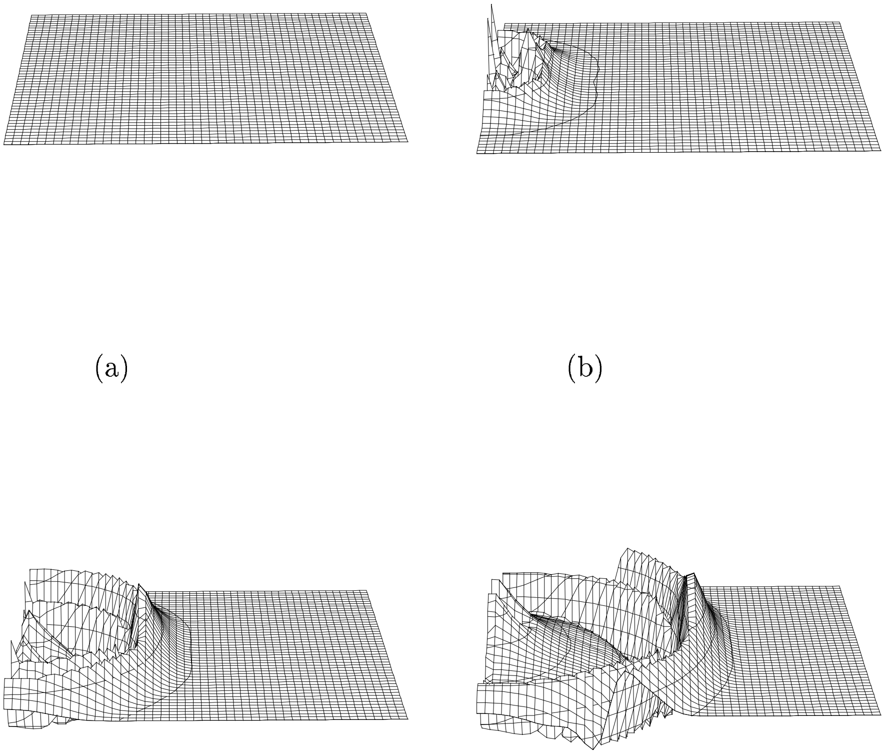

(a) (b)

(c) (d)

Figure 7.16: A time series showing Ξ for a two-body collision.

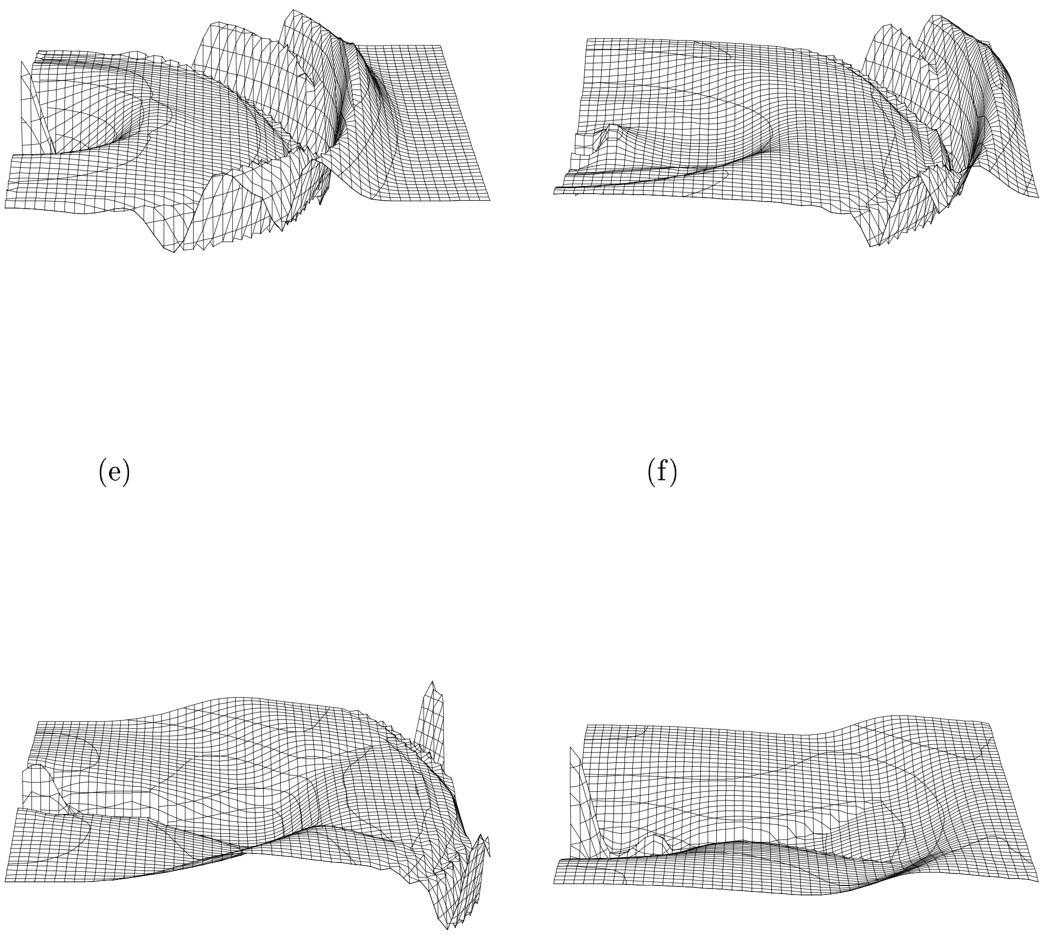

(e) (f)

(g) (h)

Figure 7.17: A time series showing Ξ for a two-body collision (continued).

Chapter 8

Conclusion

Perfect fluids have a rich phenomenology, and for relativistic fluids the range of solutions is just beginning to be explored. Certainly some of the most dynamic solutions are the Type II critical solutions presented here. These solutions contain both collapsing and exploding regions, and as $\Gamma \to 2$, the transition between these regions becomes more and more abrupt. Indeed, these solutions are "extreme" in many senses of the word, including their ultrarelativistic velocities ($W \gg 10^6$), the range of length scales required to capture their evolution in time, and the strong coupling between the fluid and the space-time geometry at the verge of black hole formation.

These characteristics of the perfect fluid critical solutions make them difficult to investigate using numerical techniques. However, using careful numerical analyses, we studied these solutions using *both* the full set of Einstein-fluid equations and a reduced set of equations adapted to the critical solutions' scale-invariance. Many of our results for $1.89 \lesssim \Gamma \leq 2$, reported here and in [96], were unexpected by the community, and, in part, they have been confirmed by independent researchers [24, 67].

Following the seminal work of Evans and Coleman [52], we construct globally regular, CSS solutions for $1.89 \lesssim \Gamma \leq 2$ using the *ansatz* of continuous self-similarity.

These solutions are difficult to find—in some cases double precision arithmetic is insufficient—and they were previously not thought to exist [86, 68, 60, 16]. We find good evidence that the sonic point is a degenerate *node* for the $\Gamma_{\mathrm{dn}} \simeq 1.8896244$ solution, and not a focal point as previously reported [86].

Using the full Einstein-fluid equations we are able to verify that these new CSS solutions are indeed the unique critical solutions, i.e., the solutions which separate the solutions that ultimately disperse (in the high-energy limit) from those which form black holes. We also calculate the mass-scaling exponents by evolving supercritical initial data, which are in good agreement with the results of perturbation theory. We have also investigated critical collapse using the ideal-gas equation of state, and, as expected, have found that the fluid *is* well-described in the near-critical regime by an ultrarelativistic approximation, and thus has critical solutions identical to those generated using $P = (\Gamma - 1)\rho$.

Solving the Einstein-fluid system for these solutions presents several computational challenges. We developed a code to solve these equations, whose success in the ultrarelativistic regime is enabled only through: (i) solving the fluid equations with modern methods for conservation laws, (ii) introducing a new set of fluid variables ($\{\,\Pi, \Phi\,\}$) with superior properties for spherically symmetric, stiff fluids, *and* (iii) developing algorithms optimized for extremely relativistic velocities. A complete description of this code, along with extensive tests, is given in Chapter 4, with reference to the general numerical techniques given in Chapter 3.

The final part of this dissertation introduces some preliminary two-dimensional studies. A new code for solving two-dimensional, relativistic fluid systems is described in Chapter 6, and the first shock tube tests are presented. Currently this code can evolve fluids only on a static space-time, but future plans are focused on developing a fully general relativistic fluid code.

Finally, a “toy” gravitation model called scalar gravity is used to demonstrate the kind of physical problems we hope this code will be able to address.

Future work will undoubtedly be focused on developing a fully general relativistic fluid code, where a number of problems can be explored in axial symmetry, including: critical phenomena, supernovæ core collapse, the possible appearance of naked singularities in the collapse of rotating objects, and the production of gravitational waves in neutron star collisions.

Bibliography

[1] M. Alcubierre, S. Brandt, B. Brügmann, D. Holz, E. Seidel, R. Takahashi, and J. Thornburg, "Symmetry without symmetry: Numerical simulation of axisymmetric systems using Cartesian grids," `gr-qc/9908012` (1999).

[2] D.A. Anderson, J.C. Tannehill, and R.H. Pletcher, *Computational fluid mechanics and heat transfer* (Hemisphere Publishing Corp., New York, 1984).

[3] A.M. Anile, *Relativistic fluids and magneto-fluids,* (Cambridge University Press, Cambridge, 1989).

[4] R. Arnowitt, S. Deser, and C.W. Misner, "The dynamics of general relativity", *Gravitation: An introduction to current research*, edited by L. Witten (John Wiley, New York, 1962).

[5] D. Bale, "A Riemann solver based on the arithmetic average", unpublished (1998).

[6] D.S. Balsara, "Riemann solver for relativistic hydrodynamics", *J. Comput. Phys.* **114**, 284–297 (1994).

[7] F. Banyuls, J.A. Font, J.Mª. Ibáñez, J.Mª Martí, and J.A. Miralles, "Numerical 3+1 general relativistic hydrodynamics: A local characteristic approach", *ApJ* **476**, 221–231 (1997).

[8] J.M. Bardeen and T. Piran, "General relativistic axisymmetric rotating systems: coordinates and equations", *Physics Reports* **96**, 205–250 (1983).

[9] M.J. Berger and J. Oliger, "Adaptive mesh refinement for hyperbolic partial differential equations", *J. Comput. Phys.* **53**, 484–512 (1984).

[10] M.J. Berger and P. Colella, "Local adaptive mesh refinement for shock hydrodynamics", *J. Comput. Phys.* **82** 64–84 (1989).

[11] M.J. Berger and R.J. LeVeque, "Adaptive mesh refinement using wave-propagation algorithms for hyperbolic systems", *SIAM J. Numer. Anal.* in press (1997); available at `ftp://amath.washington.edu/pub/rjl/papers/mjb-rjl:amr.ps`.

[12] G.V. Bicknell and R.N. Henriksen, "Self-similar growth of primordial black holes. I. Stiff equation of state", *ApJ* **219**, 1043–1057 (1978).

[13] G.V. Bicknell and R.N. Henriksen, "Self-similar growth of primordial black holes. II. General sound speed", *ApJ* **225**, 237–251 (1978).

[14] O.I. Bogoyavlenskii, "General relativistic self-similar solutions with a spherical shock wave", *Sov. Phys. JETP* **46**, 633–640 (1977).

[15] P. Brady, "Phases of massive scalar field collapse", *Phys. Rev.* D **56**, 6057–6061 (1997).

[16] P. Brady and M.J. Cai, "Critical phenomena in gravitational collapse", `gr-qc/9812071` (1998).

[17] P. Brady, C. Gundlach, D.W. Neilsen, and M.W. Choptuik, "Black-hole threshold solutions in stiff fluid collapse", in preparation (1999).

[18] S.R. Brandt and E. Seidel, "Evolution of distorted rotating black holes. I. Methods and tests", *Phys. Rev.* D **52**, 856–869, (1995).

[19] S.R. Brandt and E. Seidel, "Evolution of distorted rotating black holes. II. Dynamics and analysis", *Phys. Rev.* D **52**, 870–886, (1995).

[20] S.R. Brandt and E. Seidel, "Evolution of distorted rotating black holes. III. Initial data", *Phys. Rev.* D **54**, 1403–1416, (1996).

[21] S.R. Brandt, J.A. Font, J.Mª Ibáñez, J. Massó, and E. Seidel, "Numerical evolution of matter in dynamical axisymmetric black hole spacetimes. I. Methods and tests", `gr-qc/9807017` (1998).

[22] M.E. Cahill and A.H. Taub, "Spherically symmetric similarity solutions of the Einstein field equations for a perfect fluid", *Comm. Math. Phys.* **21**, 1–40 (1971).

[23] B.J. Carr and A.A. Coley, "Self-similarity in general relativity", `gr-qc/9806048` (1998).

[24] B.J. Carr, A.A. Coley, M. Goliath, U.S. Nilsson, and C. Uggla, "Critical phenomena and a new class of self-similar spherically symmetric perfect-fluid solutions", `gr-qc/9901031` (1999).

[25] B.J. Carr and A.A. Coley, "A complete classification of spherically symmetric perfect fluid similarity solutions", `gr-qc/9901050` (1999).

[26] B.J. Carr, A.A. Coley, M. Goliath, U.S. Nilsson, and C. Uggla, "Physical interpretation of self-similar spherically symmetric perfect-fluid models: Combining the comoving and homothetic approach", `gr-qc/9902070` (1999).

[27] S. Chandrasekhar, *An introduction to the study of stellar structure* (University of Chicago Press, Chicago, 1939).

[28] M.W. Choptuik, "Consistency of finite-difference solutions of Einstein's equations", *Phys. Rev.* D **44**, 3124–3135 (1991).

[29] M.W. Choptuik, “Universality and scaling in gravitational collapse of a massless scalar field”, *Phys. Rev. Lett.* **70**, 9–12 (1993).

[30] M.W. Choptuik, T. Chmaj, and P. Bizon, “Critical behaviour in gravitational collapse of a Yang-Mills field”, *Phys. Rev. Lett.* **77**, 424–427 (1996).

[31] M.W. Choptuik, “The 3+1 Einstein equations”, unpublished (1998).

[32] M.W. Choptuik, “The (unstable) threshold of black hole formation”, `gr-gc/9803075` (1998).

[33] M.W. Choptuik, personal communication (1998).

[34] M.W. Choptuik, personal communication (1998).

[35] M.W. Choptuik, E.W. Hirschmann, and R.L. Marsa, “New critical behavior in Einstein-Yang-Mills collapse”, `gr-qc/9903081` (1999).

[36] M.W. Choptuik, “Lectures for Taller de Verano 1999 de FENOMEC: Numerical analysis with applications in theoretical physics”, unpublished (1999).

[37] A.J. Chorin and J.E. Marsden, *A mathematical introduction to fluid mechanics* (Springer-Verlag, New York, 1992).

[38] D. Christodoulou, “A mathematical theory of gravitational collapse”, *Commun. Math. Phys.* **109**, 613–647 (1987).

[39] D. Christodoulou, *Commun. Pure Appl. Math.* **44**, 339 (1991).

[40] D. Christodoulou, *Commun. Pure Appl. Math.* **46**, 1131 (1993).

[41] D. Christodoulou, *Ann. Math.* **140**, 607 (1994).

[42] P. Colella and P. Woodward, “The piece-wise parabolic method (PPM) for gas-dynamical simulations,” *J. Comput. Phys.* **54**, 174–201 (1984).

[43] R. Courant and K.O. Friedrichs, *Supersonic flow and shock waves* (Interscience Publishers, New York, 1948).

[44] W. Dai and P.R. Woodward, "An iterative Riemann solver for relativistic hydrodynamics", *SIAM J. Sci. Comput.* **18**, 982–995 (1997).

[45] R. Donat and A. Marquina, "Capturing shock reflections: an improved flux formula", *J. Comput. Phys.* **125**, 42–58 (1996).

[46] R. Donat, J.A. Font, J.Mª. Ibáñez, and A. Marquina "A flux-split algorithm applied to relativistic flows", *J. Comput. Phys.* **146**, 58–81 (1998).

[47] B. Einfeldt, "On Godunov-type methods for gas dynamics", *SIAM J. Numer. Anal.* **25**, 294–318 (1988).

[48] B. Einfeldt, C.D. Munz, P.L. Roe, and B. Sjögreen, "On Godunov-type methods near low densities", *J. Comput. Phys.* **92**, 273–295 (1991).

[49] F. Eulderink and G. Mellema, "General relativistic hydrodynamics with a Roe solver", *Astronomy and Astrophysics Suppl.* **110**, 587–623 (1995).

[50] C.R. Evans, "A method for numerical relativity: Simulation of axisymmetric gravitational collapse and gravitational radiation generation" Ph.D. Thesis, The University of Texas at Austin, unpublished (1984).

[51] C.R. Evans, "Self-similarity: The heart of critical phenomena", in *Lecture Notes of the Numerical Relativity Conference, Penn State University, 1993,* unpublished (1993).

[52] C.R. Evans and J.S. Coleman, "Critical phenomena and self-similarity in the gravitational collapse of radiation fluid", *Phys. Rev. Lett.* **72** 1782-1785 (1994).

[53] T. Foglizzo and R.N. Henriksen, "General relativistic collapse of homothetic ideal gas spheres and planes", *Phys. Rev.* D **48**, 4645–4657 (1993).

[54] J.A. Font, J.Mª. Ibáñez, A. Marquina, and J.Mª Martí, "Multidimensional relativistic hydrodynamics: Characteristic fields and modern high-resolution shock-capturing schemes", *Astron. Astrophys.* **282**, 304–314 (1994).

[55] J.A. Font, M. Miller, W. Suen, and M. Tobias, "Three dimensional numerical general relativistic hydrodynamics I: Formulations, methods, and code tests", `gr-qc/9811015` (1998).

[56] J.A. Font, N. Stergioulas, and K.D Kokkotas, "Nonlinear hydrodynamical evolution of rotating relativistic stars: Numerical methods and code tests", *Mon. Not. R. Astron. Soc.* in press (1999); `gr-qc/9908010`.

[57] D. Garfinkle, "Choptuik scaling in null coordinates", *Phys. Rev.* D **51**, 5558–5561 (1995).

[58] S.K. Godunov *Mat. Sb.* **47,** 271 (1959).

[59] M. Goliath, "Self-Similar spherically symmetric perfect-fluid models", Filosofie Licenciatexamen, Stockholm University, unpublished (1998).

[60] M. Goliath, U.S. Nilsson, and C. Uggla, "Timelike self-similar spherically symmetric perfect-fluid models", *Class. Quantum Grav.* **15**, 2841–2863 (1998).

[61] J.B. Goodman and R.J. Leveque, "A geometric approach to high resolution TVD schemes", *SIAM J. Numer. Anal.* **25**, 268–284 (1988).

[62] N. Grossman, *The sheer joy of celestial mechanics,* (Boston, Birkhäuser, 1996).

[63] C. Gundlach, "Critical phenomena in gravitational collapse", *Adv. Theor. Math. Phys.* **2** 1-49 (1998); `gr-qc/9712084`.

[64] C. Gundlach, "Nonspherical perturbations of critical collapse and cosmic censorship", *Phys. Rev.* D **57**, R7075 (1998).

[65] C. Gundlach, "Angular momentum at the black hole threshold", *Phys. Rev.* D **57**, R7080 (1998).

[66] C. Gundlach, private communication (1999).

[67] C. Gundlach, "Critical gravitational collapse of a perfect fluid with $p = k\rho$: Nonspherical perturbations", `gr-qc/9906124` (1999).

[68] T. Hara, T. Koike, and S. Adachi, "Renormalization group and critical behavior in gravitational collapse", `gr-qc/9607010` (1996).

[69] A. Harten and J.M. Hyman, "Self-adjusting grid methods for one-dimensional hyperbolic conservation laws", *J. Comput. Phys.* **50**, 235–269 (1983).

[70] A.C. Hindmarsh, "ODEPACK, a systematized collection of ODE solvers", in *Scientific Computing,* edited by R.S Stepleman *et al.* (North-Holland, Amsterdam, 1983).

[71] J.Mª. Ibáñez, J.Mª Martí, J.A. Miralles and J.V. Romero, in *Approaches to Numerical Relativity,* ed. R. D'Inverno (Cambridge University Press, Cambridge, 1992).

[72] J.Mª. Ibáñez and J.Mª Martí, "Riemann solvers in relativistic astrophysics", *J. Comput. Appl. Math.* in press (1999).

[73] T. Koike, T. Hara, and S. Adachi, "Critical behaviour in gravitational collapse of radiation fluid: A renormalization group (linear perturbation) analysis", *Phys. Rev. Lett.* **74**, 5170–5173 (1995).

[74] T. Koike, T. Hara, and S. Adachi, "Critical behavior in gravitational collapse of a perfect fluid", *Phys. Rev.* D **59**, 104008 (1999).

[75] R.H. Kraichnan, "Special-relativistic derivation of generally covariant gravitation theory", *Phys. Rev.* **98**, 1118–1122 (1955).

[76] H.O. Kreiss and J. Oliger, *Methods for the approximate solution of time-dependent problems,* GARP Publication Series No. 10 (World Meteorological Organization, Geneva, 1973).

[77] L.D. Landau, *Fluid mechanics* (Pergamon Press, London, 1959).

[78] L.D. Landau and E.M. Lifshitz, *Fluid mechanics,* Second English edition (Pergamon Press, Oxford, 1987).

[79] R.J. LeVeque, *Numerical Methods for Conservation Laws* (Birkhaüser-Verlag, Basel, 1992).

[80] R.J. LeVeque, "Wave propagation algorithms for multidimensional hyperbolic systems", *J. Comput. Phys.* **131**, 327–353 (1997).

[81] R.J. LeVeque, "Nonlinear conservation laws and finite volume methods for astrophysical fluid flow", in *Computational Methods for Astrophysical Fluid Flow,* 27th Saas-Fee Advanced Course Lecture Notes (Springer-Verlag, Berlin, to be published); also available at `ftp://amath.washington.edu/pub/rjl/papers/saasfee.ps.gz` (1998).

[82] A. Lichnerowicz, *Relativistic hydrodynamics and magnetohydrodynamics* (W.A. Benjamin, New York, 1967).

[83] S.L. Liebling *Nonlinear field dynamics in general relativity: Black hole critical phenomena and topological defects*, Ph.D. Thesis, The University of Texas at Austin, unpublished (1998).

[84] M.K. Madsen, "A note on the equation of state of a scalar field", *Astrophys. Space Sci.* **113**, 205–207 (1985).

[85] M.K. Madsen, "Scalar fields in curved spacetimes", *Class. Quantum Grav.* **5**, 627–639 (1989).

[86] D. Maison, “Non-universality of critical behaviour in spherically symmetric gravitational collapse”, *Phys. Lett.* B **366**, 82–84 (1996).

[87] A. Marquina, “Local piecewise hyperbolic reconstruction of numerical fluxes for nonlinear scalar conservation laws”, *SIAM J. Sci. Comput.* **15**, 892–915 (1994).

[88] R.L. Marsa, *Radiative problems in black hole spacetimes*, Ph.D. Thesis, The University of Texas at Austin, unpublished (1995).

[89] J.M. Martí and E. Müller, “The analytical solution of the Riemann problem in relativistic hydrodynamics”, *J. Fluid Mech.* **258**, 317–333, (1994).

[90] J.M. Martí and E. Müller, “Extension of the piecewise-parabolic method to one-dimensional relativistic hydrodynamics”, *J. Comput. Phys.* **123**, 1–14 (1996).

[91] J.M. Martin-Garcia and C. Gundlach, “All non-spherical perturbations of the Choptuik space-time decay”, *Phys. Rev.* D **59**, 064031 (1999).

[92] M.M. May and R.H. White, “Hydrodynamic calculations of general-relativistic collapse”, *Phys. Rev.* **141**, 1232–1241 (1966).

[93] M. Miller, personal communication (1998).

[94] M. Miller, W.-M. Suen, and M. Tobias, “The Shapiro conjecture: Prompt or delayed collapse in the head-on collision of neutron stars?” `gr-qc/9904041` (1999).

[95] C.W. Misner, K.S. Thorne, and J.A. Wheeler, *Gravitation* (W.H. Freeman, San Francisco, 1973).

[96] D.W. Neilsen and M.W. Choptuik, “Critical phenomena in perfect fluids”, *Class. Quantum Grav.* in press (1999); `gr-qc/9812053`.

[97] D.W. Neilsen and M.W. Choptuik, "Ultrarelativistic fluid dynamics", *Class. Quantum Grav.* in press (1999); `gr-qc/9904052`.

[98] M.L. Norman and K-H.A. Winkler, "Why ultrarelativistic numerical hydrodynamics is difficult", in *Astrophysical Radiation Hydrodynamics*, edited by M.L. Norman and K-H.A. Winkler (Reidel, Dordrecht, 1986).

[99] T. Nozawa, N. Stergioulas, E. Gourgoulhon, and Y. Eriguchi, "Construction of highly accurate models of rotating neutron stars—comparison of three different numerical schemes", *Astron. & Astrophysics Suppl. Ser.* **132** 431–454 (1998); also `gr-qc/9804048`.

[100] A. Ori and T. Piran, "Naked singularities and other features of self-similar general-relativistic gravitational collapse", *Phys. Rev.* D **42**, 1068–1090 (1990).

[101] T.J.W. Perkins, "Exploration of critical phenomena and self-similarity in the gravitational collapse of perfect fluid", B.S. Honors Thesis, University of North Carolina at Chapel Hill, unpublished (1996).

[102] L.I. Petrich, S.L. Shapiro, and S.A. Teukolsky, "Accretion onto a moving black hole: an exact solution", *Phys. Rev. Lett.* **60**, 1781–1784 (1988).

[103] L.R. Petzold, *J. Sci. Stat. Comput.* **4**, 136 (1983).

[104] T. Piran, in *Gravitational Radiation*, edited by N. Druelle and T. Piran (North-Holland, Amsterdam, 1983).

[105] J.A. Pons, J.A. Font, J.M$^{\underline{a}}$. Ibáñez, J.M$^{\underline{a}}$. Martí, and J.A. Miralles, "General relativistic hydrodynamics with special relativistic Riemann solvers", *Astron. Astrophys.* **339** 638–642 (1998); `astro-ph/9807215`.

[106] J.J. Quirk, "A contribution to the great Riemann solver debate", *Int. J. Numer. Methods Fluids* **18**, 555–574 (1994).

[107] L.F. Richardson, "The approximate arithmetical solution by finite differences of physical problems involving differential equations, with an application to the stresses in a masonry dam", *Phil. Trans. Roy. Soc.* **210**, 307–357 (1910).

[108] M.D. Roberts, "A scalar polynomial singularity without an event horizon", *Gen. Rel. Grav.* **17**, 913–926 (1985).

[109] M.D. Roberts, "Spacetime exterior to a star", `gr-qc/9811093` (1998).

[110] P.L. Roe, "Approximate Riemannn solvers, parameter vectors, and difference schemes", *J. Comput. Phys.* **43**, 357–372 (1981).

[111] P.L. Roe, "Some contributions to the modeling of discontinuous flows," Lect. Notes Appl. Math. **22**, 163–193 (1985).

[112] J.V. Romero, J.Mª. Ibáñez, J.Mª. Martí, and J.A. Miralles, "A new spherically symmetric general relativistic hydrodynamical code", *ApJ* **462**, 839–854 (1996).

[113] M.A. Scheel, S.L. Shapiro, and S.A. Teukolsky, "Scalar gravitation: A laboratory for numerical relativity. III. Axisymmetry", *Phys. Rev.* D **49**, 1894–1905 (1994).

[114] V. Schneider, U. Katscher, D.H. Rischke, B. Waldhauser, J.A. Maruhn, and C-D. Munz, "New algorithms for ultra-relativistic numerical hydrodynamics", *J. Comput. Phys.* **105**, 92–107 (1993).

[115] B.F. Schutz, "Perfect fluids in general relativity: Velocity potentials and a variational principle", *Phys. Rev.* D **2**, 2762–2773 (1970).

[116] B.F. Schutz, *A first course in general relativity* (Cambridge University Press, Cambridge, 1985).

[117] S.L. Shapiro and S.A. Teukolsky, *Black holes, white dwarfs, and neutron stars: The physics of compact objects* (New York, John Wiley & Sons, 1983).

[118] S.L. Shapiro and S.A. Teukolsky, "Scalar gravitation: A laboratory for numerical relativity", *Phys. Rev.* D **47**, 1529–1540 (1992).

[119] S.L. Shapiro and S.A. Teukolsky, "Scalar gravitation: A laboratory for numerical relativity. II. Disks", *Phys. Rev.* D **49**, 1886–1893 (1994).

[120] S.L. Shapiro, "Head-on collision of neutron stars as a thought experiment," *Phys. Rev.* D **58** 103002 (1998).

[121] C-W. Shu and S. Osher, "Efficient Implementation of Essentially Non-oscillatory shock-capturing schemes", *J. Comput. Phys.* **77**, 439–471 (1988).

[122] C-W. Shu and S. Osher, "Efficient Implementation of Essentially Non-oscillatory shock-capturing schemes, II", *J. Comput. Phys.* **83**, 32–78 (1989).

[123] J. Smoller and B. Temple, "Global solutions of the relativistic Euler equations", *Commun. Math. Phys.* **156**, 67–99 (1993).

[124] R.F. Stark and T. Piran, "A general relativistic code for rotating axisymmetric configurations and gravitational radiation: numerical methods and tests," *Computer Phys. Reports* **5**, 221–264 (1987).

[125] J.M. Stewart, "Numerical relativity", in *Classical general relativity*, edited by W.B. Bonnor, J.N. Isham, and M.A.H. MacCallum (Cambridge University Press, Cambridge, 1984).

[126] J.L. Synge, *The relativistic gas* (North-Holland, Amsterdam, 1957).

[127] A.H. Taub, "On circulation in relativistic hydrodynamics", *Arch. Rat. Mech. Anal.* **3**, 312–324 (1959).

[128] A.H. Taub, "Relativistic hydrodynamics", in *Studies in applied mathematics* Volume 7, edited by A.H. Taub (Prentice-Hall, New York, 1971).

[129] J. Thornburg, "A 3+1 computational scheme for dynamics spherically symmetric black hole spacetimes. II. Time evolution", `gr-qc/9906022` (1999).

[130] B. van Leer, "Towards the ultimate conservative difference scheme. II. Monotonicity and conservation combined in a second-order scheme", *J. Comp. Phys.* **14**, 361–370 (1974).

[131] B. van Leer, "Towards the ultimate conservative difference scheme. IV. A new approach to numerical convection", *J. Comp. Phys.* **23**, 276–299 (1977).

[132] B. van Leer, "Towards the ultimate conservative difference scheme. V. A second-order sequel to Godunov's method", *J. Comp. Phys.* **32**, 101–136 (1979).

[133] K.A. van Riper, "The hydrodynamics of stellar collapse", *ApJ* **221**, 304–319 (1978).

[134] K.A. van Riper, "General relativistic hydrodynamics and the adiabatic collapse of stellar cores", *ApJ* **232**, 558–571 (1979).

[135] S. Weinberg, *Gravitation and cosmology: Principles and applications of the general theory of relativity* (John Wiley & Sons, New York, 1972).

[136] P.R. Woodward, "PPM: Piecewise-parabolic methods for astrophysical fluid dynamics", in *Astrophysical Radiation Hydrodynamics*, edited by M.L. Norman and K-H.A. Winkler (Reidel, Dordrecht, 1986).

[137] J.W. York, "Kinematics and dynamics of general relativity", in *Sources of gravitational radiation* edited by L.L. Smarr (Cambridge University Press, Cambridge, 1979).

[138] J.W. York "The initial value problem and dynamics", in *Gravitational Radiation*, edited by N. Deruelle and T. Piran (North-Holland, Amsterdam, 1983).

Vita

David Wayne Neilsen was born in Salt Lake City, Utah, on July 1, 1968, the son of Wayne Leland Neilsen and Wanda Mae Self. He attended Bingham High School in South Jordan, Utah, and then went on to better things at Brigham Young University. After serving a two-year mission for the Church of Jesus Christ of Latter-Day Saints in Vienna, Austria, he graduated with a BS in physics in April, 1992. David then began graduate work at Brigham Young University, studying Lie-Bäcklund symmetries in axisymmetric, rigidly rotating perfect fluids, receiving an M.S. in August, 1995. While finishing his thesis work, David wooed and courted Tracianne Beesley, and they were married in December, 1994. After graduation, David and Tracianne both entered the Graduate School at The University of Texas in August, 1995. While in the midst of numerical studies of relativistic fluids under the guidance of Matthew Choptuik, their daughter Grace was born in June, 1997. After graduation, David will continue as a Postdoctoral Fellow at the Center for Relativity.

Permanent Address: 2432 W 12600 S
Riverton, UT 84065

This dissertation was typeset with LaTeX 2_ε by the author.